Turbulent entrainment in flows induced by distributed buoyancy sources

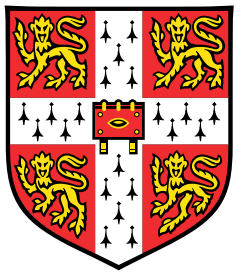

David Parker

Department of Applied Mathematics and Theoretical Physics
University of Cambridge

This dissertation is submitted for the degree of
Doctor of Philosophy

Magdalene College

September 2019

Declaration

This thesis is the result of my own work and includes nothing which is the outcome of work done in collaboration except as declared in the Preface and specified in the text. It is not substantially the same as any that I have submitted, or, is being concurrently submitted for a degree or diploma or other qualification at the University of Cambridge or any other University or similar institution except as declared in the Preface and specified in the text. I further state that no substantial part of my thesis has already been submitted, or, is being concurrently submitted for any such degree, diploma or other qualification at the University of Cambridge or any other University or similar institution except as declared in the Preface and specified in the text. It does not exceed the prescribed word limit for the relevant Degree Committee

David Parker
September 2019

Acknowledgements

First and foremost, I would like to thank my supervisor Professor Paul Linden for his guidance and support throughout my PhD. This gratitude is extended to Dr Henry Burridge who has acted as my co-supervisor and has taken the brunt of my stupid questions. I would also like to thank my industrial supervisor Dr Jake Hacker for his support and the sponsorship of Arup through the Industrial CASE studentship, in particular, for guiding the direction of chapter 6.

Thank you to the laboratory technicians, in particular David Pagecroft and Colin Hitch, who designed and built the excellent experimental apparatus used in this thesis.

This thesis would not be nearly as good without the help of Jamie Partridge who has taken the brunt of my *deliberately* stupid questions. *A friend first, and a boss second, probably an entertainer third.*

I was lucky to be part of the best office in Pavilion H, with two fantastic office mates Emily and Katherine and one particularly diligent frog, Dr Frog, and, although we rarely actually spoke about mathematics, they helped me, one way or another, through my PhD. An honourable mention goes to JP, who had the enviable experience of living with me for two years and always took his Croquet defeats so graciously, and Maksim, who has put up with my incessant questions about Russia.

There have been many others in Cambridge who have made my time there special and, outside of Cambridge, I am always grateful to the Welwyn boys, Patrick and of course my family.

Abstract

Free shear and wall-bounded buoyancy-driven turbulent flows occur in both natural environments and industrial situations. In this thesis, to better understand the entrainment process within these flows, experiments and theory have been used to investigate point and distributed buoyancy sources and, in particular, the effect of a bounding vertical wall on these flows.

A free shear flow was first investigated by performing velocity and scalar edge measurements on an axisymmetric plume created by a continuous point source release of buoyancy. By conditionally sampling the velocity measurements based on the presence of both eddies and plume fluid, engulfment, whereby large pockets of ambient are engulfed in to the plume, was shown to be a dominant turbulent entrainment process.

To isolate the effect of a wall on a turbulent buoyancy-driven flow, a line plume distant from all vertical boundaries and a wall plume, adjacent to a vertical wall were also studied. Simultaneous velocity and buoyancy field measurements were performed and a reduction in the net entrainment, and entrainment coefficient, for a wall plume were found. This reduction was investigated by considering an energy decomposition of the entrainment coefficient where the relative contributions of turbulent production, buoyancy and viscous terms were calculated. The reduced entrainment was also investigated by considering the statistics of the turbulent interface.

Finally, simultaneous velocity and buoyancy field measurements on a vertically distributed buoyant plume were performed by forcing relatively dense fluid through a very low porosity plate. A reduced entrainment coefficient, compared to that of a wall plume, was observed. In order to model the ventilation of a room with a heated or cooled wall the flow was then enclosed within a mechanically ventilated model room. The evolving and steady-state ambient stratification was measured using dye-attenuation with an LED-light bank for varying buoyancy fluxes and ventilation flow rates.

Table of contents

1 Introduction **1**

2 Theory **5**

3 Experimental details **15**
3.1 Salt-bath modelling 15
3.2 Particle Image Velocimetry 18
3.3 Planar laser-induced fluorescence 20

4 Turbulent axisymmetric plumes **21**
4.1 Introduction 21
4.2 Experimental details 25
4.2.1 Detecting the plume edges 32
4.3 Validation of the PIV Data 34
4.4 Results in an Eulerian coordinate system and discussion 38
4.4.1 The statistics of the scalar edges 39
4.4.2 Conditional results in an Eulerian coordinate system 40
4.4.2.1 The velocity field and fluxes when eddies are present and absent 45
4.4.2.2 The distribution, velocity profile and vertical transport of engulfed fluid 49
4.5 Results in a Plume coordinate system 54
4.5.0.1 Plume properties when eddies are present and absent . . . 56
4.6 Comparison with axisymmetric jets 61
4.7 Limitations of planar measurements in a three-dimensional flow 63
4.8 Conclusions 64

5 Turbulent free line and wall line plumes **67**
5.1 Introduction 67

5.2 Theory and previous work on entrainment in free and wall plumes 69
5.2.1 Energy decomposition of entrainment in turbulent wall plumes . . . 74
5.3 Experiments and analysis 77
5.3.1 Experimental details 77
5.3.1.1 Planar laser-induced fluorescence 85
5.3.1.2 Detection of the TNTI 88
5.4 Validation of the PIV and PLIF data 92
5.5 Results in an Eulerian coordinate system 93
5.5.1 Turbulent fluxes 93
5.5.2 Entrainment coefficient 95
5.5.2.1 Direct calculation of $\alpha_{viscous}$ 96
5.5.3 Entrainment flux 97
5.5.4 The statistics of the TNTI 100
5.5.4.1 Plume meandering mechanism 101
5.5.4.2 TNTI length 102
5.5.5 Conditional vertical transport 105
5.5.6 Discussion 106
5.6 Results in a plume coordinate system 107
5.6.1 Plume coordinate system definition 107
5.6.2 Velocity and buoyancy in plume coordinates 108
5.6.3 Turbulent fluctuations and fluxes in plume coordinates 111
5.6.4 Summary of results in the plume coordinate 113
5.7 Limitations of planar measurements in a three-dimensional flow 114
5.8 Integral turbulent Prandtl number for the free line plume 115
5.8.1 Integral Prandtl number model for the free line plume 116
5.8.2 Experimental measurements of the turbulent Prandtl number for the free line plume 120
5.9 Conclusions 122

6 Turbulent vertically distributed buoyant plumes 127
6.1 Introduction 127
6.2 Theory 129
6.3 Experiments and analysis 135
6.3.1 Experimental details 135
6.4 Results 140
6.4.1 Velocity measurements over the full height 140
6.4.2 Velocity and buoyancy measurements 144

6.4.3 Turbulent fluctuations . . . 147
6.4.4 Comparison with wall line plume . . . 149
6.5 Application to a confined space . . . 150
6.5.1 Sealed confined space . . . 150
6.5.2 Ventilated confined flow . . . 155
6.5.3 Experimental details . . . 158
6.5.4 Dye attenuation . . . 158
6.5.5 Results . . . 162
6.5.5.1 Filling-box experiment . . . 162
6.5.5.2 Mechanically ventilated experiments . . . 169
6.6 Conclusions . . . 175

7 Conclusions **177**
7.1 Review of findings . . . 177
7.1.1 Axisymmetric plume . . . 177
7.1.2 Free and wall line plume . . . 177
7.1.3 Vertically distributed plume . . . 179
7.2 Further work and applications . . . 180
7.3 Conclusions on turbulent entrainment . . . 181

References **183**

Appendix A **193**
A.1 Free and wall plume experiments . . . 193
A.2 Vertically distributed plume . . . 197
A.3 Calibration of extinction coefficients . . . 197

Chapter 1

Introduction

Turbulent flows driven by continuous buoyancy sources occur in both industrial and geophysical environments. This thesis considers four separate turbulent buoyancy-driven flows that often occur within industrial settings. Firstly, an axisymmetric plume, the result of a point source of buoyancy, that may occur for example as a result of the heat from a computer in an office. Secondly, a line plume, the result of a horizontal line source of buoyancy, that may occur within a building as a result of a chilled beam acting to cool down the room. Thirdly, a wall line plume, where a line plume is placed immediately adjacent to a wall, for example the region directly above a radiator. Finally, a vertically distributed buoyant plume, the result of a vertically distributed wall source of buoyancy, for example the downdraught resulting from a relatively cold, natural convective, flow from a glazed façade within a building in winter (Heiselberg, 1994).

Central to the modelling of the flows described above are 'plume models' that provide parametrisation of the turbulent mixing that occurs within the flow. The modelling of plumes dates back to Zeldovich (1937) who used the assumption of self-similarity combined with a mixing-length model (Prandtl, 1925), where the mixing-length was assumed to be proportional to the plume width, to derive a system of ordinary differential equations that determine the velocity and buoyancy profiles which, however, were not presented. Schmidt (1941) used a similar mixing-length model and presented numerical solutions of the velocity and buoyancy profiles. Taylor (1945) provided a simple yet effective alternative parametrisation based on macroscopic flow dynamics, where the mean horizontal entrained velocity is assumed to be directly proportional to a characteristic vertical velocity scale via a constant entrainment coefficient. Although Taylor (1945) was the first to propose the entrainment assumption the plume model is typically cited as the Morton et al. (1956) plume model. The value of the entrainment coefficient has been the focus of much work on plumes since the proposed model of Taylor (1945). Although there is reasonable consensus on the value of

the entrainment coefficient (van Reeuwijk and Craske, 2015) in an axisymmetric plume, the dynamical process of turbulent entrainment is not yet fully understood.

Compared to the numerous recent studies on axisymmetric plumes (e.g. Ezzamel et al. (2015); Van Reeuwijk et al. (2016)) the line plume has received relatively little attention, which may reflect the difficulty in experimentally achieving a line source of uniform buoyancy flux. There is, however, reasonable agreement on the entrainment value of the line plume.

The presence of a wall immediately adjacent to the line plume adds complexity to the simple plume theory of Morton et al. (1956), such as the addition of shear stress at the wall, and necessarily leads to the question of whether the flow is sufficiently self-similar. Despite their obvious applications, wall line plumes, referred to hereafter as wall plumes, have received very little attention, especially in the previous two decades where advancement in experimental techniques has led to a flurry of papers in other buoyancy-driven configurations. Of the few studies of wall plumes available (Grella and Faeth, 1975; Lai and Faeth, 1987; Sangras et al., 2000) there is agreement in the observation of significantly reduced entrainment as a result of the presence of the wall. However, the processes behind the reduction in entrainment, or indeed the turbulent entrainment process itself, were not investigated deeply.

Given the additional difficulty of producing a vertically distributed buoyancy source, the numerous recent studies on this flow (Cooper and Hunt, 2010; Gayen et al., 2016; Kaye and Cooper, 2018; McConnochie and Kerr, 2015) seems somewhat at odds with the lack of literature on wall plumes. However, of particular application to this problem, aside from the industrial application of heated or cooled walls, is the dissolution of vertical ice sheets. While there is a very large field of natural convective studies to guide this problem (see Miroshnichenko and Sheremet (2018) for a broad review of the numerical and experimental natural convective literature), the application of plume theory to the flow is relatively recent (Cooper and Hunt, 2010; Wells and Worster, 2008) with the motivation of providing simple yet robust models governing the melting of the ice and ultimately predicting future rises in sea level (Gayen et al., 2016). Despite the recent interest, however, there is relatively little consensus on the entrainment coefficient for this type of flow with reported values ranging across an order of magnitude.

Given that plume theory is able to simply and effectively model buoyancy sources frequently occurring within buildings, the plume theory of Morton et al. (1956) naturally lends itself well to the modelling of ventilation, and the resulting stratification that develops, within rooms. While the literature has primarily focussed on localised buoyancy sources by successfully modelling the developing stratifications resulting from a point source of buoy-

ancy within sealed or ventilated environments (Linden et al., 1990), adapting the theory to vertically distributed buoyancy sources to effectively model the developing stratification has proven more challenging (Bonnebaigt et al., 2018; Cooper and Hunt, 2010).

This thesis aims to extend the knowledge of plumes by performing high-resolution velocity and buoyancy measurements on the configurations described above. In doing so, we aim to aid consensus to the previously reported entrainment coefficients, particularly in the wall-bounded configurations described above, and provide insights into the dynamical entrainment process of both the free and wall-bounded flows, while examining the mechanisms that inhibit the entrainment of buoyancy-driven turbulent wall-bounded flows. Further, we provide buoyancy measurements of the sealed and mechanically ventilated vertically distributed buoyant plume.

Throughout this thesis, the introduction and description of the theory of the flows are mostly self-contained within the respective chapters so that they may be set in context with the various configurations studied. However, in chapters 2 and 3 we describe the theory of entrainment and experimental techniques which are common across all, or most, of the chapters.

In chapter 4 we present simultaneous two-dimensional velocity and scalar measurements on a central vertical plane in an axisymmetric pure turbulent plume. We use an edge-detection algorithm to determine the edge of the plume and compare the data obtained in both a fixed Eulerian frame and a dynamical plume coordinate system defined in terms of the instantaneous turbulent/non-turbulent interface (TNTI). In chapter 5 we present simultaneous two-dimensional measurements of the velocity and buoyancy fields on a central vertical plane in two-dimensional line plumes: a free plume distant from all vertical boundaries and a wall plume, adjacent to a vertical wall. Data are again presented in both an Eulerian frame of reference and a plume coordinate system that follows the instantaneous TNTI of the plume. In chapter 6 we present simultaneous velocity and buoyancy field measurements of a vertically distributed buoyancy source. The buoyancy source is created by forcing salt water through a plate with very low porosity, thus creating a distributed source. We then consider the confined sealed and confined ventilated flow and measure the resulting buoyancy stratification within the enclosure using dye attenuation. Finally, we present the conclusions of the thesis in chapter 7.

The structure of the thesis follows the chronological order of the plume configurations investigated. The sequence of investigations follows a path of increasing complexity in the flow configuration which broadly correlates with the currently available literature on that particular flow. That is, there are more studies on axisymmetric plumes than free line plumes and, similarly, more studies on free line plumes than wall line plumes. With this

in mind, the sequence of investigations was chosen deliberately; the results from the study of the axisymmetric plume are able to inform the free line plume study, which in turn are able to inform the wall line plume study which ultimately guide the investigation into the vertically distributed wall plume.

The material in chapter 4 comprises a significant proportion of the following collaborative publication

- Burridge, H., Parker, D., Kruger, E., Partridge, J., & Linden, P. (2017). Conditional sampling of a high Péclet number turbulent plume and the implications for entrainment. *Journal of Fluid Mechanics*, 823, 26-56.

Some of the analysis and material in the chapter was performed in collaboration, which we include to preserve the narrative of the work performed solely by the author and it is made clear in the chapter 4 sections as to where this is the case.

The material in chapter 5, with the exception of § 5.8, comprises the following publication

- Parker, D., Burridge, H., Partridge, J., & Linden, P. (2020). A comparison of entrainment in turbulent line plumes adjacent to and distant from a vertical wall. *Journal of Fluid Mechanics*, 882, A4.

The material presented in this chapter is the sole work of the author, however, an appendix related to this chapter was performed in collaboration as specified in the appendix.

Chapter 2

Theory

In this section we describe the theory of turbulent entrainment and introduce the classical plume entrainment model of Morton et al. (1956).

A continuous release of buoyant fluid into an ambient environment of uniform density leads to a buoyancy force on the surrounding fluid particles. This buoyancy force leads to convective motion. By assuming that gravity is aligned with the vertical acting in the negative direction, a positive buoyancy force results in a positive vertical (upward) motion of the fluid particles and vice versa. For the purposes of describing the theory we restrict attention to a positive buoyancy force. The continuous release of buoyancy, therefore, results in a continuous upward motion of buoyant fluid. Through mixing, and ultimately diffusion, buoyancy is imparted into the initially quiescent ambient fluid and, as a result, the volume flux of buoyant fluid increases with vertical distance from the buoyancy source. The term 'plume' has come to describe the flows resulting from a localised source of buoyancy, e.g. a point source or a horizontal line source which is localised within the plane normal to the line source, characterising the spread of buoyancy with vertical distance from the source.

In particular, we are concerned with the above process within a turbulent regime. This process may broadly be described as turbulent entrainment. Although turbulent entrainment is not restricted to the mixing of irrotational and turbulent fluid, or indeed the mixing of active scalars, in this thesis we define turbulent entrainment as the process by which momentum, through both pressure gradients and viscous effects at the plume edge, vorticity, through molecular diffusion (Batchelor, 1954), and the active scalar be it heat or a solute, through molecular diffusion, are conferred upon initially irrotational ambient fluid. The diffusion of scalars (i.e. heat or a solute) will occur wherever there are scalar gradients such as the interface between the turbulent plume and irrotational fluid, but also through scalar gradients within the turbulent plume. Turbulent mixing is the process whereby diffusion

is increased due to stretching of the scalar interfaces by the turbulent dynamics. Turbulent entrainment is a process whereby entrainment is enhanced through turbulent mixing.

In describing the theory we consider the case of the flow resulting from a point source of buoyancy flux, which results in a turbulent axisymmetric plume, however, the physical processes described are analogous in all the plumes considered in this thesis. We therefore first describe the coordinate system and introduce the flow quantities for an axisymmetric plume.

We adopt a cylindrical coordinate system, such that the point source of buoyancy flux is at the origin, and define the velocity $w(r,\phi,z,t)$ in the vertical z-direction, the velocity $u(r,\phi,z,t)$ in the radial r-direction, the plume and initial ambient density $\rho(r,\phi,z,t)$ and ρ_a, respectively, the buoyancy $b(r,\phi,z,t) = g(\rho_a - \rho(r,\phi,z,t))/\rho_a$ and the vorticity $\boldsymbol{\omega}(r,\phi,z,t)$. The pressure $p(r,\phi,z,t)$ is defined relative to the hydrostatic pressure so that $\mathrm{d}P(r,\phi,z,t)/\mathrm{d}z = \mathrm{d}p(r,\phi,z,t)/\mathrm{d}z + \rho_a g$, where $P(r,\phi,z,t)$ is the total pressure. Since the flows are statistically steady these quantities may be decomposed into time-averaged and fluctuating components $w(r,\phi,z,t) = \overline{w}(r,z) + w'(r,\phi,z,t)$, $u(r,\phi,z,t) = \overline{u}(r,z) + u'(r,\phi,z,t)$, $b(r,\phi,z,t) = \overline{b}(r,z) + b'(r,\phi,z,t)$, $\rho(r,\phi,z,t) = \overline{\rho}(r,z) + \rho'(r,\phi,z,t)$ and $p(r,\phi,z,t) = \overline{p}(r,z) + p'(r,\phi,z,t)$ where the overbar indicates the time-average. Further, we assume that the time-averaged flow quantities are statistically axisymmetric so that any gradients in the azimuthal direction vanish. We assume that the initial ambient environment is of uniform density and quiescent (which also implies the ambient is initially irrotational). We define, respectively, the time-averaged volume flux πQ, momentum flux πM, integral buoyancy πB and buoyancy flux πF per unit length by

$$Q(z) = 2\int_0^\infty r\overline{w}(r,z)\mathrm{d}r, \tag{2.1}$$

$$M(z) = 2\int_0^\infty r\overline{w}^2(r,z)\mathrm{d}r, \tag{2.2}$$

$$B(z) = 2\int_0^\infty r\overline{b}(r,z)\mathrm{d}r, \tag{2.3}$$

$$F(z) = 2\int_0^\infty r\overline{w}(r,z)\overline{b}(r,z)\mathrm{d}r. \tag{2.4}$$

A characteristic plume width R, vertical velocity scale W and plume buoyancy scale G may then be defined as

$$R = \frac{Q}{M^{1/2}}, \tag{2.5}$$

$$W = \frac{M}{Q}, \tag{2.6}$$

$$G = \frac{F}{Q}. \tag{2.7}$$

Before describing the mechanisms of turbulent entrainment, it is useful to introduce the mechanisms of vorticity production. By examining the vorticity equation we may examine the contributions that result in an increase in the vorticity magnitude. The vorticity equation for an incompressible fluid is given by

$$\frac{\mathrm{D}\boldsymbol{\omega}}{\mathrm{D}t} = (\boldsymbol{\omega}\cdot\nabla)\,\boldsymbol{u} + \nu\nabla^2\boldsymbol{\omega} + \nabla P \times \nabla\left(\frac{1}{\rho}\right), \tag{2.8}$$

where $\frac{\mathrm{D}}{\mathrm{D}t} = \frac{\partial}{\partial t} + \boldsymbol{u}\cdot\nabla$ is the material derivative. The following discussion describes a three-dimensional flow.

The first term on the right hand side (rhs) of (2.8) represents vortex stretching; when the velocity is aligned with the direction of the vorticity the fluid elements are stretched along this direction and, due to the conservation of volume flux and angular momentum, the vorticity magnitude increases. The opposite process may be defined as vortex squeezing, however, on average vortex stretching occurs more often than vortex squeezing which results in the energy cascade of three-dimensional turbulent flow from large to small scales of motion.

The second term on the rhs of (2.8) represents the diffusion of vorticity via viscous diffusion and is directly analogous to the diffusion of momentum. As in the case of the momentum equation, it may be shown that vorticity diffusion is important only at sufficiently small length scales.

The final term on the rhs of (2.8) represents the baroclinic generation of vorticity (which is not present in flows of uniform density) and is largest where the pressure gradient is normal to the density gradient. This term, therefore, provides an additional vorticity generating mechanism as compared to non-buoyant flows.

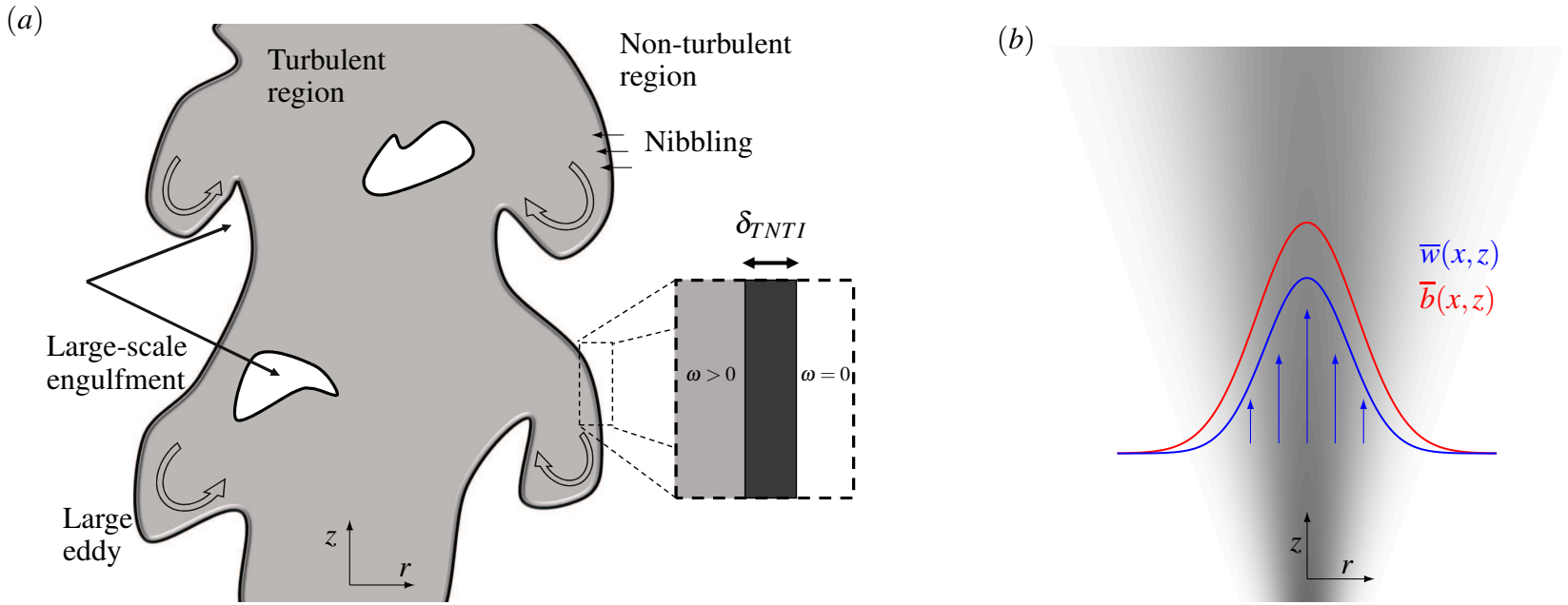

Fig. 2.1 (*a*) Schematic of an instantaneous cross-section of the buoyancy field of a turbulent axisymmetric plume in a vertical plane aligned with the source. The irrotational non-turbulent ambient region and turbulent region are separated by a turbulent/non-turbulent interface (TNTI) with thickness δ_{TNTI} (see (*a*) inset). Large-scale processes, including large eddies and engulfment, and small-scale processes, such as nibbling, are represented. (*b*) Time-average schematic of the cross-section of the buoyancy field showing the typical Gaussian-like time-averaged vertical velocity $w(r,z)$ (blue) and buoyancy $b(r,z)$ (red) profiles.

Sufficiently far from the plume source, the flow will consist of a turbulent plume region and an irrotational ambient region separated by a turbulent/non-turbulent interface (TNTI). Figure 2.1 (*a*) shows a schematic of the instantaneous buoyancy field resulting from a point source of buoyancy in a vertical plane aligned with the source. Figure 2.1 (*a*) highlights the instantaneous view of entrainment in a plume: turbulent entrainment is a multi-scale continuous process in which ambient fluid is drawn in from the far-field and, at the large scales, fluxes are transported over relatively smooth surfaces at relatively high velocities, for example via the process of engulfment, and, at the small scales, transport occurs across the TNTI, with thickness δ_{TNTI}, at relatively low velocities. As the schematic shows, through entrainment, the initially irrotational fluid acquires vorticity across the TNTI. The TNTI consists of two layers: the viscous superlayer, which is adjacent to the ambient fluid, and the turbulent sublayer, which is adjacent to the turbulent region and the viscous superlayer (da Silva et al., 2014). An initially irrotational and homogeneous fluid element can only acquire vorticity through molecular diffusion (Batchelor, 1954), so that a viscous superlayer imparts vorticity to the ambient fluid while contributing negligible vorticity production. The turbulent sublayer matches the vorticity magnitude between the turbulent plume region and the viscous superlayer. A viscous superlayer separating turbulent and non-turbulent regions was first proposed by Corrsin and Kistler (1955), where it was suggested that *'its thickness should be less than a length characterising vorticity fluctuations on the turbulent side of the boundary'*, in other words the Taylor microscale, and might be the same order as the Kolmogorov length scale. Experimental and numerical observations have confirmed that the viscous superlayer is of the order of the Taylor microscale in jets, mixing layers and wakes (Attili and Bisetti, 2012; Bisset et al., 2002; da Silva and Taveira, 2010; Mistry et al., 2016), whereas in shear-free turbulence the viscous superlayer is of the order of the Kolmogorov length scale (da Silva and Taveira, 2010; Holzner et al., 2011). A review of the previous literature on TNTIs is given in § 4.1.

Given the complexity of the entrainment process and the common applications of plume theory models, which mostly require only knowledge of the average bulk flow quantities, entrainment is typically parametrised by considering the time-averaged flow. Figure 2.1 (*b*) shows a schematic of the time-averaged flow considered in figure 2.1 (*a*), whereby ambient fluid is drawn in from the far-field and momentum, buoyancy and vorticity are gradually imparted to the ambient fluid since the TNTI is no longer defined. Although a well defined plume boundary, such as the TNTI, is not defined, the characteristic plume width R may be defined as the plume 'edge'. The entrainment model of Taylor (1945) assumes that the velocity of entrained fluid u_e at the plume 'edge' may be expressed in terms of the characteristic vertical velocity via a constant entrainment coefficient α, that must be empirically

determined, so that $u_e = -\alpha W$. Through both experimental and numerical investigations, the parametrisation of Morton et al. (1956) has been shown to provide remarkably effective descriptions of both buoyancy and momentum-driven turbulent flows, including axisymmetric plumes (Ezzamel et al., 2015; Van Reeuwijk et al., 2016), free line plumes (Paillat and Kaminski, 2014a; Ramaprian and Chandrasekhara, 1989), jets (Mistry et al., 2016) and vortex rings (Olsthoorn and Dalziel, 2017).

In order to derive a set of closed plume conservation equations, Morton et al. (1956) additionally assumed that the density differences between plume and initial density of the ambient were small and that the first-order mean flow quantities (velocity and buoyancy) were self-similar. We discuss these in the following derivation of the plume conservation equations for an axisymmetric turbulent plume.

The incompressible Reynolds-averaged continuity, streamwise momentum and buoyancy equations are given by

$$\frac{1}{r}\frac{\partial}{\partial r}\left(r\overline{u}\right) + \frac{\partial \overline{w}}{\partial z} = 0, \tag{2.9}$$

$$\overline{\rho}\frac{1}{r}\frac{\partial}{\partial r}\left(r\overline{uw} + r\overline{u'w'}\right) + \overline{\rho}\frac{\partial}{\partial z}\left(\overline{w}^2 + \overline{w'^2}\right) = -\frac{\partial \overline{p}}{\partial z} + g(\rho_a - \overline{\rho}) + \mu\nabla^2\overline{w}, \tag{2.10}$$

$$\frac{1}{r}\frac{\partial}{\partial r}\left(r\overline{u}\overline{b} + r\overline{u'b'}\right) + \frac{\partial}{\partial z}\left(\overline{w}\overline{b} + \overline{w'b'}\right) = \kappa\nabla^2\overline{b}, \tag{2.11}$$

where μ and κ are the dynamic viscosity and molecular diffusivity of the fluid, respectively. Integration of (2.9) gives

$$0 = \int_0^\infty \frac{1}{r}\frac{\partial}{\partial r}\left(r\overline{u}\right) r\mathrm{d}r + \int_0^\infty \frac{\partial \overline{w}}{\partial z} r\mathrm{d}r, \tag{2.12}$$

$$= \left(\overline{u}r\right)\big|_0^\infty + \frac{\mathrm{d}}{\mathrm{d}z}\int_0^\infty r\overline{w}\mathrm{d}r. \tag{2.13}$$

The entrainment assumption of Taylor (1945), by using continuity, may be expressed as $\left(\overline{u}r\right)\big|_{r=\infty} = -\alpha WR$ (van Reeuwijk and Craske, 2015). Using the entrainment assumption and the definitions given in (2.5), equation (2.13) results in the relation

$$\frac{\mathrm{d}Q}{\mathrm{d}z} = 2\alpha M^{1/2}. \tag{2.14}$$

By assuming high Reynolds number *Re*, which characterises the ratio of inertial to viscous forces, and high Péclet number *Pe*, which characterises the ratio of convective to diffusive

heat/molecular transfer, defined as

$$Re = \frac{WR}{\nu}, \qquad Pe = Re\frac{\nu}{\kappa}, \tag{2.15}$$

where $\nu = \mu/\rho$ is the kinematic viscosity of the fluid, the viscous term $\mu\nabla^2\overline{w}$ in the momentum equation (2.10) and the molecular diffusion term $\kappa\nabla^2\overline{b}$ in the buoyancy equation (2.11) may be neglected. Further, as assumed by Morton et al. (1956), only small deviations in the density field relative to the initial ambient density are assumed (i.e. $\overline{\rho} - \rho_a \ll \rho_a$) so that the Boussinesq approximation may be invoked by using ρ_a as a reference density. Under these assumptions integration of (2.10) gives

$$\left(r\overline{uw} + r\overline{u'w'}\right)\Big|_0^\infty + \frac{\mathrm{d}}{\mathrm{d}z}\int_0^\infty \overline{w}^2 r + \overline{w'^2} r \mathrm{d}z = \int_0^\infty -\frac{1}{\rho_a}\frac{\partial\overline{p}}{\partial z}r + \overline{b}r\mathrm{d}z. \tag{2.16}$$

By using the boundary conditions $\overline{w}|_{r=\infty} = \overline{u'w'}\big|_{r=\infty} = 0$, (2.16) becomes

$$\frac{\mathrm{d}M}{\mathrm{d}z} = B - 2\int_0^\infty \overline{w'^2} r + \frac{1}{\rho_a}\frac{\partial\overline{p}}{\partial z}r\mathrm{d}z. \tag{2.17}$$

The contributions from the integral of the velocity fluctuations and pressure term are neglected in the original first-order integral plume model of Morton et al. (1956); this is partially due to fact that the pressure term is extremely difficult to measure experimentally. Second-order plume integral models typically approximate the pressure by $\overline{p} \approx (\overline{u'^2} + \overline{v'^2})/2$, where v is the velocity fluctuation in the azimuthal direction. A recent direct numerical simulation (DNS) study by Van Reeuwijk et al. (2016) showed the approximation to be valid to within 20%. However, measuring the three velocity components simultaneously is challenging; this thesis is restricted to measurements in the w and u direction only. We therefore restrict attention to the first-order integral model.

A non-dimensional buoyancy flux, θ, may be defined as

$$\theta = \frac{FQ}{BM}, \tag{2.18}$$

which may be used to close equation (2.17) so that we finally have the plume momentum conservation equation

$$\frac{\mathrm{d}M}{\mathrm{d}z} = \frac{FQ}{\theta M}. \tag{2.19}$$

The third assumption of Morton et al. (1956) was that the mean flow quantities are self-similar. This is consistent with a constant entrainment coefficient. This assumption allows

the vertical velocity, horizontal velocity and buoyancy to be expressed as

$$\overline{w}(r,z) = W(z)f(r/R), \tag{2.20}$$

$$\overline{u}(r,z) = W(z)g(r/R), \tag{2.21}$$

$$\overline{b}(r,z) = G(z)h(r/R), \tag{2.22}$$

where f, g and h are non-dimensional similarity profiles. This similarity assumption results in constant θ (van Reeuwijk and Craske, 2015).

Using the boundary conditions $\overline{b}\big|_{r=\infty} = \overline{u'b'}\big|_{r=\infty} = 0$, and ignoring the diffusion term on the right hand side of (2.11), integration of (2.11) gives

$$\frac{\mathrm{d}}{\mathrm{d}z}\int_0^\infty r\overline{w}\overline{b} + r\overline{w'b'}\mathrm{d}r = 0. \tag{2.23}$$

Assuming similarity of the second-order statistics, in particular that

$$\overline{w'b'}(r,z) = W(z)G(z)j(r/R), \tag{2.24}$$

suggests that

$$\frac{\int_0^\infty r\overline{w'b'}\mathrm{d}r}{\int_0^\infty r\overline{w}\overline{b}\mathrm{d}r} = \lambda = \text{const.}, \tag{2.25}$$

so that (2.23) may be expressed as

$$(1+\lambda)\frac{\mathrm{d}F}{\mathrm{d}z} = 0. \tag{2.26}$$

The first-order integral plume conservations equations may therefore be expressed as

$$\frac{\mathrm{d}Q}{\mathrm{d}z} = 2\alpha M^{1/2}, \tag{2.27}$$

$$\frac{\mathrm{d}M}{\mathrm{d}z} = \frac{FQ}{\theta M}, \tag{2.28}$$

$$\frac{\mathrm{d}F}{\mathrm{d}z} = 0, \tag{2.29}$$

with solutions given by

$$Q(z) = \frac{6}{5}\left(\frac{9}{10}\right)^{1/3} \alpha^{4/3}\theta^{-1/3}F^{1/3}z^{5/3}, \tag{2.30}$$

$$M(z) = \left(\frac{9}{10}\right)^{2/3} \alpha^{2/3}\theta^{-2/3}F^{2/3}z^{4/3}, \tag{2.31}$$

$$F(z) = F = \text{const.}, \tag{2.32}$$

which results in the following relations for the characteristic plume quantities

$$R(z) = \frac{6}{5}\left(\frac{9}{10}\right)^{1/3} \alpha^{4/3}\theta^{-1/3}F^{1/3}z^{5/3}, \tag{2.33}$$

$$W(z) = \frac{5}{6}\left(\frac{9}{10}\right)^{1/3} \alpha^{-2/3}\theta^{-1/3}F^{1/3}z^{-1/3}, \tag{2.34}$$

$$G(z) = \frac{5}{6}\left(\frac{9}{10}\right)^{-1/3} \alpha^{-4/3}\theta^{1/3}F^{2/3}z^{-5/3}. \tag{2.35}$$

The similarity profiles f and g are determined from experimental or numerical measurements and in most cases it is not necessary to define an associated analytical function that approximately follows the observations. However, in some cases theoretical models, for example the integral Prandtl number model of Craske et al. (2017), may benefit from ascribing analytic functions to the plume profiles. These typically take the form of the Gaussian profiles

$$f(r/R) = \exp\left(-\left(\frac{r}{k_w R}\right)^2\right), \tag{2.36}$$

$$h(r/R) = \exp\left(-\left(\frac{r}{k_b R}\right)^2\right), \tag{2.37}$$

where k_w and the k_g are shape profile constants. While these profiles have been shown to provide an accurate model of experimental measurements (e.g. Shabbir and George, 1994), there are some limitations to this assumed model based on experimental observations. Most notably, a Gaussian profile is non-zero everywhere, whereas experiments are performed in bounded environments so that both boundary effects and characteristics resulting from the finite boundary, such as negative velocities in the far-field resulting from conservation of volume flux, will affect the observed plume profile.

The derivations of the plume conservations equations for the other configurations considered in this thesis are contained within the respective chapters.

Chapter 3

Experimental details

The primary focus of this thesis is the experimental investigation of turbulent buoyancy-driven plumes. In-depth descriptions of the experiments are given in context in their respective sections. However, all, or a majority, of the experiments share techniques which we describe here.

3.1 Salt-bath modelling

The motivation for the experiments are primarily concerned with heat-driven industrial or environmental flows in air. In order to model the full scale flows accurately, dynamic similarity must be achieved. This relies on matching the characteristic parameters of the flow, in particular the Reynolds number and the Péclet number which may be expressed by

$$Re = \frac{\left(bH^3\right)^{1/2}}{\nu}, \qquad Pe = \frac{\left(bH^3\right)^{1/2}}{\kappa}, \tag{3.1}$$

respectively, where H is the characteristic height of the flow, ν is the kinematic viscosity of the fluid and κ is the scalar diffusivity. The buoyancy $b = g\Delta\rho/\rho = g\beta\Delta T$, where ΔT is the temperature difference and β is the fluid thermal expansion coefficient. In order to achieve dynamic similarity in our experiments we use the salt-bath modelling approach of Linden et al. (1990), whereby sodium chloride solution, and in our case sodium nitrate solution, is used to achieve relatively dense fluid.

Large density differences may be achieved using salt water as compared to heat in air while maintaining the Boussinesq approximation, with $b_F \sim 0.1\,\mathrm{m\,s^{-2}}$ and $b_M \sim 0.5\,\mathrm{m\,s^{-2}}$ so that $b_F \ll b_M$, where the subscripts 'M, F' refer to the model and full scales, respectively. Further, $\nu_F \approx 10^{-5}\,\mathrm{m^2\,s^{-1}}$ and $\nu_M \approx 10^{-6}\,\mathrm{m^2\,s^{-1}}$ so that $\nu_F \gg \nu_M$ and $\kappa_F \approx 10^{-5}\,\mathrm{m^2\,s^{-1}}$ and

Ion	Diffusivity ($10^{-9}\,\mathrm{m^2\,s^{-1}}$)
Cl^-	2.032
Na^+	1.334
NO_3^-	1.902

Table 3.1 The diffusivities of the ionic species used in the sodium chloride and sodium nitrate solutions. The table is replicated from Olsthoorn and Dalziel (2017), however the data can be found in Rumble (2019).

$\kappa_M \approx 10^{-9}\,\mathrm{m^2\,s^{-1}}$ so that $\kappa_F \gg \kappa_M$, where κ_F is the diffusivity of heat in air and κ_M is the diffusivity of salt in water, and comparing the vertical extent of the experiments considered in this thesis, $H_M \sim 1\,\mathrm{m}$, to the vertical extent of industrial applications, $H_F \sim 10\,\mathrm{m}$, gives $H_F \gg H_M$. Therefore, by suitable choice of the experimental parameters $Re_F \sim Re_M$. To ensure that $Pe_F \sim Pe_M$ is more challenging while maintaining similarity in Re, however, Crapper and Linden (1974) suggest that rate of turbulent entrainment is independent of the Péclet number for $Pe > 10^4$ which is applicable in the full scale flow and easily achieved in the salt-bath model.

The main advantage of salt-bath modelling over full-scale measurements is that, given the relatively small scale of the experiments, flow-visualisation is straightforward and measurements over a relatively large proportion of the flow may be performed. Salt-bath modelling also has a clear advantage over (water) heat-bath modelling, since the refractive indices of sodium chloride and sodium nitrate can be almost exactly matched at different densities. This is crucial for high precision velocity measurements using particle image velocimetry (PIV), described below in § 3.2, and density measurements using planar laser-induced fluorescence (PLIF), described in § 5.3.1.1. Figure 3.1 shows the densities of the sodium chloride and sodium nitrate aqueous solutions as a function of the refractive index at a wavelength of 589 nm. The data are taken from Rumble (2019). A least-squares quadratic curve was fitted to the data in each case which gives the following relation between density ρ and refractive index n for sodium chloride aqueous solution

$$\rho_{NaCl} - \rho_0 = 5.13(n-n_0)^2 + 4.04(n-n_0), \tag{3.2}$$

and sodium nitrate aqueous solution

$$\rho_{NaNO_3} - \rho_0 = 18.41(n-n_0)^2 + 5.89(n-n_0), \tag{3.3}$$

where the subscript 0 is the measured quantity in pure water.

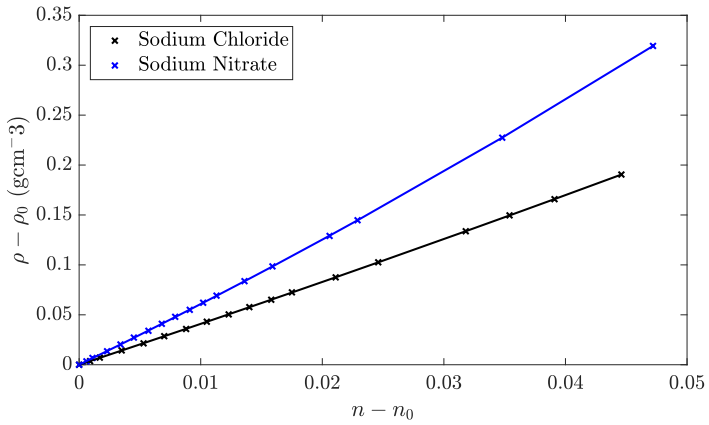

Fig. 3.1 Refractive indices of sodium chloride (black) and sodium nitrate (blue) aqueous solutions at a wavelength of 589 nm and temperature at 20 °C. The data are taken from Rumble (2019) and a least-squares quadratic curve (solid lines) is shown in each case as given in (3.2) and (3.3).

The saturation of the sodium chloride and sodium nitrate solutions occur at approximately $\rho_{NaCl} = 1.18 \times 10^3\,\mathrm{kg\,m^{-3}}$ and $\rho_{NaNO_3} = 1.31 \times 10^3\,\mathrm{kg\,m^{-3}}$. This results in a range of possible relative density differences of

$$0 \leq \frac{\rho_{NaNO_3} - \rho_{NaCl}}{\rho_{NaCl}} \leq 0.085, \tag{3.4}$$

such that the two solutions have matching refractive indices. The combination of sodium chloride and sodium nitrate as working fluids has successfully been used in experimental studies of turbulent flows by Olsthoorn and Dalziel (2017) and Linden et al. (2018). Olsthoorn and Dalziel (2017) highlight that the diffusion rate of the two salts are not significantly different since they have a similar molecular mass and the difference in the ionic diffusivity between chlorine and nitrate is significantly lower than the ionic diffusivity of both NaCl and $NaNO_3$ (see table 3.1). This suggests that double diffusion will not play a significant role in the flows. Further, given the Schmidt number of the flows, $Sc = \nu/\kappa \approx 700$, the transport of scalar by diffusion is expected to be small compared to the turbulent transport of scalar, based on a Reynolds number of $Re \approx 1000$ in our experiments, i.e. $Pe = ReSc \gg 1$. This is discussed further in the section outlining the experimental details of the axisymmetric plume experiments in § 4.2.

3.2 Particle Image Velocimetry

In order to measure the velocity field of the experiments we use particle image velocimetry (PIV). PIV is a non-intrusive experimental technique for computing the velocity field aligned with a plane from a recording of the flow. In our case, a fixed vertical plane is illuminated using a thin light sheet so that the motion of tracer particles seeded in the fluid may be recorded. Figure 3.2 shows an example of a cropped region of a typical PIV image taken from the free line plume experiments described in chapter 5. This results in a sequence of images, separated by a small time-step Δt, of particle images. By measuring the displacement of the particles between each time-step from the images the velocity may be determined. The images are split into interrogation windows of size $n \times n$ pixels^2 per vector, which overlap by 50%, and a single displacement vector, defined at the central point of the window, is then determined for each window by using pattern matching techniques. This results in a velocity field resolution of $n/2$ pixels. A 50% overlap was chosen to improve the resolution of the velocity measurements. High overlaps will add no new information but it is common in the literature for overlaps in the range $50-75\%$ (Prasad, 2000).

Polyamide particles with a mean diameter in the range $2-5\times10^{-2}\,\mathrm{mm}$ and density $1.02\times10^{3}\,\mathrm{kg\,m^{-3}}$ were added to the ambient, and in some configurations the source fluid, to act as tracer particles. The images of the particles appear larger than their physical size due to the scattering of the light by the particles and the optics. All the PIV experiments studied in this thesis were started with an initially quiescent ambient environment. This involved mixing the seeding particles within the ambient and allowing the tank to settle for approximately 30 minutes. It was therefore necessary to approximately match the density of the ambient fluid and the seeding particles, to both ensure there remains a high seeding density in the measurement window when the experiment is started and to minimise the settling velocity of the particles. The settling velocity w_s of the particles may be calculated using Stokes' law which results in

$$w_s = \frac{9}{8}\frac{b_p d^2}{\nu}, \tag{3.5}$$

where d and b_p are the diameter and buoyancy of the particle, respectively. We perform the calculation for the axisymmetric plume experiments in chapter 4 which results in $w_s = 0.027\,\mathrm{mm\,s^{-1}}$ compared to typical velocities measured at the plume centreline of $w_c = 60\,\mathrm{mm\,s^{-1}}$, so that $w_s/w_c \approx 5\times10^{-4}$. The other configurations considered in this thesis result in corresponding values of $w_s/w_c < 10^{-3}$. We therefore may ignore the motion of the seeding particles due to their own weight.

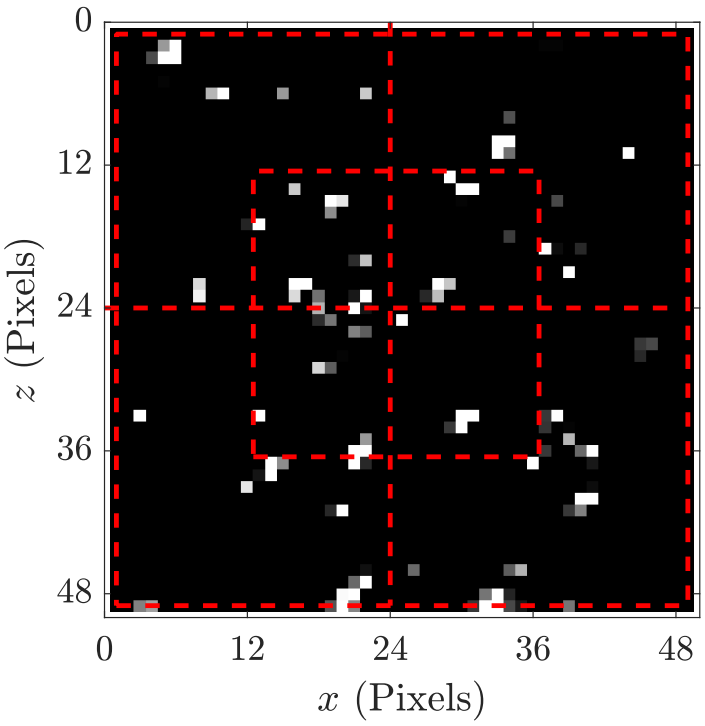

Fig. 3.2 A cropped region with dimension 48×48 pixels^2 of an instantaneous image from the PIV capture of a free plume experiment in chapter 5 demonstrating the typical seeding density and the relative (image) particle diameter to pixel size. The figure image shows five interrogation windows each of dimension 24×24 pixels^2 with an overlap of 50% (12 pixels) where the resulting velocity vectors will be determined for the central point of each interrogation window. The seeding density is approximately 10 particles per interrogation window.

To ensure accurate PIV measurements the seeding density (the number of seeding particles per interrogation window) must be sufficiently high to provide reliable pattern matching, however must not be so high as to saturate the image and reduce the quality of the signal as the scattered light passes from the light sheet to the camera. An average seeding density of 10 particles per interrogation window is standard for most PIV algorithms. The time-step Δt between the recorded images is chosen so that the maximum velocities of the particles are less than $\Delta x/2\Delta t$, where Δx is the size of the interrogation window. The PIV computations in this thesis were calculated using DigiFlow (Dalziel Research Partners), details of which may be found in Dalziel (2017), where in § 4 the 2014a Digiflow PIV algorithm was used and in § 5 and § 6 the 2017a Digiflow PIV algorithm was used. With the correct seeding density and time-step the PIV algorithm is able to compute particle displacement to an accuracy of 0.02 pixel.

3.3 Planar laser-induced fluorescence

In order to measure the density field along a vertical plane, fluorescent tracer is mixed in to the source plume fluid and a thin light-sheet, illuminated using the laser, excites the fluorescent tracer. The light intensity P of the fluoresced dye at a given local illumination intensity I exhibits a linear relationship with the dye concentration c (Shan et al., 2004), $P \propto g(I)c$, where g is a function of the local illumination intensity (the form of which need not be known). By assuming that the system is optically thin, that is to assume that the dye absorption does not produce significant variations in I, $g(I)$ remains approximately constant. Assuming that the density of the source plume fluid is directly proportional to the concentration, the light intensity of the fluoresced tracer is then directly proportional to the density of the plume fluid. Further assuming that the intensity response of the camera is known, then the density of the fluid may be inferred from the camera intensity response. This technique is popularly known as planar laser-induced fluorescence (PLIF). While this method has successfully been used on previous buoyancy-driven configurations (e.g. Linden et al. (2018); Odier et al. (2014); Olsthoorn and Dalziel (2017)) there are numerous difficulties associated with the technique. These mostly arise from the error associated with the variation in light intensity at a particular point in space due to fluctuations of the laser intensity and the variable attenuation of the laser light path. The method of PLIF is described in detail, along with a discussion of the errors associated with the technique, in § 5.3.1.1 since it is helpful to describe the technique in context with the particular experimental configuration.

Chapter 4

Turbulent axisymmetric plumes

In this chapter we examine a turbulent axisymmetric plume. The plume is created using a continuous point source release of relatively dense salt water solution and velocity and scalar field measurements are performed on a vertical two-dimensional plane aligned with the mean centreline of the plume. Some of the material presented in this chapter was performed in collaboration and we indicate using footnotes to section titles where this is the case.

4.1 Introduction

Turbulent plumes are of real significance to the environment and the economy. For example, in 2010 plumes produced by the eruption of the Icelandic volcano *Eyjafjallajökull* and the *Deepwater Horizon* oil leak in the Gulf of Mexico had huge environmental impacts and very significant economic consequences. The impact of such events and the ultimate fate of the plume fluid, often containing pollutants or contaminants, is largely determined by turbulent entrainment by the plume. The focus of this study is to examine the mechanisms responsible for this turbulent entrainment through an experimental investigation of saline plumes in a freshwater environment. At the largest scale turbulent entrainment in plumes may be viewed as the action by which ambient fluid is drawn in towards the central axis (or plane in the two-dimensional case) of the plume. At the smallest scale it is the process by which irreversible mixing of ambient and plume fluid occurs as a result of molecular interactions.

In this chapter, we consider the canonical case of a plume produced by a steady localised source of buoyancy within a quiescent environment of uniform density. The flow is examined sufficiently far from the source such that the ratio of inertia and buoyancy within the plume has obtained an invariant balance in which the flow is described as being a 'pure-plume'. By making simultaneous measurements of the flow velocities, using particle image

velocimetry (PIV), and the scalar edge, using planar light induced fluorescence (PLIF), of high Péclet number saline plumes we show that vertical velocities at, and outside, the edge of the plume are significant. The vertical velocities at the plume edge agree with recent measurements obtained by tracking the evolution of coherent structures at the plume edge that showed these structures travel at approximately 30% of the centreline velocity (Burridge et al., 2016). We further identify significant vertical mass transport outside the plume associated with these vertical velocities.

As we define in chapter 2, turbulent entrainment is the process by which momentum, through both pressure gradients and viscous effects at the plume edge, vorticity, through molecular diffusion, and the active scalar through molecular diffusion, are conferred upon initially irrotational ambient fluid. Here, we focus on the large-scale aspects of entrainment.

Much attention has been devoted to parameterising the process of turbulent entrainment in plumes, starting from the early closure models (e.g. Morton et al., 1956; Priestley and Ball, 1955) to closures accounting for higher order effects (e.g. Carazzo et al., 2006; Kaminski et al., 2005). More recent studies have contributed a wealth of experimental and numerical data in order to guide the parameterisation, and indeed choice, of the closure model and improve the understanding of the entrainment process (e.g. Ezzamel et al., 2015; van Reeuwijk and Craske, 2015). Other studies, presumably inspired by the work of Corrsin and Kistler (1955), have sought to untangle the complexities of turbulent flows by considering the entrainment and mixing across 'surfaces' within the flow. The study by Prasad and Sreenivasan (1989), for example, reasoned that since, at large scales, dramatic differences are evident between the various canonical turbulent flows in which entrainment is a crucial process (e.g. jets, boundary layers, mixing layers and wakes) it was reasonable to seek universality in, and hence generate a fundamental understanding of, the processes at the small scales. Their elegant theoretical considerations, assuming Reynolds number independence, identified relationships for the transport across surfaces within the flow at a wide range of spatial scales. They identified a degree of universality in the fractal dimension of the turbulent/non-turbulent interfaces (TNTI) in turbulent boundary layers, jets, wakes and mixing layers.

Turbulent flow statistics are heavily utilised in the study of turbulent entrainment. While time-averaged statistics are typically used, some authors have sought to separate the turbulent and non-turbulent flow properties via conditional statistics. Townsend (1948) introduced the use of the intermittency factor, the mean fractional duration of turbulent flow at any given point, in the context of a turbulent wake resulting from the flow past a heated cylinder. A radial profile of the intermittency factor may used to determine the variation in position, relative to its mean, of the TNTI. While the variation in the position of the

TNTI may easily be calculated from flow visualisation and edge detection techniques widely available today, such techniques were not so readily available at the time of publication of Townsend (1948). In addition to the measure of the TNTI variation, Townsend (1949a) and Townsend (1949b) suggested that the intermittency could be used to recover conditional time-averages of flow quantities in the turbulent region from the full-time averaged flow quantities, based on the assumption that certain flow quantities are negligible in the non-turbulent region. Corrsin and Kistler (1955) outlined further restrictions on obtaining mean turbulent-region flow quantities in this way. Townsend (1976) outlined how to obtain valid mean turbulent-region flow quantities irrespective of the restrictions outlined by Corrsin and Kistler (1955) by utilising 'gate' signals in the flow-quantity average. Conditional statistics, for both turbulent and non-turbulent quantities, have since been widely used for a variety of applications including the calculation of the conditional Prandtl number in a turbulent wake (Antonia and Browne, 1987) and the calculation of vertical transport of unmixed 'engulfed' fluid within a jet (Bisset et al., 2002; Westerweel et al., 2009).

Some recent studies have decomposed the process of turbulent entrainment by describing the large-scale incorporation of ambient fluid as 'engulfment' and the smaller scale actions at the interface between turbulent and non-turbulent fluids as 'nibbling'. It is not immediately obvious that such a distinction offers real merit but, at the very least, the widespread use of the terms in recent literature requires that they cannot be ignored. For example, some studies have suggested that engulfment does not contribute significantly to the process. In their study of turbulent jets, Westerweel et al. (2009) suggested that "*the entrainment process is dominated by small-scale eddying at the highly sheared interface ('nibbling'), with large-scale engulfment making a small (less than 10%) contribution*". Studies of high Reynolds number boundary layers (de Silva et al., 2013; Philip et al., 2014) examining the transport and fractal dimensions of the TNTI within the flow draw quite different conclusions. For example Philip et al. (2014) state "*large-scale transport due to energy-containing eddies determines the overall rate of entrainment, while viscous effects at the smallest scale provide the mechanism ultimately responsible for entrainment*".

The process of turbulent entrainment in a plume must ultimately result in fluid being irreversibly mixed at scales on which molecular diffusivity dominates (the Batchelor scale). This irreversible mixing is well known to occur at greatly enhanced rates due to the stretching of surfaces by the vorticity in turbulent flows (Ottino, 1989). For irreversible mixing to occur efficiently it is therefore evident that prior to this, at some larger scale, vorticity must be imparted to the fluid entrained from the ambient environment. This imparting of vorticity has been shown to occur due to viscous stresses at the interface between turbulent and non-turbulent flow at a length scale close to the Taylor microscale (Terashima et al.,

2016), where the Taylor microscale characterises the largest length scale in which viscous dissipation significantly affects the turbulent dynamics of the flow. It is this process that has been termed 'nibbling' and for the ultimate mixing to be efficient one must expect that all entrained fluid undergoes this nibbling process prior to being mixed. In this regard the importance of nibbling within the process of turbulent entrainment must not be overlooked. The nibbling process has also been shown to be enhanced in buoyancy driven flows; (Krug et al., 2017) decomposed the entrainment flux local to the TNTI of a temporal plume into relative contributions and observed a relatively significant contribution from the term representing baroclinic torque. A similar approach was performed in Krug et al. (2015) for an inclined gravity current, however a negligible contribution from the baroclinic torque was observed. These studies suggest that the role of baroclinic torque is important in configurations only where the streamwise direction is approximately aligned with gravity such as axisymmetric plumes studied in this chapter.

It, therefore, remains to define 'engulfment' in a meaningful sense. In the spirit of other studies, we define engulfment as the transport of ambient fluid to within the envelope of the turbulent flow at scales larger than the Taylor microscale in order to distinguish these large scale processes process from nibbling. This envelope is defined by the loci of the outermost points at which turbulent mixed plume fluid is found at a given instant, with mixed plume fluid being defined as all fluid of a density altered by the presence of the plume source. One can then describe the transport of ambient fluid across the envelope of the turbulent flow as being engulfment if, during this transport, local to the envelope edge there is insignificant mixing (as distinct from stirring). As such, one must expect engulfment to be driven by large-scale coherent structures (eddies) near the envelope edge. It is then reasonable to ask how significant is this process of engulfment within turbulent entrainment? For example, does engulfment contribute significantly to the stretching of the TNTI (required to enhance transport by nibbling) and smaller-scale surfaces (required for efficient mixing) within the flow?

In this chapter we investigate the role of engulfment in turbulent entrainment by plumes. We argue that without the large-scale action of engulfment one might expect the process of nibbling to be the rate-limiting process within entrainment. Through simultaneous PIV and PLIF measurements, Mistry et al. (2016) examine the TNTI in a turbulent jet. They conclude that the entrainment in jets is a multi-scale continuous process in which, at the large scales, fluxes are transported over relatively smooth surfaces at relatively high velocities and, at the small scales, transport occurs across contorted surfaces at relatively low velocities. Our findings, based on measurements in plumes, provide a view of the entrainment which is consistent with that reported by Philip et al. (2014) for turbulent boundary layers and Mistry

et al. (2016) for turbulent jets and, akin to Philip et al. (2014), we suggest that engulfment is the rate-limiting process for the turbulent entrainment by plumes.

It is our intention to provide new insights into the process of turbulent entrainment and we analyse our data in a manner different to that which has typically been carried out in the study of the TNTI in other flows (a detailed review of which is presented by da Silva et al., 2014). We provide simultaneous PIV and PLIF measurements in turbulent high Péclet number plumes (§ 4.2) and define the edge of the plume by identifying the outermost edge of the high Schmidt number scalar field. In § 4.3 we provide a robust validation of our PIV measurements by comparing our measurements to theoretical, experimental and numerical results presented for plumes in other studies. Our results (§ 4.4) initially examine the statistics of the plume edge (§ 4.4.1).

In § 4.4.2 we couple our PIV measurements with those for the plume edge, using Heaviside step functions to provide insights into the process of entrainment by examining the velocity profiles and the fluxes conditional on being inside or outside the plume and whether eddies within the plume are present or absent. In § 4.4.2.2 we present results for engulfment as part of the process of entrainment. We then present results for the velocity field in coordinates which follow the meandering and fluctuations in width of the plume (§ 4.5). By identifying events according to whether large-scale plume eddies are present or absent we include conditional averages of these statistics (§ 4.5.0.1), and use our measurements to provide statistical reconstructions of the velocity field in and around the plume.

4.2 Experimental details[1]

The experiments were designed to create high Péclet number turbulent plumes that would enable us to collect data on the instantaneous scalar edges of the plume while simultaneously measuring the velocity field. The experiments were performed in a glass tank of horizontal cross-section $1.00\,\mathrm{m} \times 0.80\,\mathrm{m}$ filled with dilute saline solution (of uniform density ρ_a) to a depth of $0.85\,\mathrm{m}$. Relatively dense source fluid was supplied via an apparatus providing a constant gravitational head, thereby ensuring a steady flow, to a plume nozzle of radius $r_0 = 2.5\,\mathrm{mm}$ that was rigidly clamped centrally within the walls of the tank and near the free surface. The Reynolds numbers at the source across the experiments, given in table 4.1, are relatively low and would typically describe laminar flow. The plume nozzle (illustrated in figure 4.1) was specifically designed to promote turbulence at the source based on a design originally developed by Dr Paul Cooper of the Faculty of Engineering, University of

[1]The experiments were performed in collaboration with Emily Kruger.

Parameter	Definition	Plume 1	Plumes 2 and 3
At the source			
Volume flux	$\pi Q_0\,[\times 10^{-6}\,\mathrm{m^3\,s^{-1}}]$	1.27	1.78
Buoyancy	$b_0\,[\mathrm{m\,s^{-2}}]$	0.734	0.791
Source radius	$r_0\,[\times 10^{-3}\,\mathrm{m}]$	2.5	2.5
Source Reynolds number	$Re = 2Q_0/r_0\nu$	320	450
Plume parameter	$\Gamma_0 = 5r_0^5 b_0/8\alpha Q_0^2$	2.49	1.37
In the measurement region			
Distance from the origin		$64 \leq z/r_0 \leq 130$	
Volume flux	$\pi Q\,[\times 10^{-6}\,\mathrm{m^3\,s^{-1}}]$	$53 \leq \pi Q \leq 196$	
Plume width	$R = Q/M^{1/2}\,[\times 10^{-2}\,\mathrm{m}]$	$2.25 \leq R \leq 4.50$	
Reynolds number	$Re = \overline{w}_c R/\nu$	$2\,380 \leq Re \leq 4\,490$	
Péclet number	$Pe = Re\,\mathrm{Sc}\,[\times 10^6]$	$1.19 \leq Pe \leq 2.24$	
Kolmogorov length scale	$\eta = R/Re^{3/4}\,[\times 10^{-4}\,\mathrm{m}]$	$1.15 \leq \eta \leq 1.64$	
Batchelor length scale	$\lambda_B = \eta/Sc^{1/2}\,[\times 10^{-6}\,\mathrm{m}]$	$5.13 \leq \lambda_B \leq 7.34$	
Pixel scale	$[\times 10^{-4}\,\mathrm{m\,pixel^{-1}}]$	0.95 – 1.05	
PIV scale	$[\times 10^{-3}\,\mathrm{m\,pixel^{-1}}]$	1.5 – 1.7	

Table 4.1 Experimental parameters for the three plumes studied at both the source and in the region of examination.

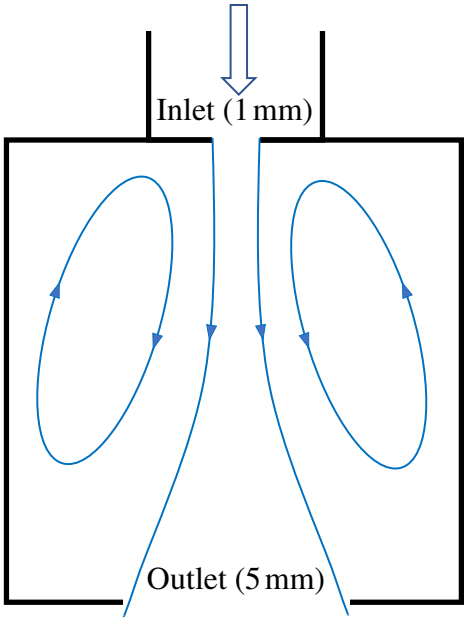

Fig. 4.1 Schematic of the plume nozzle used in the experiments (not to scale) showing the time-averaged streamlines of the flow inside the nozzle chamber. The small inlet causes a sharp expansion in the chamber creating a recirculation region resulting in turbulence at the outlet. The nozzle is based on a design originally developed by Paul Cooper (see text) and the schematic is based on figure 10 in Kaye and Linden (2004).

Wollongong, NSW, Australia. The source volume flux, πQ_0, was precisely controlled using a needle valve.

The source fluid was an aqueous saline (NaCl) solution of density ρ_0 with reduced gravity (buoyancy) at the source in the range $0.734\,\mathrm{m\,s^{-2}} \leq b \equiv g(\rho_0 - \rho_a)/\rho_a \leq 0.791\,\mathrm{m\,s^{-2}}$. With this set-up we created plumes with (conserved) buoyancy fluxes πF_0 in the range $0.93 \times 10^{-6}\,\mathrm{m^4\,s^{-3}} \leq \pi F_0 \equiv \pi F \leq 1.42 \times 10^{-6}\,\mathrm{m^4\,s^{-3}}$. Three experimental plumes were analysed, two of which were of notionally identical source conditions in order to assess the repeatability of the experiments. The experimental parameters are provided in table 4.1. Throughout § 4.3 and § 4.4 we present results from all three plumes. No significant bias could be identified between the datasets of each plume, implying that the experiments were repeatable and that all three plumes exhibit identical behaviours which we show to be consistent with that expected for self-similar turbulent pure-plumes, see § 4.3. Hence, these three experiments were sufficient to provide statistically significant data to assess the process of entrainment in pure plumes.

We collected data within a vertical region sufficiently far from the source so that the plumes were both fully turbulent and were notionally pure, i.e. the plumes had attained an invariant balance between inertia and buoyancy. As such we created plumes which, at

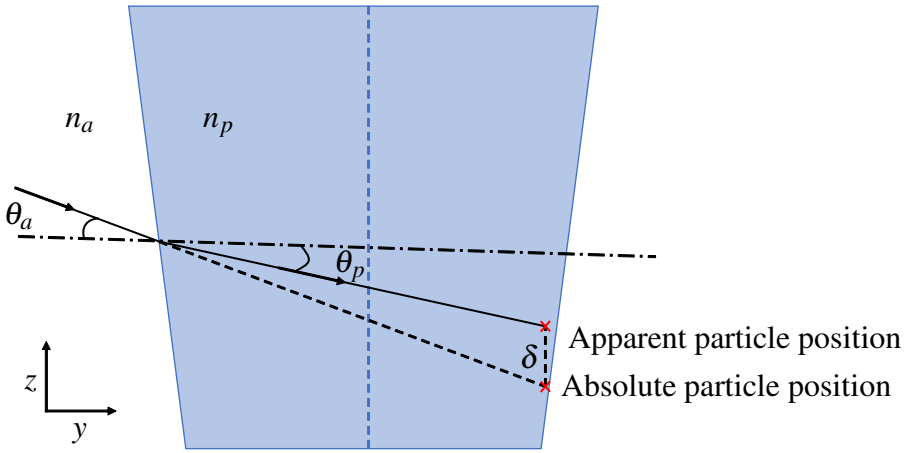

Fig. 4.2 A schematic showing the calculation used to estimate the error δ in the apparent particle position compared to the absolute particle position during the experiments as a result of the varying refractive index of the fluid. The calculation uses Snell's law based on the refractive indices of the ambient, n_a, and plume fluid, n_p, respectively. The y direction is normal to the measurement plane and the deviation in the plume boundary relative to the vertical is neglected.

the source, were relatively close to being pure or slightly lazy, as indicated by the source plume parameter $\Gamma_0 = 5r_0^5 b_0/8\alpha Q_0^2 \gtrsim 1$ (see table 4.1), where $\alpha = 0.11$ is the entrainment coefficient, the value of which is determined in § 4.3. The appropriate length scale is the source scale r_0 (Hunt and Kaye, 2001) and, to ensure that the flow can be expected to be in a pure-plume balance, we allowed the flow to develop for at least sixty dominate length scales, $60\,r_0 \approx 0.15\,\mathrm{m}$ from the source before the flow entered the region in which we recorded data.

We took care to ensure that within this region reliable PIV measurements were obtained, for example by ensuring that the level of PIV particle seeding was appropriate and that the 50 µm diameter particles were approximately neutrally buoyant (by filling the tank with a dilute saline solution, such that $\rho_a = 1.02 \times 10^3\,\mathrm{kg\,m^{-3}}$, so that the Stokes settling velocity of the particles, $w_s = 2.7 \times 10^{-5}\,\mathrm{m\,s^{-1}}$, was small compared with the typical velocities measured on the plume centreline $\overline{w}_c \approx 6 \times 10^{-2}\,\mathrm{m\,s^{-1}}$). Moreover, by selecting our measurement region a suitably large distance from the plume source we ensured that, due to the rapid dilution of the buoyancy scalar that results from the turbulent entrainment by plumes, the variations in refractive index did not significantly affect our results; within the measurement window characteristic normalised density differences were in the range $0.065\% - 0.148\%$. As a qualitative measure that the refractive variations were small we always verified that the PIV particles were clearly visible in the raw images, which provides a 'line of sight' integrated indication that the refractive index variations were not significant.

More quantitatively, using scalings from plume theory it is possible to calculate estimates of the refractive index variations within the plume within our measurement region, i.e. $b_p \sim z^{-5/3}$ and so $\Delta n \sim z^{-5/3}$, where Δn is the difference in refractive index between the plume fluid and the ambient fluid. By assuming the top-hat plume model, where the density difference is assumed to span the entire plume width (with both the density difference and width evolving as the plume descends and entrains), the greatest refractive index variations occur at the top of the measurement region (closest to the source), for which $\Delta n \sim 10^{-4}$. At this height plume fluid with this refractive index jump spanning the entire width of the plume (see figure 4.2) implies a maximum error due to refractive index variations of $\delta \sim 0.1$ pixels (or $O(10^{-5})$ m). The refraction introduces an apparent shift to the particles and therefore an error in the absolute location (of less than a pixel as discussed). However, providing the mixing, and therefore change in refractive index, is slow compared to the acquisition of the images the error in the velocity fields themselves will be less severe, with only an error on absolute position of the velocity vector (Dalziel et al., 2007). This estimate shows that refractive index variations did not affect our ability to detect the plume edges (to within an accuracy of one pixel), and only affects the accuracy of our velocity measurements at the sub-pixel resolution. Hence we do not expect our results to be affected by the experimental uncertainties arising from differences in refractive index.

For severe refractive index mismatch, the particles will become hard to discern and even relatively small refractive index mismatch can cause the particles to appear out of focus which will hinder the pattern matching. Unfortunately, when dealing with stratified flows and even nominally refractive index matched fluids, residual refractive index mismatch will remain. The nature of the PIV algorithm can deal with this to an extent through the effective averaging of the velocity field over a number of particles in an interrogation window.

From our PIV measurements we were able to check that our measurements of the velocity field exhibit the scaling relations expected for self-similar turbulent pure-plumes and compare well with existing data sets. We provide a full validation of the PIV measurements in § 4.3.

From our PIV measurements we obtain the time-averaged vertical velocity

$$\overline{w}(x, y = 0, z) = \frac{1}{T} \int_0^T w(x, y = 0, z, t) \, \mathrm{d}t \,, \tag{4.1}$$

as a function of the horizontal coordinate x, the vertical coordinate z and we assume that the light sheet is aligned with the plane $y = 0$. The total recording time is given by T. For the remainder of this chapter we adopt the cylindrical coordinate notation (r, z), where it is implied that $r = r(x, y = 0)$. We then define the time-averaged fluxes of volume πQ,

momentum πM, and a characteristic radial scale R by

$$Q = \int_0^\infty r\,\overline{w}(r,z)\,\mathrm{d}r \;,\quad M = \int_0^\infty r\,\overline{w}(r,z)^2\,\mathrm{d}r\,,\quad \text{and}\quad R = \frac{Q}{M^{1/2}}\,, \tag{4.2}$$

respectively. We note that throughout we reserve the 'overbar symbol' to denote a time-average. The integrals in (4.2) were performed across the whole width of the interrogation window, measuring approximately 0.18 m. The integrals are affected by both the noise in the far field ambient and the backward flow resulting from the finite tank. The effect of the noise on the volume flux integral is assumed to be negligible, assuming zero-mean noise. The contribution of noise to the momentum flux may be estimated from assuming an error in the PIV measurements of 0.02 pixels per frame, as discussed in § 3.2, which corresponds to $0.19\,\mathrm{mm\,s^{-1}}$. Using this value in the momentum flux integral gives a value of $1.9\times10^{-10}\,\mathrm{m^4\,s^{-2}}$. The time-averaged momentum flux across the plume experiments is in the range $2.0\times10^{-6}\,\mathrm{m^4\,s^{-2}}$ to $6.3\times10^{-6}\,\mathrm{m^4\,s^{-2}}$, suggesting that the contribution from the ambient noise is negligible.

The backward flow in the tank may be estimated from the volume flux of the plume and the tank dimensions, resulting in an average velocity of $-0.25\,\mathrm{mm\,s^{-1}}$. This value is comparable to the value of the PIV error, so it is not expected to significantly affect the momentum flux as demonstrated above.

In order to obtain simultaneous measurements of the scalar edge of the plumes we added a small quantity (approximately $5\times10^{-4}\,\mathrm{kg\,m^{-3}}$) of sodium fluorescein to the source saline solution in order to stain the plume fluid. Lighting the central plane within the plume, we recorded images of both the light emitted by the fluorescein and that reflected by the PIV particles. Given that the molecular diffusivity of the dye (sodium fluorescein) and the buoyancy scalar (sodium chloride) are similar and that the flow was high Péclet number (see table 4.1), we could be certain that by tracking the light emitted by the fluorescein we were tracking the location of the plume buoyancy scalar.

For logistical reasons we used broad spectrum white light generated by three arc lamps (rather than a laser) to illuminate a central (vertical) plane within the plume. We positioned the arc lamps behind vertical slits separated by a width of 2 mm (created using thin sheets of metal) to create a light sheet which was approximately 20 mm thick at the centre of the measuring window, suggesting that that thickness of the light sheet varied by at most 20% of the centreline thickness. A plumbline was temporarily attached through the nozzle outlet in order to align the light sheet with the centreline of the plume. As a result of using broad spectrum light, we were unable to use narrow band light filters in order to distinguish between the light emitted by the flourescein and that reflected by the PIV particles. To mitigate

this restriction, care was taken to tune the light levels within the recorded images with the aim that: (i) ambient fluid was of near zero light intensity, (ii) PIV particles were indicated by bright, near saturated, light levels, and (iii) mixed plume fluid was of intermediate light levels (approximately halfway between pure black and pure white). These were achieved by adjusting both the fluorescein concentration and the camera aperture while keeping the arc lamp light intensity fixed. Such careful tuning of the light levels took considerable effort and, due to the rapid dilution of plume fluid resulting from turbulent entrainment of ambient fluid, reliable results were only obtained over approximately half the vertical height (1,400 pixel rows) within the images.

Moreover, at least in part due to the light reflected by the PIV particles, it was not possible to measure precisely the scalar concentration from the light intensity levels within the images captured. Consequently, we do not report results for the full scalar field within the plumes. However, we were able to reliably detect the scalar edges of the plume from our measurements of light intensity (see § 4.2.1) thereby enabling us to report new results on turbulent plumes. Due to the number of arc lamps used we initially found that they produced a significant level of heat, driving a convective flow at the walls of the tank. In order to reduce this effect we displaced the metal sheets (that created the slits) slightly from the walls of the tank in order to provide a small air gap between them. With the metal sheets displaced the flow at the sides of the tank was no longer observable and so did not affect our results.

Once the correct lighting had been established so that both the plume edge and PIV particles were visible, experiments were carried out in darkened surroundings. The experiments were captured using a Dalsa Falcon 2 4 megapixel 8-bit camera with a 85 mm f1.8 Nikon lens. The camera was positioned normal to the vertical light sheet to capture a measurement window that was approximately 0.25 m ($100\,r_0$) high by 0.18 m ($72\,r_0$) wide. Images were recorded at 50 frames per second over recording durations of 240 s, providing datasets of 12 001 individual images per experiment. The equal time spacing between images resulted in PIV datasets containing 12 000 observations per experiment. For each experiment the entire PIV dataset was used when calculating full time-averaged statistics and appropriate subsets used when calculating conditional averages. For example, statistics for eddy present and eddy absent events (e.g. § 4.5.0.1) were calculated from datasets of approximately 2 000 observations. Spatially the PIV data were obtained from particle pattern correlations in regions measuring 32×32 pixels^2 with a 50% overlap, i.e. one vector in every 16×16 pixel^2 region.

In addition to the source conditions, table 4.1 provides the Reynolds number, $Re = \overline{w}_c\, R/\nu$ (where $\overline{w}_c$ is the time-averaged velocity on the plume centreline and ν the kinematic viscos-

ity), and Péclet number, $Pe = ReSc$ (where $Sc = \nu/\kappa$ is the Schmidt number, with κ the molecular diffusivity of NaCl in water), of the plumes within the region of examination. Following Papantoniou and List (1989) we calculate the Kolmogorov length scale $\eta = R/Re^{3/4}$ and the Batchelor scale $\lambda_B = \eta/Sc^{1/2}$, as indicative of the scales at which viscous and diffusive effects are dominant. Table 4.1 shows that the resolution of our measurements of the scalar edge were well above the Batchelor scale, suggesting that the effects of diffusion at these scales are negligible.

4.2.1 Detecting the plume edges[2]

A crucial step in our analysis was to detect the scalar edge of the plume reliably. This was possible since, as discussed above, the length scale at which molecular diffusion is expected to dominate, the Batchelor scale, was small (between $5 \times 10^{-6}\,\mathrm{m} - 7.5 \times 10^{-6}\,\mathrm{m}$) compared to one pixel ($10^{-4}\,\mathrm{m}$) but remains challenging due the nature of the turbulent billows at the plume edge. Purely for the purposes of visualisation by eye, we first inverted the recorded light intensities within the images so that plume fluid appeared dark while the background appeared light. In order to enable the detection of the plume edges we removed the PIV particles from the images by subjecting them to a (minimum) nearest-neighbour filter (of tuned spatial extent).

To gain confidence in the edges detected we employed two independent edge-detection algorithms. Our standard algorithm first overlaid edges onto the normalised image (these edges were identified using the Canny algorithm, provided within Matlab (Canny, 1986)) and then identified the two plume edges within each pixel row from the maximum (positive) and minimum (negative) horizontal light intensity gradient. Our alternate algorithm identified a threshold light intensity which changed for each pixel row (height) within each image (time) and defined the plume edges as the first and last location at which the light intensity fell below the threshold value. This threshold value was defined as the light intensity at which a minimum occurred, between the two peaks (corresponding to the presence and absence of plume fluid) in the histogram of light intensity within the given pixel row (similar methods based on the histogram of light intensity have been successfully used to detect scalar interfaces in other studies e.g. Gampert et al., 2014). Full details of the two algorithms are provided in Appendix B of Burridge et al. (2016). The edges detected by the two fundamentally different algorithms typically agreed well with each other. However, on occasion, differences between the algorithms did arise (see for example figure 4.3 (*a*)). Consequently, we calculated all statistics using the edges detected by each algorithm, and in

[2]The edge detection was performed in collaboration with Henry Burridge.

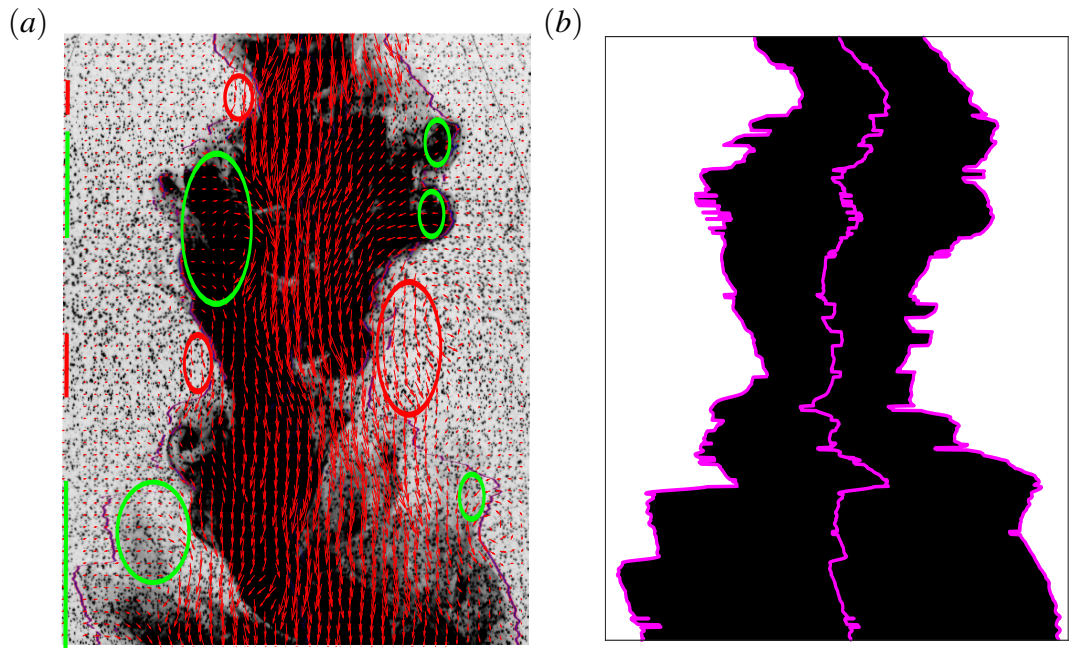

Fig. 4.3 (*a*) A typical experimental image of a plume. The small dark 'spots' in the image are the 50 μm particles used to obtain PIV measurements. Dense 'plume fluid', stained by dye, is indicated by dark regions. The edges detected by both algorithms are marked by the red solid lines (7 pixels wide) and blue solid lines (3 pixels wide). Velocity vectors (red arrows) indicate the local two-dimensional velocity on the vertical central plane of the plume. Notice that where large-scale eddies are locally present the vertical velocities are small just outside and inside the plume edge (circled in green). At the locations where eddies are locally absent the vertical velocities outside the plume are significant (circled in red). (*b*) An image of the plume envelope determined from (*a*). The left edges $E_L(z,t)$, right edges $E_R(z,t)$ and mid point between the left and right edges, defined by $\left(E_L(z,t)+E_R(z,t)\right)/2$, are highlighted by the magenta lines. For clarity, the edges shown are from a single edge detection algorithm corresponding to the blue edges in (*a*).

figures 4.10, 4.11, 4.13, 4.14, 4.9, 4.16, 4.17 and 4.18 we plot the statistics calculated using both algorithms. Crucially, as can be seen from the data in these figures, any differences between the detected edges were minor and did not significantly alter our results.

Figure 4.3 (*a*) shows a typical image of a plume in which red and blue solid lines mark the outermost edges (the plume envelope) detected by each algorithm and highlight the broad agreement between the two independent edge detection algorithms. From the distance between the edges, at any given height we define the instantaneous plume width based on the scalar field edge, denoted $2R_p(z,t)$, from which we calculate the mean (time-averaged) plume half-width $\overline{R_p(z)}$ based on edges of the scalar field, and we define a coordinate r_p following the plume (see § 4.5. Furthermore, from these measurements we define the (instantaneous) plume envelope as the loci of the outermost points at which (turbulent) mixed plume fluid is found at a given instant (mixed plume fluid being all fluid of a density altered by the presence of the plume source). In our experiments on high Péclet number plumes mixed plume fluid is inferred from the light intensity levels indicative of dye concentration.

Due to the finite thickness of the light sheet the images are effectively averaged (via some weighted average depending on the light sheet cross-section intensity profile) in the *y*-direction over this thickness. Assuming that the light intensity is Gaussian within the sheet, then the images will be weighted to the centre of the light sheet as we desire. This could be reduced using a laser as the light source with better control over the focusing of the light. Unfortunately, such technology was not available at the time of this work. The finite light sheet thickness also results in an effective averaging of the velocity field. However, the thickness of the light sheet is approximately equal to the PIV vector spacing which already provides a limit to the precision obtainable.

In figure 4.3 (*a*) the two-dimensional velocity vectors obtained from the PIV analysis are overlaid as red arrows. The heights at which eddies were deemed to be present (see § 4.4.2.1) are highlighted by the green bars on the left edges of the images. The vertical velocities just outside the plume edge in these regions are almost zero. The heights at which plume eddies were deemed to be absent are highlighted by the red bars on the left edges of the images and in these regions the vertical velocities outside the plume are significant. We return to these observations in § 4.5.0.1.

4.3 Validation of the PIV Data

We validate the PIV data by checking for self-similarity in the velocity distributions and evaluating the entrainment coefficient. Figure 4.4 displays the vertical and radial velocity distributions for 80 different heights normalised by the theoretical (top-hat) velocity and ra-

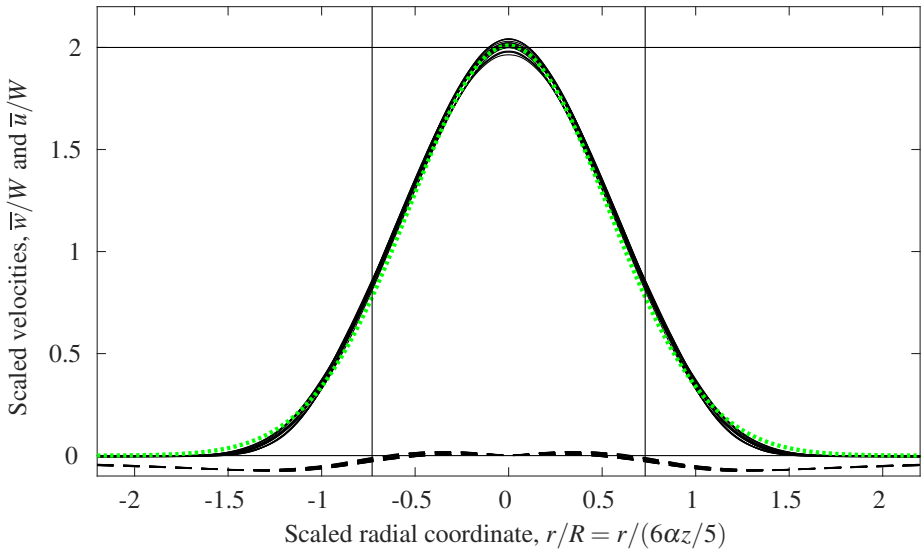

Fig. 4.4 The time-averaged scaled velocities of the three plumes at 80 different heights, spanning $75 \leq z/r_0 \leq 125$, plotted against the scaled radial coordinate: vertical (solid black lines) and radial (dashed black lines) velocities. The velocities and coordinate are scaled by the predicted top-hat velocity scale $W = (5/6\alpha)(9\alpha/10)^{1/3}F^{1/3}z^{-1/3}$ and top-hat radius $R = 6\alpha z/5$, respectively, with $\alpha = 0.11$. The good collapse of the data indicates that the flow exhibits the behaviour of a turbulent pure-plume and that the value of α and the location of the virtual origin are correct to suitable accuracy. A best-fit normalised Gaussian distribution (dotted green line) exhibits a good fit to the vertical velocity data with a root-mean-square error of 0.0296 which was found using the Matlab 'fit' function. A horizontal line marks $\overline{w} = 2W$, the relationship expected between the top-hat velocity and the centreline velocity assuming a Gaussian distribution. Vertical lines mark the e-folding width $\tilde{R}_w$ which shows a close agreement to the expected relationship $\sqrt{2}\tilde{R}_w = R$.

dial scales, $W = (5/6\alpha)(9\alpha/10)^{1/3}F^{1/3}z^{-1/3}$ and $R = 6\alpha z/5$, respectively (Morton et al., 1956), taking $\alpha = 0.11$. Both the vertical and horizontal velocity profiles are self-similar, collapsing to a single curve when scaled by the pure-plume velocity scale and radial scale. The scaled vertical velocity data are well fitted by a Gaussian curve (marked in green) as has been observed previously (e.g. Shabbir and George, 1994). The accuracy of our measurements and ability of our experiments to generate the appropriate physics is clearly evidenced by the good agreement of our data to the theoretical relationships expected between top-hat and Gaussian distributions for the vertical velocity. Specifically, our data show $\overline{w}_c \approx 2W$, where $\overline{w_c(z)}$ is the time-averaged vertical velocity on the centreline, and $\sqrt{2}\tilde{R}_w \approx R$, with $\tilde{R}_w$ the e-folding width defined by the radial position at which $\overline{w}(r,z) = \overline{w}_c(z)/e$. Hence, our PIV measurements of the velocities exhibit behaviours expected on theoretical grounds for turbulent pure-plumes, which provides assurance that the measurements are accurate and valid.

Measurements of the horizontal velocities, marked by black dashed curves in figure 4.4, show radially inward (negative) velocities of increasing magnitude as one travels inwards towards the plume. The magnitude then begins to decrease, for $|r| \lesssim R$, then becomes positive (indicating a radially outward flow) before finally approaching zero on the centreline. This reversal in the radial direction of the flow has been observed in jets and plumes (e.g. Ying et al., 2004). Reassuringly, just such a profile is expected (Ying et al., 2004) since the vertical velocities in the flow decrease in the axial direction (most significantly near the centreline), and continuity thereby requires an outward radial flow local to the centreline (see, for example, Panchapakesan and Lumley, 1993; Shabbir and George, 1994).

For further validation, we determined the entrainment coefficient α using two different methodologies. First, α was determined from the solutions to the conservation equations for a pure-plume (Morton et al., 1956), namely,

$$\frac{\mathrm{d}R}{\mathrm{d}z} = \frac{6\alpha}{5}, \quad \text{with} \quad R = \frac{Q}{M^{1/2}}. \tag{4.3}$$

We note that R can be regarded as the top-hat plume half-width (or radius) since, upon assuming a Gaussian distribution for the radial distribution of $\overline{w}$ (figure 4.4), it follows that $R = \sqrt{2}\tilde{R}_w$, which is precisely the relation between the classical top-hat width of a plume (e.g. Morton et al., 1956) and the Gaussian plume width (e.g. Ezzamel et al., 2015). Hence, all values of α reported herein represent values for the top-hat entrainment coefficient. We plot R/r_0 as a function of z/r_0 in figure 4.5 and a best fit to the data provides a value of $\alpha = 0.11 \pm 0.01$, where the tolerances indicate the standard deviation within our measurements. This value falls within the range of $\alpha = \{0.095, 0.15\}$, the median value being

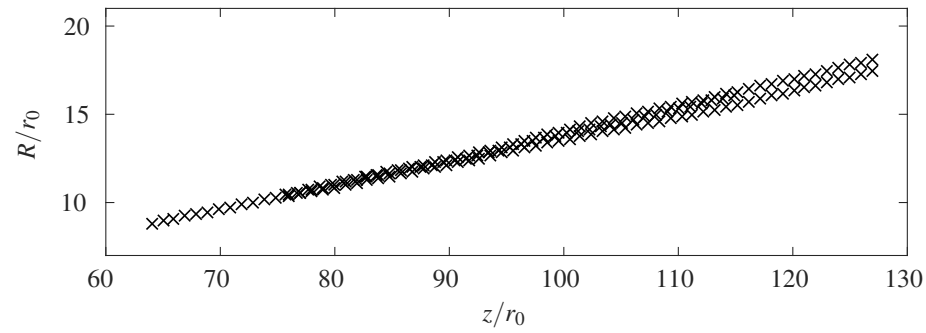

Fig. 4.5 The variation in the 'top-hat' plume radius, $\overline{R}/r_0$ (4.3), for the three plumes.

$\alpha = 0.12$, from the six independent studies for which data are reported within van Reeuwijk and Craske (2015).

From the gradient $\mathrm{d}\overline{R}/\mathrm{d}z$, identifying the vertical location at which the plume width is zero provides a means of assessing the virtual origin for the plume. For all data reported herein the vertical coordinate z is measured from the virtual origin, i.e. the point at which our measurements (4.3) imply $R(z=0) = 0$. For our data the virtual origin was located $5r_0$–$8r_0$ above (behind) the location of the physical source.

As a second method for assessing the entrainment coefficient we consider the findings of van Reeuwijk and Craske (2015) in which they showed, for a time-averaged self-similar pure-plume, that α can be expressed in terms of turbulence production, energy flux and buoyancy effects. This decomposition allows a deeper physical insight of the entrainment coefficient beyond the original hypothesis provided by Morton et al. (1956) (i.e. that $\alpha = U_E/W$) where U_E and W are characteristic (horizontal) entrainment and (vertical) plume velocities, respectively. In particular, van Reeuwijk and Craske (2015) show that α can be written as

$$\alpha = -\frac{\delta}{2\gamma} + \left(1 - \frac{\theta}{\gamma}\right) Ri, \tag{4.4}$$

where

$$\gamma = \frac{2}{W^3 R^2}\int_0^\infty \overline{w}^3 r\mathrm{d}r, \quad \delta = \frac{4}{W^3 R}\int_0^\infty \overline{w'u'}\frac{\mathrm{d}\overline{w}}{\mathrm{d}r} r\mathrm{d}r, \tag{4.5}$$

$W = M/Q$ and θ is a profile coefficient associated with non-dimensional buoyancy flux defined from the relation (2.18). For a pure-plume the Richardson number is invariant and by definition $\Gamma \equiv 1$ so

$$\Gamma \equiv \frac{5}{8\alpha} Ri = 1, \tag{4.6}$$

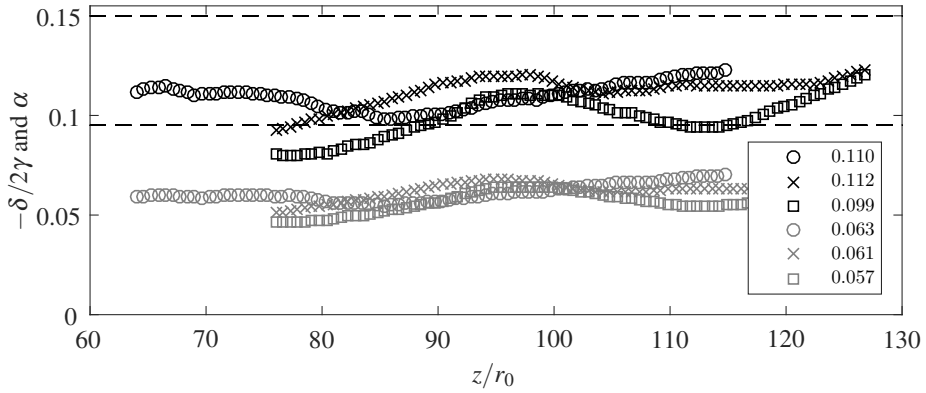

Fig. 4.6 The values of $-\delta/2\gamma$ (grey) and α (black) calculated from our data, plotted against the vertical distance from the virtual origin z/r_0. The mean values for each experiment taking all data at all heights plotted are shown in the legend. The dashed lines show the minimum and maximum values of α presented in van Reeuwijk and Craske (2015).

which combined with (4.4) gives

$$\alpha = -\frac{5\delta}{16}\left(\theta - \frac{3\gamma}{8}\right)^{-1}. \tag{4.7}$$

Values of $\delta/2\gamma$ calculated from our data are plotted in figure 4.6. From our data we are unable to provide reliable estimates of the profile coefficient θ. However, van Reeuwijk and Craske (2015) provide values for θ (alongside those for δ and γ) from six independent computations of plumes and we take the mean value they obtained $\theta = 0.93$ (therein table 3). The estimates of α calculated in this manner from our data are included in figure 4.6. The mean values from each of our three plumes are shown and these fall within the range of values presented in van Reeuwijk and Craske (2015). Moreover, the values of the entrainment coefficient, calculated in the second manner, are also $\alpha = 0.11 \pm 0.01$, identical to the values obtained from the plume equations. This demonstrates that the two different methodologies for assessing α are quantitatively equivalent.

4.4 Results in an Eulerian coordinate system and discussion

In order to provide novel insights for the dynamics that arise within turbulent plumes we combine measurements of the velocity field with data for the edges of the scalar field. We do so using two distinct methods, the first of which exploits the Heaviside step function (§ 4.4.2) and the second establishes a coordinate system which follows the meandering

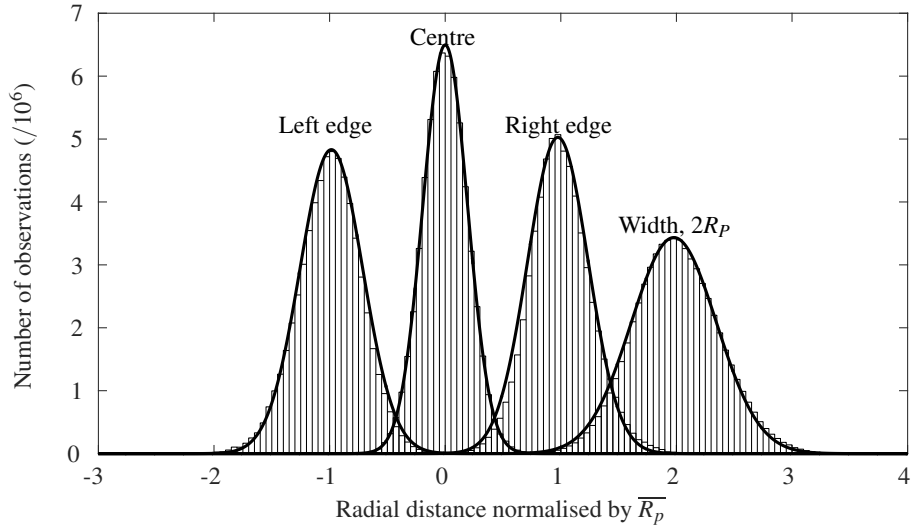

Fig. 4.7 Histograms of the location of the centre, left and right edge of the plume scalar field and the magnitude of the width of the plume scalar field. All distances have been normalised by the time-average of the local half-width of the scalar edges of the plume, $\overline{R_p}$. The histograms contain observations from each of the three plumes, from both edge detection algorithms and at all heights for which reliable data was obtained, in excess of 6×10^7 observations of each statistic. The best-fit Gaussian distribution is overlaid on each histogram.

fluctuating plume (§ 4.5). In order to set these methods in context we first examine results following directly from our measurements of the scalar edges.

4.4.1 The statistics of the scalar edges[3]

The radial location of the outermost left and right edges of the plume fluid are plotted in figure 4.7, in which all distances have been normalised on the time-averaged half-width of the scalar field edges $\overline{R_p}$. These outermost left and right edges define the plume envelope, which is highlighted in figure 4.3. The plume envelope was defined in this way, partly, in order to provide unique values for the left and right edges. Alternative plume envelope definitions, and justification for the construction chosen, are discussed further in § 4.4.2.2. The left and right edges of the plume are well approximated by the normalised Gaussian distributions $E_L \sim N(\mu=-1,\sigma^2=0.072)$ and $E_R \sim N(\mu=1,\sigma^2=0.070)$ for the left and right edges, respectively, where μ denotes the mean and σ the standard deviation. From the instantaneous locations of the left and right edges we define the instantaneous centre

[3]The analysis presented in this section was performed in collaboration with Henry Burridge.

of the plume fluid and the width $2R_p$ which approximately follow the normalised Gaussian distributions $C \sim N(0, 0.036)$ and $2R_p \sim N(2, 0.140)$, respectively.

The relatively small variation in the central point, C, highlights that the meandering of the plume centreline is small in comparison to the fluctuations in the plume width; where by fluctuations we refer to variations about the mean. Moreover, since $C = (E_L + E_R)/2$ and $2R_p = E_R - E_L$ it follows from the observed distributions that the covariance, $cov(E_L, E_R)$, is not statistically significantly different from zero. Hence, the location of the left and right edges of the plume are not correlated. Such a finding implies an absence of coherent structures forming across the full width of the plume, since such structures would simultaneously affect the locations of the left and right edges and result in their locations being correlated.

Alternative definitions of the plume centreline could be used. For example, Hübner (2004) also studied turbulent axisymmetric plumes in a quiescent environment and defined the instantaneous plume centreline to be the centroid, for a given height, of the plume concentration field. This method would be of limited value with our data because the light intensity of the plumes does not correspond with the plume concentration. Hübner (2004) used the plume centreline definition to disentangle two distinct processes that contribute to the time-averaged growth rate of the plume width: The plume centreline meandering and the isolated 'spreading' of plume relative to that instantaneous centreline. In a quiescent environment, it was found that the growth rate of the isolated plume spreading constituted 96% of the overall plume spreading. These results support our findings that the plume centreline meandering is not significant.

4.4.2 Conditional results in an Eulerian coordinate system

Given that the extent of the meandering is small relative to the width of the plume (figure 4.7) there will be regions near the centreline where, almost always, plume fluid will be present. Conversely, sufficiently far from the centreline, no plume fluid will ever be present. The balance of these probabilities alters at intermediate radial locations.

Scase et al. (2007) developed a plume model that utilised this concept, in the time-averaged sense, where the fluid at a given point is defined as superposition of unmixed ambient fluid, with volume fraction a, and unmixed sourced fluid, with volume fraction p, so that $a + p = 1$. The model was used to show how realisable velocity and buoyancy profiles may be reconciled with the top-hat plume model of Morton et al. (1956). In particular, unlike the model of Morton et al. (1956), the model explicitly describes how ambient fluid is converted into plume fluid. Despite these differences between the two models they remain consistent. In this section, we consider an instantaneous view of the separation between the unmixed ambient fluid and mixed plume fluid.

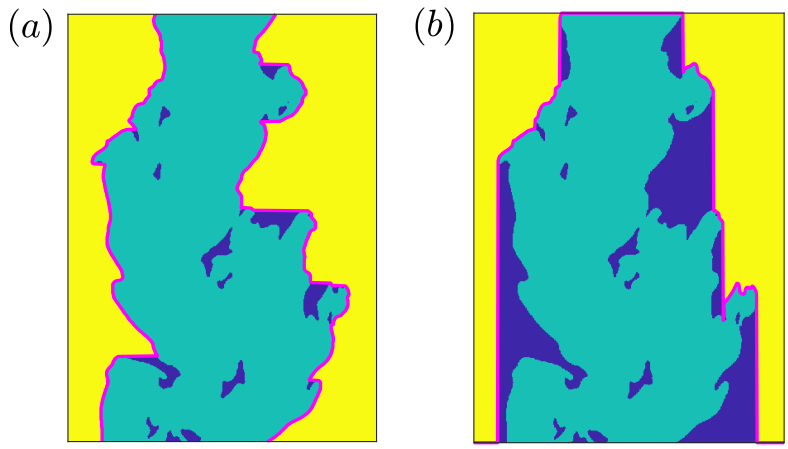

Fig. 4.8 A plume image highlighting the regions outside the plume (H_{out}) by yellow, inside the plume (H_{in}) by the union of green and blue, the engulfed ambient fluid (H_{eng}) by blue and the mixed plume fluid (H_{mix}) by green. (a) demonstrates the radially-defined plume envelope (magenta lines) used in this thesis and (b) shows an alternative definition using a vertically-defined plume envelope.

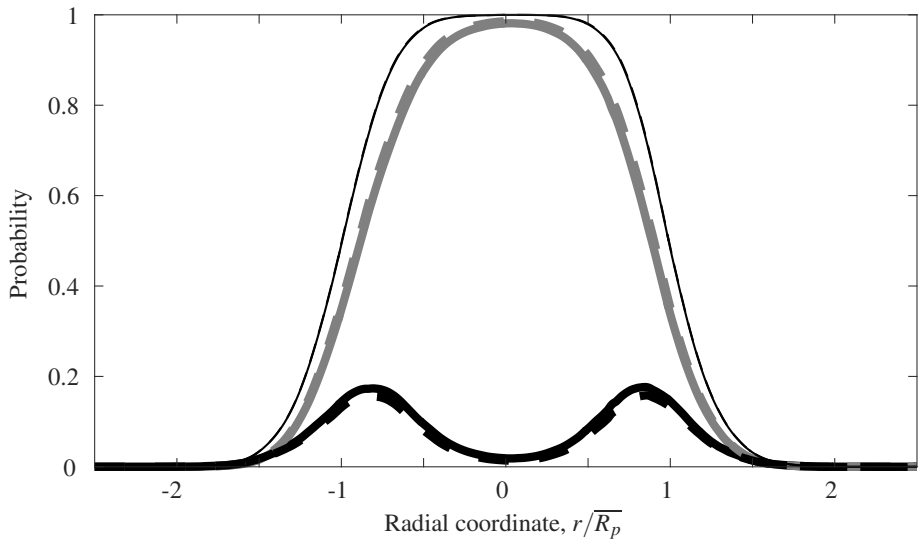

Fig. 4.9 The probability, at a given radial location, of being within the plume (thin black lines), finding mixed fluid (thick grey lines) and finding engulfed fluid (thick black lines), from ensemble averages of the three plumes over all heights for which reliable data was obtained. Solid lines mark the results from the standard edge detection algorithm and dashed lines those from the alternate algorithm.

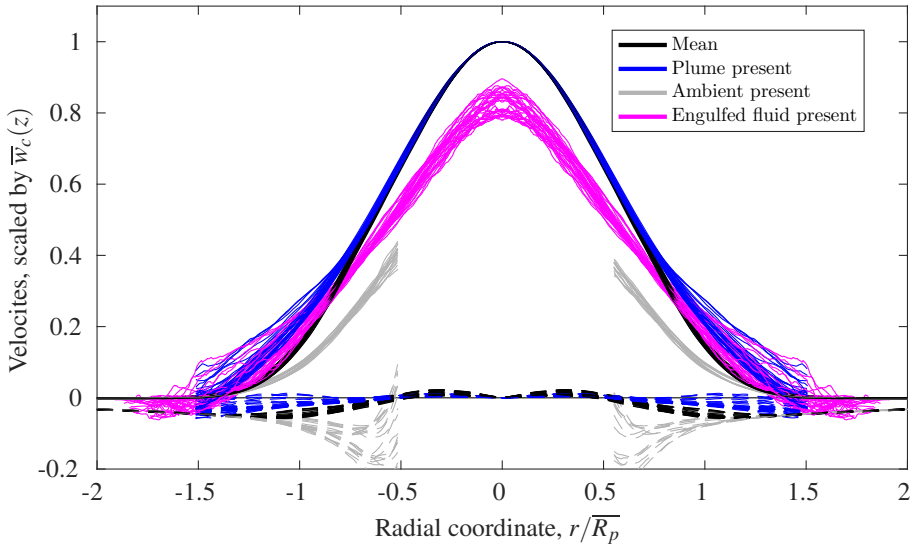

Fig. 4.10 The radial distributions of vertical (solid lines) and horizontal (dashed lines) velocities, in the scaled Eulerian plume coordinate. The velocities are conditioned on the presence of plume fluid or ambient fluid, plotted at radial locations where the probability of observation exceeded 3%. The data show that fluid inside the plume moves vertically faster (by $0.1-0.2\overline{w}_c$) than ambient fluid at the same vertical location. Ambient fluid is accelerated both horizontally and vertically in the regions $r/\overline{R_p} \approx \pm 0.5 - \pm 1.0$. The velocity profile observed when engulfed fluid is present shows that much of the vertical acceleration occurs as ambient fluid is engulfed, with engulfed fluid travelling at approximately 80% of the velocity of plume fluid locally.

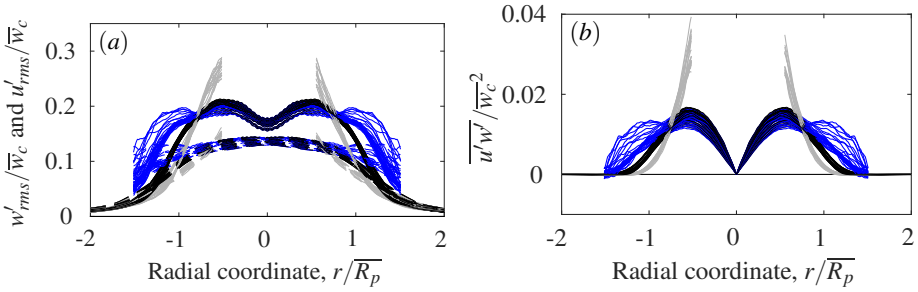

Fig. 4.11 The radial distributions of a) vertical (solid lines) and horizontal (dashed lines) velocity fluctuations and b) Reynolds stresses, in the Eulerian plume coordinate. Observations are conditioned on presence of the plume or the ambient (colour scheme as in figure 4.10). The data show large Reynolds stresses in ambient fluid when in the regions $r/\overline{R_p} \approx \pm 0.5 - \pm 0.8$.

At a fixed location in the intermediate regions, where both ambient or plume fluid may exist it is possible to make conditional observations, based on whether fluid at that location is instantaneously inside or outside the plume, which are statistically representative of these two states. As such, we couple our measurements of the velocity field with our data for the edges of the scalar field via a plume step function which is unity within the plume and zero outside and is defined by

$$H_{in}(r,z,t) = H[r - E_L(z,t)] - H[r - E_R(z,t)] \tag{4.8}$$

where H is the Heaviside step function, $H(x) = 0$, for $x < 0$ and $H(x) = 1$, for $x \geq 0$. We can then determine the time-averaged vertical velocity, at a given location, conditional on being inside, $\overline{w_{in}}$, or outside, $\overline{w_{out}}$, the plume by defining

$$\overline{w_{in}}(r,z) = \frac{1}{T_{in}} \int_0^T H_{in} w(r,z,t)\,\mathrm{d}t\,, \tag{4.9}$$

and

$$\overline{w_{out}}(r,z) = \frac{1}{T_{out}} \int_0^T (1 - H_{in}) w(r,z,t)\,\mathrm{d}t\,, \tag{4.10}$$

where $T_{in}(r,z)$ and $T_{out}(r,z)$ correspond to the total amount of time fluid at a given location is inside and outside the plume, respectively. The methodology described here to determine conditional statistics is outlined in Townsend (1976), where therein statistics are conditioned on the presence or absence of turbulent fluid. We revisit the latter case in § 4.4.2.2. We note that the equivalent notation used in Townsend (1976) used to define (4.9) would be $\overline{\overline{w}} = \overline{w(r,z,t)\delta(t)}/\overline{\delta(t)}$, where δ is the step function equivalent to (4.8). We define the horizontal velocities conditional on being inside $\overline{u_{in}}$ or outside $\overline{u_{out}}$ the plume in an equivalent manner. Figure 4.8 (*a*) highlights the regions inside and outside the plume defined by H_{in} and H_{out} for an instantaneous plume.

The probability of being within the plume envelope at a given radial location is defined by $P_{in}(r,z) = (1/T)\int_0^T H_{in}(r,z,t)\,\mathrm{d}t$ and is shown in figure 4.9 by the thin black curve. This probability differs from the intermittency factor that is often calculated in turbulent statistics (Townsend, 1948), which calculates the probability that turbulent fluid, which would correspond here to plume fluid, is present. The intermittency factor is discussed further in § 4.4.2.2. P_{in} exhibits a broad single peak indicating that the central regions, $-0.5\overline{R_p} \lesssim r \lesssim 0.5\overline{R_p}$, are almost certain to be within the plume envelope.

Figure 4.10 shows the radial variation of the vertical (solid lines) and horizontal (dashed lines) velocities. Data obtained from the three different plumes at 18 different heights and plume edges calculated from both edge-detection algorithms (see § 4.2.1) are plotted in each

of figures 4.10, 4.11, 4.13, 4.14, 4.9, 4.16, 4.17 and 4.18. Black curves mark the full time-averaged data (akin to the black curves in figure 4.4), overlaid (in blue) are the velocities when inside the plume and (in grey) the velocities when outside the plume. Data are plotted only in regions where the probability of observing a given state exceeds 3% (equivalent to approximately 400 observations). The probability exceeding 3% that the radial location is inside the plume occurs for $|r| \lesssim 1.5\overline{R_p}$ and the probability exceeding 3% that the radial location is outside the plume occurs for $|r| \gtrsim 0.5\overline{R_p}$. Note that, while we choose to scale the radial coordinate by the plume half-width defined by the edges of the scalar field $\overline{R_p}$, notionally identical plots would be produced should the radial coordinate be scaled by the top-hat half-width, R since our measurements show that $\overline{R_p} \approx R$.

Figure 4.10 shows that at a given radial location the vertical velocity is significantly larger inside the plume compared with the velocity outside (an increase of approximately $0.1\overline{w}_c$–$0.2\overline{w}_c$). This indicates that, as expected, fluid is accelerated vertically as it transitions from outside to inside the plume (i.e. transported across the plume envelope). At first thought this result may seem trivial, however, we return to its full implications in § 4.4.2.2. Figure 4.10 also indicates that when ambient fluid outside the plume is drawn radially inwards towards the plume, but still remains outside the plume in the region $|r| < \overline{R_p}$, then this fluid experiences significant accelerations both vertically and radially (with radial velocities reaching $|\overline{u_{out}}| \approx 0.15\overline{w}_c$ being approximately five times larger than the largest horizontal velocities observed in the mean). From observations in this reference frame it is not clear whether this acceleration is driven by short-range viscous effects at the plume edge or longer-range pressure gradients, since the distance between the fluid outside the plume and the plume edge at a given instant is unknown. We will show that this acceleration must result from long-range pressure gradients in § 4.5.

Figure 4.11 (*a*) shows the root mean square of the velocity fluctuations, defined, for example, by $w'_{rms}(r,z) = [(1/T)\int_0^T [w'(r,z,t)]^2 \mathrm{d}t]^{1/2}$, where $w'(r,z,t) = w(r,z,t) - \overline{w}(r,z)$. The full time-average of the vertical velocity fluctuations shows a bi-modal peak, qualitatively similar to observations in previous studies of jets (e.g. Shabbir and George, 1994) and quantitatively similar to previous observations of plumes (Van Reeuwijk et al., 2016). We find that the vertical velocity fluctuations within fluid inside the plume exhibit an approximately flat peak for $|r| \lesssim \overline{R_p}$. The vertical velocity fluctuations for fluid outside the plume exhibit a sharp peak as $|r| \to 0.5\overline{R_p}$, indicating that large velocity fluctuations occur in ambient fluid when it is found relatively close to the centreline, although the occurrence of such events is relatively rare. Mean profiles of the Reynolds stress, figure 4.11 (*b*), show peaks (of $\overline{u'w'}/\overline{w}_c^2 \approx 0.015$) at $r \approx 0.5\overline{R_p}$ which drop off rapidly at larger radial locations, e.g. $\overline{u'w'}/\overline{w}_c^2 \leq 0.001$ for $|r| \gtrsim 1.2\overline{R_p}$. These mean Reynolds stress profiles are similar to those

reported in previous studies of plumes (e.g. Van Reeuwijk et al., 2016). However, for fluid inside the plume the magnitude of the Reynolds stress remains close to these peak values at far larger radial locations, e.g. $\overline{u'_{in}w'_{in}}/\overline{w}_c^2 \approx 0.015$ at $r \approx 1.2\overline{R_p}$. Outside the plume, when ambient fluid is relatively close to the centreline the Reynolds stress exhibits a sharp peak, reaching $\overline{u'_{out}w'_{out}}/\overline{w}_c^2 \gtrsim 0.03$ at $r \approx 0.5\overline{R_p}$. These peaks in the Reynolds stress suggest that when ambient fluid is relatively close to the centreline the local turbulence production is at its largest, presumably as this ambient fluid is about to be entrained into the plume.

Figure 4.10 indicates that the vertical velocities in the ambient fluid can be significant, for example $\overline{w_{out}} \approx 0.4\overline{w}_c$ for ambient fluid at $r \approx 0.5\overline{R_p}$, suggesting that the vertical volume (mass) transport within the ambient fluid outside the plume, might also be significant. We calculate an estimate of the vertical volume flux inside the plume from

$$\overline{Q_{in}(z)} = \frac{1}{T}\int_{-\infty}^{\infty} r \int_0^T H_{in} w(r,z,t)\ \mathrm{d}t\ \mathrm{d}r, \tag{4.11}$$

and hence obtain an estimate for the transport outside the plume from $\overline{Q_{out}(z)} = Q(z) - \overline{Q_{in}(z)}$. Figure 4.12 shows these values from the three plumes and shows that, as expected for a self-similar flow, the proportion of the vertical transport outside the plume is constant with height and constitutes approximately 5% of the total vertical transport ($\overline{Q_{out}(z)}/Q(z) = 0.046 \pm 0.006$, where the tolerances indicate the standard deviation within our measurements).

4.4.2.1 The velocity field and fluxes when eddies are present and absent

Having identified that approximately 5% of the vertical volume flux is associated with flow outside the plume, we investigate the role of the large-scale coherent structures on this transport and, more broadly, their role in the process of turbulent entrainment. To do so, we examine our measurements of the velocity field conditional on whether one might reasonably expect a large-scale coherent structure (eddy) to be locally present or absent at a given height. We reason that the presence of an eddy results in an increase in the local width of the flow and a similar reasoning enabled the evolution of these structures to be successfully tracked in turbulent plumes (Burridge et al., 2016). As such, the presence of an eddy within the plume is inferred when the local plume width is greater than the mean plume width by more than one standard deviation, $\sigma_R(z)$. Conversely, we infer that no eddy is present (eddy absent) when the local plume width is less than the mean plume width by more than one standard deviation. Note that the threshold used to define eddy present and absent events (i.e. $\pm 1 \times \sigma_R(z)$) is in some sense arbitrary. However, our results are not dramatically affected

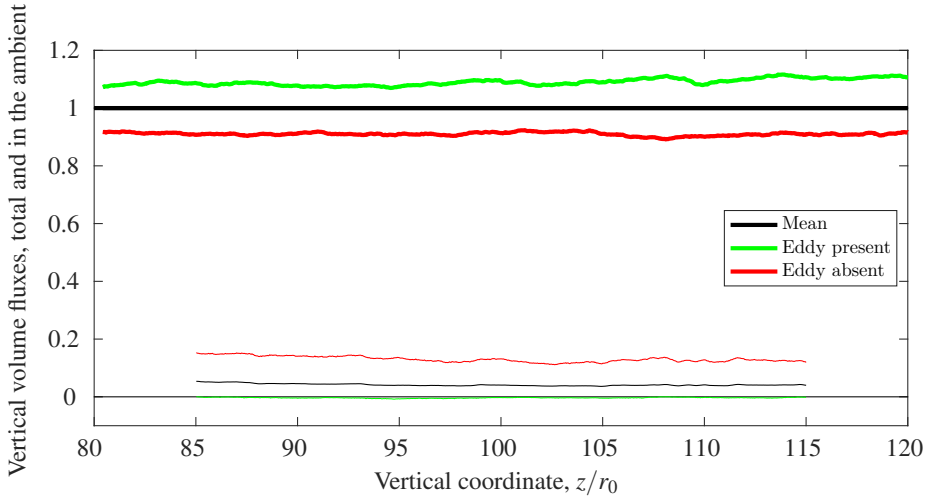

Fig. 4.12 The dimensionless volume fluxes (thick lines) when eddies are present $\overline{Q_e}/Q$ (green) and absent $\overline{Q_n}/Q$ (red) relative to the mean. The proportion of the vertical transport occurring outside the plume are also shown for each of the three states, mean $\overline{Q_{out}}/Q$ (thin black lines), eddy present $\overline{Q_{(out,e)}}/\overline{Q_e}$ (thin green lines) and absent $\overline{Q_{(out,n)}}/\overline{Q_n}$ (thin red lines).

if the threshold is pre-multiplied by a value differing moderately from unity. Moreover, our choice of a single standard deviation ensured that we were able to average a statistically significant sample size. With our choice of threshold eddy present and eddy absent events constituted approximately 30% of all observations (figure 4.7).

We define eddy present, $H_e(z,t)$, and eddy absent, $H_n(z,t)$, step functions by

$$H_e = \begin{cases} 0 \text{ for } R_p(z,t) < \overline{R_p(z)} + \sigma_R(z) \\ 1 \text{ for } R_p(z,t) \geq \overline{R_p(z)} + \sigma_R(z) \end{cases} \text{ and } H_n = \begin{cases} 1, R_p(z,t) < \overline{R_p(z)} - \sigma_R(z) \\ 0, R_p(z,t) \geq \overline{R_p(z)} - \sigma_R(z), \end{cases} \tag{4.12}$$

respectively. From (4.12) we can estimate the total volume flux $\overline{Q_e}$ in the presence of eddies by

$$\overline{Q_e(z)} = \frac{1}{T_e} \int_{-\infty}^{\infty} r \int_0^T H_e \, w(r,z,t) \, \mathrm{d}t \, \mathrm{d}r \,, \tag{4.13}$$

where $T_e = T_e(z)$ is the total time of eddy present events defined by

$$T_e(z) = \int_0^T H_e \, \mathrm{d}t \,, \tag{4.14}$$

and further determine the fluxes inside and outside the plume in the presence of eddies by

$$\overline{Q_{in,e}(z)} = \frac{1}{T_e} \int_{-\infty}^{\infty} r \int_0^T H_{in} H_e \, w(r,z,t) \, \mathrm{d}t \, \mathrm{d}r \,, \tag{4.15}$$

$$\overline{Q_{out,e}(z)} = \frac{1}{T_e}\int_{-\infty}^{\infty} r \int_0^T H_{out}\, H_e\, w(r,z,t)\ \mathrm{d}t\ \mathrm{d}r\,, \tag{4.16}$$

The total volume flux $\overline{Q_n}$ in the absence of eddies, and further conditioned on being inside and outside the plume, are similarly defined. We note that definitions (4.12) do not distinguish between one eddy or two eddies present, where the latter may occur from an eddy on either side of the plume. This issue may be resolved by defining eddies present or absent independently for each side as outlined below, however, adds complexity to the conditional averages as also discussed below. The definition is also limited from the restriction of planar measurements. It may be that the model (4.12) highlights an eddy absent event when in fact the plume has meandered outside the plane (thus resulting in a relatively small plume width in the measured plane) and there are actually no eddies present. The results of § 4.4.1 do suggest, however, that the centreline plume meandering is insignificant as compared to the left and right edge fluctuations that ultimately determine whether an eddy is present or absent in (4.12). Similarly, eddy absent events may be highlighted where an eddy is significantly affecting the measurement plane but not observed in the plane. These are limitations that any conditional statistics based on eddies present or absent events from single plane measurements must face.

Figure 4.12 shows the resulting vertical volume fluxes in the presence and absence of eddies. The figure shows that the total vertical transport is increased or decreased by approximately 9% when eddies are present or absent, respectively, with $\overline{Q_e(z)}/Q(z) = 1.085 \pm 0.013$ and $\overline{Q_n(z)}/Q(z) = 0.908 \pm 0.006$. More insightful are the fluxes outside the plume in the presence and absence of eddies. Figure 4.12 further shows that when eddies are present almost all of the vertical transport occurs inside the plume, $\overline{Q_{(out,e)}}/\overline{Q_e} = -0.001 \pm 0.009$. Conversely, when no eddies are present the vertical transport outside the plume is significant, $\overline{Q_{(out,n)}}/\overline{Q_n} = 0.135 \pm 0.010$. Such findings clearly illustrate the importance of coherent structures for the turbulent entrainment by plumes. At 'eddy-present' events there is virtually no vertical transport outside the plume while between eddies this transport is significant, so ambient fluid must be accelerated vertically outside the plume between eddy present events.

We now examine the radial profiles of velocity, in a fixed Eulerian frame, conditional on the presence and absence of eddies. However, given that the profiles observed in an Eulerian frame of reference take no account of the spatial extent or location of the radial distribution at a given instant, interpretation of these data requires care. For example, the profiles in figure 4.13 show larger vertical velocities when eddies are present but in effect this is merely an alternate illustration of the associated larger vertical volumes fluxes. The vertical lines in figure 4.13, however, mark the time-averaged position of the plume edge in each of the

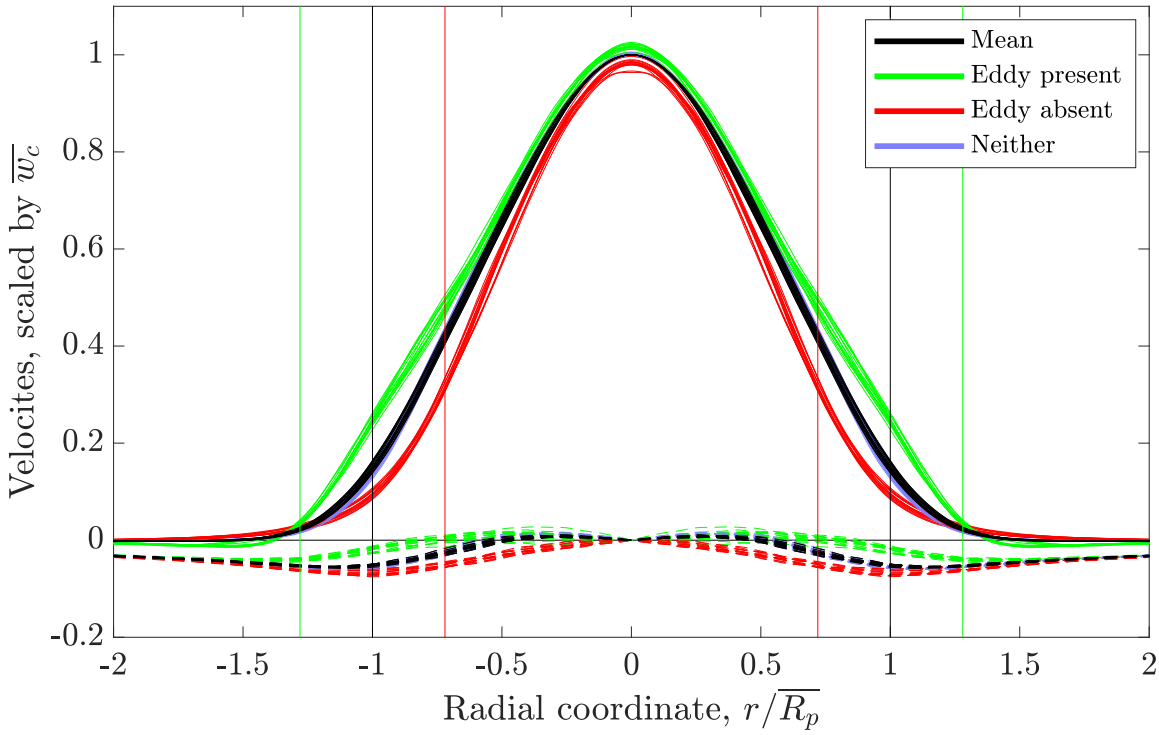

Fig. 4.13 Radial distributions of vertical (solid lines) and horizontal (dashed lines) velocities, in the scaled plume coordinate. Vertical lines mark the time-averaged position of the plume edge in the mean (black), eddy present (green), eddy absent (red) and neither presence nor absence of eddies (blue). The data show significant vertical velocites outside the plume when eddies are absent and almost no vertical flow outside the plume when eddies are present.

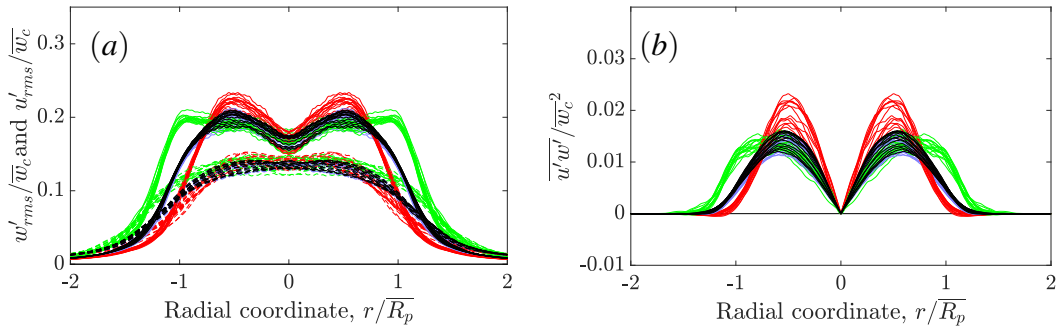

Fig. 4.14 Radial distributions of a) vertical (solid lines) and horizontal (dashed lines) velocity fluctuations and b) Reynolds stresses, in the scaled plume coordinate. The data show Reynolds stresses of slightly greater magnitude when coherent structures are absent.

three states and suggest that the vertical velocities near the plume edge are significantly different depending on whether an eddy is locally present or not. In order, to provide more physical insight we re-examine these profiles in § 4.5 within a plume coordinate that follows the meanders and fluctuations in width of the plume. However, before moving on, we note that observations in the fixed Eulerian coordinate indicate that changes in the vertical velocity fluctuations between the three states (figure 4.14 (*a*)) appear to produce greater Reynolds stresses (figure 4.14 (*b*)) in the absence of eddies. If velocity gradients remain broadly similar between the three states, then these peaks imply that the local turbulence production is greatest at locations between eddies. This supports our findings regarding the Reynolds stresses in § 4.4.2 and our suggestion that the local turbulence production is greatest as ambient fluid is being entrained within the plume. However, these findings should be compared with observations in the plume coordinate (§ 4.5). We also include the results of events where eddies are neither present nor absent in figures 4.13 and 4.14. These data closely follow the results of the mean statistics across all events.

Alternative criteria for defining eddy present and eddy absent events are possible. For example, by allowing independent eddy present events on either side of the plume so that an eddy is present on the left side of the plume if $E_L(z,t) - \overline{E_L}(z) < \sigma_L$ and an eddy is absent if $E_L(z,t) - \overline{E_L}(z) > \sigma_L$. While our model has three possible events for each height and time, namely an eddy present, absent or neither, the model described above has eight possible events, for example an eddy present on the left but neither on the right, adding complexity to the model.

In addition to eddy present/absent criteria based on the scalar edges of the plume, eddy identification methods could be implemented. Methods for identifying eddies include using the vorticity magnitude (Kim, 1987) and identifying regions that form closed streamlines. The latter technique, proposed by Robinson (1991), has been successfully used by Landel et al. (2012) to identify eddies in a quasi two-dimensional jet. Due to the three-dimensional nature of the axisymmetric plume studied here, and in particular given the restriction of plane velocity measurements, this approach was not explored in this thesis.

4.4.2.2 The distribution, velocity profile and vertical transport of engulfed fluid

We have shown that significant vertical transport (approximately 14%) occurs outside the plume at locations between the eddies in the plume (i.e. where eddies are absent). In order to shed-light on the process through which this ambient fluid is entrained and ultimately mixed within the plume we now consider the fluid inside the plume envelope. In accordance with (4.8), we define the plume envelope as the flow between the instantaneous outermost left and right edges of the plume scalar field (§ 4.2.1), as shown by the magenta lines in

figure 4.8 (*a*). As has been reported for turbulent jets (Westerweel et al., 2009), we find that there are pockets of unmixed ambient fluid inside the plume envelope which, under our definition (§ 4.1), have been engulfed as part of the process of turbulent entrainment. We define engulfed fluid as any fluid within the plume envelope which exhibits lower light intensity levels than that of the fluid at the instantaneous edge of the plume. Naturally, the light intensity level at any instant may be different at the left, $c_L(z,t)$, and right, $c_R(z,t)$, hand edges of the plume. To test the sensitivity of our findings to the precise light intensity threshold, $c_T(z,t)$, used to determine engulfed fluid we examined three alternate methods to determine the threshold namely:

(i) the minimum of the light intensity level at the two edges, $c_T(z,t) = \min[c_L(z,t), c_R(z,t)]$,

(ii) the maximum of the light intensity level at the two edges, $c_T(z,t) = \max[c_L(z,t), c_R(z,t)]$,

(iii) the light intensity level determined by the (radially) closest edge, $c_T(z,t) = c_L(z,t)$ for $r_p < 0$ and $c_T(z,t) = c_R(z,t)$ for $r_p \geq 0$.

We report results determined when engulfed fluid is defined by criterion (iii) and we include tolerances to indicate the maximum variation in our results should we have chosen criteria (i) or (ii). Moreover, should our experiments have resolved the scalar field to the precision of the Batchelor length scale then some variation in the detection of engulfed fluid could be expected since diffusion would act to smear the scalar edges of the plume over a length scale larger than one pixel. However, we expect that these variations would fall well within the tolerances indicated for our results.

In order to examine the location and fluxes of engulfed fluid we define an ambient fluid step function

$$H_{amb}(r,z,t) = \begin{cases} 1 \text{ for } c(r,z,t) < c_T(z,t) \\ 0 \text{ for } c(r,z,t) \geq c_T(z,t) \end{cases}, \tag{4.17}$$

where $c(r,z,t)$ is the local light intensity level. From (4.17) we can determine the presence of engulfed fluid from $H_{eng}(r,z,t) = H_{amb}(r,z,t) \times H_{in}(r,z,t)$, and mixed plume fluid, $H_{mix}(r,z,t) = H_{in}(r,z,t)[1 - H_{amb}(r,z,t)]$. Figure 4.9 includes the observed probability distributions of engulfed fluid (thick black curves) and mixed fluid (thick grey curves), e.g. $P_{mix}(r,z) = (1/T)\int_0^T H_{mix}(r,z,t)\,\mathrm{d}t$. We note that the qualitative shape of the data shown in figure 4.9 is unaffected by the choice of engulfed fluid threshold criterion. The engulfed fluid exhibits a bi-modal distribution with the probabilities of finding engulfed fluid peaking at value of almost $20\% \pm 2\%$, located just inside the time-averaged locations of the edges.

We can examine the radial distribution of velocity within engulfed fluid in a manner similar to that described in § 4.4.2 for fluid inside and outside the plume. We define the

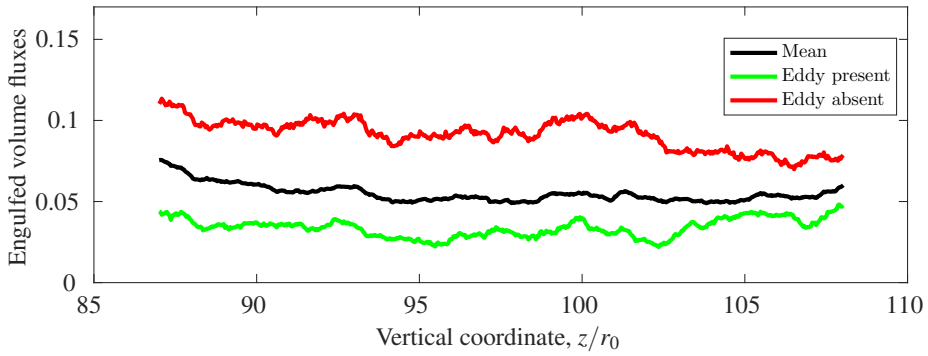

Fig. 4.15 The proportion of the vertical transport which occurs as engulfed (unmixed) fluid within the plume envelope for each of the three states: mean $\overline{Q_{eng}}/Q$, eddy present $\overline{Q_{(eng,e)}}/\overline{Q_e}$ and absent $\overline{Q_{(eng,n)}}/\overline{Q_n}$.

velocity $\overline{w_{eng}}$ within engulfed fluid by

$$\overline{w_{eng}}(r,z) = \frac{1}{T_{eng}} \int_0^T H_{eng} w(r,z,t)\,\mathrm{d}t\,, \tag{4.18}$$

where $T_{eng} = T_{eng}(r,w)$ is the total time for which engulfed fluid is observed at a given location. The radial profiles of $\overline{w_{eng}}$ are included in figure 4.10 (magenta curves). The velocity of engulfed fluid is fairly close to (approximately 80% of) the mean velocity within the plume. This indicates that there is significant vertical acceleration as ambient fluid is transported across the plume envelope by engulfment. There must also then be a more moderate vertical acceleration during the mixing process (at smaller scales).

The methodology used to calculate (4.18) is outlined in Townsend (1976). In particular, P_{mix} is equivalent to the intermittency factor denoted as γ in Townsend (1976).

Comparing the magnitude of the vertical fluxes of transport outside the plume with those of engulfed fluid within the plume provides a measure of the proportion of ambient fluid that is engulfed into the plume envelope. One might be tempted to try to estimate the flux of engulfed fluid by evaluating the integral

$$I = \int_{-\infty}^{\infty} \mathrm{P}_{eng}\, r\,\overline{w}(r,z)\,\mathrm{d}r, \tag{4.19}$$

since results determined by similar methods have been reported previously, e.g. Westerweel et al. (2009). However, the observed velocity depends on whether the fluid is inside or outside the plume (figure 4.10) and whether it is ambient fluid or mixed plume fluid. Hence

we estimate the flux of engulfed fluid as

$$\overline{Q_{eng}(z)} = \frac{1}{T}\int_{-\infty}^{\infty} r \int_0^T H_{eng}(r,z,t)\, w(r,z,t)\ \mathrm{d}t\ \mathrm{d}r\,, \tag{4.20}$$

and we do so both in the presence and absence of eddies by evaluating, for example,

$$\overline{Q_{eng,e}(z)} = \frac{1}{T}\int_{-\infty}^{\infty} r \int_0^{T_e} H_e(z,t)\, H_{eng}(r,z,t)\, w(r,z,t)\ \mathrm{d}t\ \mathrm{d}r\,. \tag{4.21}$$

The results, figure 4.15, indicate that on average the flux of engulfed fluid is nearly 7% of the total volume flux, $\overline{Q_{eng}(z)}/Q(z) = 0.065 \pm 0.018$. We note that this should not be compared to values determined by calculations of the form presented by (4.19) since these, in effect, assume that the vertical velocity is independent of whether fluid at a given instant was engulfed or mixed plume fluid which we have shown is not the case (figure 4.10). Indeed, making a similar assumption with our data has a dramatic impact, approximately doubling the estimate of the engulfed vertical volume flux. Figure 4.15 also shows that proportion of the volume flux consisting of engulfed fluid is lower when eddies are present ($\overline{Q_{eng,e}(z)}/\overline{Q_e(z)} = 0.039 \pm 0.015$) and increases when eddies are absent ($\overline{Q_{eng,n}(z)}/\overline{Q_n(z)} = 0.081 \pm 0.024$). This indicates that the eddies may be mixing much of the engulfed fluid, i.e. transforming engulfed fluid into mixed plume fluid and not just stirring fluid.

Our estimate of the vertical volume flux of ambient fluid outside the plume envelope is nearly 5% of the total volume flux. It is assumed that, through nibbling along the plume envelope or engulfment, the ambient fluid becomes, and remains, ultimately enclosed within the plume envelope at some height downstream. The fact that the engulfed flux is larger than the flux outside the plume suggests that the ambient fluid is accelerated vertically during this engulfment, see also figure 4.10. This illustrates the significant role that engulfment plays within the process of turbulent entrainment by plumes.

While conditional statistics based on the presence or absence of plume fluid are independent of how the plume envelope is defined, the statistics conditioned on engulfed ambient fluid are not. In this thesis we have used a radially-defined plume envelope, also used by Westerweel et al. (2009) for an axisymmetric jet, where the plume envelope, for each height and time, is defined to be the region between the outermost left and right scalar edges (see figure 4.8 (*a*)). Engulfed fluid is then defined as any ambient fluid within this plume envelope. Alternative definitions for the plume envelope, and therefore the engulfed fluid, may be constructed. For example, a vertically-defined plume envelope may be constructed as in figure 4.8 (*b*). The two definitions result in an engulfed fluid parcel being either always bounded by plume fluid along a radial or vertical line. A radial definition ensures that en-

gulfed parcels (that are still connected to the ambient far field) are defined as a result only of the plume overturning relative to the streamwise direction, which is better aligned with the concept of engulfment. In addition, our definition ensures that there is a scalar edge at the outer most left and right edges of the plume envelope. This is important for the definition of our plume coordinate system defined in § 4.5.

The engulfed ambient fluid could also have been defined by the completely engulfed ambient regions. However, this does not resolve the issue of measuring only completely engulfed fluid because the region may be connected to the ambient far field in an unobserved plane. The measurements may therefore change as a result of three-dimensional data, but not in the case of our definition.

The finite thickness of the light sheet presents challenges when attempting to identify statistics confined to a single plane, in particular identifying engulfed fluid. It is useful to adopt Cartesian coordinates for the following discussion. The light sheet spans the volume $-y_T/2 < y < y_T/2$, where $y_T \approx 2\,\text{mm}$ is the thickness of the light sheet and we assume that $y = 0$ is the central plane of the light sheet. Therefore, a pixel intensity reading $P_{m,n}$ is an integral intensity measurement of the volume $V_{m,n}$ (ignoring parallax error) $x_{p_n} < x < x_{p_{n+1}}$, $z_{p_m} < z < z_{p_{m+1}}$, $-y_T/2 < y < y_T/2$, where x_{p_n} and z_{p_n} define the regions observed by pixel $P_{m,n}$. There are three scenarios that may occur during an experiment in the region $V_{m,n}$. The region $v_{m,n}$ may contain only plume fluid, only unmixed engulfed fluid or a combination of both. The identification criteria (i) - (iii) are likely to obtain robust classifications for the cases of only plume or only engulfed ambient fluid. However, the identification criteria will tend to identify regions containing both as plume fluid regions. Indeed, it is possible that intensity readings of volumes containing both plume and engulfed fluid are larger than regions containing only plume fluid. It is important that regions containing both plume and ambient fluid are identified as plume fluid for the following reason. The primary aim for identifying the engulfed fluid was to determine the vertical transport of engulfed fluid. Ignoring regions that contain both plume and engulfed fluid provides a lower bound to this statistic (assuming positive vertical velocities). However, our conclusions rely on the observation of a relatively large vertical transport of engulfed fluid, so that measuring a lower bound is sufficient for our arguments (an upper bound achieved from including false positive engulfed regions would not support our claims). In addition, the probability of the presence of engulfed unmixed fluid is very small compared to the presence of plume fluid, suggesting that the false positives of the presence of plume fluid will not significantly affect the plume present statistics.

One of the central questions that our results have been unable to answer is what is the length scale over which engulfed fluid is mixed into the plume? Lagrangian statistics could

have been used to track and measure the decay of engulfed parcels, however, planar measurements impose a severe restriction on this methodology. It should be noted that acquiring such a length scale, say l_{eng}, would provide a key step in quantitatively measuring the contribution of engulfment to entrainment. From l_{eng} an 'engulfment entrainment velocity' may be obtained from the transport of engulfed fluid $v_{eng} = Q_{eng}/l_{eng}$ providing a velocity scale that may be compared to the total entrainment velocity $\mathrm{d}Q_{mix}\mathrm{d}z$, where

$$\overline{Q_{mix}(z)} = \frac{1}{T}\int_{-\infty}^{\infty} r \int_0^T H_{mix}(r,z,t)\, w(r,z,t)\ \mathrm{d}t\ \mathrm{d}r. \tag{4.22}$$

4.5 Results in a Plume coordinate system[4]

To provide further insights into the process of entrainment by plumes we examine the flow in a coordinate system which follows the plume as it meanders and fluctuates in width. At each time and height, we defined a local coordinate system $r_p(r,z,t)$, where

$$r_p(r,z,t) = \frac{2\,(r - E_R(z,t))}{E_R(z,t) - E_L(z,t)} + 1 = \frac{(r - E_R(z,t))}{R_p(z,t)} + 1, \tag{4.23}$$

where, by construction, $r_p = -1$ and $r_p = 1$ at the left and right edges, respectively. Further, $r_p = 0$ at the mid point between the left and right edges. The velocity data were then time-averaged to obtain the average vertical velocity in this plume coordinate system, defined by

$$\overline{w_p} = \overline{w(r_p,z)} = \frac{1}{T}\int_0^T w(r_p,z,t)\ \mathrm{d}t\,, \tag{4.24}$$

and the equivalently defined horizontal velocity $\overline{u_p}$. These data are plotted as the black curves in figure 4.16. The figure shows data from the three different plumes at 18 different heights and with the plume coordinate system calculated from both edge-detection algorithms (see § 4.2.1), as is also the case in figures 4.16, 4.18 and 4.17. To our knowledge, this is the first time that velocity data for either jets or plumes have been conditionally averaged in this manner, *cf.* Wang and Law (2002), Westerweel et al. (2009) and Mistry et al. (2016).

The average data collapse onto a single curve showing that the velocities are self-similar when viewed in plume coordinates. The average vertical velocities at the plume edge (black vertical lines at $\{-1,1\}$) are significant, and almost 20% of the velocities on the centreline. The velocities at the plume edge are significantly higher than the velocities at the edge of an axisymmetric jet of approximately 5% observed by Westerweel et al. (2009). Similar

[4]The analysis presented in this section was performed in collaboration with Henry Burridge.

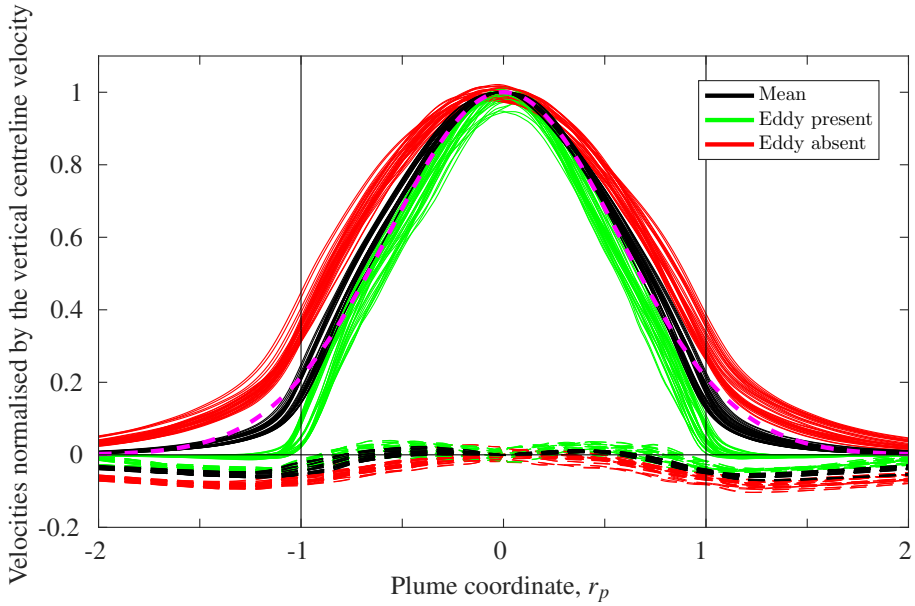

Fig. 4.16 Vertical (solid lines) and horizontal (dashed lines) velocities averaged in the plume coordinate system, r_p. The full time-averaged velocities, $\overline{w_p}$ and $\overline{u_p}$, are marked in black; average velocities when eddies are present, $\overline{w_{(p,e)}}$ and $\overline{u_{(p,e)}}$, are marked in green; average velocities when no eddies are present, $\overline{w_{(p,n)}}$ and $\overline{u_{(p,n)}}$, are marked in red. The data from three different plumes at 18 different heights exhibit a broad collapse indicating self-similarity. The vertical velocities outside the plume are significant near the plume edge and are, indeed, greater than the horizontal velocities at the same location. The dashed magenta curve is a Gaussian of variance equal to mean variance of the ensemble data (black curves).

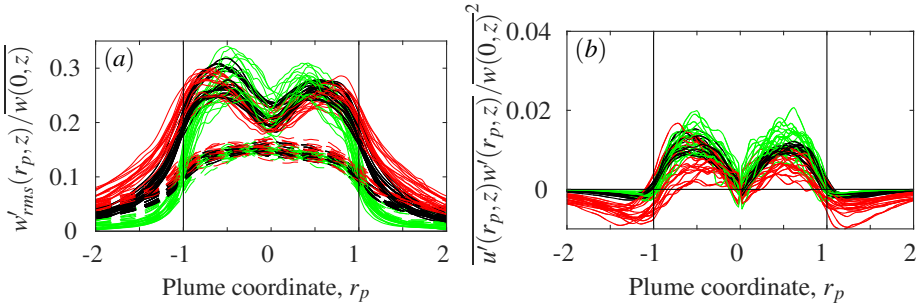

Fig. 4.17 (*a*) The root mean square of the fluctuations in vertical (solid lines) and horizontal (dashed lines) velocities and (*b*) $\overline{u_p'(z)w_p'(z)}/\overline{w_p(z)|_{r_p=0}}^2$ averaged in the plume coordinate system, r_p. The vertical velocity fluctuations exhibit bi-modal peaks of approximately 25%–30% of the mean velocities at $r_p \approx \{-0.5, 0.5\}$. The horizontal velocity fluctuations exhibit a broad peak around the centreline, the peak values are almost 15% of the mean vertical velocities. This corresponds to the fluctuations being approximately three times larger than the maximum time-averaged horizontal velocities within the plume.

vertical velocities at the plume edge were also observed by the recent study of Burridge et al. (2016) in which visible coherent structures were tracked using a cross-correlation technique. These structures at the plume edge (found to be of width $\sim 0.4R_p$) travelled at approximately 30% of the centreline velocities, similar to the velocities just inside of the plume edge shown in figure 4.16.

The root mean square of the velocity fluctuations in the plume coordinate are shown in figure 4.17 (*a*). When observed in this frame of reference the mean profiles for the vertical velocity fluctuations exhibit bi-modal peaks of approximately 25%–30% of the mean velocities, somewhat larger than when observed in a fixed Eulerian coordinate (*cf.* figure 4.11 (*a*) or 4.14 (*a*). This suggests that the spatial intermittency (the meandering and fluctuations in width) of the plume must, to some extent, mask the scale of the turbulent velocity fluctuations. The same effects are not evident in the quantities of the form $\overline{u'_p(z)w'_p(z)}$ (*cf.* figure 4.11 (*b*) and 4.14 (*b*). It is not obvious why this should be the case.

The locations of the peaks in the vertical velocity fluctuations, at $r_p \approx \{-0.5, 0.5\}$, roughly correspond to the locations at which the radial velocities in the plume are zero. The radial velocity fluctuations exhibit a single broad peak about the centreline, with peak values that are almost 15% of the mean vertical velocities. This value corresponds to the fluctuations in horizontal velocities being approximately 300% of the maximum time-averaged horizontal velocities within the plume. Thus the mean horizontal velocities established by the process of entrainment are small compared with the fluctuating horizontal velocities within the falling, swirling coherent structures which form (with some complex and chaotic orientation) within the plume.

4.5.0.1 Plume properties when eddies are present and absent

We extend our examination of the velocity fields in the plume coordinate and compare how they vary from the mean depending on whether one might reasonably expect an eddy to be locally present or absent at a given height. We recalculate the statistics in § 4.5 conditioned on the presence or absence of a large-scale eddy in a similar manner to that described for the fixed Eulerian coordinate in § 4.4.2.1. For example, we calculate the vertical velocity in the plume coordinate in the presence of an eddy as

$$\overline{w_{(p,e)}} = \overline{w_{(p,e)}(r_p, z)} = \frac{1}{T_e} \int_0^T H_e(r_p, z, t) w(r_p, z, t) \, \mathrm{d}t \, . \tag{4.25}$$

The data for the velocities when eddies are present (green curves) and absent (red curves) are plotted in figure 4.16. As is the case for the ensemble data (black curves), these conditional data collapse for each state, showing that the plume statistics are approximately self-

similar in all three states when viewed in the plume coordinate r_p. The data in figure 4.16 are normalised by the ensemble mean centreline velocity. It is noteworthy that the mean velocity in the middle of the plume (i.e. $r_p = 0$) systematically varied by a few percent between the three states. Larger vertical velocities were observed in the middle of the plumes when eddies were locally *absent*; however, in the fixed Eulerian coordinate larger vertical velocities were observed on the centreline, $r = 0$, when eddies were *present*. This difference highlights the sensitivity of the observations to the choice of reference frame.

The velocity profiles plotted in figure 4.16 show large vertical velocities outside the plume (up to 40% of the maximum velocities) when eddies are absent. Conversely, when eddies are present there is almost zero vertical velocity at and beyond the plume edge. Such findings are in agreement with, and provide an alternative illustration of, our results for the vertical transport outside the plume presented in § 4.4.2.1. Moreover, the velocity data differ significantly between the three states. For example, when an eddy is locally present, the vertical velocities at the plume edge are *smaller* by about a factor of four compared to the mean, and by about a factor of ten compared to when an eddy is absent. Horizontal velocities, on the other hand, are *larger* by about a factor of four when an eddy is absent compared to when present, indicating that ambient fluid is drawn towards the plume at height between eddies.

Figure 4.17 includes the velocity fluctuations and quantities of the form $\overline{u'_p(z)w'_p(z)}$, conditioned on the presence and absence of eddies. When viewed in this coordinate the data from inside the plume are broadly similar for each of the three states, which is in contrast to the measurements of velocity fluctuations and Reynolds stresses in the Eulerian coordinate (*cf.* figure 4.14). This may indicate that the velocity field within the plume scales more appropriately on a radial coordinate based on the local instantaneous width of the plume (our plume coordinate) than on the local time-averaged width (as is the case for the Eulerian coordinate), confirming that variations in plume width are correlated with the internal flow structures. Outside the plume the data for the velocity fluctuations (figure 4.17 (*a*)) show variations from the mean when eddies are both present or absent. However, the data for $\overline{u'_p(z)w'_p(z)}$, figure 4.17 (*b*), show a significant variation from the mean only when eddies are absent. Both in the mean and when eddies are present, $\overline{u'_p(z)w'_p(z)}$ is positive within the plume and zero outside which implies that the unsteady transport of vertical momentum is radially outwards. In the case when eddies are absent, $\overline{u'_p(z)w'_p(z)}$ is positive within the plume and negative outside suggesting that at heights between eddies the unsteady transport of vertical momentum is radially inwards. Such a finding is supportive of our view that vertical momentum is imparted on ambient fluid at heights between eddies, before this ambient fluid is engulfed.

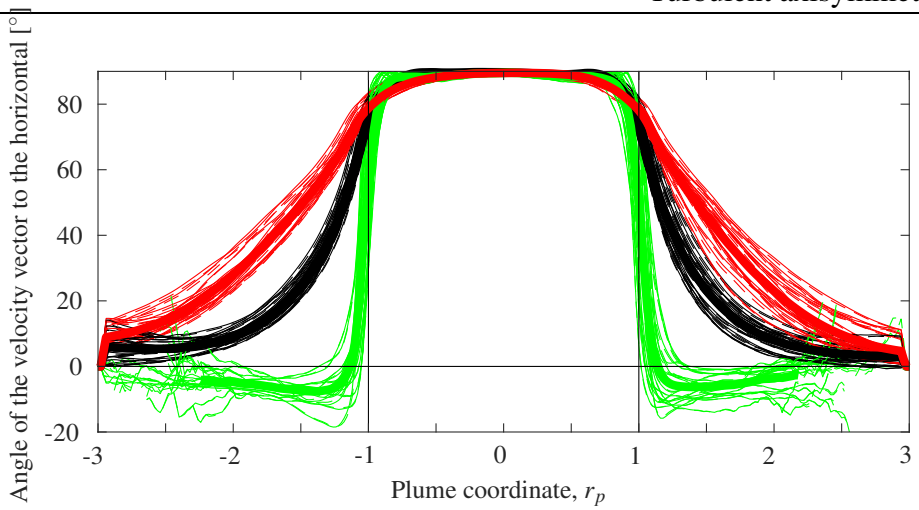

Fig. 4.18 The angle to the horizontal of the velocity vectors averaged in the plume coordinate system, r_p. The angles from the full time-averages are marked in black, those averaged only when eddies are present are marked in green, and those when no eddies are present are marked in red. Steep radial gradients in the angles are only observed at the plume edge when eddies are present.

The relative magnitude of the vertical and horizontal velocities in the plume are illustrated by calculating the angle formed by the local velocity vectors to the horizontal. The data shown in figure 4.18 marked by the black curves illustrate the ensemble mean and show that, at the plume edge, the average vertical velocities are large compared with the horizontal velocities (the angle being approximately 70°). The mean the vertical and horizontal velocities are only of equal magnitude (and the angle close to 45°) at distances of approximately $\pm 1.2R_p$, i.e. some distance outside the plume. Differences in the velocity field between eddy present and absent events are also clearly highlighted in figure 4.18. When an eddy is present (green curves), the angle increases rapidly from close to horizontal (0°) just outside the plume edge to being close to vertical ($\sim 90°$) just within the plume edge. When eddies are absent vertical and horizontal velocities are only of equal magnitude at distances significantly outside the plume, of approximately $\pm 1.7R_p$. These findings support the suggestion (§ 4.4.2) that prior to being engulfed or entrained, ambient fluid already has a significant component of vertical velocity and thereby momentum.

The data for the horizontal and vertical velocities in the plume coordinate r_p (figure 4.16) and the time-averaged position of the plume edge $\overline{R_p}$ (figure 4.5) allow us to reconstruct the velocity field induced by and within a plume, relative to the scalar edge of the plume. These data are plotted in figure 4.19 (*a*) and we note that the data from a simple Eulerian view of the plume would look notionally identical. The figure shows that ambient fluid outside the scalar edge is drawn towards the plume, by the process of turbulent entrainment, but that as part of

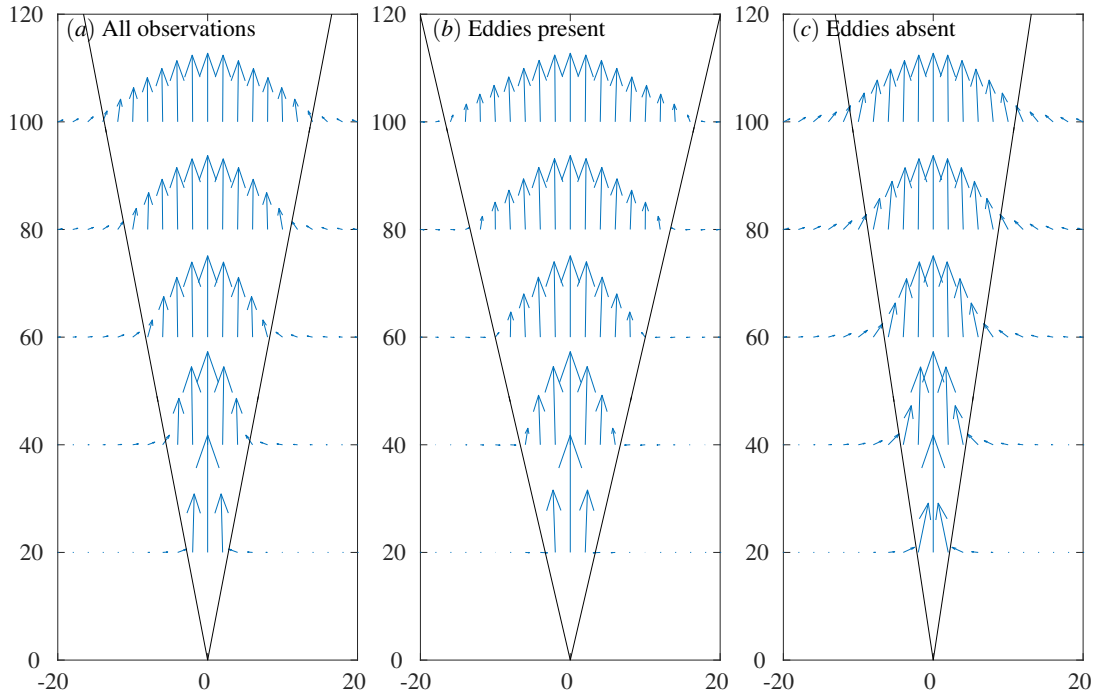

Fig. 4.19 Time-averaged views of a turbulent plume: (*a*) all observations, (*b*) observations when eddies are present, (*c*) when eddies are absent. The black lines mark the time-averaged position of the edge of the plume scalar field in each of the three states. The (blue) arrows mark the magnitude and direction of the measured velocity vectors (ensemble averaged over the 18 heights shown in figure 4.16). The axis are marked in arbitrary units.

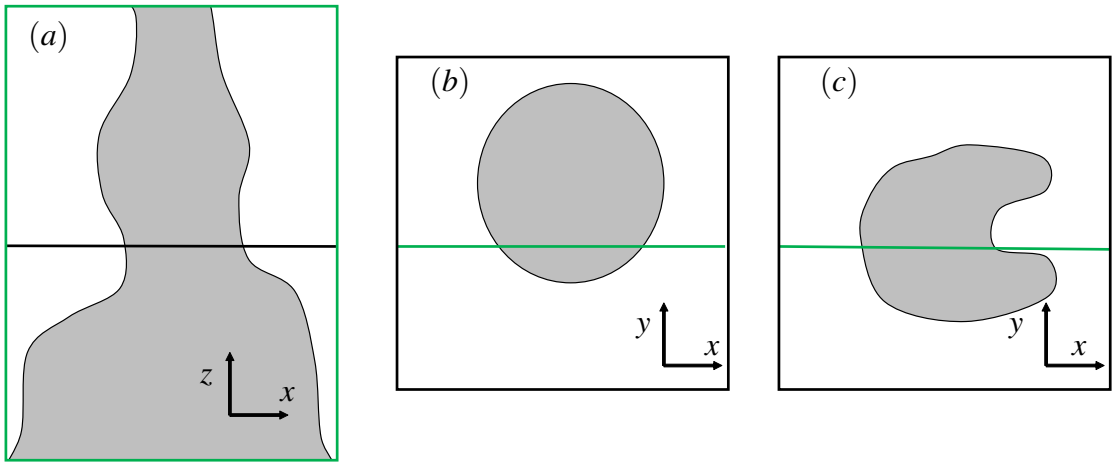

Fig. 4.20 An illustration of an instantaneous plume image (*a*) aligned with the laser sheet (represented by the green box) and (*b, c*) two possible horizontal cross sections of the plume corresponding to (*a*) at the height marked by the black line. The green line in (*b, c*) highlights the laser sheet. (*b*) and (*c*) highlight that it is not possible to determine whether a relatively narrow plume width in a measurement plane corresponds to the plume body meandering out of the plane, as in (*b*), or an eddy absent event, as in (*c*).

this process significant vertical velocity is induced within the ambient fluid before reaching the edge of the plume. The role that coherent structures play in this process is indicated by comparing equivalent reconstructions of the velocity field using data from observations when one can expect large-scale eddies to be present or absent, figures 4.19 (*b*) and 4.19 (*c*), respectively. When eddies are present, the velocities within the (relatively wide) plume are almost entirely vertical and the flow outside predominately horizontal. Conversely, when eddies are absent the velocities within the (relatively thin) plume show a marked component of horizontal velocity well within the scalar edge and, crucially, ambient fluid far outside the scalar edges exhibits a significant component of vertical velocity and therefore momentum, before it is entrained into the plume. Physically, a plume is never in a state of having either eddies present or absent throughout its height; quite the contrary is typical. At any instant, a plume exhibits an alternating pattern of eddies being locally present and absent throughout its height (see, for example, the image in figure 4.3 (*a*)). Figures 4.19 (*b*) and 4.19 (*c*) illustrate that between the eddies, vertical momentum is imparted (presumably by pressure gradients) to pockets of ambient fluid that are, in a relative sense, quite close to the plume centreline. The vertical momentum of these pockets of ambient fluid enable them to be engulfed into the plume more easily, providing a source for the volume flux of engulfed fluid identified in our measurements (§ 4.4.2.2 and figure 4.15). The larger outward

spreading of the plume in the eddies present events, combined with the smaller magnitude horizontal velocities observed at the scalar edge (figure 4.13), and vice versa for the eddies absent, appears at odds with the theory of Turner (1986). However, care should be taken with observations based on figures 4.19 (*b*) and (*c*) because conservation of volume flux is not valid and therefore not applicable to, for example, Turner (1986).

These findings suggest that ambient fluid is being accelerated vertically before reaching the plume edge. This acceleration of ambient fluid cannot be as a result of viscous effects at the plume edge and must result from relatively long-range pressure gradients, as has been shown for planar jets (Taveira and da Silva, 2013; Terashima et al., 2016) and (shear-free) oscillating grids (Holzner et al., 2009). Thus turbulent entrainment must, at the initial engulfment stage, be driven by these pressure gradients and not by viscous effects at the plume edge (*cf.* Westerweel et al., 2009). Such a view of entrainment is entirely consistent with the view of entrainment expressed by Philip et al. (2014) for turbulent boundary layers and by Mistry et al. (2016) for turbulent (non-buoyant) jets.

Providing a full three-dimensional picture of the instantaneous plume with planar measurements is challenging if not impossible (discussed further in § 4.7). As well as variations in height, along any horizontal cross section eddies may be present, absent or neither along any azimuthal angle in addition to the plume body meandering about the mean centreline. Observations using only planar measurements necessarily make defining regions of eddy absent regions challenging. For example figure 4.20 (*a*) highlights a height (along the black line) where a relatively narrow plume width is measured, which in our definition would define a region where an eddy is absent. Figures 4.20 (*b*) and (*c*) show that the relatively narrow width measured on the fixed plane in (*a*) may be a result of the plume body meandering towards the positive y direction, as in (*b*), or a true eddy absent event, as in (*c*). However, the results of § 4.4.1 suggests that the meandering of the plume body is relatively insignificant.

4.6 Comparison with axisymmetric jets

Our methodology closely follows that of Westerweel et al. (2005) and Westerweel et al. (2009) where axisymmetric turbulent jets were studied. Westerweel et al. (2009) concluded that the dominant process in turbulent entrainment in axisymmetric jets is nibbling and that the contribution of engulfment is negligible in an axisymmetric jet. Herein we conclude that, while nibbling is ultimately responsible for entrainment across the turbulent interface, the engulfment process provides a significant contribution to the turbulent entrainment process. The contrast in conclusions stem from both different observed results, suggesting

differences between jets and plumes, and different interpretations of the results. It is worth highlighting these differences. In addition we discuss why plumes entrain more than jets.

Westerweel et al. (2009) observed relatively insignificant vertical velocities outside the turbulent region of the jet (5% of the centreline velocities) while herein we observed velocities at 20% of the centreline plume velocities and 35% of the centreline plume velocities in regions absent of eddies. From these measurements we concluded that significant momentum is imparted to the ambient fluid outside the plume at heights between large eddies. A similar conclusion can not be made from the measurements of Westerweel et al. (2005) suggesting a key difference between jets and plumes.

Westerweel et al. (2005) find the transport of engulfed ambient fluid Q_{eng}/Q to be between 7% and 10%, whereas we find a value of 6.5%. Westerweel et al. (2005) and Westerweel et al. (2009) partly deduce the insignificance of the engulfment process from the relatively small value of Q_{eng}/Q. We, however, do not directly relate Q_{eng} to a qualitative or quantitative measure of the contribution of engulfment to entrainment because without a time scale associated with the engulfment, as discussed in § 4.4.2.2, it is difficult to determine the rate at which the engulfed fluid is nibbled into the plume fluid.

Experimental observations have consistently shown larger entrainment coefficients in jets as compared to plumes (see van Reeuwijk and Craske (2015) Table 3 and references therein). In the time-averaged sense, van Reeuwijk and Craske (2015) showed that, by performing an energy decomposition of the entrainment coefficient resulting in (4.5), the buoyancy provides an entrainment mechanism that does not directly rely on turbulence. In addition, it was shown that it is this contribution, as opposed to buoyancy-enhanced turbulence manifesting itself through an increase in the turbulent production (i.e. the first term on the right hand side of (4.5)) that results in the increase in the entrainment coefficient. Alternatively, Sreenivas and Prasad (2000) provide an instantaneous physical model that explains the increase in entrainment in plumes. In particular, the model suggests why engulfment may contribute more significantly to plumes than jets. The unstable stratification within a plume, as a result of plume density increasing with height, provides a baroclinic torque that assists the overturning of an eddy. It is this overturning mechanism of the plume that is associated with engulfment and therefore is expected to be more dominant in the plume than the jet, where baroclinic torque is absent.

4.7 Limitations of planar measurements in a three-dimensional flow

A turbulent axisymmetric plume is a highly three-dimensional, albeit statistically axisymmetric, flow. Therefore, planar measurements restrict observations of the three-dimensional flow dynamics. Here we discuss the limitations of planar measurements.

The definitions in this chapter, e.g. the plume envelope, have been constructed in a way that are blind to the out-of-plane flow dynamics. Therefore, using the same definition with three-dimensional measurements would not lead to different results. In addition, certain statistics, in particular the time-averaged vertical and horizontal velocities and the turbulent statistics, are statistically axisymmetric so that three-dimensional measurements do not offer a real advantage in this regard.

There are cases, however, where our definitions would be more appropriately defined with three-dimensional measurements. For example, it would be more appropriate to define the instantaneous plume widths in 3-D along lines intersecting the instantaneous plume centroid at a given height. This definition, given the probable change in results, would lead to a reinterpretation of the instantaneous plume width and the associated meandering of the plume. In particular, it could disentangle the motion of eddies passing through a given height and the bulk meandering of the body of the plume.

Planar measurements restrict a robust definition (i.e. a definition independent of out-of-plane flow dynamics) of engulfed ambient fluid to unmixed ambient fluid within a plume envelope. As discussed in § 4.4.2.2 we believe that our definition of a plume envelope, and therefore engulfed fluid, is consistent with the process of engulfment. In this respect, three-dimensional measurements do not offer a real advantage either. However, it is desirable to obtain a universally consistent definition of engulfment by defining engulfed fluid as unmixed ambient fluid that is not connected to the ambient far field via ambient fluid (completely engulfed fluid). Clearly, identification of completely engulfed fluid is not possible with planar measurements so that three-dimensional data could help to reinterpret the role of ‘complete’ engulfment in turbulent entrainment.

Similarly, planar measurements restrict a robust definition of eddy present and eddy absent events. Through our definition, eddies are defined as present (absent), when the instantaneous plume width is defined as relatively wide (narrow). Therefore, events where eddies are actually absent or the plume has meandered out of the plane are not distinguishable. These could be distinguished using three-dimensional measurements, for example, by defining the instantaneous plume width relative to the instantaneous plume centroid based on buoyancy.

While the planar measurements do not significantly restrict the validity of the conditional bulk flow quantities (that is by assuming statistic axisymmetry) it is not possible to determine the distance of a point on the measurement plane to the nearest point along the TNTI, which may be out of the measurement plane. However, the measurements close to the interface are robust, since the closest point along TNTI is more likely to be in the measurement plane.

4.8 Conclusions

Simultaneous measurements of the velocity field and the scalar edge of a plume have shown that significant vertical velocities exist outside the plume. Velocities beyond the plume edge cannot be induced by viscous effects at the plume edge and must be induced by relatively long-range pressure gradients (consistent with findings for other entraining flows, e.g. (Holzner et al., 2009; Taveira and da Silva, 2013; Terashima et al., 2016)). The vertical transport outside the plume (i.e. within ambient fluid) is in the mean approximately 5% of the total vertical transport, with this rising to almost 14% at heights between eddies. These (and others of our findings) indicate that significant vertical momentum is imparted to ambient fluid, at least, at heights between eddies before this ambient fluid comes into contact with the edge (turbulent/non-turbulent interface, TNTI) of the plume.

Our measurements show that, in the mean, the flux of engulfed fluid (i.e. unmixed fluid within the plume envelope) is $6.5\% \pm 2\%$ of the total vertical transport. We can account for the suggestion that the flux of engulfed fluid is greater than the transport outside the plume since we have shown that engulfed fluid at a given radial location travels faster than ambient at the same location, i.e. fluid must be accelerated vertically as it is engulfed. Even with this in mind, we are still able to conclude that our findings show that almost all the ambient fluid moving vertically outside the plume must be engulfed into the plume. It is not trivial to relate findings regarding the vertical fluxes of ambient or engulfed fluid to statements of the bulk entrainment rate ($\mathrm{d}Q/\mathrm{d}z$), since to do so requires knowledge of the length and time scales associated with the processes of engulfment and ultimately mixing. However, it is something that we hope is addressed in the near future.

Examining our measurements when we expect eddies to be locally either present or absent has highlighted substantial differences in the velocity field in the two cases, and we conclude that the passage of large-scale eddies at the plume edge drives pockets of ambient fluid at significant vertical velocities. The vertical momentum induced within these pockets of ambient fluid enables it to be engulfed within the plume. We conclude that the engulfment

of ambient fluid by large-scale eddies at the plume edge constitutes a significant part of the process of turbulent entrainment by plumes.

We have shown that observing significant vertical velocities outside the scalar edge of the plume should not be taken to imply that the velocity field is wider than the scalar field. Indeed, we show that different mechanisms drive the mixing, and thereby distributions, of momentum (velocities) and scalars. Through observations following the meandering and fluctuations in the plume, we remove the effects of spatial intermittency. By utilising our plume coordinate, we show that it is only as a result of spatial and temporal intermittency that a Gaussian distribution is observed for the scalar but that a distribution close to a Gaussian is still observed for the velocity. We conclude that the mixing of momentum (velocity) across the plume results in a distribution for which the differential entropy is, at least, close to maximal when the mixing is not bounded by the TNTI of the plume, indicating that the mixing of momentum must be controlled by the pressure field.

Chapter 5

Turbulent free line and wall line plumes

In this chapter we examine a turbulent free line plume, the flow resulting a horizontal line source of buoyancy in an environment absent of any boundaries, and a wall line plume, the flow resulting from a horizontal line source of buoyancy placed immediately adjacent to a wall. Simultaneous velocity and buoyancy field measurements on a vertical two-dimensional plane normal to the line source are performed and the two flow configurations are compared.

5.1 Introduction

Buoyancy-driven wall bounded flows occur in both natural environments and industrial situations. The presence of a vertical wall in such flows is known to inhibit the process of turbulent entrainment (Lee and Emmons, 1961) and thereby affect the mixing that arises. Here we investigate the effects of introducing a vertical wall to the flow generated by a line source of buoyancy. Applicable flows within effectively unbounded environments include the descending 'free' plume resulting from a chilled ceiling beam in the middle of a room, wherein the mixing of the plume affects the resulting thermal conditions within the room. In this chapter we investigate the entrainment mechanisms and determine the extent to which the mixing of such plumes is altered if a chilled ceiling beam was placed adjacent to a wall, thereby producing a 'wall plume'.

A broad finding among the early studies of wall plumes (Ellison and Turner, 1959; Lee and Emmons, 1961; Turner, 1973) is that the entrainment rates are significantly lower than those found in free plumes. Although velocity or buoyancy profile measurements were not presented in these studies, it was suggested that the wall suppresses the formation of large-scale structures and inhibits mixing, resulting in reduced entrainment into the plume. Velocity and buoyancy profiles are presented in later studies by Grella and Faeth (1975) and Lai and Faeth (1987), but in regions relatively close to the source where the flow was not

self-similar. To our knowledge, the only experimental velocity and buoyancy measurements of a wall plume in a self-similar region are those of Sangras et al. (1998) and Sangras et al. (2000), but they did not present simultaneous measurements. Nevertheless, the early findings of a reduced entrainment coefficient were confirmed, and entrainment approximately half that of a free plume was observed (Sangras et al., 1998). This reduction in entrainment was largely attributed to the reduced meandering of the large-scale structures and suppression of cross-stream turbulent fluxes (Ellison and Turner, 1959; Sangras et al., 2000; Turner, 1973).

Despite these insights, to our knowledge, a study examining and comparing the large-scale structures and cross-stream turbulent fluxes of a wall plume to those of a free plume does not exist. However, much attention has recently been devoted to turbulent entrainment in other free-shear and wall-bounded flows, providing a framework which may be extended to wall plumes. Based on the formalism of Priestley and Ball (1955), Paillat and Kaminski (2014b) suggested an entrainment model for turbulent plane jets, later extended to turbulent plane plumes Paillat and Kaminski (2014a) where relative contributions of turbulent production, $\alpha_{production}$, and net buoyancy, $\alpha_{buoyant}$, to the entrainment coefficient could be distinguished and quantified. A similar decomposition was performed by van Reeuwijk and Craske (2015) for a turbulent axisymmetric plume and by Holzner et al. (2016) on turbulent entrainment in an inclined gravity current, where the contribution from the viscous terms, $\alpha_{viscous}$, which are non-negligible due to the viscous boundary layer was also calculated but found to be relatively small compared to the combined contributions of turbulent production and net buoyancy.

Other studies have sought to understand turbulent flows by examining the small scale processes ultimately responsible for turbulent entrainment (Philip et al., 2014) by considering the entrainment across surfaces within the flow and relating this to the bulk entrainment. In doing so, some authors have attempted to disentangle dominant large-scale processes, whereby ambient fluid is 'engulfed' by the plume, with small scale processes close to the TNTI termed 'nibbling', whereby vorticity is imparted to the ambient fluid via viscous stresses across the TNTI at a length scale close to the Taylor microscale (Terashima et al., 2016). While Philip et al. (2014) suggest that large-scale eddies determine the overall rate of entrainment, Westerweel et al. (2009) conclude that the entrainment process is dominated by 'nibbling'. However, it is agreed that mixing is greatly enhanced due to stretching of surfaces by vorticity (Ottino, 1989). By experimentally examining a turbulent jet Mistry et al. (2016) show that turbulent entrainment in jets is a multi-scale process where at large scales ambient fluid is transported across smooth surfaces, but ultimately transported across the TNTI, which exhibits fractal qualities, at smaller scales at relatively low velocities. This

is consistent with Meneveau and Sreenivasan (1990) who suggested that the total flux across the TNTI should be independent of scale. Burridge et al. (2017) examined an axisymmetric plume and suggested that engulfment of ambient fluid by the large scale structures is the rate-limiting process for turbulent entrainment, consistent with Philip et al. (2014).

In this chapter we use an energy decomposition to examine the reduced entrainment in a wall plume. We follow the free plume entrainment decomposition developed by Paillat and Kaminski (2014a) and extend the theory to a wall plume, which closely follows the entrainment decomposition of Holzner et al. (2016) in an inclined turbulent gravity current, where relative contributions of turbulent production, buoyant and viscous terms may be calculated directly. In doing so relative contributions to the entrainment coefficient may be compared between the free and wall plume. We also use methods developed by Mistry et al. (2016) and Burridge et al. (2017) to examine the statistics of the TNTI by both quantifying the increased meandering in a free plume and relating this to the increased length of the TNTI in the free plume. This is achieved by making simultaneous measurements of velocity and buoyancy in self-similar line plumes adjacent to and far from a vertical wall.

The chapter is organised as follows. We review plume theory for two-dimensional free and wall plumes and the results of previous studies and extend the entrainment decomposition of Paillat and Kaminski (2014a) to wall plumes in § 5.2. The experimental methods and data analysis are presented in § 5.3, and the validation of the data is described in § 5.4. The experimental results are presented and discussed in an Eulerian coordinate system § 5.5 and in a plume coordinate system in § 5.6. In § 5.7 we discuss the limitations of performing planar measurements on a three-dimensional flow. In § 5.8 the turbulent Prandtl number of the free plume is investigated by following a framework developed by Craske et al. (2017) for a turbulent axisymmetric plume. Finally, the conclusions are presented in § 5.9.

5.2 Theory and previous work on entrainment in free and wall plumes

A turbulent line plume is the flow driven by an infinitely long horizontal line source of buoyancy. The wall plume differs from the free plume by the presence of a vertical wall that is placed immediately adjacent to, and spans the entire length of, the line source. We consider a uniform ambient fluid and restrict attention to the case where the wall is adiabatic so that there is no loss nor addition of buoyancy into the plume. Consequently, the buoyancy flux is constant with height in both the free plume and the wall plume. Here we outline the theory of entrainment in free and wall plumes in a quiescent environment and adapt the

entrainment coefficient decomposition of free plumes developed by Paillat and Kaminski (2014a) to wall plumes.

In both flows we define the velocity $w(x,z,t)$ in the vertical z-direction, horizontal velocity $u(x,z,t)$ in the across-plume x-direction, the deviation from hydrostatic pressure $p(x,z,t)$ and the buoyancy $b(x,z,t) = g(\rho_a - \rho(x,z,t))/\rho_a$, where ρ and ρ_a are the density of the plume and ambient, respectively and we assume that $\rho_a - \rho \ll \rho_a$. Since the flows are statistically steady, these quantities may be decomposed into time-averaged and fluctuating components $w(x,z,t) = \overline{w}(x,z) + w'(x,z,t)$, $u(x,z,t) = \overline{u}(x,z) + u'(x,z,t)$ and $b(x,z,t) = \overline{b}(x,z) + b'(x,z,t)$, and we denote the time-averaged maximum vertical velocity and buoyancy as $\overline{w}_m(z)$ and $\overline{b}_m(z)$. We assume all quantities are independent of the y-direction aligned along the plume source. We define, respectively, the time-averaged volume flux, momentum flux, energy flux, integral buoyancy and buoyancy flux per unit length by

$$Q_f(z) = \int_{-\infty}^{\infty} \overline{w}(x,z)\mathrm{d}x, \qquad Q_w(z) = \int_{0}^{\infty} \overline{w}(x,z)\mathrm{d}x, \tag{5.1}$$

$$M_f(z) = \int_{-\infty}^{\infty} \overline{w}^2(x,z)\mathrm{d}x, \qquad M_w(z) = \int_{0}^{\infty} \overline{w}^2(x,z)\mathrm{d}x, \tag{5.2}$$

$$E_f(z) = \int_{-\infty}^{\infty} \overline{w}^3(x,z)\mathrm{d}x, \qquad E_w(z) = \int_{0}^{\infty} \overline{w}^3(x,z)\mathrm{d}x, \tag{5.3}$$

$$B_f(z) = \int_{-\infty}^{\infty} \overline{b}(x,z)\mathrm{d}x, \qquad B_w(z) = \int_{0}^{\infty} \overline{b}(x,z)\mathrm{d}x, \tag{5.4}$$

$$F_f(z) = \int_{-\infty}^{\infty} \overline{w}(x,z)\overline{b}(x,z)\mathrm{d}x, \qquad F_w(z) = \int_{0}^{\infty} \overline{w}(x,z)\overline{b}(x,z)\mathrm{d}x, \tag{5.5}$$

where the suffices f and w denote the free and wall plumes, respectively. In addition, we define the source buoyancy flux per unit length as F_0. From these relations we define the characteristic scales for plume width R and velocity W by

$$R_f = \frac{Q_f^2}{2M_f}, \qquad R_w = \frac{Q_w^2}{M_w}, \tag{5.6}$$

$$W_f = \frac{M_f}{Q_f}, \qquad W_w = \frac{M_w}{Q_w}. \tag{5.7}$$

Note that in the case of the free plume, R_f is equivalent to a 'top-hat' half-width, whereas for the wall plume, R_w is equivalent to a 'top-hat' full-width, which is used since it is analogous to the half-width of the free plume. Under the Boussinesq approximation, the Reynolds time-

averaged mass, vertical momentum and buoyancy conservation equations may be written

$$\frac{\partial \overline{u}}{\partial x}+\frac{\partial \overline{w}}{\partial z}=0, \tag{5.8}$$

$$\overline{u}\frac{\partial \overline{w}}{\partial x}+\overline{w}\frac{\partial \overline{w}}{\partial z}+\frac{\partial}{\partial z}\left(\overline{w'^2}\right)+\frac{\partial \overline{u'w'}}{\partial x}=-\frac{1}{\rho_a}\frac{\mathrm{d}\overline{p}}{\mathrm{d}z}+\overline{b}+\nu\frac{\partial^2 \overline{w}}{\partial x^2}, \tag{5.9}$$

$$\overline{u}\frac{\partial \overline{b}}{\partial x}+\overline{w}\frac{\partial \overline{b}}{\partial z}+\frac{\partial \overline{u'b'}}{\partial x}+\frac{\partial \overline{w'b'}}{\partial z}=\kappa\frac{\partial^2 \overline{b}}{\partial x^2}, \tag{5.10}$$

where ν and κ are the kinematic viscosity and mass diffusivity of the fluid, respectively. For the free plume, assuming that the Reynolds number $Re=w_m R/\nu \gg 1$ and the Péclet number $Pe=ReSc \gg 1$, where $Sc=\nu/\kappa$ is the Schmidt number, the viscous and diffusion terms in (5.9) and (5.10), respectively, may be ignored. In § 5.3.1 the experimental conditions $Re \gg 1$ and $Pe \gg 1$ are justified. The integration of equations (5.8)-(5.10) gives

$$\frac{\mathrm{d}Q_f}{\mathrm{d}z}=\overline{u}(-\infty,z)-\overline{u}(\infty,z), \tag{5.11}$$

$$\frac{\mathrm{d}M_f}{\mathrm{d}z}+\left[\overline{uw}+\overline{u'w'}\right]\Big|_{-\infty}^{\infty}=B_f-\frac{\mathrm{d}}{\mathrm{d}z}\left(\int_{-\infty}^{\infty}\overline{w'^2}+\frac{1}{\rho_a}\frac{\mathrm{d}\overline{p}}{\mathrm{d}z}\mathrm{d}x\right), \tag{5.12}$$

$$\frac{\mathrm{d}}{\mathrm{d}z}\left(\int_{-\infty}^{\infty}\overline{w}\overline{b}+\overline{w'b'}\mathrm{d}x\right)+\overline{u'b'}\Big|_{-\infty}^{\infty}=0. \tag{5.13}$$

Measurements by Bradbury (1965) and Miller and Comings (1957) in a turbulent free line jet showed that

$$\int_{-\infty}^{\infty}\overline{w'^2}\mathrm{d}x\approx-\int_{-\infty}^{\infty}\frac{1}{\rho_a}\frac{\mathrm{d}\overline{p}}{\mathrm{d}z}\mathrm{d}x, \tag{5.14}$$

we will therefore ignore these terms in the integral (5.12). Using the entrainment assumption, that the inflow velocity at any height is proportional to the local vertical plume velocity i.e. $\overline{u}(-\infty,z)=-\overline{u}(\infty,z)=\alpha_f W_f$, where α_f is the 'top-hat' entrainment coefficient (Morton et al., 1956), the equations (5.11)-(5.13), with the boundary conditions $\overline{w}(-\infty,z)=\overline{u'w'}(-\infty,z)=\overline{u'b'}(-\infty,z)=\overline{w}(\infty,z)=\overline{u'w'}(\infty,z)=\overline{u'b'}(\infty,z)=0$, gives the free plume conservation equations for the time-averaged volume, momentum and buoyancy flux

$$\frac{\mathrm{d}Q_f}{\mathrm{d}z}=2\alpha_f\frac{M_f}{Q_f}, \tag{5.15}$$

$$\frac{\mathrm{d}M_f}{\mathrm{d}z}=B_f=\frac{F_f Q_f}{\theta_f M_f}, \tag{5.16}$$

$$\frac{\mathrm{d}F_f}{\mathrm{d}z}=0, \tag{5.17}$$

where θ_f encapsulates the relation between the integral buoyancy B_f and the buoyancy flux F_f (which may also be interpreted as the non-dimensional buoyancy flux (van Reeuwijk and Craske, 2015)), which by assuming self-similarity we may take as constant. Further, by self-similarity we have assumed that

$$\int_{-\infty}^{\infty} \overline{w'b'}\mathrm{d}x = \gamma F_f, \tag{5.18}$$

for some constant γ_f, so that

$$\int_{-\infty}^{\infty} \overline{w}\overline{b} + \overline{w'b'}\mathrm{d}x = F_f + \int_{-\infty}^{\infty} \overline{w'b'}\mathrm{d}x = F_f + \gamma F_f = (1+\gamma)F_f. \tag{5.19}$$

Note that in (5.15) the factor of two occurs as α_f represents the entrainment into one side of the plume only. The solutions to the free plume equations (5.15)-(5.17) are

$$Q_f(z) = \left(2\alpha_f\right)^{2/3}\left(\frac{F_f}{\theta_f}\right)^{1/3} z, \tag{5.20}$$

$$M_f(z) = \left(2\alpha_f\right)^{1/3}\left(\frac{F_f}{\theta_f}\right)^{2/3} z, \tag{5.21}$$

$$F_f(z) = F_f. \tag{5.22}$$

For the wall plume, the viscous term in (5.9) is assumed to be non-negligible as it characterises the effect of the no-slip boundary condition on the wall. The integration of equations (5.8)-(5.10) gives

$$\frac{\mathrm{d}Q_w}{\mathrm{d}z} = -\overline{u}(\infty, z), \tag{5.23}$$

$$\frac{\mathrm{d}M_w}{\mathrm{d}z} + \left[\overline{uw} + \overline{u'w'}\right]\Big|_0^{\infty} = B_f - \frac{\mathrm{d}}{\mathrm{d}z}\left(\int_0^{\infty} \overline{w'^2} + \frac{1}{\rho_a}\frac{\mathrm{d}\overline{p}}{\mathrm{d}z}\mathrm{d}x\right) + \nu\frac{\partial \overline{w}}{\partial x}\bigg|_0^{\infty}, \tag{5.24}$$

$$\frac{\mathrm{d}}{\mathrm{d}z}\left(\int_0^{\infty} \overline{w}\overline{b} + \overline{w'b'}\mathrm{d}x\right) + \overline{u'b'}\Big|_0^{\infty} = \kappa\frac{\partial \overline{b}}{\partial x}\bigg|_0^{\infty}. \tag{5.25}$$

Using the same entrainment assumption that $\overline{u}(\infty, z) = -\alpha_w W_w$, (5.14) and with the boundary conditions $\overline{w}(0,z) = \overline{u}(0,z) = \overline{u'w'}(0,z) = \overline{u'b'}(0,z) = \overline{w}(\infty,z) = \overline{u'w'}(\infty,z) = \overline{u'b'}(\infty,z) = 0$ and $\left.\frac{\partial b}{\partial x}\right|_0 = 0$, since the wall is adiabatic, gives the wall plume conservation equations for

the time-averaged volume, momentum and buoyancy flux

$$\frac{\mathrm{d}Q_w}{\mathrm{d}z} = \alpha_w \frac{M_w}{Q_w}, \tag{5.26}$$

$$\frac{\mathrm{d}M_w}{\mathrm{d}z} = B_w - \nu \frac{\partial w}{\partial x}\bigg|_0 = \frac{F_w Q_w}{\theta_w M_w} - C\left(\frac{M_w}{Q_w}\right)^2, \tag{5.27}$$

$$\frac{\mathrm{d}F_w}{\mathrm{d}z} = 0, \tag{5.28}$$

where θ_w encapsulates the relation between the integral buoyancy B_w and the buoyancy flux F_w (again, this may be interpreted as the non-dimensional buoyancy flux), and we express the wall shear stress in terms of the characteristic velocity W_w and a skin friction coefficient C. The assumption of self-similarity in the wall plume is more problematic because of the existence of a viscous boundary layer in order to satisfy the no-slip condition on the vertical wall. However, throughout this chapter we assume that the wall plume is self-similar, an assumption which we show to be valid in § 5.4. Therefore, we take θ_w and C to be constants and we again assume that the turbulent buoyancy flux may be expressed in terms of the buoyancy flux (c.f. (5.19)). For a free stream turbulent boundary layer the skin friction coefficient follows $C = 0.0576 Re_x^{-1/5}$ (Schlichting and Gersten, 2017), where Re_x is based on the boundary layer thickness. While this flow is not directly applicable to the wall plume, it does suggest that the wall plume skin friction coefficient will decrease with increasing Reynolds number. However, it also suggests that the skin friction coefficient will not vary significantly over a height with a small variation in Reynolds number, as in our experiments.

The solutions to the wall plume equations (5.26)-(5.28) are

$$Q_w(z) = \left(\frac{F_w}{1+\frac{C}{\alpha_w}}\right)^{1/3} \theta_w^{-1/3} \alpha_w^{2/3} z, \tag{5.29}$$

$$M_w(z) = \left(\frac{F_w}{1+\frac{C}{\alpha_w}}\right)^{2/3} \theta_w^{-2/3} \alpha_w^{1/3} z, \tag{5.30}$$

$$F_w(z) = F_w. \tag{5.31}$$

The constants α_w and α_f are the standard top-hat entrainment coefficients. However, it has been widely observed in previous studies that the vertical velocity and buoyancy profiles of a free plume are well fitted by a Gaussian curve, (e.g. Paillat and Kaminski (2014a), Ramaprian and Chandrasekhara (1989)) and the conservation of volume flux in the free and wall plume may also be expressed in terms of the maximum vertical velocity and a Gaussian

entrainment coefficient α_G, in the form

$$\frac{\mathrm{d}Q_f}{\mathrm{d}z} = 2\alpha_{f,G}\overline{w}_m, \quad \frac{\mathrm{d}Q_w}{\mathrm{d}z} = \alpha_{w,G}\overline{w}_m. \tag{5.32}$$

The top-hat entrainment coefficient in the free plume is related to the Gaussian coefficient by $\alpha_f = \sqrt{2}\,\alpha_{f,G}$ and most studies choose to calculate $\alpha_{f,G}$. At present there is significant disagreement about the value of the entrainment coefficient, with previously reported Gaussian entrainment values in the range $\alpha_{f,G} = \{0.10, 0.16\}$ (table 5.1).

Most studies on wall plumes also focus on the Gaussian entrainment coefficient $\alpha_{w,G}$, although in some cases, notably Grella and Faeth (1975), the top-hat value α_w was also calculated. Since the velocity profile of the wall plume is not a known analytic function a theoretical relation between α_w and $\alpha_{w,G}$ cannot been derived, although Grella and Faeth (1975) find that $\alpha_w/\alpha_{w,G} \approx 1.4$. There is broad agreement with previously measured Gaussian entrainment values of the wall plume (table 5.1). This is somewhat surprising given the additional difficulties associated with measuring the velocity of the wall-plume, which is perhaps reflected in the variation in other parameters between these experiments, especially the maximum mean velocity used in the calculation of $\alpha_{w,G}$. Further, Grella and Faeth (1975) and Lai and Faeth (1987) emphasise that their data were not in a self-similar region as the flow appeared to be evolving over the whole range of heights where the measurements were taken. For these reasons it appears that, to our knowledge, an experimentally determined top-hat entrainment value for a wall-plume within a self-similar region does not exist in the literature. This is problematic given the unknown relationship between $\alpha_{w,G}$ and α_w in a self-similar region and that, despite the consistency between the previously determined $\alpha_{w,G}$, the closure model of (5.32) relies on an established maximum velocity for which there is significant disagreement.

Our study is focused on the comparison of the top-hat entrainment values for a free and a wall plume. Since these two flows have different velocity profiles it is natural to compare the entrainment rates without any assumption on profile shapes. It is, therefore, unfortunate that for the wall plume case previous work has paid less attention to the top-hat value.

5.2.1 Energy decomposition of entrainment in turbulent wall plumes

Paillat and Kaminski (2014a) used the formalism of Priestley and Ball (1955) and Kaminski et al. (2005) to develop a theoretical model of entrainment in free turbulent plumes, which had previously been adapted to free turbulent planar jets by Paillat and Kaminski (2014b). This involved decomposing the entrainment coefficient into relative contributions from buoyancy and turbulent production. A similar analysis has also been performed on

Experiment	Plume type	α	α_G	$\overline{w}_m/F_0^{1/3}$	$\frac{\mathrm{d}Q}{\mathrm{d}z}/F_0^{1/3}$
Lee and Emmons (1961)	Free	-	0.16	-	-
Kotsovinos (1975)	Free	-	0.10	1.66	-
Yuana and Cox (1996)	Free	-	0.13	2.04	-
Paillat and Kaminski (2014a)	Free	-	0.12	$2.1-2.2$	-
Ramaprian and Chandrasekhara (1989)	Free	0.16	0.11	2.13	0.48
Rouse et al. (1952)	Free	-	0.11	1.91	-
Present study	Free	0.14	0.10	2.10	0.40
Grella and Faeth (1975)	Wall	0.095	0.067	3.16	0.21
Lai and Faeth (1987)	Wall	-	0.071	2.14	0.15
Sangras et al. (2000)	Wall	-	0.068	2.84	0.19
Present study	Wall	0.08	0.061	2.89	0.17

Table 5.1 Entrainment values, scaled vertical velocities and scaled rate of change of mean volume flux of previous work, where F_0 is the source buoyancy flux.

turbulent inclined gravity currents by Holzner et al. (2016), where the contributions from the viscous terms due to the wall were also included and found to be small compared to the buoyant and turbulent production terms. Here we outline a similar decomposition of the entrainment coefficient of the wall plume into separate turbulent production, buoyant and viscous terms.

An expression for the conservation of vertical kinetic energy may be obtained by multiplying (5.24) by $\overline{w}$, ignoring the pressure and vertical velocity fluctuations, and using the continuity equation to obtain (Priestley and Ball, 1955),

$$\frac{\partial}{\partial z}\left(\frac{1}{2}\overline{w}^3\right)+\frac{\partial}{\partial x}\left(\frac{1}{2}\overline{u}\,\overline{w}^2\right)=\overline{w}\overline{b}-\overline{w}\frac{\partial}{\partial x}\left(\overline{u'w'}\right)+\nu\overline{w}\frac{\partial^2\overline{w}}{\partial x^2}, \tag{5.33}$$

where integrating with the wall plume boundary conditions gives

$$\frac{\mathrm{d}E_w}{\mathrm{d}z}=2F_w+2\int_0^\infty\frac{\partial\overline{w}}{\partial x}\overline{u'w'}\mathrm{d}x-2\nu\int_0^\infty\left(\frac{\partial\overline{w}}{\partial x}\right)^2\mathrm{d}x. \tag{5.34}$$

The conservation of volume flux may be expressed as (Paillat and Kaminski, 2014a)

$$\frac{\mathrm{d}Q_w}{\mathrm{d}z}=2\frac{Q_w}{M_w}\frac{\mathrm{d}M_w}{\mathrm{d}z}-\frac{Q_w}{E_w}\frac{\mathrm{d}E_w}{\mathrm{d}z}+\frac{M_w^2}{E_w}\frac{\mathrm{d}}{\mathrm{d}z}\left(\frac{Q_wE_w}{M_w^2}\right), \tag{5.35}$$

where, assuming self-similarity, the last term is zero. By equating (5.26) and (5.35) the entrainment coefficient may be expressed as

$$\alpha_w = 2\frac{Q_w^2}{M_w^2}\frac{\mathrm{d}M_w}{\mathrm{d}z} - \frac{Q_w^2}{E_w M_w}\frac{\mathrm{d}E_w}{\mathrm{d}z}, \tag{5.36}$$

and substituting equation (5.27) and (5.34) into (5.36) gives

$$\alpha_w = \alpha_{buoyant} + \alpha_{production} + \alpha_{viscous}, \tag{5.37}$$

where

$$\alpha_{buoyant} = 2Ri\left(\frac{1}{\theta_w} - \frac{M_w^2}{Q_w E_w}\right), \tag{5.38}$$

$$\alpha_{production} = -2\frac{Q_w^2}{E_w M_w}\int_0^\infty \frac{\partial \overline{w}}{\partial x}\overline{u'w'}\mathrm{d}x, \tag{5.39}$$

$$\alpha_{viscous} = \frac{2Q^2\nu}{E_w M_w}\int_0^\infty \left(\frac{\partial \overline{w}}{\partial x}\right)^2 \mathrm{d}x - 2C, \tag{5.40}$$

where Ri is the Richardson number defined by $Ri = F_w Q_w^3/M_w^3$ and C is the skin friction coefficient. The first term, $\alpha_{buoyant}$, is a result of both a positive contribution, resulting from the effect of buoyancy on the momentum flux, and a negative contribution, resulting from the effect of buoyancy on the energy flux, to entrainment. However, for Gaussian vertical velocity and buoyancy profiles the net contribution may be shown to be positive. $\alpha_{buoyant}$ may be interpreted as the net effect of buoyancy contributing to entrainment which, as noted by van Reeuwijk and Craske (2015), provides plumes with a mechanism for entrainment not directly associated with turbulence. The second term, $\alpha_{production}$, corresponds to the efficiency of turbulent entrainment driven by the turbulent production (Paillat and Kaminski, 2014a) and is the dominant positive contribution to α. The final term $\alpha_{viscous}$ corresponds to the viscous processes of the flow. The first term on the right hand side of (5.40), which contributes positively to entrainment, is the mean dissipation rate and the second term, which is the dominant negative contribution to entrainment, represents the inner boundary layer processes that require energy but are not directly related to entrainment (Holzner et al., 2016).

A similar decomposition of the free plume entrainment coefficient gives (Paillat and Kaminski, 2014a)

$$\alpha_f = \alpha_{buoyant} + \alpha_{production}, \tag{5.41}$$

where

$$\alpha_{buoyant} = Ri\left(\frac{1}{\theta_f} - \frac{M_f^2}{Q_f E_f}\right), \tag{5.42}$$

$$\alpha_{production} = -\frac{Q_f^2}{E_f M_f}\int_{-\infty}^{\infty}\frac{\partial \overline{w}}{\partial x}\overline{u'w'}\mathrm{d}x, \tag{5.43}$$

where Ri is the Richardson number similarly defined by $Ri = F_f Q_f^3/M_f^3$ and the decomposed terms may be interpreted as above for the wall plume. Using experimental data we show the validity of the decomposition of the free plume, also shown by Paillat and Kaminski (2014a), and we calculate the relative contributions to the entrainment coefficient for the wall plume.

5.3 Experiments and analysis

5.3.1 Experimental details

The experiments were designed to create turbulent free and wall plumes that would enable us to make simultaneous measurements of the buoyancy and velocity fields of the flow. The experiments were performed in a Perspex (acrylic) tank (figure 5.1) of horizontal cross-section $1.2\,\mathrm{m} \times 0.4\,\mathrm{m}$ filled with dilute saline solution of uniform density ρ_a to a depth of $0.75\,\mathrm{m}$. Relatively dense sodium nitrate solution was used as source fluid which enabled refractive indices of the plume fluid and ambient to be matched as is needed for accurate measurements of the velocity field as described below. The source fluid, at a reduced gravity of b_0, was supplied using a Cole-Parmer Digital Gear Pump System, 0.91 mL/rev, which was calibrated for each experiment with a separate flow rate. The gear pump provided uniform volume, Q_0, and buoyancy, $F_0 = Q_0 b_0$, fluxes per unit length, via a line source of dimension $L = 0.15\,\mathrm{m}$ and width $d = 1\,\mathrm{mm}$ (figure 5.2). The nozzle was constructed in order to create a uniform spanwise velocity profile at the source by using a modular design. The nozzle structure consisted of four valves, from which the source fluid is supplied via the gear pump, which enter a chamber filled with reticulated polyether foam designed to equalise the incoming flow. The first chamber is connected to a second chamber, via very small holes that were used to increase the pressure in the first chamber and promote flow uniformity along the length of the source, which was also packed with reticulated foam. The line source nozzle exit was connected to the second chamber, which can be see in figure 5.2. Figure 5.3 (*b*) shows the line source exit velocity profile along the length of the source. This was measured by performing PIV along a plane aligned with the line source.

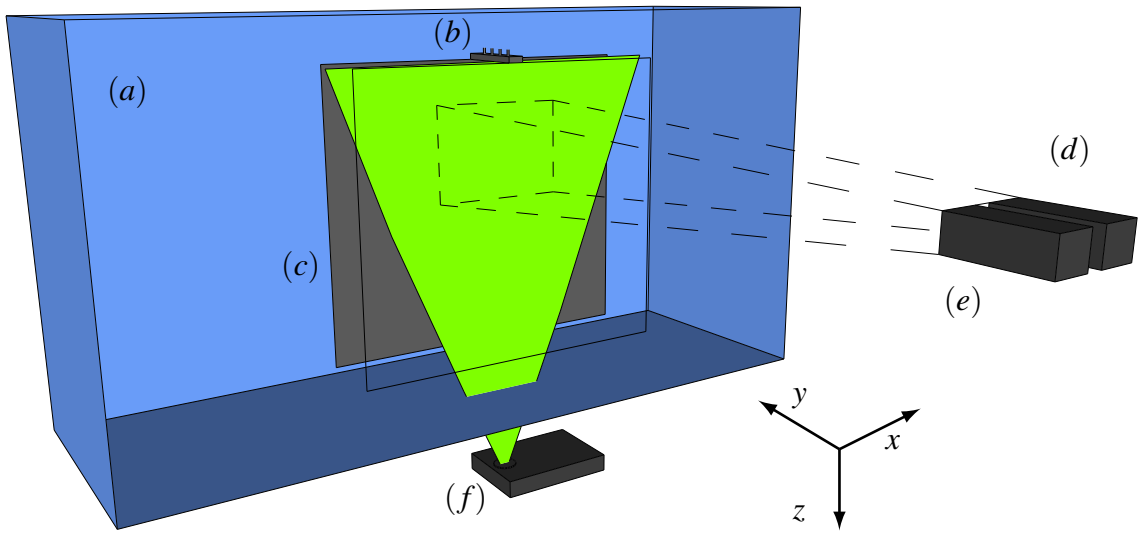

Fig. 5.1 Diagram of the experimental setup for the free plume showing the (*a*) water tank, (*b*) line source (see figure 5.2), (*c*) bounding walls perpendicular to the line source (see text and figure 5.4), (*d*) PIV camera, (*e*) PLIF camera and (*f*) Laser. The illuminated plane (green) created by the laser shows the plane that the measurements were taken, perpendicular to the line source. The experimental setup for the wall plume experiments differ only by the presence of a wall immediately adjacent to the line source (figure 5.3).

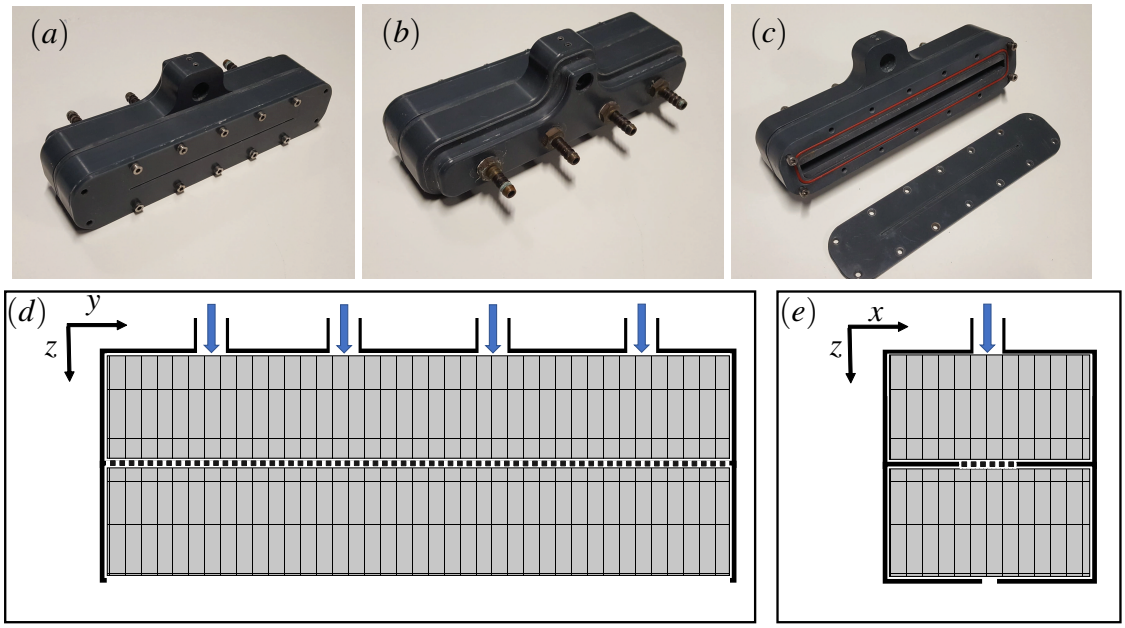

Fig. 5.2 The source nozzle was constructed using a modular design (see text). (*a*) and (*b*) show the completed nozzle structure and (*c*) shows the nozzle structure with the source exit piece removed. This allowed for the same nozzle structure to be used for both the free and wall plume by changing only the exit nozzle piece. (*d*) and (*e*) illustrate the nozzle design through a cross section of the nozzle in the plane $x = 0$ and $y = 0$, respectively. The grey blocks inside the structure in (*d*) and (*e*) highlight the reticulated foam (not shown in (*c*)).

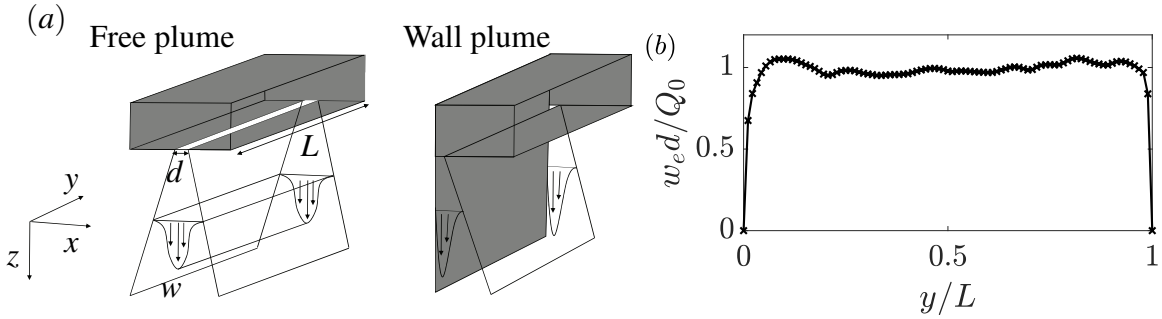

Fig. 5.3 (*a*) The coordinate system of the free and wall plume and (*b*) the exit velocity, measured at 4 mm from the source exit, of the line source along the length of the source with a flow rate per unit length of $Q_0 = 1.00 \times 10^{-4}\,\mathrm{m^2\,s^{-1}}$. The structure of the line source nozzle of the free and wall plume were identical.

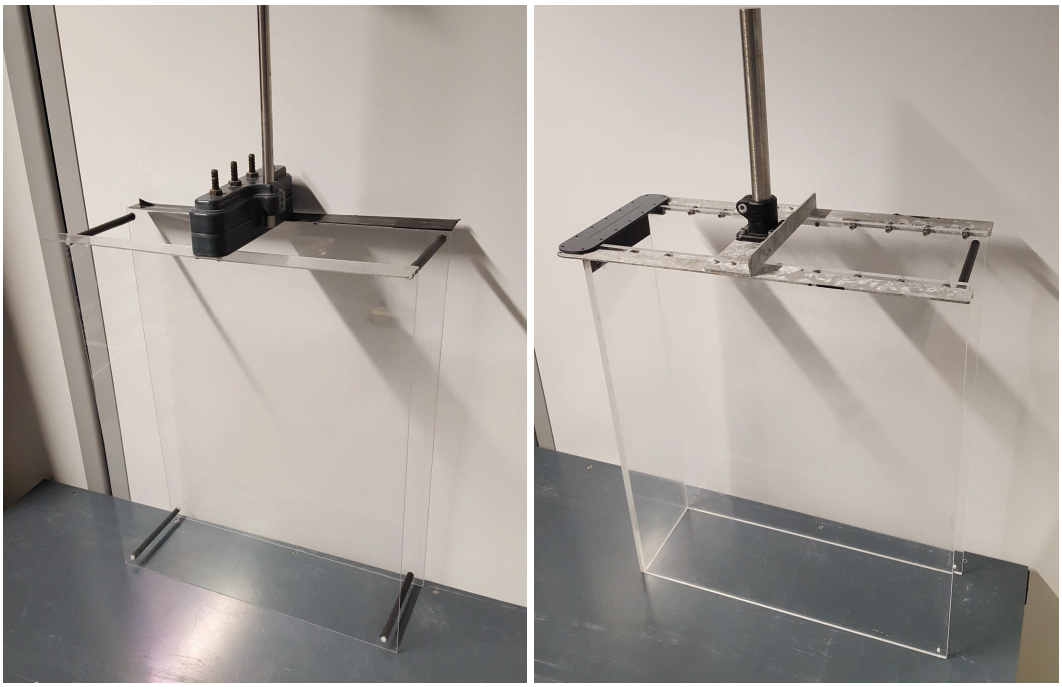

Fig. 5.4 The free (left) and wall (right) plume structure used to enclose the flow within the large reservoir tank. The stainless steel rods seen in each picture are used to support the structure in the reservoir. The complete source nozzle structure is shown in the free plume structure whereas only the source nozzle exit piece is shown in wall plume structure (see figure 5.2).

Parameter	Definition	Exp 1	Exp 2	Exp 3	Exp 4	Exp 5
Source volume flux	$Q_0\,[\times 10^{-4}\,\mathrm{m^2\,s^{-1}}]$	1.33	1.33	1.00	1.22	1.22
Source buoyancy	$b_0\,[\mathrm{m\,s^{-2}}]$	0.24	0.24	0.24	0.21	0.21
Plume parameter	Γ	0.9	0.9	0.9	0.7	0.8
Reynolds number (z=0.25 m)	Re	1960	2020	1640	1730	1900
Turbulent Reynolds number (z=0.25 m)	Re_λ	148	135	147	160	158
Kolmogorov length scale (z=0.25 m)	$\eta\,[\times 10^{-4}\,\mathrm{m}]$	4.0	3.7	4.2	4.0	4.0
Batchelor length scale (z=0.25 m)	$\lambda_B[\times 10^{-5}\,\mathrm{m}]$	1.7	1.6	1.8	1.7	1.8
Taylor microscale (z=0.25 m)	$\lambda\,[\times 10^{-2}\,\mathrm{m}]$	0.9	0.9	1.0	1.0	1.0
PIV vector spacing	-	2.8η	3.0η	2.6η	2.8η	2.7η
pixel spacing	-	0.23η	0.25η	0.22η	0.23η	0.23η
Kolmogorov time scale (z=0.25 m)	$\tau_\eta\,[\mathrm{s}]$	0.15	0.13	0.17	0.15	0.15

Table 5.2 Experimental parameters and measured length and time scales of the free plume experiments. Definitions are provided in the text.

Parameter	Definition	Exp 6	Exp 7	Exp 8	Exp 9	Exp 10
Source volume flux	$Q_0\,[\times 10^{-4}\,\mathrm{m^2\,s^{-1}}]$	0.79	0.79	1.03	1.02	1.02
Source buoyancy	$b_0\,[\mathrm{m\,s^{-2}}]$	0.33	0.33	0.33	0.16	0.16
Plume parameter	Γ	1.3	1.0	1.2	1.3	1.2
Reynolds number (z=0.40 m)	Re	2820	2530	2980	2420	2870
Turbulent Reynolds number (z=0.40 m)	Re_λ	163	185	186	167	180
Kolmogorov length scale (z=0.40 m)	$\eta\,[\times 10^{-4}\,\mathrm{m}]$	3.8	3.9	3.7	4.3	4.5
Batchelor length scale (z=0.40 m)	$\lambda_B\,[\times 10^{-5}\,\mathrm{m}]$	1.7	1.7	1.6	1.9	2.0
Taylor microscale (z=0.40 m)	$\lambda\,[\times 10^{-2}\,\mathrm{m}]$	1.0	1.0	1.0	1.1	1.2
PIV vector spacing	-	2.9η	2.9η	3.0η	2.6η	2.5η
PLIF pixel spacing	-	0.24η	0.24η	0.24η	0.21η	0.21η
Kolmogorov time scale (z=0.40 m)	$\tau_\eta\,[\mathrm{s}]$	0.14	0.14	0.13	0.19	0.20

Table 5.3 Experimental parameters and measured length and time scales of the wall plume experiments.

The non-uniformity of the velocity profile is most prominent close to the walls, however, as highlighted by Krug et al. (2013) in their experimental investigation of a gravity current, the region close to the walls at $y/L = 0$ and $y/L = 1$ are subjected to boundary effects anyway so should not be of any additional concern with respect to the two-dimensional nature of the flow within the central region, $0.15 < y/L < 0.85$, where the exit velocity varies by at most 6% of the mean velocity. The initial density of the ambient and source fluid was measured using an Anton Paar DMA 5000 density meter to an accuracy of $1 \times 10^{-3}\,\mathrm{kg\,m^{-3}}$, at 20 °C. The ambient and source solution were both left overnight to reach a uniform, and equal, temperature of 20 °C and were measured to be within 0.1 °C of this temperature. This corresponds to a maximum error of 0.15% of the initial density differences used in our experiments. To promote the two-dimensionality of the flow by eliminating any entrainment from beyond the length of the source, the flow was enclosed by two $0.6\,\mathrm{m} \times 0.6\,\mathrm{m}$ transparent walls (x-z planes) perpendicular to the line source, separated by the length of the source, see figure 5.4. To create the wall plume a further vertical wall in the y-z plane was mounted immediately adjacent to one edge of the line source.

Simultaneous measurements of the velocity and density fields on a x-z plane were taken using particle image velocimetry (PIV) and planar laser-induced fluorescence (PLIF). A frequency-doubled dual-cavity Litron Nano L100 Nd:YAG pulsed laser with wavelength 532 nm was used to create a light sheet with a thickness of 2 mm in the measurement section. The illuminated sheet was then imaged using two AVT Bonito CMC-4000 4 megapixel CMOS cameras, as shown in figure 5.1. For the PIV measurements, polyamide particles with a mean diameter $2 \times 10^{-2}\,\mathrm{mm}$ and density $1.02 \times 10^{3}\,\mathrm{kg\,m^{-3}}$ were added to both the ambient and source fluid. To allow PLIF measurements, which we discuss in detail in § 5.3.1.1, a low concentration of the fluorescent dye Rhodamine 6G ($2 \times 10^{-4}\,\mathrm{kg\,m^{-3}}$ for all the experiments) was added to the source fluid. To separate the two signals, i.e. separate light scattered from the particles and that fluoresced by the dye, a 3 nm wide notch filter centred at 532 nm (i.e. centred at the wavelength of the laser) was placed in front of the PIV camera and a 570 nm low pass (with respect to frequency) filter was placed in front of the PLIF camera. Images for both PIV and PLIF were simultaneously captured at 100 Hz before being processed.

To determine the velocity fields, the raw particle images were processed using the 2017a PIV algorithm of Digiflow (Olsthoorn and Dalziel, 2017). Interrogation windows were chosen to be 24×24 pixels^2 with an overlap of 50%. Given the field of view of the camera, we were able to obtain one velocity vector per $1.12\,\mathrm{mm^2}$ and $1.09\,\mathrm{mm^2}$ for the free and wall plume, respectively. For the density field, given the low concentrations of Rhodamine 6G in the measurement section used ($\sim 1 \times 10^{-5}\,\mathrm{kg\,m^{-3}}$ due to dilution through entrain-

ment) a linear relationship between the light intensity perceived by the camera and the dye concentration was used to determine the density field as in Ferrier et al. (1993). For the experiments described in this chapter, a two-point calibration was performed for each experiment by capturing an image of the background light intensity and an image at a known dye concentration. Both calibration images were captured with the polyamide particles within the tank, at the seeding density used for the experiment, to account for differences in the laser intensity due to the presence of the particles. As the maximum dye concentration in the measurement section was small, attenuation of the laser beam was neglected in the PLIF image processing. An analysis of the error in the PLIF measurements as a result of the attenuation of the laser beam is given in appendix A.

The finite thickness of the laser sheet results in a limit to the resolution of the measurements obtainable from both PIV and LIF. The cross section of the laser sheet light intensity follows an approximately Gaussian curve profile. This improves the precision of the PIV because the brightest PIV particles (i.e. the particles within the central region of the laser sheet) contribute a larger weight to the correlation than dimmer particles outside the central part of the laser sheet. This suggests that the minimum reliable velocity resolution obtainable is within 10 mm - 20 mm. Similar arguments may be made for the PLIF measurements. In addition, it is assumed that, as in most PLIF analyses, the flow variables change sufficiently slowly across the laser sheet (Vanderwel and Tavoularis, 2014), i.e. it is assumed that

$$y_T \left| \frac{1}{w} \frac{\partial w}{\partial y} \right| \ll 1, \tag{5.44}$$

where y_T is the thickness of the light sheet and similarly for the vertical velocity u and buoyancy b. The PLIF images were processed at pixel resolution, 0.093 mm and 0.091 mm for the free and wall plume, respectively. However, due to the limitation of the resolution imposed by the thickness of the laser sheet, results are only presented, unless explicitly stated, at resolutions of the PIV vector spacing or greater, i.e. at a resolution approximately equal to the thickness of the light sheet.

After the images were processed, the velocity and density fields were mapped to a common world coordinate system. This was accomplished for both cameras by imaging a calibration target of regular dots aligned with the laser sheet. As an additional calibration step, a sequence of particle images were captured on both cameras simultaneously. Similar to stereo PIV calibration, e.g. Willert (1997), these particle images were then cross-correlated to determine a disparity map and shift the coordinate mappings to compensate for any small misalignment between the calibration target and the light sheet. Further details of this calibration step is given in Partridge et al. (2019) Appendix B.

For both PIV and PLIF, it is necessary to eliminate refractive index variations within the fluid as these produce distortions of the light paths and lead to errors in determining the positions of the PIV particles and uncertainty in the location of the dye measurements. To obtain a negatively buoyant plume, we used sodium nitrate solutions as the plume source and sodium chloride solutions as the ambient fluid to match refractive indices while maintaining a density difference (Olsthoorn and Dalziel, 2017). The refractive indices of the ambient and source fluid were matched using (3.2) and (3.3), which is based on measurements at a wavelength of 589 nm from Rumble (2019). The ambient and source fluid were matched to within 0.15% (based on relative refractive indices $n - n_0$) but, due to entrainment, any mismatch was further reduced by the point at which the plume was in the measurement region.

Measurements for the free plume were collected over a measurement window height of 0.160 m starting at a distance 0.165 m from the physical source of the free plume and a window height of 0.157 m starting at a distance 0.316 m from the physical source of the wall plume. These regions were sufficiently far from the source so that the plumes can be considered pure and self-similar (see figure 5.8). In order to minimise backflow effects the plumes were first run at relatively low flow rate. This ensured the resulting gravity current at the base of the tank had little effect on the ambient motion at the height of the measurement window. The flow rate was then gradually increased so that the higher momentum plumes entered a stratified region at the base of the tank which helped to mitigate the effects of the resulting gravity current. Each experiment was recorded for 100 s, corresponding to 10^4 simultaneous velocity/density fields. We verified that the plumes satisfy the pure-plume criterion used by Paillat and Kaminski (2014a) of an invariant maximum velocity with height. In addition, we checked that the Richardson number was invariant with height. A total of 10 plumes were studied, 5 free plumes and 5 wall plumes, and the experimental source parameters are given in tables 5.2 and 5.3, respectively. Also given are the Reynolds number $Re = \overline{w}_m R/\nu$ at the minimum and maximum height of the region examined, where R is the plume half-width (free) and width (wall) defined in (5.6) and the plume parameter Γ, averaged over the total height of the region examined, where

$$\Gamma_f = \frac{Q_f^3 F_f}{2\alpha_f M_f^3} = \frac{Ri_f}{2\alpha_f}, \qquad \Gamma_w = \frac{Q_w^3 F_w}{\alpha_w M_w^3} = \frac{Ri_w}{\alpha_w}. \tag{5.45}$$

We also calculate the turbulent Reynolds number, $Re_\lambda = \overline{w'}_{rms}\lambda/\nu$, the Kolmogorov length scale, $\eta = \left(\nu^3/\varepsilon\right)^{1/4}$, the Taylor microscale, $\lambda = \overline{w'}_{rms}\sqrt{15\nu/\varepsilon}$, the Batchelor length scale, $\lambda_B = \eta/Sc^{1/2}$ and the Kolmogorov time scale, $\tau_\eta = (\nu/\varepsilon)^{1/2}$, where $\varepsilon = 15\nu\overline{(\partial w/\partial z)^2}$ and Sc is the Schmidt number. The subscript *rms* denotes the root mean square of the

data. Tables 5.2 and 5.3 shows that the Batchelor length scale was much smaller than the resolution of the PLIF images across for all the experiments, suggesting that the effects of diffusion at these scales may be ignored in our analysis.

5.3.1.1 Planar laser-induced fluorescence

In order to measure the density field we used Planar laser-induced fluorescence introduced in § 3.3. Fluorescent tracer is mixed into the source plume fluid and a thin light-sheet, illuminated using the laser, excites the fluorescent tracer. The light intensity P of the fluoresced dye at a given local illumination intensity I any point exhibits a linear relationship with the dye concentration c (Shan et al., 2004), $P \propto g(I)c$, where g is a function of the local illumination intensity (the form of which need not be known). At the dye concentrations used $g(I) \approx$ const., i.e. the system was optically thin. By assuming that the density of the source plume fluid is directly proportional to the concentration, the light intensity of the fluoresced tracer is then directly proportional to the density of the plume fluid. The intensity response of the camera is linear so that the density of the fluid may be inferred from the camera intensity response.

Typically, however, the local illumination intensity is not known since it varies spatially and temporally as a function of the power fluctuations of the laser and the absorption of the laser light that occurs along its path (Crimaldi, 2008) or, as it is typically referred to, attenuation. The Bouguer-Lambert-Beer law may be used to relate the local illumination intensity of a non-absorbing medium reference case $I_0(x,z)$ to the local illumination intensity $I(x,z,t)$ in an absorbing medium, where the light is assumed to travel parallel to the z direction, as follows

$$I(x,z,t) = I_0(x,z)\exp\left(-\int_0^z \sum_{i=1}^{N} \varepsilon_i c_i(x,\zeta,t)\mathrm{d}\zeta\right), \tag{5.46}$$

where ε_i are the extinction coefficients of the absorbing media with concentrations c_i such as the tracer dye or additional salts used to achieve density differences. The attenuation along the path may be considered negligible if

$$\int_0^z \sum_{i=1}^{N} \varepsilon_i c_i(x,\zeta,t)\mathrm{d}\zeta \ll 1. \tag{5.47}$$

In appendix A we show that the above condition is satisfied so that from hereon in we assume that the attenuation is negligible.

The fluorescent dye used as a tracer is Rhodamine 6G. Rhodamine 6G exhibits peak light absorptivity at a wavelength of 525 nm and peak light emissivity at a wavelength of

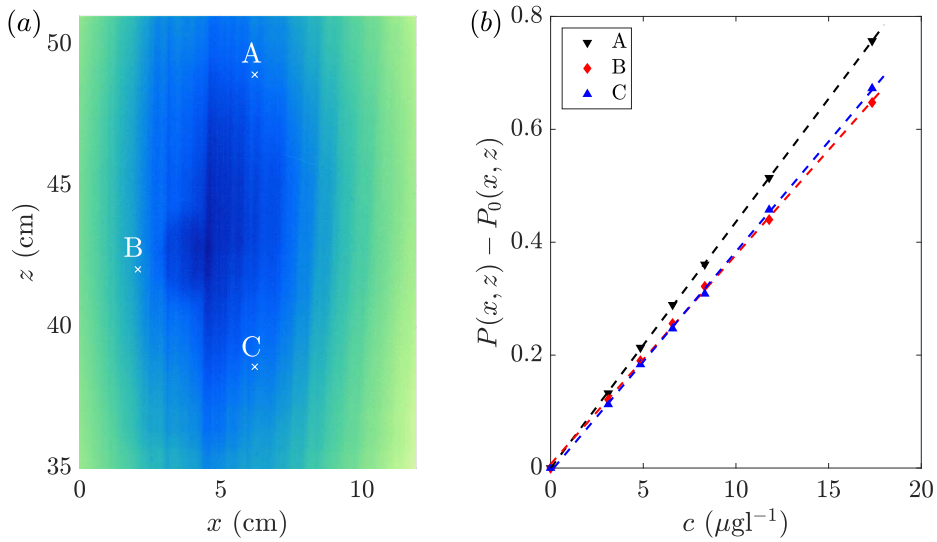

Fig. 5.5 (*a*) Calibration image, $P(x,z)$, taken for experiments 1, 2 and 3. (*b*) Corrected camera pixel intensity readings at positions *A*, *B* and *C* from (*b*) against dye concentration. The lines are linear best-fits to the data.

555 nm (Crimaldi, 2008), and has been observed to exhibit a linear relationship between the dye concentration and fluorescent emission intensity up to concentrations of 100 µgl^{-1} (Borg et al., 2001; Odier et al., 2014). A frequency-doubled dual-cavity Litron Nano L100 Nd:YAG pulsed laser with wavelength 532 nm was used to create a light sheet in the experiments, approximately equal to the wavelength of the peak light absorptivity of the dye used.

The water tank, laser and camera used for all the free and wall plume experiments were identical. However, the camera and laser position changed between the free and wall plume experiments. Further, experiments were performed for initial ambients of varying densities for both the free and wall plume. In order to account for attenuation resulting the sodium chloride in the ambient solution, calibrations were performed for each set of experiments with different ambient densities. Further, in order to verify the linear relationship between the dye concentration and the light intensity, in particular the intensity measured by the camera, a calibration was performed before each of these experiments. After the calibration for each set of experiments the camera and laser position and optical settings of the camera remained unchanged. The calibration was performed by filling the tank with a uniform solution of ambient fluid that would be used for the experiments, in our case a sodium chloride solution, and a uniform concentration of Rhodamine 6*G*. The camera then recorded 200 images of the laser-illuminated test section and the images were time-averaged in order to find the camera intensity at each pixel $P(x,z)$. We demonstrate the calibration technique

using the calibration for the free plume experiments 1, 2 and 3 (table 5.2). The calibration was repeated for concentrations of Rhodamine $6G$ of $c = 0, 3.11, 4.85, 6.67, 8.32, 11.79$ and $17.35\,\mu g\,l^{-1}$. The measurements for $c = 0\,\mu g\,l^{-1}$ give a background reference intensity, $P_0(x,z)$. Figure 5.5 (a) shows an example of the corrected intensity, $P(x,z) - P_0(x,z)$, for the calibration concentration of $c = 6.67\,\mu g\,l^{-1}$. Figure 5.5 (b) shows the normalised pixel intensities at three locations shown in (a) as a function of the dye concentration. A line of best fit is fitted to each set of data which shows the data is well represented by a linear relationship.

In order to process raw images from an experiment, that is determine the concentration of the dye $c(x,z,t)$ based on pixel light intensity measurements $P(x,z,t)$ we perform a two point calibration based on the background reading before each experiment $P_b(x,z)$ and a uniformly mixed image $P_m(x,z)$ of a known dye concentration $c_m(x,z)$ by the following calculation

$$c(x,z,t) = \frac{P - P_b}{\frac{1}{c_m}(P_m - P_b)}. \tag{5.48}$$

The resulting density field, $\rho(x,z,t)$, can therefore be calculated for a given initial uniform ambient density ρ_a and source density and dye concentration of ρ_s and c_s, respectively, by the following calculation

$$\rho(x,z,t) = \rho_a + \frac{c(x,z,t)\,(\rho_s - \rho_a)}{c_s} = \frac{(P - P_b)\,(\rho_s - \rho_a)}{\frac{c_s}{c_m}(P_m - P_b)}. \tag{5.49}$$

There are four main sources of error that may result in the final density calculation of (5.49). These are

(i) The noise associated with the camera.

(ii) The error in measurements of the dye concentration in the source and calibration solutions and the error in the initial ambient and source density.

(iii) The change in local illumination intensity due to the attenuation of the laser along its path.

(iv) The change in local illumination intensity due to the energy variation of the laser.

In order determine the noise of the camera the lens cap was placed over the lens to eliminate any variation in light. A video was then recorded for 1000 frames. The standard deviation of the pixel intensities were then measured for every pixel and the mean value across all the pixels was measured to be 0.0022 (where the maximum pixel intensity is 1). We therefore assume the error from the camera noise may be neglected. The camera noise

is affected by the camera gain, however the camera gain remained constant for all the PLIF experiments performed, so the above analysis is identical for all the experiments. The black level of the camera was tested suggesting that $< 1\%$ of the pixels measured 0 with the lens cap on (including some dead pixels) so we are confident the measurements are not clipped. As already discussed, the initial density differences used in the experiments were accurate to a maximum error of 0.15%. A batch of Rhodamine solution of $0.02\,\mathrm{g\,l^{-1}}$ was made for each set of experiments, which included an independent calibration. Equation (5.49) shows that the inferred density only depends on the ratio of the source and calibration solution c_s/c_m, therefore the inaccuracy of the concentration of the batch solution does not lead to error assuming the same batch solution is used for the calibration and experiments. It is necessary, however, to accurately measure the concentration, relative to the batch solution, of the calibration and experiment source solutions. Weighing scales were used to measure a known mass, to an accuracy of $0.1\,\mathrm{g}$, of the batch solution to the calibration tank or the source solution. The smallest concentration used required $50\,\mathrm{g}$ of the batch solution, corresponding to 0.2% error in the concentration measurements. We provide an analysis of the errors associated with (iii) and (iv) in appendix A.

5.3.1.2 Detection of the TNTI

The TNTI of the plume and statistics conditional on the presence or absence of plume fluid were used to characterise the flow. Therefore, it was crucial that we were able to accurately detect and distinguish between ambient fluid and plume fluid. Given that the Batchelor length scale of the plumes was small compared to the resolution of the PLIF measurements, we were able to employ a similar method to that used by Prasad and Sreenivasan (1989) and Mistry et al. (2016) to find the TNTI in an axisymmetric jet. We identify the TNTI by a non-dimensional scalar threshold, $\phi_t = b_t(z)/b_m(z)$, which coincides with the inflection point of the area-averaged conditional mean buoyancy $\widetilde{b}(\phi_t)$ and spanwise vorticity magnitude $\widetilde{|\omega_y|}(\phi_t)$, where the conditional mean is an area-averaged quantity of regions where the buoyancy satisfies $\phi_t < b/b_m$. The area-averaged conditional mean of the scaled buoyancy

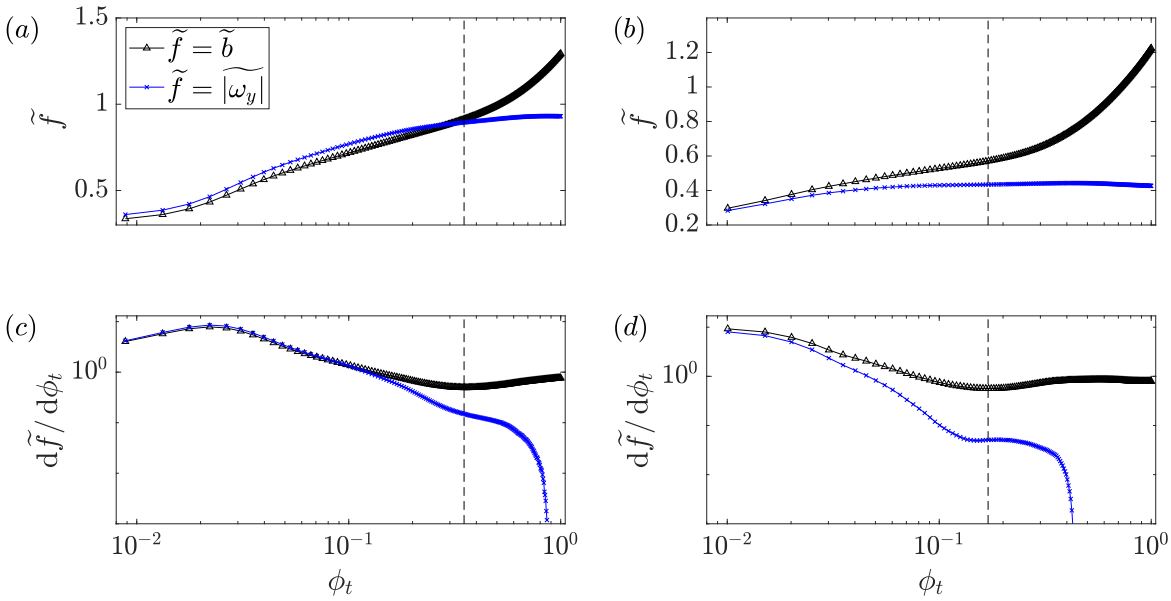

Fig. 5.6 Identification of the scalar threshold $\phi_t = b_t/b_m$ used to identify the TNTI of the (*a*) free and (*b*) wall plume. Plots (*c*) and (*d*) show the gradient of the conditionally average profiles of (*a*) and (*b*), respectively. The vertical dashed line shows the position of the inflection point of the conditionally averaged buoyancy data of free plume, $\phi_t = 0.35$, and wall plume, $\phi_t = 0.17$.

and spanwise vorticity magnitude are defined as

$$\widetilde{b}(\phi_t) = \frac{\frac{1}{T}\int_0^T \int\int H\left(\frac{b(x,z)}{b_m(z)} - \phi_t\right) \frac{b(x,z)}{b_m(z)} \mathrm{d}x\,\mathrm{d}z\,\mathrm{d}t}{\frac{1}{T}\int_0^T \int\int H\left(\frac{b(x,z)}{b_m(z)} - \phi_t\right) \mathrm{d}x\,\mathrm{d}z\,\mathrm{d}t}, \tag{5.50}$$

$$\widetilde{|\omega_y|}(\phi_t) = \frac{\frac{1}{T}\int_0^T \int\int H\left(\frac{b(x,z)}{b_m(z)} - \phi_t\right) \frac{|\omega_y|(x,z)\overline{R}(z)}{\overline{w}_m} \mathrm{d}x\,\mathrm{d}z\,\mathrm{d}t}{\frac{1}{T}\int_0^T \int\int H\left(\frac{b(x,z)}{b_m(z)} - \phi_t\right) \mathrm{d}x\,\mathrm{d}z\,\mathrm{d}t}, \tag{5.51}$$

where H is the Heaviside step function. Mistry et al. (2016) also consider the conditional mean vertical velocity in their identification of ϕ_t, however, given the finding that significant vertical velocities exist outside the scalar edge of an axisymmetric plume (Burridge et al., 2017), we chose to consider instead only the buoyancy and spanwise vorticity magnitude, as the flow outside the plume is irrotational. The conditional buoyancy and spanwise vorticity magnitude, with their gradients, are shown in figures 5.6 (*a*)-(*d*). For the wall plume an inflection point was identified from the conditionally averaged buoyancy and vorticity data with a value of $\phi_t = 0.15$ and $\phi_t = 0.17$, respectively. Although these values do not coincide

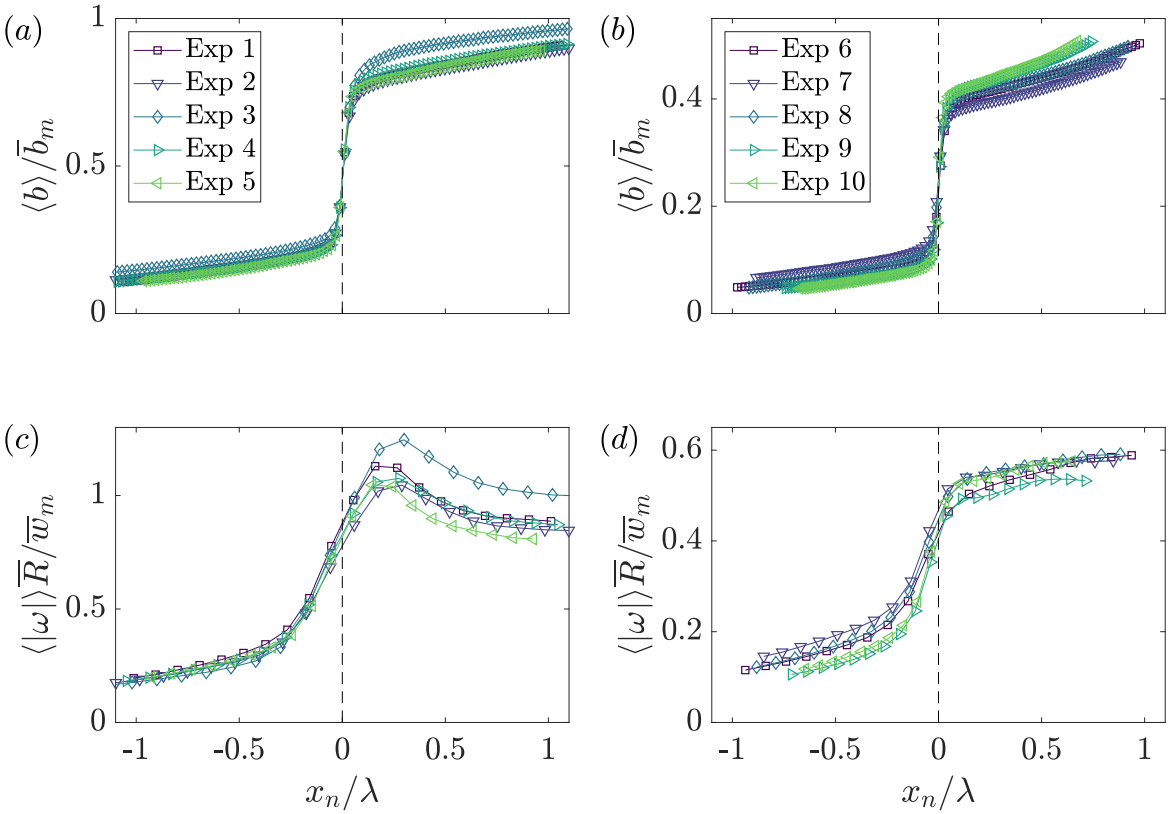

Fig. 5.7 The conditionally averaged profiles of (*a*), (*b*) buoyancy, b, and (*c*), (*d*) vorticity magnitude, $|\omega_y|$, shown for the (*a*), (*c*) free (see table 5.2) and (*b*), (*d*) wall (see table 5.3) plume experiments, respectively. Note that the buoyancy is presented at the camera pixel resolution.

exactly, the inflection point of the conditionally averaged spanwise vorticity magnitude falls within $0.17 \pm 20\%$. We show our results are not sensitive to the choice of threshold within this range. For the free plume an inflection point was identified from the conditionally averaged buoyancy data with a value of $\phi_t = 0.35$. An inflection point for the conditionally averaged vorticity data could not be identified, although as we show, this choice of threshold clearly identifies a region separating a significant jump in spanwise vorticity magnitude. In addition, in the following sections, we show that the results are insensitive to the choice of the threshold within a range of $\phi_t = 0.35 \pm 20\%$.

Figure 5.7 shows conditionally averaged profiles of buoyancy and spanwise vorticity magnitude, for both the free and wall plume. The data are ensemble-averaged, represented by $\langle \sim \rangle$, in a coordinate system by a coordinate x_n defined relative and normal to the TNTI, so that positive x_n lies within the turbulent region of the plume (Chauhan et al., 2014; Mistry et al., 2018, 2016). The TNTIs were identified using the threshold determined above. As noted by Mistry et al. (2016), there may be multiple TNTI crossings along x_n. Only regions that are identified with plume fluid are included in the ensemble-average of $x_n > 0$ and vice versa. Figures 5.7(a) and (b) shows there is a rapid increase in measured buoyancy across the identified TNTI, $x_n = 0$, in the free and wall plume, respectively. Analogous observations, where a passive scalar is measured, are also found in the near and far field of a turbulent jet (Mistry et al., 2018, 2016; Westerweel et al., 2009). A jump in spanwise vorticity magnitude can also be observed in the free and wall plume in figures 5.7 (c) and (d), respectively, which coincides with the jump in buoyancy at $x_n = 0$. As a result of the lower resolution of the velocity field data the relative increase in spanwise vorticity magnitude is not as sharp as that for the buoyancy (note that for measurements based on both the velocity and buoyancy field the jumps occur over approximately $4-5$ data points). Furthermore, the spanwise vorticity magnitude jump occurs across a distance approximately equal to the Taylor microscale. This is consistent with the results of direct numerical simulations results of a turbulent wake by Bisset et al. (2002) and the experimental results of a turbulent free line jet by Terashima et al. (2016) where in both cases the TNTI thickness was found to be almost equal to the Taylor microscale. It is apparent from figures 5.7(a) and (b) as to why the threshold in the free plume is approximately double that of the wall plume. As will be discussed in § 5.6, the free plume is more uniformly mixed within the plume region resulting in larger buoyancy, relative to the maximum buoyancy, within the plume close to the interface. Given that the jump in relative buoyancy in the free plume is approximately double that of the wall plume, a larger threshold may be chosen to identify the region separating the ambient and plume fluid. From this analysis we are therefore confident that the threshold identified is robust in identifying the TNTI across all the experiments. We therefore choose $\phi_t = 0.17$ as the

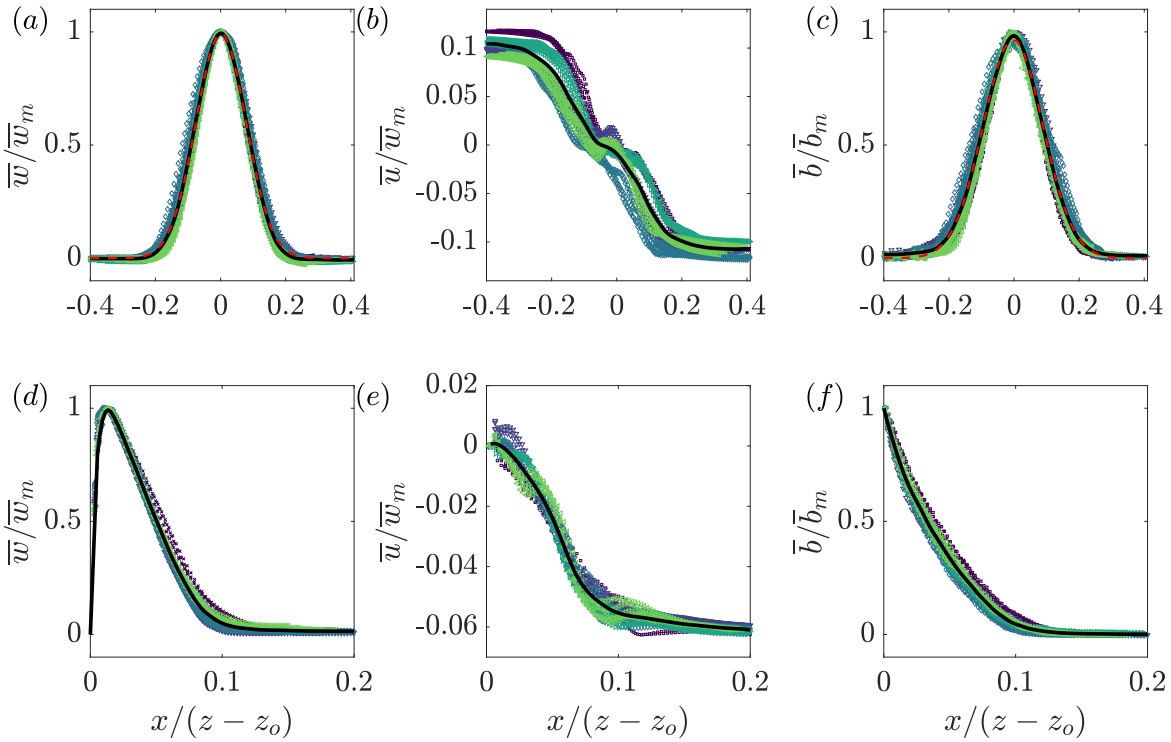

Fig. 5.8 Time-averaged scaled vertical and horizontal velocity and buoyancy profiles of the (*a*)-(*c*) free and (*d*)-(*f*) wall plume. For each experiment, five different heights spanning the studied region are plotted. The average values across all experiments are shown in each case by the solid black curve. In addition, a Gaussian least-squares fit was performed on the average values of the vertical velocity and buoyancy of the free plume and are shown by the dashed red curves.

threshold of the wall plume and $\phi_t = 0.35$ as the threshold of the free plume throughout the study. We may now consider regions $b/b_m < \phi_t$ to be ambient fluid and regions $b/b_m > \phi_t$ to be plume fluid.

5.4 Validation of the PIV and PLIF data

We first validate the plume data by demonstrating the self-similar behaviour of the velocity and buoyancy profiles. Figure 5.8 shows the vertical and horizontal velocities and buoyancy profiles for five different heights spanning the whole height of the measurement window for each experiment, with horizontal distances scaled on the distance from the virtual source, $z-z_0$, where z_0 is the virtual origin. The virtual origin was calculated by identifying, by linear extrapolation, the vertical location at which the time-average plume width is zero. A good collapse of data on to a single curve is seen in each plot, thereby demonstrating

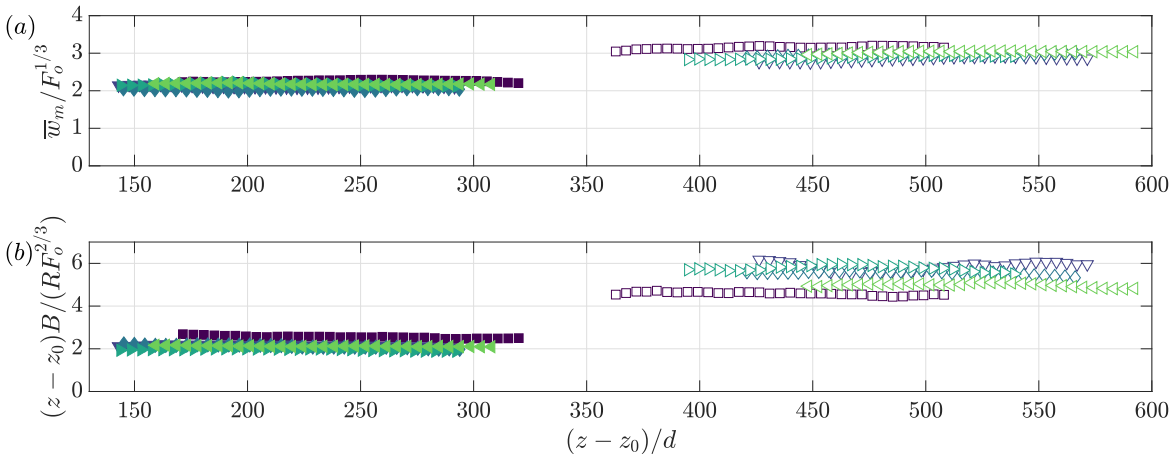

Fig. 5.9 (*a*) Maximum vertical velocities of the free, filled markers, and wall plume, unfilled markers, scaled using the source buoyancy flux. (*b*) Time-averaged top-hat buoyancy of the free and wall plume, scaled using the vertical distance and source buoyancy flux.

self-similarity. The self-similar vertical velocity and buoyancy profiles of the free plume are fitted well by a Gaussian curve (shown by the dashed red curve) as has been previously observed (e.g. Ramaprian and Chandrasekhara (1989), Paillat and Kaminski (2014a)) and the wall plume profiles agree well with those of Sangras et al. (1999) and Sangras et al. (2000). Further confidence in the self-similarity of the plumes is given by the invariance with height of the maximum vertical velocity, scaled by the buoyancy flux $F_0^{1/3}$, shown in figure 5.9 (*a*), and the inverse linear decay $\sim 1/z$ (Fischer et al., 1979) of the top-hat buoyancy B/R shown in the compensated plot in figure 5.9 (*b*).

5.5 Results in an Eulerian coordinate system

5.5.1 Turbulent fluxes

Measurements of velocity and buoyancy fluctuations, Reynolds stress and turbulent transport for the free and wall plume experiments are shown in figures 5.10 and 5.11, respectively. Our results for the free plume turbulent transport of buoyancy closely follow those of Ramaprian and Chandrasekhara (1989), and the turbulent buoyancy fluctuations are consistent with those of Sangras et al. (1998). For both plumes we note that the turbulent buoyancy fluxes are at most about 5% of the mean vertical buoyancy flux. The turbulent fluctuations for the wall plume agree well with those of Sangras et al. (1999) and Sangras et al. (2000). To our knowledge, turbulent transport quantities for a wall plume in a self-similar region have not been calculated in previous studies, except within a developing region by Lai and

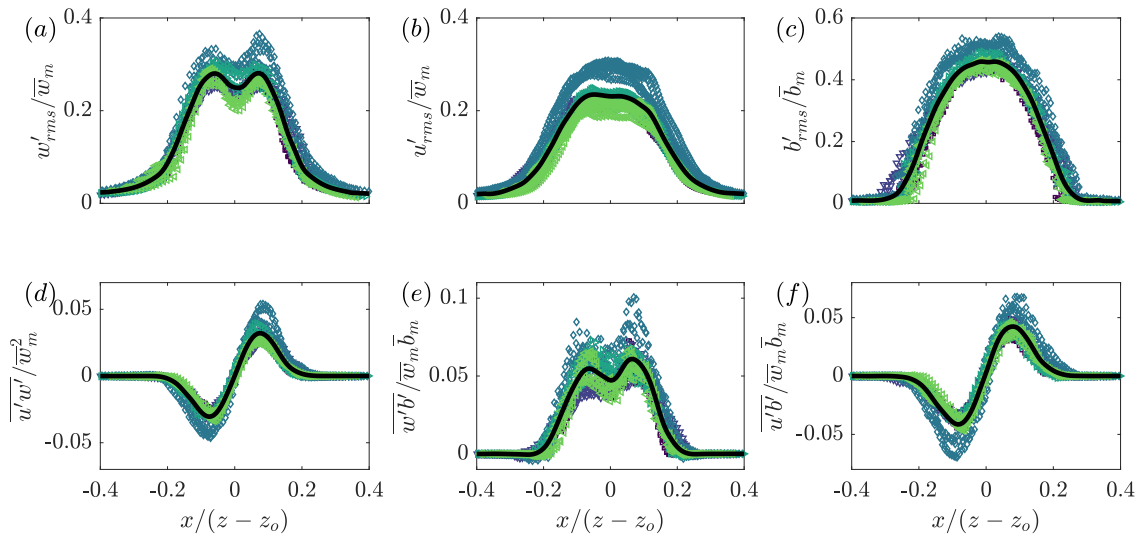

Fig. 5.10 Time-averaged scaled free plume turbulent fluctuations of (*a*) vertical velocity, (*b*) horizontal velocity and (*c*) buoyancy and (*d*) Reynolds stress, (*e*) vertical and (*f*) horizontal turbulent buoyancy flux. The black curves are the averages of the data.

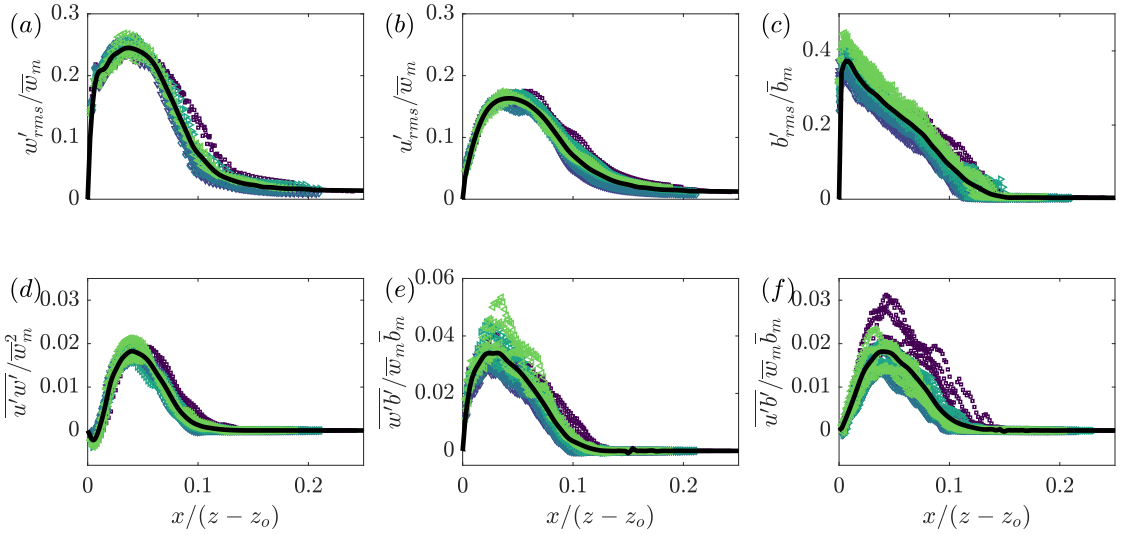

Fig. 5.11 Time-averaged scaled wall plume turbulent fluctuations of (*a*) vertical velocity, (*b*) horizontal velocity and (*c*) buoyancy and (*d*) Reynolds stress, (*e*) vertical and (*f*) horizontal turbulent buoyancy flux. The black curves are the averages of the data.

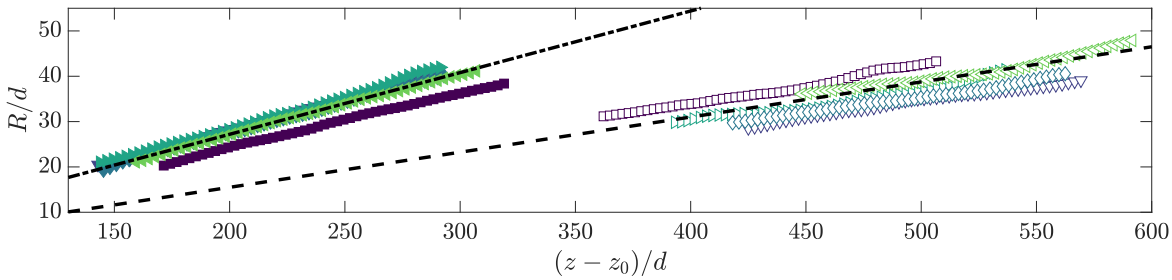

Fig. 5.12 The variation in the mean free plume half-width, filled markers, and wall plume width, unfilled markers. Lines of best fit, used to calculate the entrainment values (table 5.4), are shown by the respective dashed lines.

Plume type	$\alpha_{production}$	$\alpha_{buoyant}$	$\alpha_{production} + \alpha_{buoyant}$	$\alpha\,(= \mathrm{d}R/\mathrm{d}z)$
Free	0.103 ± 0.010	0.047 ± 0.004	0.149 ± 0.019	0.135 ± 0.010
Wall	0.067 ± 0.010	0.043 ± 0.008	0.109 ± 0.006	0.076 ± 0.006

Table 5.4 Entrainment coefficient for the free and wall plumes, calculated using $\mathrm{d}R/\mathrm{d}z$ (figure 5.12) and from the decomposition of entrainment coefficients described in § 5.2.1. The error margins denote the standard deviation for each quantity across all five experiments.

Faeth (1987). It is clear that their flow is not self-similar where their measurements are taken, and both the present study and Sangras et al. (2000) find significantly larger velocity turbulent fluctuations compared to Lai and Faeth (1987) and, therefore, further comparison between our results is not insightful.

Larger maximum values for the normalised Reynolds stress at 0.30 are found in the free plume compared with 0.18 in the wall plume. The maximum values for the normalised turbulent horizontal and vertical fluxes are also significantly higher in the free plume being, in both cases, approximately double those of the wall plume. The kink observed in the vertical buoyancy flux, figure 5.11 (*e*), at about $x/(z - z_0) = 0.08$ appears to be real, as opposed to resulting from scattered data, since it is reflected in the turbulent buoyancy fluctuations, also observed by Sangras et al. (1999).

5.5.2 Entrainment coefficient

The top-hat entrainment coefficients for the free and wall plume were determined from the solutions of the conservation equations (5.20)-(5.22) and (5.29)-(5.31), respectively. The values were obtained from a least squares best-fit to the time-average plume widths R at each height (figure 5.12). The calculated values are shown in table 5.4 where the tolerances indicate the standard deviation in the values measured across the five independent

experiments examined for each flow. Our value of α_f is consistent with previously reported Gaussian entrainment values of $\alpha_{f,G} = \{0.10, 0.16\}$ which correspond to approximately $\alpha_f \approx \sqrt{2}\alpha_{f,G} = \{0.14, 0.22\}$. Our value of α_w is lower than the previously reported value of $\alpha_w = 0.095 \pm 0.005$ in Grella and Faeth (1975). In particular, our results support previous studies that find α_w is slightly more than half of α_f. We note that if we were to consider the wall plume as 'half' the free plume, we would expect the top-hat entrainment values to be equal to one another since the equation expressing conservation of volume flux in the free plume (5.15) accounts for the double-sided entrainment with the factor of 2. Consequently, this difference is a result of the absence or presence of the wall.

We also calculate the entrainment coefficient based on the decomposition outlined in § 5.2.1. The relative contributions of $\alpha_{production}$ and $\alpha_{buoyant}$, and their sum, are shown in table 5.4 compared to the entrainment coefficient calculated directly from $\mathrm{d}R/\mathrm{d}z$.

There is good agreement between the calculated entrainment coefficients of the free plume between the two methods. Our values of $\alpha_{production} = 0.103 \pm 0.010$ and $\alpha_{buoyant} = 0.047 \pm 0.004$ are in good agreement with those measured by Paillat and Kaminski (2014a), where they find that $\alpha_{production} = 0.104$, and $\alpha_{buoyant} = 0.04$, where the latter has been inferred from the Richardson number given in Paillat and Kaminski (2014a) of $Ri = 0.14$.

The terms $\alpha_{production}$ and $\alpha_{buoyant}$ for the wall plume may be accurately determined from our data. However, the component $\alpha_{viscous}$ for the wall plume is difficult to measure directly. Given such good agreement is found in the free plume, it is suggestive that the discrepancy between α_f and the turbulent production and buoyant terms, $\alpha_{production}$ and $\alpha_{buoyant}$, may be attributed to the viscous term $\alpha_{viscous}$ since the discrepancy lies outside the range of error values calculated. We therefore estimate that for the wall plume $\alpha_{viscous} \approx -0.03$.

The contribution from the buoyancy, $\alpha_{buoyant}$, is approximately the same in both the free and wall plume. The reduction in entrainment in the wall plume may then be attributed to both a significant reduction in turbulent production, $\alpha_{production}$, and viscous dissipation in the inner layer, $\alpha_{viscous}$. The reduction in $\alpha_{production}$ between the free and wall plume is approximately equal to $\alpha_{viscous}$ in the wall plume, which shows that both contribute significantly to reducing entrainment.

Based on previous observations of suppression of cross-stream turbulent fluxes in the wall plume (Ellison and Turner, 1959; Sangras et al., 2000; Turner, 1973), which are also observed in this study, the reduction in $\alpha_{production}$ in the wall plume is expected.

5.5.2.1 Direct calculation of $\alpha_{viscous}$

In order to estimate $\alpha_{viscous}$ we compared the energy decomposition of α to $\alpha_R = \mathrm{d}R/\mathrm{d}z$. Here we estimate $\alpha_{viscous}$ directly from velocity measurements. (5.40) may be expressed in

terms of the wall shear stress by

$$\alpha_{viscous} = \frac{2Q^2\nu}{E_w M_w}\int_0^\infty \left(\frac{\partial\overline{w}}{\partial x}\right)^2 \mathrm{d}x - 2\nu\frac{Q^2}{M^2}\left.\frac{\partial\overline{w}}{\partial x}\right|_0. \tag{5.52}$$

The nearest-to-wall PIV measurements were obtained at a distance $x_1 = 1.3\,\mathrm{mm}$. We estimate the velocity gradient at the wall by

$$\left.\frac{\partial\overline{w}(x,z)}{\partial x}\right|_0 \approx \frac{w(x_1,z)}{x_1}, \tag{5.53}$$

and assume that

$$\overline{w}(x,z) = x\frac{w(x_1,z)}{x_1}, \tag{5.54}$$

for the region $0 \leq x_1$. Using (5.53) and (5.54) we find that

$$\frac{2Q^2\nu}{E_w M_w}\int_0^\infty \left(\frac{\partial\overline{w}}{\partial x}\right)^2 \mathrm{d}x = 0.0161 \pm 0.0011, \tag{5.55}$$

and

$$2\nu\frac{Q^2}{M^2}\left.\frac{\partial\overline{w}}{\partial x}\right|_0 = 0.0187 \pm 0.0014 \tag{5.56}$$

resulting in an estimate of $\alpha_{viscous} = -0.0026 \pm 0.0005$. The magnitude of this estimate is significantly lower than $\alpha_{viscous} = -0.03$ obtained in § 5.5.2, however it should be emphasised that the validity of the approximation (5.53) is uncertain. (5.56) also provides an estimate for the skin friction coefficient of $C = 0.0093 \pm 0.0007$.

5.5.3 Entrainment flux

The entrainment coefficient may be viewed as a measure of the plume entrainment efficiency. However, to interpret the physical implications we consider how much fluid is entrained into the free and wall plume per unit height. For a given buoyancy flux $F = F_w = F_f$, (5.20) and (5.29) give

$$\frac{2u_{\infty,f}}{u_{\infty,w}} = \frac{\mathrm{d}Q_f}{\mathrm{d}z}\left(\frac{\mathrm{d}Q_w}{\mathrm{d}z}\right)^{-1} = 2^{2/3}\left(\frac{\alpha_f}{\alpha_w}\right)^{2/3}\left(1+\frac{C}{\alpha_w}\right)^{1/3}, \tag{5.57}$$

where we have used that $\left(\theta_f/\theta_w\right)^{1/3} \approx 1$, as verified from our data.

The skin friction coefficient has already been calculated by estimating the wall shear stress in § 5.5.2.1. The skin friction coefficient may also be calculated by balancing bulk flow quantities using the momentum equation (5.27), which results in a mean value of $C =$

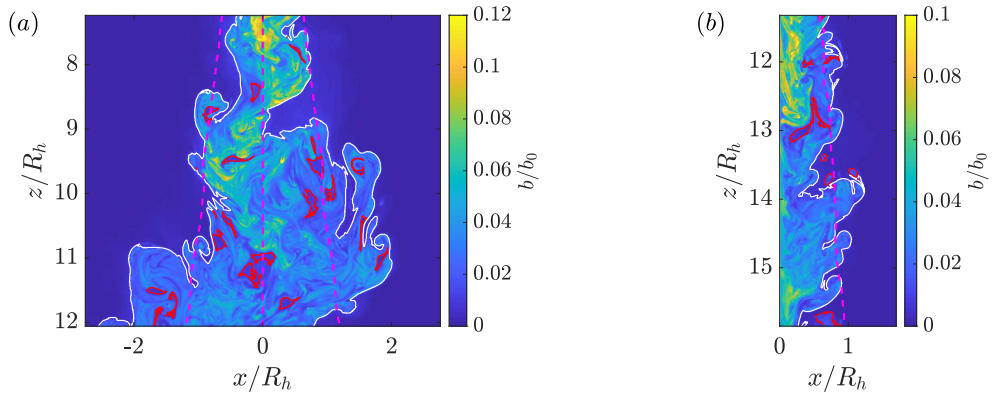

Fig. 5.13 Instantaneous buoyancy field of the (a) free and (b) wall plume. The figures shown are the processed PLIF images at full resolution. In both cases the outer continuous TNTI is highlighted by the solid white line and the TNTIs of unconnected regions and completely engulfed regions (within the plane) of ambient fluid are highlighted by the red lines. The TNTIs were identified from the threshold b_t determined in § 5.3.1.2. In (a) the mean position of the outer left TNTI, centreline and outer right TNTI are denoted by the dashed magenta lines from left to right and the distances have been scaled using the free plume half-width at the mid height of the image, R_h. In (b) the position of the mean outer TNTI of the free plume is denoted by the dashed magenta line and the distances have been scaled using the wall plume half at the mid height of the image, R_h.

0.015 ± 0.005. We note the difficulties in experimentally determining this value due to the omission of the vertical velocity fluctuations and pressure term (the latter of which can not be measured directly) in the vertical momentum equation, which together have been shown to account for up to 8% of the mean vertical momentum in an axisymmetric plume (Van Reeuwijk et al., 2016). Therefore, we do not place emphasis on our result of the skin friction coefficient, and note that our conclusions are qualitatively the same for any (reasonable) values of $C \geq 0$.

Using the determined entrainment values in the right hand side of (5.57) we find that $2u_{\infty,f}/u_{\infty,w} = 2.5 \pm 0.4$. This agrees with direct measurements of $(\mathrm{d}Q_f/\mathrm{d}z)/(\mathrm{d}Q_w/\mathrm{d}z) = 2.4 \pm 0.1$. Hence, despite the value of the entrainment coefficient for a free plume being less than double that of the wall plume, the increase in volume flux with height in a free plume is significantly greater than double that of a wall plume with equal forcing, i.e. equivalent buoyancy flux. This implies that each edge of the free plume entrains ambient fluid more efficiently than the wall plume, per unit height.

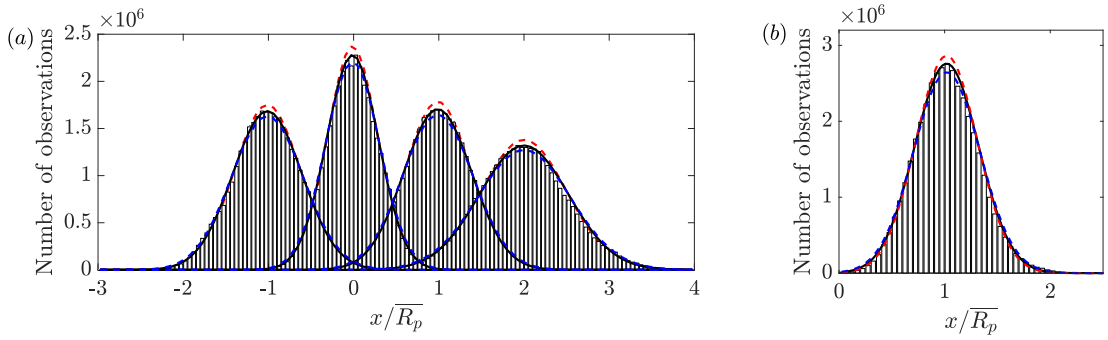

Fig. 5.14 Histograms of (a) the locations (from left to right) of the left-TNTI, the centre, the right-TNTI and the plume scalar width of the free plume, where distances are normalised by the plume scalar half-width and (b) the plume scalar width of the wall plume normalised by the time-average scalar width, $\overline{R_p}$. The solid curves are Gaussian best fits to the data. The red and blue dashed curves show the Gaussian best fits to data of the statistics performed with a threshold of $\phi_t = 0.17 - 20\%$ and $\phi_t = 0.17 + 20\%$, respectively, for the wall plume and $\phi_t = 0.35 - 20\%$ and $\phi_t = 0.35 + 20\%$, respectively, for the free plume, highlighting the insensitivity of our results to the choice of threshold.

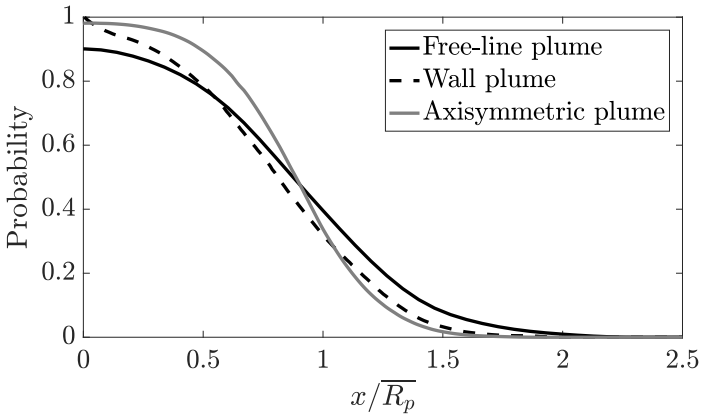

Fig. 5.15 The probability, at a given horizontal location, of being within the plume region bounded by the outer TNTI for the free plume, solid black line, wall plume, dashed black line, and for comparison an axisymmetric plume, grey line (Burridge et al., 2017).

5.5.4 The statistics of the TNTI

Figure 5.13 shows instantaneous images of a free and a wall plume. The continuous outer TNTI has been identified and highlighted in white. Also highlighted, in red, are the TNTIs of regions of unmixed ambient fluid completely engulfed, within the plane, by plume fluid. In both flows, there are significant deviations from the positions of the mean outer TNTI, denoted by the dashed magenta lines. The meandering nature of the free plume is evident from figure 5.13(a), where in addition to the relatively small coherent structures forming, i.e. eddies along the outer TNTI, which are also seen in the wall plume, the free plume also forms coherent structures at the length scale of the full plume width. As a result the instantaneous edge of the wall plume is comparatively closer to the mean TNTI (figure 5.13(b)) than for the free plume.

We define the left, $E_L(z,t)$, and right, $E_R(z,t)$, points along the outermost TNTI for a given height, and time, as the outermost left and right points along that TNTI at that height. Therefore, the positions are uniquely defined for each height and time. Similarly, we define the outermost point, at a given height and time, of the wall plume $R_p(z,t)$. Histograms of $E_L(z,t)$ and $E_R(z,t)$ of the free plume and $R_p(z,t)$ of the wall plume are shown in figure 5.14, normalised by the time-averaged scalar widths of the plumes. We define the instantaneous plume scalar half-width and centreline as $R_p = (E_R - E_L)/2$ and $C_p = (E_R + E_L)/2$, respectively, for the free plume and the scalar width as the distance from the wall to the outer TNTI in the wall plume. We find that the positions of the left and right TNTI of the free plume are both well represented by Gaussian distributions $E_L \sim N(\mu = -1, \sigma^2 = 0.16)$, $E_R \sim N(\mu = 1, \sigma^2 = 0.16)$, respectively, where μ denotes the mean and σ the standard deviation. The sensitivity of the results to the particular choice of threshold were tested, for $b_t/\overline{b}_m = 0.35 \pm 20\%$, also shown in figure 5.14, in each case the standard deviation varied by at most 5% as compared to the standard deviation of the chosen threshold. The free plume scalar half-width and centreline are also approximated by Gaussian distributions $2R_p \sim N(\mu = 2, \sigma^2 = 0.27)$ and $C_p \sim N(\mu = 0, \sigma^2 = 0.093)$. For the wall plume we find that $R_p \sim N(\mu = 1, \sigma^2 = 0.091)$, again the sensitivity of the results to the particular choice of threshold was tested, for $b_t/\overline{b}_m = 0.17 \pm 20\%$, also shown in figure 5.14, in each case the standard deviation, σ, varied by at most 4% as compared to σ of the chosen threshold. In the case of the free plume, since $C_p = (E_R + E_L)/2$, it follows that the Pearson's correlation coefficient is $\rho_{E_R,E_L} = 0.16$. This may be compared to an axisymmetric plume where it was found that $\rho_{E_R,E_L} = 0$ (Burridge et al., 2017). So although the correlation between the two edges is larger than that for an axisymmetric plume, it is still small.

However, this statistic masks the true meandering nature of the plume as is evident from figure 5.13 (a). The position of the outer left and right TNTI of the free plume at, say, $z/R =$

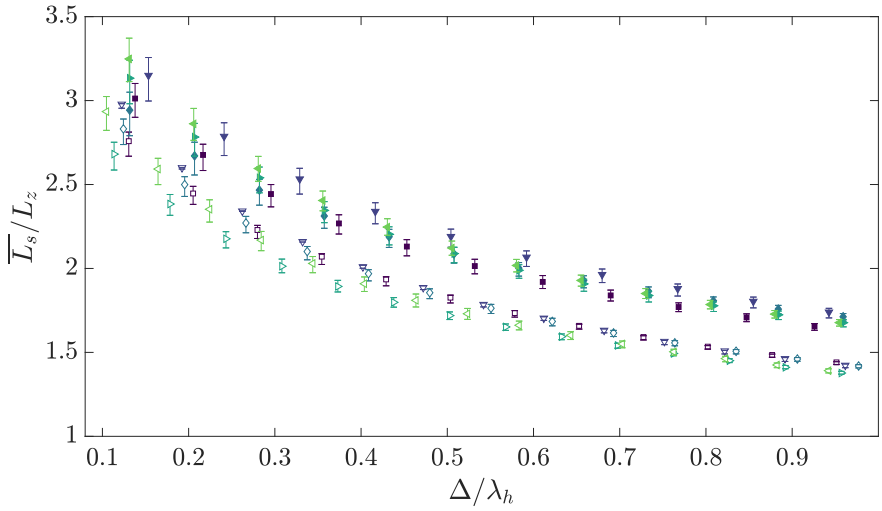

Fig. 5.16 The mean TNTI length for varying box filter sizes, $0.1 \leq \Delta/\lambda_h \leq 1$, for the free, filled, and wall, unfilled, plume. The lengths have been scaled by the projected length of the interface. The error bars show the statistics performed with a threshold of $\phi_t = 0.35 \pm 20\%$ and $\phi_t = 0.17 \pm 20\%$ for the free and wall plume, respectively.

9.0 line do not demonstrate meandering, even though the body of the plume has clearly meandered to the left and overturned. For this reason, the meandering nature of the plume is more robustly demonstrated by considering the probability, at given horizontal location, of plume fluid being within the connected region that is bounded by the outer plume TNTI, as shown in figure 5.15. This demonstrates that there is a significant probability $\sim 15\%$ that a connected region of ambient fluid exists at the mean centreline of the plume, as a result of the plume meandering. For comparison, the equivalent probability function for an axisymmetric plume, which does not demonstrate a meandering behaviour, is shown (Burridge et al., 2017) and the probability is much lower $\sim 1\%$. Kotsovinos (1975) and Westerweel et al. (2005) have performed similar statistics for a free line and axisymmetric jet, respectively, and also find that there is a finite but very low probability of ambient fluid existing at the mean centreline. We note that Kotsovinos (1975) also calculated the plume fluid intermittency for a free line plume, and found it was almost identical to that free jet, which appears to be inconsistent with his observations of plume meandering.

5.5.4.1 Plume meandering mechanism

Here we describe the basic mechanism of the wavering of the plume body, which can be observed in both the axisymmetric plume (figure 4.3) and free line plume (figure 5.13 (*a*)),

and suggest why this leads to strong correlated meandering (i.e. a correlated left and right TNTI wavering) in the free line plume but not the axisymmetric plume.

Due to entrainment, in a coordinate system as used in the experiments with negatively buoyant plumes, the density of the plume decreases as distance from the source increases. The plume is therefore, on average, unstably stratified. This leads to overturning of the plume body as illustrated in figure 5.17. The mechanism described here was used as a model to explain the wavering observed in free line plumes by Kotsovinos (1975), however the mechanism is also applicable to axisymmetric plumes as described by Sreenivas and Prasad (2000). This mechanism does not, alone, however explain the differences observed between the free line and axisymmetric plume. Figure 5.18 illustrates the meandering mechanism of the free line plume. The free line plume tends to overturn about an axis that is aligned with the y-direction, which explains the relatively large correlation coefficient between the outermost left and right TNTI measured in a plane normal to the y-direction. The axes of these overturning structures (blue dashed lines), which occur in different x-z planes along the y-direction, tend to correlate and reinforce the overturning structure resulting in strong correlated meandering. The axisymmetric plume, however, is equally likely to overturn along any azimuthal direction, leading to a small correlation coefficient between the outermost left and right TNTI from measurements in a fixed plane. In addition, for a given time the plume will tend to overturn along different axes at different heights, preventing correlated meandering.

5.5.4.2 TNTI length

The effect of the meandering can be quantified by considering the length of the TNTI of the free and wall plume. We use a methodology similar to that of Mistry et al. (2018), where box filtering, of size Δ, is applied to each instantaneous image and the TNTI is identified from the scalar threshold b_t. Figure 5.13 shows an instantaneous buoyancy image at full resolution of the free and wall plume highlighting the identified TNTI. Completely engulfed, within the plane, and unconnected regions are included in the calculation which are non-negligible in the flows we are considering.

The results for varying box sizes $0.1 < \Delta/\lambda_h < 1$ are shown in figure 5.16, where λ_h is the Taylor microscale measured at the mid height of the studied regions of the respective data and $0.1\lambda_h$ approximately corresponds to the thickness of the light sheet used in the experiments. The mean interface length $\overline{L_s}$ is normalised by the projected interface length L_z, which is defined by the vertical distance of the region considered in the wall-plume and twice the vertical distance in the free plume. We find that the mean length of the TNTI of the free plume is larger than that of the wall plume at all filter sizes measured by a

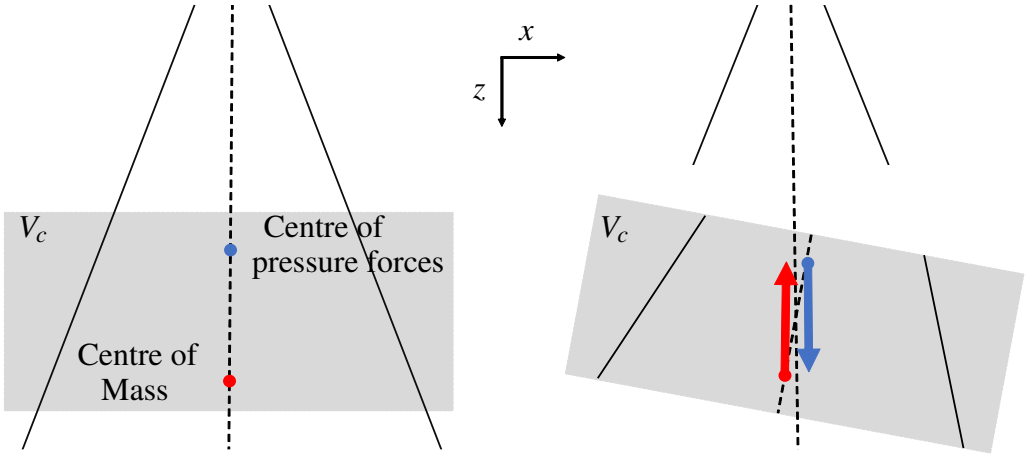

Fig. 5.17 The mechanism of the overturning of the plume body observed in both free plume and axisymmetric plume experiments which is based on the description by Kotsovinos (1975) figures A.6 and A.7. By considering a control volume V_c in an idealised instantaneous plume, with coordinate system as shown, the centre of mass is lower than the centre of the pressure forces due to the increasing density of the plume fluid with increasing z. The gravitational force (blue arrow) and Archemidian force (red arrow) results in an unstable plume body and overturning.

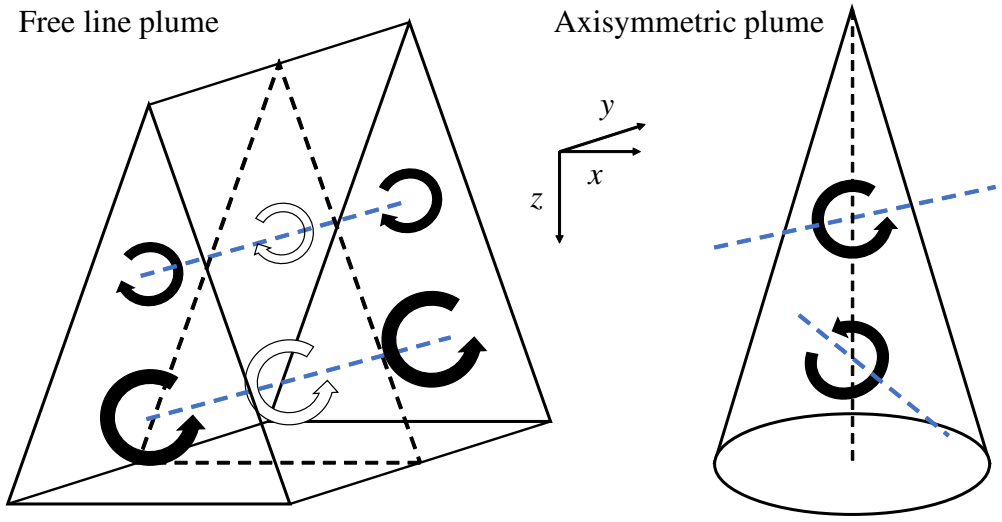

Fig. 5.18 The mechanism leading to meandering in the free line plume. The free line plume tends to overturn along an axis in the y-direction (blue dashed lines) so that the overturning in different planes is correlated. The axisymmetric plume is equally likely to overturn in any azimuthal direction preventing correlated meandering.

factor, on average, of at least 2.2. The sensitivity of the results to the particular choice of thresholds were tested for $b_t/\overline{b}_m = 0.35 \pm 20\%$ and $b_t/\overline{b}_m = 0.17 \pm 20\%$ for the free and wall plume, respectively. These data are shown by the error bars in figure 5.16. Although there is some sensitivity to the results the conclusion that $\overline{L_s}/L_z$ is larger in the free plume remains unchanged. The data does not exhibit any dependence on the turbulent Reynolds number which may be because of the limited range of turbulent Reynolds numbers across the experiments, further, the free and wall plume turbulent Reynolds are similar, in particular experiments 4 and 5 of the free plume and experiments 6 and 7 of the wall plume where the turbulent Reynolds number at the mid height of the plumes differ by at most 5%. Mistry et al. (2016) found a similar value for the length of the TNTI of an axisymmetric jet, measured at $\Delta/\lambda_h \approx 1$, to our measurements of the free plume of $\overline{L_s}/L_z \approx 2$.

The measurements of the mean TNTI length $\overline{L_s}$ in a single plane are an attempt to estimate the mean three-dimensional turbulent/non-turbulent surface area per unit length $\overline{A_s}/L_y$ (where L_y is a projected length in the spanwise direction), the latter of which is not attainable from planar measurements. While it is unclear if $\overline{L_s}$ provides a reliable estimate of $\overline{A_s}/L_y$, it is hoped that the ratio of $\overline{L_s}$ in the free plume to $\overline{L_s}$ in the wall plume is representative of the ratio of $\overline{A_s}$ in the free plume to $\overline{A_s}$ in the wall plume.

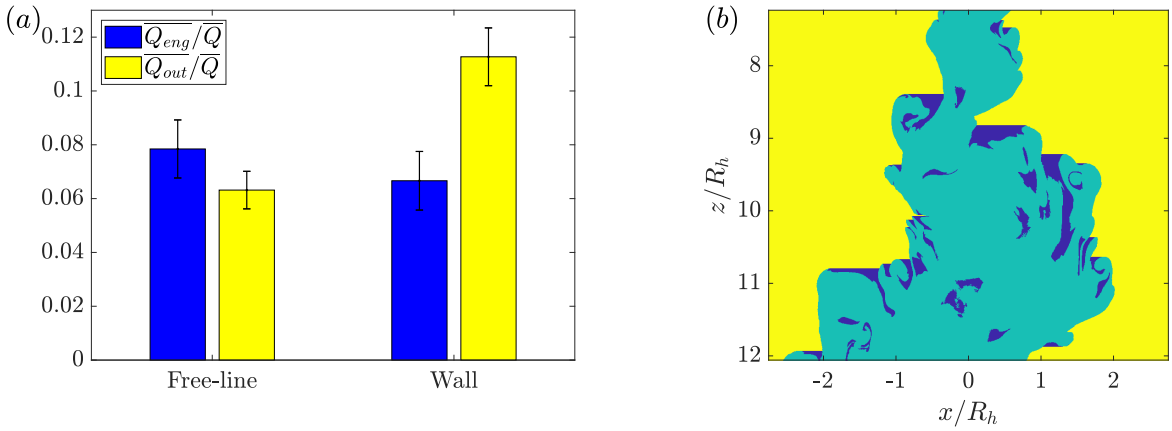

Fig. 5.19 (*a*) Time-averaged conditional volume flux of the ambient fluid outside the plume envelope (yellow) and of engulfed but unmixed ambient fluid (blue) for both the free and wall plume. The error bars indicate the mean values across the experiments of the analysis performed with a threshold of $\phi_t = 0.35 \pm 20\%$ and $\phi_t = 0.17 \pm 20\%$ for the free and wall plume, respectively. (*b*) Instantaneous image of a free-plume, shown in figure 5.13 (*a*), highlighting the different regions of ambient and engulfed fluid where the colours correspond to the bar plots in (*a*).

5.5.5 Conditional vertical transport

In order to quantify the effect of the meandering of the free plume on the large scale engulfment we calculate the conditional vertical transport of ambient fluid, for both the free and wall plumes, by considering, separately, ambient fluid outside the TNTI envelope and engulfed but unmixed fluid. In order to calculate the fluxes of the ambient fluid we follow a method equivalent to that of Burridge et al. (2017) by first defining an instantaneous step function for the outer ambient fluid

$$H_{out} = \begin{cases} 0 \text{ for } E_L(z,t) < x < E_R(z,t), \\ 1 \text{ otherwise}, \end{cases} \tag{5.58}$$

and a step function for all unmixed fluid

$$H_{amb} = \begin{cases} 0 \text{ for } b(x,z,t) > b_t(z), \\ 1 \text{ for } b(x,z,t) < b_t(z). \end{cases} \tag{5.59}$$

A step function identifying the locations of engulfed but unmixed fluid H_{eng} is then given by $H_{eng} = H_{amb}[1 - H_{out}]$. Figure 5.19 (*b*) shows an example of these regions for an instantaneous free plume image, where H_{out} and H_{eng} are highlighted in yellow and blue, respectively. The time-averaged volume flux of ambient fluid outside the plume TNTI envelope is

then given by

$$\overline{Q_{out}}(z) = \frac{1}{T}\int_0^T \int H_{out}(x,z,t)w(x,z,t)\mathrm{d}x\mathrm{d}t, \tag{5.60}$$

where the integral domains over the x-coordinate are given by the respective domains of the free plume $(-\infty,\infty)$ and wall plume $(0,\infty)$. Similarly, the time-averaged volume flux of engulfed but unmixed fluid is given by

$$\overline{Q_{eng}}(z) = \frac{1}{T}\int_0^T \int H_{eng}(x,z,t)w(x,z,t)\mathrm{d}x\mathrm{d}t. \tag{5.61}$$

Time-averaged results for both the free and wall plume are shown in figure 5.19 (*a*). We find that for the free plume $\overline{Q_{eng}}/\overline{Q} = 0.078 \pm 0.011$ and $\overline{Q_{out}}/\overline{Q} = 0.063 \pm 0.011$ and for the wall plume $\overline{Q_{eng}}/\overline{Q} = 0.067 \pm 0.007$ and $\overline{Q_{out}}/\overline{Q} = 0.113 \pm 0.011$. Again we see that more ambient fluid is engulfed by the meandering of the free plume compared with the wall plume.

Given the restriction of planar velocity and buoyancy measurements it is not possible to determine whether ambient fluid is completely engulfed or connected to the far field ambient outside the measurement plane. Therefore, any reasonable definition must include ambient fluid connected to the far field or consider the uncertainty of plane-engulfed fluid actually being completely engulfed. In this sense, although our definition of engulfed fluid includes regions that may or may not be completely engulfed, it is not clear that a definition that is based only on plane-engulfed fluid would offer any advantage. In particular, the results of the latter definition may change with full three-dimensional measurements, however, the results of our definition would not.

5.5.6 Discussion

Our results may be set in context with the original observation of Ellison and Turner (1959) that the reduced entrainment in the wall plume is due to the suppression of the meandering of the plume. We find that the meandering of the free plume creates coherent structures at the size of the total plume width that frequently overturn and engulf ambient fluid. This in turn stretches the interface leading to an increase in the total length of the TNTI and increased rates of entrainment (Ottino, 1989). This suggests that the entrainment process may be viewed as a multi-scale continuous process, where ultimately, at the smallest scales, fluid is nibbled across the TNTI and then irreversibly mixed, consistent with the view of turbulent entrainment in axisymmetric jets (Mistry et al., 2016), turbulent boundary layers (de Silva et al., 2013; Philip et al., 2014) and axisymmetric plumes (Burridge et al., 2017). The observation that the total TNTI length of the free plume is 2.4 times that of the wall plume

is then reflected well in the observation that the free plume entrains at a rate of approximately 2.4 times that of the wall plume. We find that the relative vertical transport of the engulfed fluid, $\overline{Q_{eng}}/\overline{Q}$, of the free plume is approximately 18% greater than the wall plume (see figure 5.19). However, the relative vertical transport of ambient fluid outside the TNTI envelope of the wall plume, $\overline{Q_{out}}/\overline{Q}$, is approximately double that of the free plume. Further, $\overline{Q_{out}}$ and $\overline{Q_{eng}}$ are similar in the free plume whereas $\overline{Q_{out}}$ is almost double $\overline{Q_{eng}}$ in the wall plume, in addition to being much larger than both fluxes of the free plume. This suggests that the wall plume is relatively inefficient at engulfing the outer ambient fluid, although it transports relatively more unmixed fluid, that is $\overline{Q_{out}}$ and $\overline{Q_{eng}}$ combined, whereas the free plume is able to maintain a balance between the vertical transport of ambient and engulfed fluid.

5.6 Results in a plume coordinate system

5.6.1 Plume coordinate system definition

Following the analysis of Burridge et al. (2017) of an axisymmetric plume, we examine the two flows in a coordinate system which follows the plumes as they fluctuate in width. For the free plume the coordinate system, $x_p(x,z,t)$, is defined by

$$x_p(x,z,t) = \frac{2\left(x - E_R(z,t)\right)}{E_R(z,t) - E_L(z,t)} + 1 = \frac{\left(x - E_R(z,t)\right)}{R_p(x,t)} + 1, \tag{5.62}$$

where by construction $x_p = -1$ and $x_p = 1$ at the outermost left and outermost right points on the TNTI at a given height, respectively and $x_p = 0$ is at the mid point between these two points. The coordinate system for the wall plume is similarly defined by

$$x_p(x,z,t) = \frac{\left(x - R_p(z,t)\right)}{R_p(x,t)} + 1, \tag{5.63}$$

so that $x_p = 1$ is at the outermost TNTI position for a given height and $x_p = 0$ remains fixed at the wall. Evidently from figure 5.20 multiple points along a TNTI can exist for a given height, so the outermost points along the TNTI are taken. Further, prior to the coordinate transformation, the data are conditioned on whether plume fluid is present within the outer plume envelope using the step function H_{eng}, therefore ensuring that all statistics within the region $|x_p| < 1$ are those within plume fluid. The time-averaged vertical velocity data in

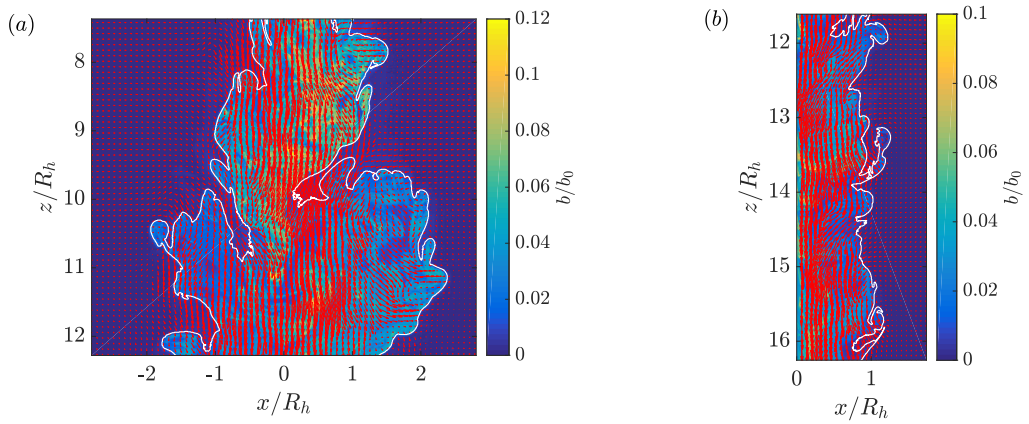

Fig. 5.20 Instantaneous buoyancy field overlayed with velocity field, red arrows, from a (*a*) free and (*b*) wall plume experiment. The outer TNTI is highlighted in white.

plume coordinates is then defined by

$$\overline{w_p} = \overline{w(x_p,z)} = \frac{1}{T_c}\int_0^T w(x_p,z,t)\,[1-H_{eng}(x_p,z,t)]\,\mathrm{d}t, \tag{5.64}$$

for the total recording time T, where $T_c(x_p,z)$ is the total amount of time at a given plume coordinate location when engulfed fluid is not present, defined by

$$T_c(x_p,z) = \int_0^T 1-H_{eng}(x_p,z,t)\mathrm{d}t. \tag{5.65}$$

This is necessary in order to omit engulfed regions within the plume from the conditional mean. The horizontal velocity $\overline{u_p}$ and buoyancy $\overline{b_p}$ are equivalently defined. The turbulent fluctuations and fluxes of the quantities in the plume coordinates are defined with respect to the time-averaged quantities in plume coordinates, e.g. for the turbulent vertical velocity fluctuations,

$$w'_{p,rms} = \left(\frac{1}{T_c}\int_0^T \left(w(x_p,z,t)\,[1-H_{eng}(x_p,z,t)] - \overline{w_p}\right)^2 \mathrm{d}t\right)^{1/2}, \tag{5.66}$$

and equivalently for the horizontal velocity $u'_{p,rms}$ and buoyancy fluctuations $b'_{p,rms}$.

5.6.2 Velocity and buoyancy in plume coordinates

The conditionally averaged velocity and buoyancy data in plume coordinates across all experiments are shown in figure 5.21. Data are taken from five heights spanning the examined region for each experiment.

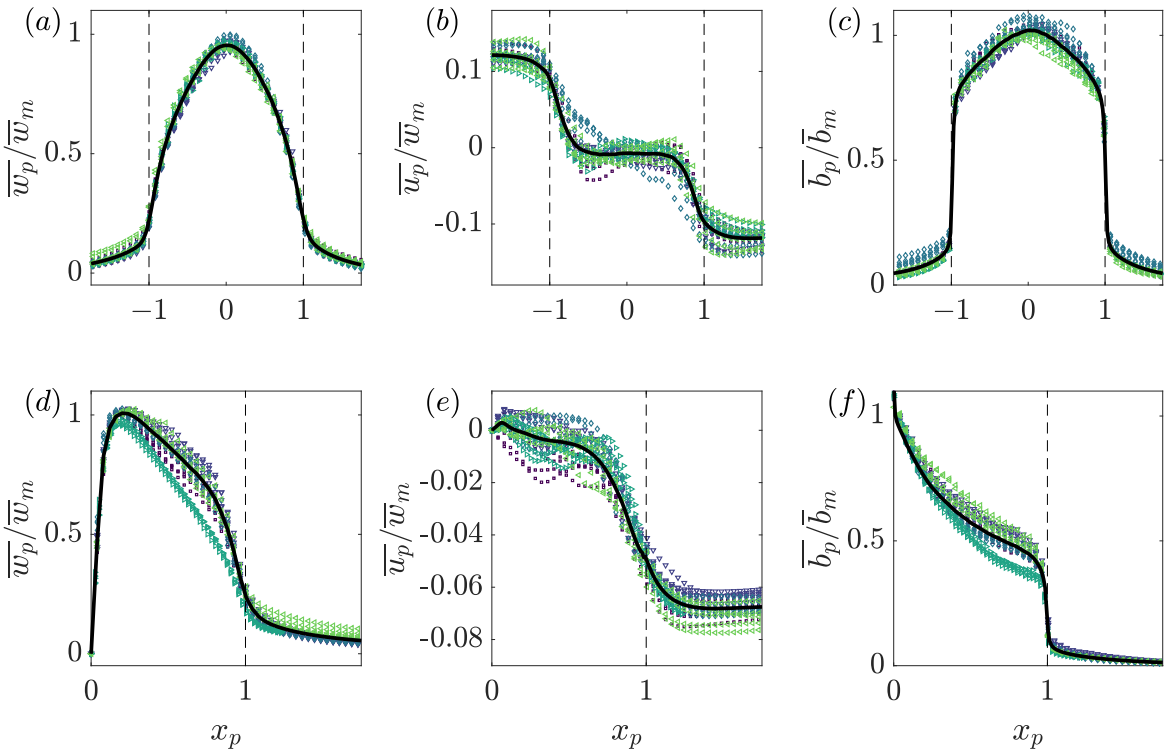

Fig. 5.21 Time-averaged scaled vertical and horizontal velocity and buoyancy profiles of the (*a*), (*b*), (*c*) free and (*d*), (*e*), (*f*) wall plume in plume coordinates. For each experiment, five different heights spanning the studied region are plotted. The black dashed lines at $x_p = \{-1, 1\}$ highlight the position of the outer TNTI. The black curves are the averages of the data.

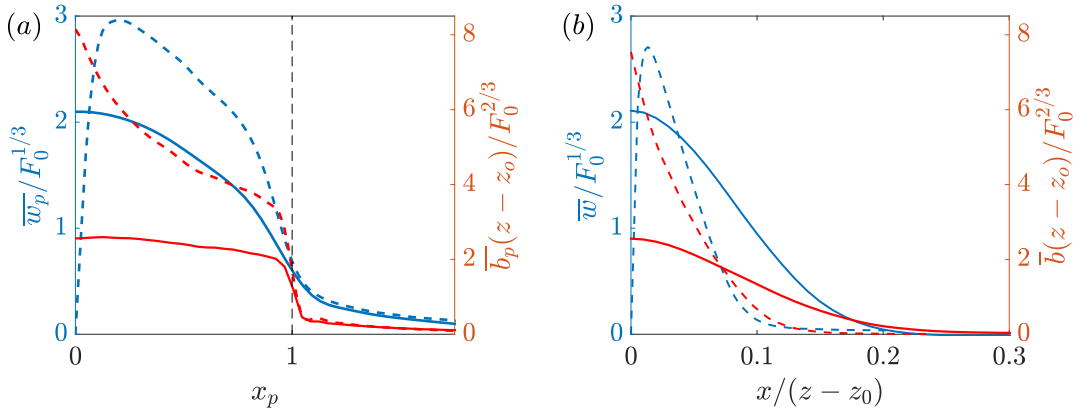

Fig. 5.22 Average profiles of the time-averaged free (solid) and wall plume (dashed) vertical velocities (blue, left) and buoyancy (red, right) in (*a*) plume coordinates and (*b*) Eulerian coordinates. Only half the region of the free plume is shown in both cases to aid comparison with the wall plume. The vertical velocities have been scaled using the buoyancy flux and the buoyancy has been scaled using the buoyancy flux and distance from the virtual origin.

The average data for both set of experiments collapse onto a single curve showing that the velocities and buoyancy are self-similar when viewed in plume coordinates. The vertical velocities and buoyancy have been scaled by the maximum, time-averaged, vertical velocity and buoyancy measured in Eulerian coordinates, respectively. The maximum time-averaged buoyancy in the plume coordinate system is greater than that in the Eulerian coordinate system for both the free and wall plume. This is to be expected, since the contribution of the ambient fluid in the calculation of the mean buoyancy is omitted in the plume coordinate system. However, it is surprising to note that the maximum vertical velocity of the free plume in the plume coordinate system is lower than that in the Eulerian coordinate system. This may be due to the meandering of the plume and is not observed in the wall plume where, as one would expect from considering the additional buoyancy, the maximum velocity is greater in the plume coordinate system.

The average vertical velocities at the plume edge (dashed vertical lines at $\{-1,1\}$) for the free plume are significant, on average 23% of the centreline velocities. This is almost identical to the behaviour of an axisymmetric plume observed by Burridge et al. (2017) where the vertical velocities at the outer TNTI of the plume were also found to be about 20% of the centreline velocities. This behaviour is similarly observed in the wall plume where the vertical velocities at the outer TNTI are on average 25% of the maximum vertical velocity.

The buoyancy profile in plume coordinates of the free plume in figure 5.21 (*c*) shows that the buoyancy just inside the interface is about 75% of the centreline buoyancy within the plume. This relative buoyancy is surprisingly large and significantly greater than the relative passive scalar of 30% observed just inside the interface in an axisymmetric jet by Westerweel et al. (2009). The relative buoyancy just inside the interface for the wall plume (figure 5.21 (*f*)) is significantly lower than the free plume at about 40% of the maximum buoyancy. These values of relative buoyancy are almost identical to the values observed from the conditional statistics in a coordinate system normal to the TNTI, shown in figure 5.7. This suggests that the statistics close to the interface are not significantly affected by defining only the outermost point along the TNTI at a given height as the plume edge, as we have done. The free plume buoyancy profile broadly exhibits a constant gradient, of opposite sign, either side of the centreline. This is in contrast to the wall plume, where the gradient is rapidly increasing in magnitude from the interface towards the wall.

To highlight differences between the two flows, figure 5.22 (*a*) shows the average of all the data of the time-averaged vertical velocities and buoyancy in plume coordinates, and for comparison in Eulerian coordinates in figure 5.22 (*b*), of the free and wall plume, where the vertical velocities have been scaled using the buoyancy flux and the buoyancy has

been scaled using the buoyancy flux and virtual distance from the source. Only the region $x_p \geq 0$ is shown for the free plume. Figure 5.22 (*a*) shows that, for a given buoyancy flux, the vertical velocity profiles of the wall plume and free plume outside the plume are almost indistinguishable, in particular the vertical velocities at the outer TNTI, $x_p = 1$, are identical. Moving towards the wall, the vertical velocity of the wall plume increases away from the TNTI more rapidly than the free plume. This is expected given that the buoyancy in the wall plume is at least 1.6 times greater than the free plume, within the region $x_p < 0.95$. In the adjustment region $0.95 < x_p < 1$ the buoyancy rapidly increases for both the free and wall plume. However, away from this adjustment region within the plume, $x_p < 0.95$, the buoyancy of the free plume changes at most by 9% of the mean buoyancy within that region, whereas the wall plume changes by 52% of the mean buoyancy within that region. This shows that in the free plume, plume fluid is more uniformly mixed than the wall plume. This implies that there is a more equal distribution of buoyancy force across the plume, which results in a more top-hat vertical velocity in plume coordinates, which can be seen in figure 5.22.

5.6.3 Turbulent fluctuations and fluxes in plume coordinates

The vertical velocity fluctuations in the plume coordinate are shown in figures 5.23 (*a*) and 5.24 (*a*) for the free and wall plume, respectively. The profile of the free plume broadly mirrors that observed in Eulerian space, with bi-modal peaks at 30% of the maximum Eulerian vertical velocity. This is larger than the bi-modal peaks observed in Eulerian space, a result similarly observed in axisymmetric plumes (Burridge et al., 2017), where it was suggested that the meandering of the plume masks the scale of the turbulent velocity fluctuations. The profile of the vertical velocity fluctuations in the wall plume is quite different from Eulerian space. Three distinct peaks are observed: one very close to the wall, a second peak within the middle of the plume region and a third peak almost exactly at the outer TNTI of the plume. The maximum peak is on average 25% of the maximum Eulerian vertical velocity. This peak value is almost identical to that observed in Eulerian space. The reduced meandering of the wall plume may explain the reduced effect of the increase in magnitude of turbulent velocity fluctuations seen in the free and axisymmetric plume.

The buoyancy fluctuations of the free and the wall plume in figures 5.23 (*c*) and 5.24 (*c*), respectively, are very different to the Eulerian statistics. This is expected, since there must be ambient fluid where $b = 0$ (except for any additional noise associated with the experiment) beyond the outer TNTI and therefore a jump is observed at $x_p = \pm 1$ in both flows. The maximum buoyancy fluctuations in both the free and wall plume are less than those in the Eulerian statistics. This results from the condition that the ambient fluid is omitted in the

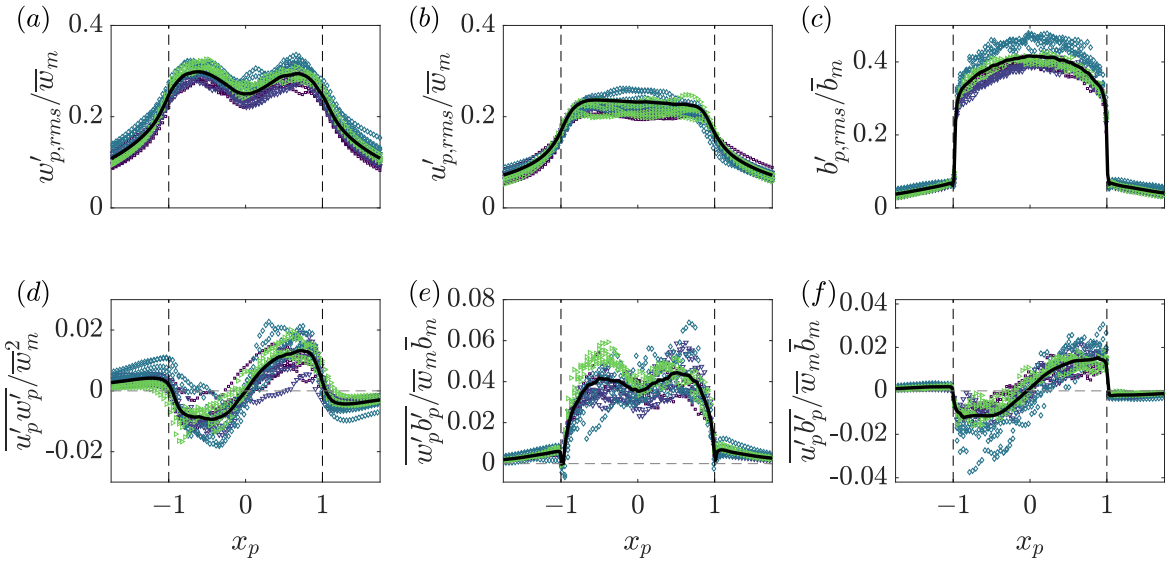

Fig. 5.23 Time-averaged scaled free plume turbulent fluctuations in plume coordinates of (*a*) vertical velocity, (*b*) horizontal velocity and (*c*) buoyancy and (*d*) Reynolds stress, (*e*) vertical and (*f*) horizontal turbulent buoyancy flux. The black curves are the averages of the data. A zero line is shown by the horizontal dashed line.

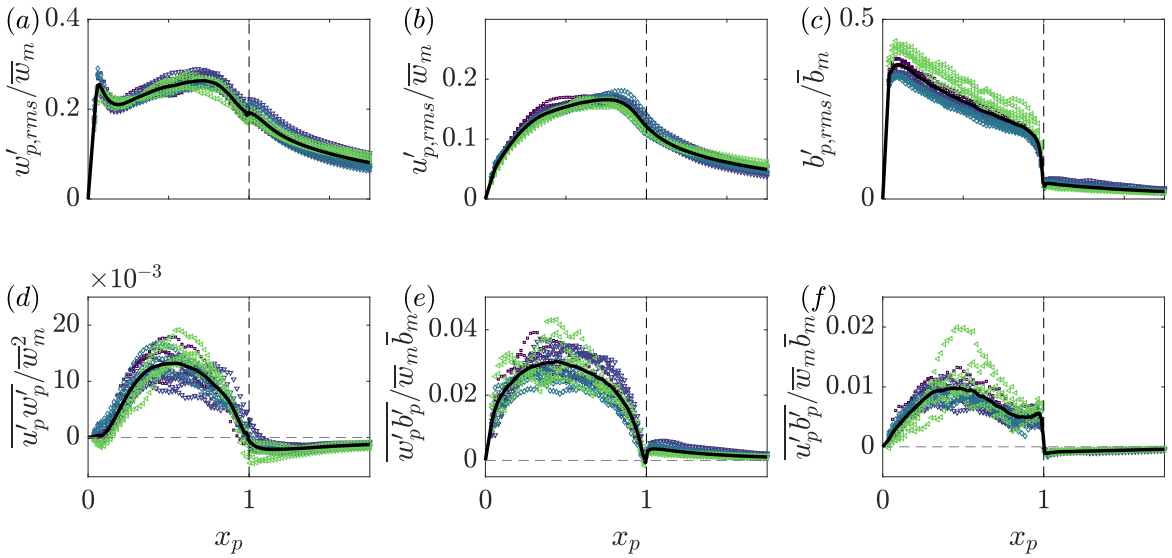

Fig. 5.24 Time-averaged scaled wall plume turbulent fluctuations in plume coordinates of (*a*) vertical velocity, (*b*) horizontal velocity and (*c*) buoyancy and (*d*) Reynolds stress, (*e*) vertical and (*f*) horizontal turbulent buoyancy flux. The black curves are the averages of the data.

calculation of the statistic. A larger discrepancy between the plume and Eulerian coordinate system is observed in the free plume, owing to the increased meandering and engulfment of the free plume.

The Reynolds stress profiles of the free and the wall plume in plume coordinates are shown in figures 5.23 (*d*) and 5.24 (*d*), respectively. An interesting feature, which is also observed in axisymmetric plumes (Burridge et al., 2017), is the change of sign across the region of the plume edge. For comparison consider only the region $x_p \geq 0$ of the free plume, but note that results are equivalent although of opposite sign for $x_p \leq 0$. In this case, as with the wall plume in the region away from the wall, $\overline{u'_p w'_p}$ is positive within the plume, however it rapidly becomes negative within the ambient fluid. This is contrast to the Eulerian statistic, where $\overline{u'w'}$ is positive and gradually tends to zero in the positive x direction, because the Reynolds stress is larger in magnitude within the plume region and, as with the velocity fluctuations, the meandering of the plume masks the ambient flow statistics. The negative Reynolds stress outside the plume may be explained from considering the entrainment process. The negative correlation $\overline{u'_p w'_p} < 0$ suggests either transport of streamwise momentum inwards or transport of negative streamwise momentum outwards. The former is consistent with the observation that $w'_{p,rms} > 0$ (figures 5.23 (*a*) and 5.24 (*a*)) and is associated with entrainment since it is necessary for transport of fluid from the non-turbulent ambient into the turbulent plume region, and is described by Odier et al. (2012) for a gravity current. The latter would imply detrainment of slower moving plume fluid which is not observed. The peak Reynolds stresses in plume coordinates, in both cases, are lower in magnitude than the Eulerian Reynolds stresses. This is also observed in axisymmetric plumes and it is not clear why this should occur.

The turbulent vertical buoyancy flux in plume coordinates of the free plume (figure 5.23 (*e*)) shows a bi-modal peak with maximum values on average of 30% larger than those observed in Eulerian coordinates. The omission of ambient data has a similar effect on reducing $\overline{w'_p b'_p}$. The turbulent buoyancy flux in plume coordinates of the wall plume, figure 5.24 (e), looks quite different from the Eulerian statistic. The profile is more similar to a top-hat profile, and the kink seen in Eulerian coordinates is not observed. This, therefore, suggests the kink is a consequence of the combined ambient and plume statistics in the Eulerian coordinate system, especially since it is located close to the mean position of the plume edge.

5.6.4 Summary of results in the plume coordinate

As shown in figure 5.22 the vertical velocity and buoyancy profiles in the ambient fluid immediately outside the plume are the same for both the free and the wall plume. This

similarity is not apparent from the Eulerian data and neither are the large gradients in vertical velocity and buoyancy at the plume edge. The plume-coordinate data also show that the fluctuations in vertical velocity at the plume edge are larger than those revealed by the Eulerian data. The fluctuations in buoyancy are also significantly different when observed in plume coordinates, since the Eulerian statistics smear the data between the plume and the ambient fluid.

The plume-coordinate data also reveal aspects concerning the entrainment process that are not evident from the Eulerian data. For example, in plume coordinates the Reynolds stress changes sign outside the plume (a change not apparent in Eulerian coordinates), which as described above is a result of ambient fluid being drawn towards the plume. Further comparison of figures 5.23 (*d*) and 5.24 (*d*) show that the reduced entrainment in the wall plume compared to the free plume is consistent with the smaller magnitude of the Reynolds stress outside the plume in the latter case.

5.7 Limitations of planar measurements in a three-dimensional flow

As highlighted for a turbulent axisymmetric plume in § 4.7, planar measurements of turbulent line and wall plumes restrict observations of the three-dimensional flow dynamics. Here we discuss the limitations of planar measurements.

As for the axisymmetric plume, where possible, the definitions in this chapter have been constructed in a way that are blind to the out-of-plane flow dynamics, so are robust to possible future three-dimensional flow field measurements. In addition, the vertical and horizontal velocities and the turbulent statistics, are statistically spanwise independent so that three-dimensional measurements do not offer a real advantage in this regard.

Further, unlike for the axisymmetric case, our definition of the instantaneous plume width would remain the most appropriate choice even with three-dimensional data, since the measurement plane is aligned normal to the line source, so that the plume width analysis would remain identical in 3-D. However, the meandering analysis in § 5.5.4 (figure 5.15) relies on identifying regions that are bounded by the outer TNTI. While it is possible to identify such regions within the measurement plane, it is not possible to determine whether regions of completely bounded fluid (within the measurement plane) are connected to the ambient far field in an unobserved plane. Therefore, the results are likely to change as a result of three-dimensional data. In particular, the measurements presented in figure 5.15 provide a lower bound for the true measurement of the probability, at a given horizontal lo-

cation, of being within the plume region bounded by the outer TNTI. With this in mind, our results are still robust in that our conclusions are based on the significant magnitude of the probability (of being within the plume region bounded by the outer TNTI) on the free plume centreline. A discussion about the relative merits and limitations of the restriction of planar measurements in analysing engulfed fluid would closely follow that of the axisymmetric plume in § 4.7 so is not discussed here.

The limitations with regard to measurements of the turbulent/non-turbulent surface area per unit length have been discussed in § 5.5.4.2.

5.8 Integral turbulent Prandtl number for the free line plume

The entrainment hypothesis of Morton et al. (1956) provides a turbulence closure model for the free plume bulk flow conservation equations (5.15) - (5.17). However, an analytical turbulence closure model, i.e. closure of the high Reynolds number, Boussinesq, simplified Reynolds averaged Navier Stokes equations (5.8) - (5.10) which we repeat here

$$\frac{\partial \overline{u}}{\partial x} + \frac{\partial \overline{w}}{\partial z} = 0, \tag{5.67}$$

$$\overline{u}\frac{\partial \overline{w}}{\partial x} + \overline{w}\frac{\partial \overline{w}}{\partial z} = \overline{b} - \frac{\partial \overline{u'w'}}{\partial x}, \tag{5.68}$$

$$\overline{u}\frac{\partial \overline{b}}{\partial x} + \overline{w}\frac{\partial \overline{b}}{\partial z} = -\frac{\partial \overline{u'b'}}{\partial x}, \tag{5.69}$$

requires a parametrisation of the turbulent shear stress in (5.68) and horizontal turbulent heat flux in (5.69). A large category of turbulence closure models make use of a 'turbulent viscosity' ν_T and a 'turbulent diffusivity' κ_T, defined by

$$\nu_T = \overline{u'w'}\left(\frac{\partial \overline{w}}{\partial x}\right)^{-1}, \qquad \kappa_T = \overline{u'b'}\left(\frac{\partial \overline{b}}{\partial x}\right)^{-1} \tag{5.70}$$

where the turbulent viscosity is modelled using the vertical and horizontal velocities, i.e. $\nu_T = \nu_T(\overline{u}, \overline{w})$ (e.g. the Eddy viscosity model, Prandtl's mixing-length model or Smagorinsky model (Pope, 2000; Tennekes et al., 1972); see Yih (1991) for the application to a free line plume). The turbulent diffusivity may then be related to the turbulent viscosity via a turbulent Prandtl number

$$Pr_T = \frac{\nu_T}{\kappa_T}, \tag{5.71}$$

which for simple shear flows is of order unity (Pope, 2000). The equations (5.67) - (5.69) may then be expressed in closed form as

$$\frac{\partial \overline{u}}{\partial x} + \frac{\partial \overline{w}}{\partial z} = 0, \tag{5.72}$$

$$\overline{u}\frac{\partial \overline{w}}{\partial x} + \overline{w}\frac{\partial \overline{w}}{\partial z} = \overline{b} - \frac{\partial}{\partial x}\left(\nu_T \frac{\partial \overline{w}}{\partial x}\right), \tag{5.73}$$

$$\overline{u}\frac{\partial \overline{b}}{\partial x} + \overline{w}\frac{\partial \overline{b}}{\partial z} = -\frac{\partial}{\partial x}\left(Pr^{-1}\nu_T \frac{\partial \overline{b}}{\partial x}\right), \tag{5.74}$$

The turbulent Prandtl number quantifies the turbulent transport of momentum relative to the turbulent transport of heat and therefore plays an important role in turbulence modelling. Experiments and direct numerical simulations indicate that the turbulent Prandtl numbers in axisymmetric plumes are less than one and in the range $Pr_T = [0.57, 1]$ (see Craske et al. (2017) table 1 and references therein). By comparison, there has been relatively little investigation into the turbulent Prandtl number of a free (line) plume. Measurements from Ramaprian and Chandrasekhara (1989) suggest that $Pr_T = 0.5$, estimated from the best-fit profiles of the vertical velocity and buoyancy and the peak turbulent transport of momentum and heat diffusivity. The aim of this section is to investigate the turbulent Prandtl number of the free plume following the theoretical framework of Craske et al. (2017) who found that the integral turbulent Prandtl number in an axisymmetric pure plume is $3/5$.

In § 5.8.1 we derive an alternative entrainment relation to that of the energy decomposition considered in § 5.2.1 by considering the squared mean buoyancy. By combining this with the energy decomposition relation we show that an integral turbulent Prandtl number may be defined in terms of the ratio of the width of buoyancy profile to the width of the velocity profile, Φ. In § 5.8.2 we compare this theory with direct measurements of the turbulent and integral turbulent prandtl number in the free plume. To draw an analogy to the work of Craske et al. (2017) we follow their convention of distinguishing the passive and active scalars by associating buoyancy with temperature differences in the flow, i.e. we use Pr_T in the context of our experiments.

5.8.1 Integral Prandtl number model for the free line plume

Following the energy decomposition of the entrainment coefficient given by Paillat and Kaminski (2014a), we derive an expression for the entrainment coefficient in terms of the squared mean buoyancy flux. An expression for the conservation of the squared mean buoyancy flux may be obtained by multiplying (5.69) by $2\overline{b}$ and using the continuity equation to

	Φ	Pr_T	Pr_{Tm}
Free line			
Ramaprian and Chandrasekhara (1989)	1.21 ± 0.17	0.46-0.70	-
Present study	1.17 ± 0.04	0.56[a]	0.58
Axisymmetric			
Wang and Law (2002)	1.04	0.62	0.62
Shabbir and George (1994)	0.92	0.70-1.00	-
Papanicolaou and List (1988)	1.06	0.57-0.71	-
Van Reeuwijk et al. (2016)	0.99	-	0.66

Table 5.5 The ratio of the buoyancy to velocity widths, Φ, and the turbulent Prandtl number, Pr_T, and integral turbulent Prandtl number, Pr_{Tm}, of previous studies on axisymmetric and free line plumes. [a] The value given here is the characteristic turbulent Prandtl number defined in §5.8.2. The values from the previous studies on axisymmetric plumes are taken from table 1 in Craske et al. (2017).

obtain,

$$\frac{\partial}{\partial x}\left(\overline{u}\overline{b}^2\right) + \frac{\partial}{\partial z}\left(\overline{w}\overline{b}^2\right) = 2\overline{u'b'}\frac{\partial \overline{b}}{\partial x}. \tag{5.75}$$

Integration of (5.75) over x gives

$$\frac{\mathrm{d}}{\mathrm{d}z}\left(\frac{M^2B^2}{2Q^3}\gamma_S\right) = \frac{M^3B^2}{2Q^5}\delta_S, \tag{5.76}$$

where

$$\gamma_S = \frac{1}{WG^2R}\int_{-\infty}^{\infty}\overline{w}\overline{b}^2\mathrm{d}x, \qquad \delta_S = \frac{1}{WG^2}\int_{-\infty}^{\infty}\overline{u'b'}\frac{\partial \overline{b}}{\partial x}\mathrm{d}x, \tag{5.77}$$

and $G = BM/Q^2$ is the characteristic buoyancy and W and R are the characteristic vertical velocity and plume width defined as in (5.6) and (5.7), respectively. We drop the f subscript with the implication that we are only considering the free plume in this section. Applying the product rule to the left hand side of (5.76) gives

$$\frac{-M^2B^2}{2Q^4}\gamma_S\frac{\mathrm{d}Q}{\mathrm{d}z} + \frac{1}{Q}\frac{\mathrm{d}}{\mathrm{d}z}\left(\frac{M^2B^2}{2Q^2}\gamma_S\right) = \frac{2M^3B^2}{Q^5}\delta_S. \tag{5.78}$$

The free plume solutions (5.20) - (5.22) may be used to show that the second term on the left hand side of (5.78) is zero. By equating (5.15) and (5.78) the following expression for

the entrainment coefficient may obtained

$$\alpha = \frac{-2\delta_S}{\gamma_S}. \tag{5.79}$$

We have already seen in § 5.2.1 that the entrainment coefficient may be expressed in terms of the mean energy flux. By adopting the notation of Craske et al. (2017) the relation (5.41) may be written in terms of the following identities

$$\gamma_E = \frac{1}{W^3 R}\int_{-\infty}^{\infty} \overline{w}^3 \mathrm{d}x, \qquad \delta_E = \frac{1}{W^3}\int_{-\infty}^{\infty} \overline{u'w'}\frac{\partial \overline{w}}{\partial x}\mathrm{d}x, \tag{5.80}$$

as

$$\alpha = Ri\left(\frac{1}{\theta} - \frac{2}{\gamma_E}\right) - \frac{2\delta_E}{\gamma_E}. \tag{5.81}$$

The free plume solutions (5.20) - (5.22) may be used to show that $\alpha\theta = Ri/2$ which may be used in (5.81) to eliminate Ri to give

$$\alpha = 2\frac{\delta_E}{\gamma_E}\left(\frac{1}{1-\frac{4\theta}{\gamma_E}}\right). \tag{5.82}$$

Equating (5.79) and (5.82) gives

$$\frac{\delta_S}{\delta_E} = -\frac{\gamma_S}{\gamma_E}\left(\frac{1}{1-\frac{4\theta}{\gamma_E}}\right). \tag{5.83}$$

As highlighted in Craske et al. (2017), although an integral representation of the turbulent Prandtl number is useful, the integral of Pr_T is not defined because both $\overline{u'b'}$ and $\frac{\partial \overline{w}}{\partial x}$ approach zero as x tends to infinity. To overcome this, Craske et al. (2017) defined an integral turbulent viscosity and an integral turbulent diffusivity analogous (i.e. in their case for an axisymmetric plume) to the following

$$\nu_{Tm} = \frac{\int_{-\infty}^{\infty} \nu_T \left(\frac{\partial w}{\partial x}\right)^2 \mathrm{d}x}{\int_{-\infty}^{\infty}\left(\frac{\partial w}{\partial x}\right)^2 \mathrm{d}x}, \tag{5.84}$$

$$\kappa_{Tm} = \frac{\int_{-\infty}^{\infty} \kappa_T \left(\frac{\partial b}{\partial x}\right)^2 \mathrm{d}x}{\int_{-\infty}^{\infty}\left(\frac{\partial b}{\partial x}\right)^2 \mathrm{d}x}. \tag{5.85}$$

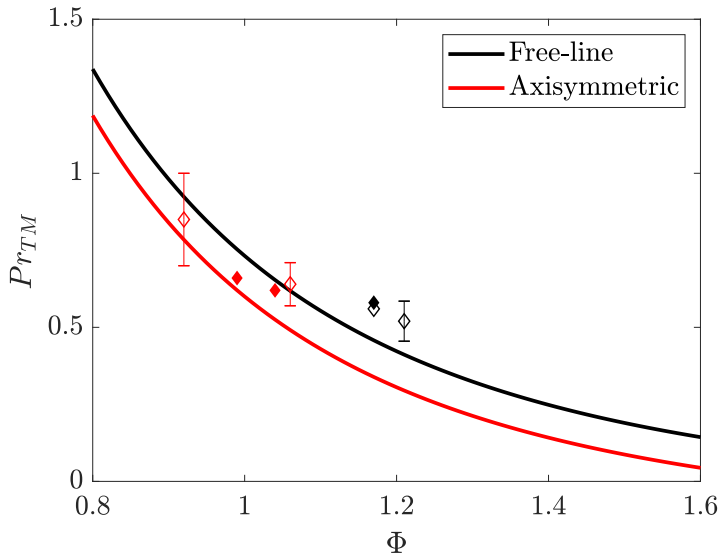

Fig. 5.25 Integral Prandtl number for the free line plume given by (5.94) (black curve) and the axisymmetric plume given by Craske et al. (2017) equation (B-4) (red curve), for a given ratio of buoyancy and vertical velocity profile widths, Φ. The data from table 5.5 are also shown with the turbulent Prandtl and integral turbulent Prandtl numbers shown by the unfilled and filled markers, respectively.

An integral turbulent Prandtl number may then be defined as

$$Pr_{Tm} = \frac{\nu_{Tm}}{\kappa_{Tm}}. \tag{5.86}$$

By introducing the similarity variable $x^* = x/R$ and assuming vertical velocity and buoyancy profiles of the same shape but relative widths Φ the vertical velocity and buoyancy may be written in terms of the similarity function $f(x^*)$ where

$$\frac{w}{W} = f(x^*), \qquad \frac{b}{G} = \frac{1}{\Phi} f\left(\frac{x^*}{\Phi}\right). \tag{5.87}$$

Substitution of (5.87) into (5.86) gives

$$Pr_{Tm} = \frac{1}{\Phi^2}\left(\frac{\int_{-\infty}^{\infty}\left(\frac{\partial f(\frac{x^*}{\Phi})}{\partial x^*}\right)^2 \mathrm{d}x^*}{\int_{-\infty}^{\infty}\left(\frac{\partial f(x^*)}{\partial x^*}\right)^2 \mathrm{d}x^*}\right)\frac{\delta_E}{\delta_S} = \frac{1}{\Phi^3}\frac{\delta_E}{\delta_S}. \tag{5.88}$$

where Φ is the ratio of the width of buoyancy profile to the width of the velocity profile. If the similarity function is assumed to follow a Gaussian profile, $f(x^*) = \exp\left(-\frac{\pi}{2}x^{*2}\right)$, then

the vertical velocity and buoyancy may be expressed as

$$\overline{w} = \sqrt{2} W f(x^*), \qquad \overline{b} = \frac{\sqrt{2}}{\Phi} G f\left(\frac{x^*}{\Phi}\right). \tag{5.89}$$

The term δ_E/δ_S may then be evaluated from (5.83) where the dimensionless energy flux is given by

$$\gamma_E = 2\sqrt{2}\int_{-\infty}^{\infty} e^{-\frac{3\pi}{2}x^{*2}}\mathrm{d}x^* = \frac{4}{\sqrt{3}}, \tag{5.90}$$

the dimensionless squared mean buoyancy flux is given by

$$\gamma_S = \frac{2\sqrt{2}}{\Phi^2}\int_{-\infty}^{\infty} e^{-\frac{\pi}{2}(1+\frac{2}{\Phi^2})x^{*2}}\mathrm{d}x^* = \frac{4}{\Phi\sqrt{\Phi^2+2}}, \tag{5.91}$$

and

$$\theta = \frac{\int_{-\infty}^{\infty} e^{-\frac{\pi}{2}(1+\frac{1}{\Phi^2})x^{*2}}\mathrm{d}x^* \int_{-\infty}^{\infty} e^{-\frac{\pi}{2}x^{*2}}\mathrm{d}x^*}{\int_{-\infty}^{\infty} e^{-\frac{\pi}{2}x^{*2}}\mathrm{d}x^* \int_{-\infty}^{\infty} e^{-\frac{\pi}{2}\left(\frac{x^*}{\Phi}\right)^2}\mathrm{d}x^*} = \frac{\sqrt{2}}{\sqrt{1+\Phi^2}}. \tag{5.92}$$

Substitution of (5.90) - (5.92) into (5.83) gives

$$\frac{\delta_E}{\delta_S} = \frac{\sqrt{3}\sqrt{1+\Phi^2}}{\Phi\sqrt{\Phi^2+2}\left(\sqrt{6}-\sqrt{1+\Phi^2}\right)}. \tag{5.93}$$

Finally, we have that

$$Pr_{Tm} = \frac{\sqrt{\Phi^2+2}\left(\sqrt{6}-\sqrt{1+\Phi^2}\right)}{\sqrt{3}\Phi^2\sqrt{1+\Phi^2}}. \tag{5.94}$$

Figure 5.25 plots the integral turbulent Prandtl number for the free plume as a function of Φ compared to the integral turbulent Prandtl number for an axisymmetric plume. The figure shows that the turbulent Prandtl number decreases for increasing Φ, also found for the integral turbulent Prandtl number an axisymmetric plume by Craske et al. (2017). The models predict a larger integral Prandtl number, for a given Φ, in the free plume compared to the axisymmetric plume. Equivalently, the models predict a larger Φ in the free plume for a given integral Prandtl number.

5.8.2 Experimental measurements of the turbulent Prandtl number for the free line plume

Experimental observations of the turbulent Prandtl number rely on both second order quantities and the gradients of first order quantities. In particular, in the core of the plume, as well

as at infinity, both the turbulent transport quantities and the gradients of the vertical velocity and buoyancy approach zero. Large errors in the calculation of the turbulent Prandtl number from experimental data may therefore by expected away from the regions with large shear. In an attempt to overcome this we first calculate the height-averaged self-similar profiles of the data. We then perform a linear least squares fit to the data with analytic functions of the form

$$\frac{\overline{w}}{\overline{w}_m} = \exp\left(-\left(\frac{\eta}{k_w}\right)^2\right), \tag{5.95}$$

$$\frac{\overline{b}}{\overline{b}_m} = \exp\left(-\left(\frac{\eta}{k_b}\right)^2\right), \tag{5.96}$$

$$\frac{\overline{u'w'}}{\overline{w}_m^2} = a_1\left(\exp\left(-\left(\frac{\eta-b_1}{k_1}\right)^2\right) - \exp\left(-\left(\frac{\eta+b_1}{k_1}\right)^2\right)\right), \tag{5.97}$$

$$\frac{\overline{u'b'}}{\overline{w}_m\overline{b}_m} = a_2\left(\exp\left(-\left(\frac{\eta-b_2}{k_2}\right)^2\right) - \exp\left(-\left(\frac{\eta+b_2}{k_2}\right)^2\right)\right), \tag{5.98}$$

for constants k_w, k_b, a_1, b_1, k_1, a_2, b_2 and k_2 and $\eta = x/(z-z_0)$. Figure 5.26 shows the data (solid) compared to the respective least-squares fit functions (dashed) for experiment 1 using the determined values given in table 5.6, showing excellent agreement for all of the quantities. Similarly good agreement was found in all the experiments. From these quantities the turbulent Prandtl number may then be evaluated as

$$Pr_T = \frac{\overline{u'w'}}{\overline{u'b'}}\left(\frac{\partial\overline{b}}{\partial\eta}\right)\left(\frac{\partial\overline{w}}{\partial\eta}\right)^{-1}. \tag{5.99}$$

Figure 5.27 shows the result of (5.99) for each experiment with the average across all the experiments shown by the dashed curve. Although the data shows there is a relatively large variability in the turbulent Prandtl number across the plume it should be noted that in the region $|\eta| > 0.25$, the turbulent quantities are less than 1% of their peak values. This suggests that the turbulent Prandtl number in this region is not characteristic of the turbulent quantities, further this region is likely to correspond to large errors. To characterise the turbulent Prandtl number in the turbulent region we define a characteristic Prandtl number Pr_{Tc} based on the average of Pr_T within the central region of the plume as

$$Pr_{Tc}(\eta_c) = \frac{1}{2\eta_c}\int_{-\eta_c}^{\eta_c} Pr_T \mathrm{d}\eta, \tag{5.100}$$

k_w	k_b	a_1	b_1	k_1	a_2	b_2	k_2
0.103	0.115	0.0270	0.0736	0.0676	0.0402	0.0716	0.0788

Table 5.6 Least-squares best-fit parameters of the data to the functions (5.95) - (5.98) for experiment 1.

where η_c is defined such that

$$\left.\frac{\overline{w}}{\overline{w}_m}\right|_{\eta_c} = 0.01. \tag{5.101}$$

This definition results in an average value of $\eta_c = 0.258$. We find that $Pr_{Tc} = 0.56 \pm 0.04$, where the error is the standard deviation of Pr_{Tc} across the experiments. Although the threshold in (5.101) is arbitrary, Pr_{Tc} is insensitive to the choice of the threshold. In particular, Pr_{Tc} varies by at most 15% within each experiment for $0 < \eta_c < 0.30$. Note that any choice of η_c would result in non-turbulent ambient fluid contributing to the calculation of Pr_{Tc}, since the pdf for the free plume in figure 5.15 is everywhere less than one. This suggests it may be useful to consider Eulerian conditional statistics to determine a conditional Prandtl number based on the presence of turbulent plume fluid. This is not explored in this thesis.

A direct calculation of the integral Prandtl number (5.86) may also be calculated using (5.84) and (5.85) and the curves of best fit described above. The data for each experiment, which give an average value of $Pr_{Tm} = 0.58 \pm 0.03$, are shown in figure 5.25 showing reasonable agreement to the theoretical integral Prandtl number (5.94) evaluated from the experimentally determined value of $\Phi = 0.47 \pm 0.05$. The integral Prandtl number shows excellent agreement with the characteristic Prandtl number suggesting that the integral turbulent Prandtl number provides an effective characterisation of the turbulent Prandtl number of the plume within the plume core.

The two flows are both buoyancy-driven free-shear turbulent plumes. Therefore, a reasonable assumption may be made that the turbulent Prandtl number in the two flows are approximately equal. The theory then predicts a larger Φ in the free plume compared to the axisymmetric plume; it is clear from figure 5.25 that there is consensus from the previous and present studies that this is the case.

5.9 Conclusions

Simultaneous velocity and buoyancy field measurements of a free and wall plume provided direct measurements of the top-hat entrainment coefficients. We found that the entrainment coefficient of the free plume $\alpha_f = 0.14$ is slightly less than double that of the wall plume

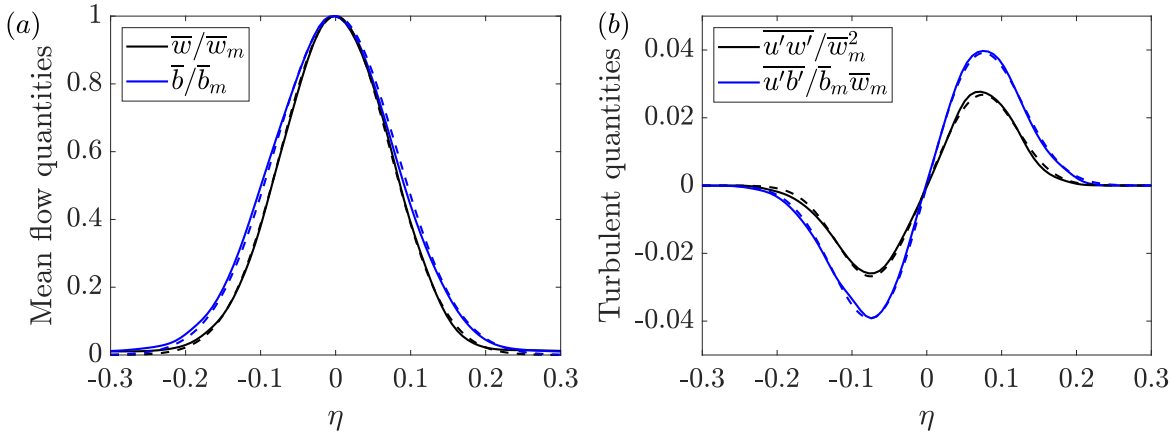

Fig. 5.26 Plume quantities for experiment 1 (solid) and their least-squares fit profiles (5.95) - (5.98) (dashed) using the values from table 5.6.

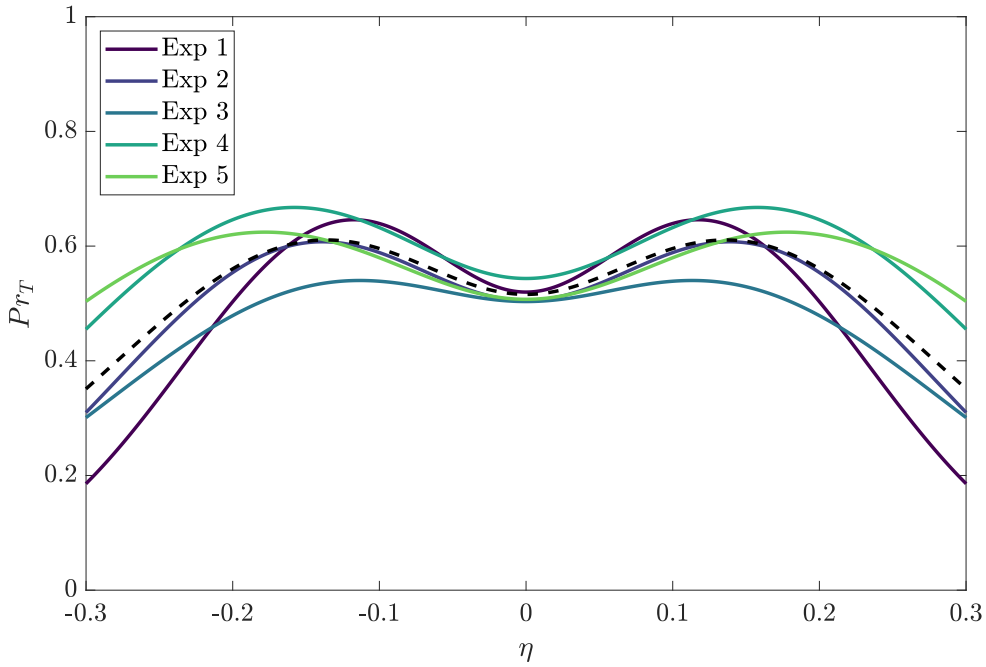

Fig. 5.27 The turbulent Prandtl number for each experiment based on (5.99) with the moving average of the data (dashed curve).

$\alpha_w = 0.08$. However, it was shown that, for a given buoyancy flux, this corresponds to the free plume physically entraining more than double per unit height than the wall plume, as expressed in terms of the rate of increase in plume volume flux with height $\mathrm{d}Q_f/\mathrm{d}z = 2.4\mathrm{d}Q_w/\mathrm{d}z$.

To examine this difference the entrainment coefficient of the wall plume was decomposed and the relative contributions from turbulence production, buoyant and viscous terms were compared to the free plume decomposition first performed by Paillat and Kaminski (2014a). A significant reduction in $\alpha_{production}$, approximately equal to the negative contribution from the viscous terms $\alpha_{viscous}$, is found in the wall plume. This suggests both the reduction in turbulent production and viscous dissipation due to the wall boundary layer, which indirectly affects entrainment by providing an energy sink (Holzner et al., 2016), are significant in the reduction of entrainment.

The statistics of the TNTI were calculated. We provided evidence of the free plume meandering and, in particular, we showed that there is a significant probability, about 15%, of ambient fluid outside the plume TNTI existing at the centreline, suggesting coherent lateral/sideways meandering of the plume centreline. This is in contrast to an axisymmetric plume where no coherence between the left and right TNTI of the plume were observed (Burridge et al., 2017). Through this meandering it was shown that the TNTI is stretched and on average the total length of TNTI of the free plume is longer than the wall plume by a factor of at least 2.2, measured at intermediate length scales $0.1 < \Delta/\lambda < 1$.

The turbulent velocity and buoyancy fluctuations were measured and the resulting turbulent fluxes and Reynolds stresses were calculated. Larger peak values were observed across all the fluctuations and turbulent fluxes in the free plume, resulting from larger turbulence production in the free plume. When the data are analysed in plume coordinates we find that the mean vertical velocity and buoyancy profiles in the ambient fluid are essentially the same, but the magnitude of the Reynolds stress is smaller in the wall plume consistent with the reduced entrainment rate compared with the free plume.

While the presence of the wall is the only fundamental difference between the free and wall plume, the effect of the wall could be viewed as two separate processes, namely the no-slip condition and the impermeability condition. We show that the wall shear stress is non-negligible and this results in a reduction of momentum of the wall plume, which could otherwise be used in the turbulent production contributing to entrainment. Alternatively, the impermeability condition prevents the wall plume meandering which both the reduces the large scale engulfment process and the stretching of the TNTI leading to a shorter total TNTI. As mentioned above this also manifests itself in smaller Reynolds stresses in the wall plume at the edge of the plume. It is difficult to separate these two processes and provide

an answer to which is the dominant effect in the reduction of entrainment in the wall plume, however the entrainment coefficient decomposition suggests that they are approximately equal in importance. It would be interesting to resolve this issue numerically by comparing a simulation of a wall plume with a no-slip and a free-slip condition, as performed for a gravity current in Holzner et al. (2016). In the case of a free-slip boundary condition $\alpha_{viscous} > 0$, however, since there is no viscous boundary layer it is expected that $\alpha_{viscous} \ll \alpha$, put another way the contribution would be comparable to the viscous effects in the free plume entrainment coefficient. This increase in $\alpha_{viscous}$, however, may be offset by a reduction in either $\alpha_{buoyant}$ or $\alpha_{production}$. It is not clear how the free-slip condition would affect $\alpha_{buoyant}$, however, Holzner et al. (2016) find a reduction in $\alpha_{production}$, for a free-slip as compared to a no-slip condition, for a turbulent gravity current inclined at 10°.

It would also be interesting to investigate the effect of Reynolds number on the energy decomposition of the wall plume entrainment coefficient, in particular a much larger Reynolds number. Assuming approximate self-similarity is maintained, it is expected that the primary effect would be a reduction in the skin-friction coefficient which would in turn increase the entrainment coefficient.

Finally, an integral turbulent Prandtl number for the free plume was defined based on the definition introduced by Craske et al. (2017) for an axisymmetric plume. An expression for the integral turbulent Prandtl number was derived in terms of the ratio of the width of the buoyancy profile to the velocity profile Φ. This was compared to the result of Craske et al. (2017) where it was found that, for a given integral turbulent Prandtl number, Φ is greater in the free plume than the axisymmetric plume, which agreed with experimental observations of the free plume compared to previous studies on axisymmetric plumes. A characteristic Prandtl number Pr_{Tc} was defined by the space-average of the turbulent Prandtl number within the turbulent region and an average value of $Pr_{Tc} = 0.56 \pm 0.04$ was determined. This value showed good agreement with the integral Prandtl number $Pr_{Tm} = 0.47 \pm 0.05$, based on the experimentally determined values of Φ, suggesting that the integral Prandtl number provides a robust characterisation of the turbulent Prandtl number within the turbulent region of the free plume.

Chapter 6

Turbulent vertically distributed buoyant plumes

In this chapter we examine a turbulent vertically distributed plume: the flow resulting from a vertically distributed source of buoyancy. The vertically distributed buoyancy source is created by forcing relatively dense salt water solution through a porous wall. Simultaneous velocity and buoyancy field measurements on a vertical two-dimensional plane normal to the wall are performed. The flow resulting from a confined environment is then studied, both the sealed (filling-box) and ventilated case (emptying filling-box), where buoyancy measurements of the ambient environment are performed using dye attenuation.

6.1 Introduction

Flows resulting from vertically distributed buoyancy sources occur in both geophysical environments, for example the dissolution of a wall of ice dissolving into seawater (McConnochie and Kerr, 2015), and built environments, for example the downdraught resulting from a relatively cold, natural convective, flow from a glazed façade within a building in winter (Heiselberg, 1994) or, similarly, any heated vertical surface within a building, be it from a radiator or from incident solar radiation.

A natural convective flow, with increasing vertical distance, will become unstable and transition to turbulence. The turbulent boundary layer comprises of three distinct layers: a viscous sub layer, a viscous-turbulent overlap layer and an outer inertial turbulent layer (Holling and Herwig, 2005). In the above examples, in most cases, the flows will become fully turbulent due to the vertical extent and sufficiently large buoyancy flux of the source. The transition to turbulence for an isothermal wall may be characterised by the Grashof

number, Gr, defined by

$$Gr = \frac{g\beta\Delta T z^3}{\nu^2}, \tag{6.1}$$

where β is the thermal expansion coefficient, ΔT is the temperature difference between the wall and the ambient and z is the vertical distance of the wall. The transition to turbulence occurs at approximately $Gr = 10^9$ (Bejan and Lage, 1990). This suggests, for example, that the transition to turbulence of an isothermal heated wall with $\Delta T = 10\,\mathrm{K}$ would occur at approximately $z \approx 0.5\,\mathrm{m}$. Considering the typical vertical extent of internal spaces within buildings, $H \sim 10\,\mathrm{m}$, it is reasonable to assume that the majority of the height of the wall is turbulent.

The primary aim of the early studies on natural convection were to determine the velocity and temperature profiles and calculate the rate of turbulent heat transfer in both the laminar and turbulent regimes. The evolution of the heat flux q'' with height z is typically represented in terms of the Nusselt number,

$$Nu = \frac{q''z}{\rho_a c_p \kappa \Delta T}, \tag{6.2}$$

where c_p is the specific heat capacity, κ is the thermal diffusivity and ρ_a is the density of the fluid. Experimental investigations of an isothermal wall in air (e.g. Cheesewright (1968); Pirovano et al. (1970); Tsuji and Nagano (1988)) have shown that in the turbulent region of the flow

$$Nu \sim Ra^r, \tag{6.3}$$

where $Ra = GrPr$ is the Rayleigh number, Pr is the Prandtl number and $r \approx 1/3$. Given that the Prandtl number is invariant with height, substituting (6.1) and (6.2) into (6.3) suggests that the heat flux is invariant with height within the turbulent regime of an isothermally heated or cooled wall (Wells and Worster, 2008) and following Batchelor (1954) the heat flux per unit area may be characterised by the buoyancy flux per unit area

$$f = \frac{g\beta q''}{\rho c_p}. \tag{6.4}$$

An equivalence may therefore be sought between the turbulent region of an isothermal wall and a vertically distributed buoyancy source which is invariant with height.

Following the framework of Morton et al. (1956), Wells and Worster (2008) and Cooper and Hunt (2010) modelled the flow resulting from a vertically distributed buoyancy source. A uniform buoyancy flux was assumed and, similar to the wall (line) plume studied in § 5.2, an entrainment coefficient was used to parametrise the mixing of the turbulent boundary layer. This results in a strong analogy to the wall plume. Cooper and Hunt (2010) tested

the model experimentally by forcing relatively dense salt solution through a porous wall into fresh water, thus creating a distributed buoyancy source. There have since been numerous investigations of vertically distributed buoyancy sources applying the plume theory developed by Cooper and Hunt (2010). McConnochie and Kerr (2015) used an ice block adjacent to fresh water to create a vertically distributed source. An analogous DNS study was subsequently performed by Gayen et al. (2016) which showed good agreement between the predicted scalings of the bulk flow fluxes by Cooper and Hunt (2010). Caudwell et al. (2016) performed velocity and temperature measurements on a heated wall placed in water and Bonnebaigt et al. (2018) approximated a distributed buoyancy source by using discrete point sources of salt water across a vertical wall. As we discuss in detail in this chapter, the studies mentioned above have found significantly different entrainment values. Kaye and Cooper (2018) have partially explained the discrepancies between these studies by accounting for the wall shear stress not considered in Cooper and Hunt (2010) and Bonnebaigt et al. (2018). Nevertheless, given the difficulty in both creating a truly uniform distributed buoyancy source and performing accurate velocity measurements of the boundary layer it is understandable as to why there is not more agreement between the studies, especially since the studies used different methods to create and measure the distributed buoyancy source.

The original motivation of Cooper and Hunt (2010) of applying a simplified plume theory to a heated wall was to develop a numerical model for evolution of the developing stratification within a sealed or ventilated environment (i.e. the classical filling and emptying filling-box problem) based on the filling-box model of Baines and Turner (1969). Both Caudwell et al. (2016) and Bonnebaigt et al. (2018) also considered the filling-box problem and adapted the numerical method suggested by Cooper and Hunt (2010).

The aim of this chapter is to study a vertically distributed buoyancy source based on the porous wall method of Cooper and Hunt (2010). We improve on the experiments described by Cooper and Hunt (2010) and perform high resolution velocity and buoyancy measurements. The unstratified case is first considered where, in particular, we determine a value of the entrainment coefficient. We then consider both a sealed and ventilated filling-box using the method of dye attenuation to determine the evolving and steady state ambient stratification.

6.2 Theory

A vertically distributed turbulent plume is the flow driven by a vertically distributed source of buoyancy. Here we outline the theory of entrainment in vertically distributed turbulent plumes in an unstratified quiescent environment. We consider the case of both an ideal

buoyancy source, where buoyancy diffuses from the boundary with no source volume flux, and a non-ideal buoyancy source with a finite source volume flux.

We define the vertical velocity $w(x,z,t)$ in the vertical z-direction, horizontal velocity $u(x,z,t)$ in the across-plume x-direction, the deviation from hydrostatic pressure $p(x,z,t)$ and the buoyancy $b(x,z,t) = g(\rho_a - \rho(x,z,t))/\rho_a$, where ρ and ρ_a are the density of the plume and ambient, respectively and we assume that $\rho_a - \rho \ll \rho_a$. Since the flow is statistically steady, these quantities may be decomposed into time-averaged and fluctuating components $w(x,z,t) = \overline{w}(x,z) + w'(x,z,t)$, $u(x,z,t) = \overline{u}(x,z) + u'(x,z,t)$ and $b(x,z,t) = \overline{b}(x,z) + b'(x,z,t)$, and we denote the time-averaged maximum vertical velocity and buoyancy as $\overline{w}_m(z)$ and $\overline{b}_m(z)$. We assume all quantities are independent of the horizontal y direction. We define the time-averaged volume flux, momentum flux, integral buoyancy and buoyancy flux per unit length by

$$Q_p(z) = \int_0^\infty \overline{w}(x,z)\mathrm{d}x, \tag{6.5}$$

$$M(z) = \int_0^\infty \overline{w}^2(x,z)\mathrm{d}x, \tag{6.6}$$

$$B(z) = \int_0^\infty \overline{b}(x,z)\mathrm{d}x, \tag{6.7}$$

$$F(z) = \int_0^\infty \overline{w}(x,z)\overline{b}(x,z) + \overline{w'(x,z)b'(x,z)}\mathrm{d}x. \tag{6.8}$$

From these relations we define the characteristic scales for plume width R, velocity W and buoyancy b_T by

$$R = \frac{Q_p^2}{M}, \tag{6.9}$$

$$W = \frac{M}{Q_p}, \tag{6.10}$$

$$b_T = \frac{F}{Q_p}. \tag{6.11}$$

Under the Boussinesq approximation, the Reynolds time-averaged mass, vertical momentum and buoyancy conservation equations may be written

$$\frac{\partial \overline{u}}{\partial x}+\frac{\partial \overline{w}}{\partial z}=0, \tag{6.12}$$

$$\overline{u}\frac{\partial \overline{w}}{\partial x}+\overline{w}\frac{\partial \overline{w}}{\partial z}+\frac{\partial \overline{w'^2}}{\partial z}+\frac{\partial \overline{u'w'}}{\partial x}=-\frac{1}{\rho_a}\frac{\mathrm{d}\overline{p}}{\mathrm{d}z}+\overline{b}+\nu\frac{\partial^2 \overline{w}}{\partial x^2}, \tag{6.13}$$

$$\overline{u}\frac{\partial \overline{b}}{\partial x}+\overline{w}\frac{\partial \overline{b}}{\partial z}+\frac{\partial \overline{u'b'}}{\partial x}+\frac{\partial \overline{w'b'}}{\partial z}=\kappa\frac{\partial^2 \overline{b}}{\partial x^2}, \tag{6.14}$$

where ν and κ are the kinematic viscosity and mass diffusivity of the fluid, respectively. Integration of (6.12) - (6.14) gives

$$\frac{\mathrm{d}Q_p}{\mathrm{d}z}=-\left.\overline{u}\right|_0^\infty, \tag{6.15}$$

$$\frac{\mathrm{d}M}{\mathrm{d}z}+\left.\left[\overline{uw}+\overline{u'w'}\right]\right|_0^\infty=B-\frac{\mathrm{d}}{\mathrm{d}z}\left(\int_0^\infty \overline{w'^2}+\frac{1}{\rho_a}\frac{\mathrm{d}\overline{p}}{\mathrm{d}z}\mathrm{d}x\right)+\nu\left.\frac{\partial \overline{w}}{\partial x}\right|_0^\infty, \tag{6.16}$$

$$\frac{\mathrm{d}F}{\mathrm{d}z}+\left.\overline{u'b'}\right|_0^\infty=\kappa\left.\frac{\partial \overline{b}}{\partial x}\right|_0^\infty, \tag{6.17}$$

Under the entrainment assumption, the inflow velocity at any height is proportional to the local vertical plume velocity (i.e. $-\overline{u}(\infty,z)=\alpha W$) where α is the integral entrainment coefficient which is equal to the 'top-hat' entrainment constant (Morton et al., 1956), and using the boundary conditions $\overline{w}(0,z)=\overline{u}(0,z)=\overline{u'w'}(0,z)=\overline{u'b'}(0,z)=\overline{w}(\infty,z)=\overline{u'w'}(\infty,z)=\overline{u'b'}(\infty,z)=0$ and $\left.\frac{\partial b}{\partial x}\right|_0=f/\kappa$, the Boussinesq time-averaged volume, momentum and buoyancy flux conservation equations may be written as (Kaye and Cooper, 2018)

$$\frac{\mathrm{d}Q_p}{\mathrm{d}z}=\alpha\frac{M}{Q_p}+q, \tag{6.18}$$

$$\frac{\mathrm{d}M}{\mathrm{d}z}=B-\left.\nu\frac{\partial w}{\partial x}\right|_0=\frac{FQ_p}{\theta M}-C\left(\frac{M}{Q_p}\right)^2, \tag{6.19}$$

$$\frac{\mathrm{d}F}{\mathrm{d}z}=f, \tag{6.20}$$

where q is the additional wall source volume flux per unit area, θ encapsulates the relation between the integral buoyancy B and the buoyancy flux F and may be interpreted as the non-dimensional buoyancy flux, which by assuming self-similarity we may take as constant, and the wall shear stress is expressed in terms of the characteristic velocity W and a constant skin friction coefficient C (Gayen et al., 2016), and, as for the free and wall line plume

considered in § 5.2, we assume that

$$\frac{\mathrm{d}}{\mathrm{d}z}\left(\int_0^\infty \overline{w'^2} + \frac{1}{\rho_a}\frac{\mathrm{d}\overline{p}}{\mathrm{d}z}\mathrm{d}x\right) \ll \frac{\mathrm{d}M}{\mathrm{d}z}. \tag{6.21}$$

We distinguish between the total plume volume flux, Q_p, and the cumulative entrained volume flux defined by

$$Q_e(z) = \int_0^z -\overline{u}(\infty, z')dz' = Q_p - qz. \tag{6.22}$$

The solutions to the plume equations (6.18) - (6.20) for a finite volume flux through the wall and no shear stress (i.e. $q > 0$ and $C = 0$) were solved numerically by (Kaye and Cooper, 2018) and compared to the idealised case of zero volume flux through the wall, $q = 0$. The ratio of the solutions for the two cases were calculated as a function of the non-dimensional height $\zeta = zf/q^3$, which in all cases monotonically tend to 1 as $z \to \infty$. This means that for a given wall source buoyancy flux per unit area f with associated volume flux per unit area q there is a height at which the two solutions are arbitrarily close and the effect of the added volume flux may be neglected. With this in mind, it is possible to justify neglecting the added volume flux term in (6.18) and use the pure plume solutions to model the experimental data. In their analysis the shear stress was considered negligible, i.e. $C = 0$. We extend the analysis of Kaye and Cooper (2018) by numerically solving (6.18) - (6.20) for the case $q > 0$ and $C > 0$.

We first give the solutions of (6.18) - (6.20), for $q = 0$, in dimensional form (Kaye and Cooper, 2018)

$$Q_p(z) = \frac{3}{4}\left(\frac{5\theta}{4}\right)^{-1/3}\alpha^{2/3}\left(\frac{f}{1+\frac{4C}{5\alpha}}\right)^{1/3} z^{4/3}, \tag{6.23}$$

$$M(z) = \frac{3}{4}\left(\frac{5\theta}{4}\right)^{-2/3}\alpha^{1/3}\left(\frac{f}{1+\frac{4C}{5\alpha}}\right)^{2/3} z^{5/3}, \tag{6.24}$$

$$F(z) = fz. \tag{6.25}$$

From herein we assume that $\theta \approx 1$ which is justified in § 6.4.2. As an aside, using the solutions above a relationship between the characteristic plume width and the entrainment coefficient, $\mathrm{d}R/\mathrm{d}z = 3\alpha/4$, may be obtained. For $q > 0$ the vertical distance and volume, momentum and buoyancy flux may be non-dimensionalised following Kaye and Cooper

(2018) by

$$\zeta = \frac{zf}{q^3}, \qquad \gamma = \frac{Q_p f}{q^4}, \qquad \mu = \frac{Mf}{q^5}, \qquad \phi = \frac{F}{q^3}. \tag{6.26}$$

The plume equations (6.18) - (6.20) may then be expressed in non-dimensional form by

$$\frac{\mathrm{d}\gamma}{\mathrm{d}\zeta} = \alpha\frac{\mu}{\gamma} + 1, \tag{6.27}$$

$$\frac{\mathrm{d}\mu}{\mathrm{d}\zeta} = \frac{\gamma\phi}{\mu} - C\left(\frac{\mu}{\gamma}\right)^2, \tag{6.28}$$

$$\frac{\mathrm{d}\phi}{\mathrm{d}\zeta} = 1. \tag{6.29}$$

The non-dimensional equations (6.27) - (6.29) were solved numerically over the range $10^{-4} < \zeta < 10^7$ which was equivalent to the range of the experiments performed, discussed further in § 6.3.1. An entrainment value of $\alpha = 0.068$ and a shear stress coefficient of $C = 0.15$ were used, which were determined experimentally (§ 6.4). The equations were solved using the MATLAB ode15s solver for ordinary differential equations. The initial conditions were imposed following the method used by Kaye and Cooper (2018) by considering the flow near the base of the plume where the source volume flux dominates. This suggests, from (6.27), that $\gamma \approx \zeta$ for small ζ. Given also that $\phi = \zeta$, the equation for the non-dimensional momentum flux may be considered for small ζ,

$$\frac{\mathrm{d}\mu}{\mathrm{d}\zeta} = \frac{\zeta^2}{\mu} - C\left(\frac{\mu}{\zeta}\right)^2. \tag{6.30}$$

By assuming $C = 0$ for small ζ the non-dimensional plume momentum flux may be calculated to give

$$\mu = \sqrt{\frac{2}{3}}\zeta^{3/2}. \tag{6.31}$$

Solution (6.31), as well as $\gamma = \zeta$ and $\phi = \zeta$, are used as the initial conditions in the numerical integration for small ζ. Figures 6.1 (*a*) and (*b*) show the results of the numerical integrations for the volume and momentum flux of finite source volume flux and shear stress equations, respectively, compared to the ideal plume volume and momentum flux solutions. The gradients of the logarithm, with respect to the logarithm of the vertical distance, of the solutions are shown in figures 6.1 (*c*) and (*d*) and figures 6.1 (*e*) and (*f*) show the ratio of the ideal plume and finite source flux solutions. Similar to the findings of Kaye and Cooper (2018), who considered the case for $C = 0$, the solutions of the finite flux plume equations

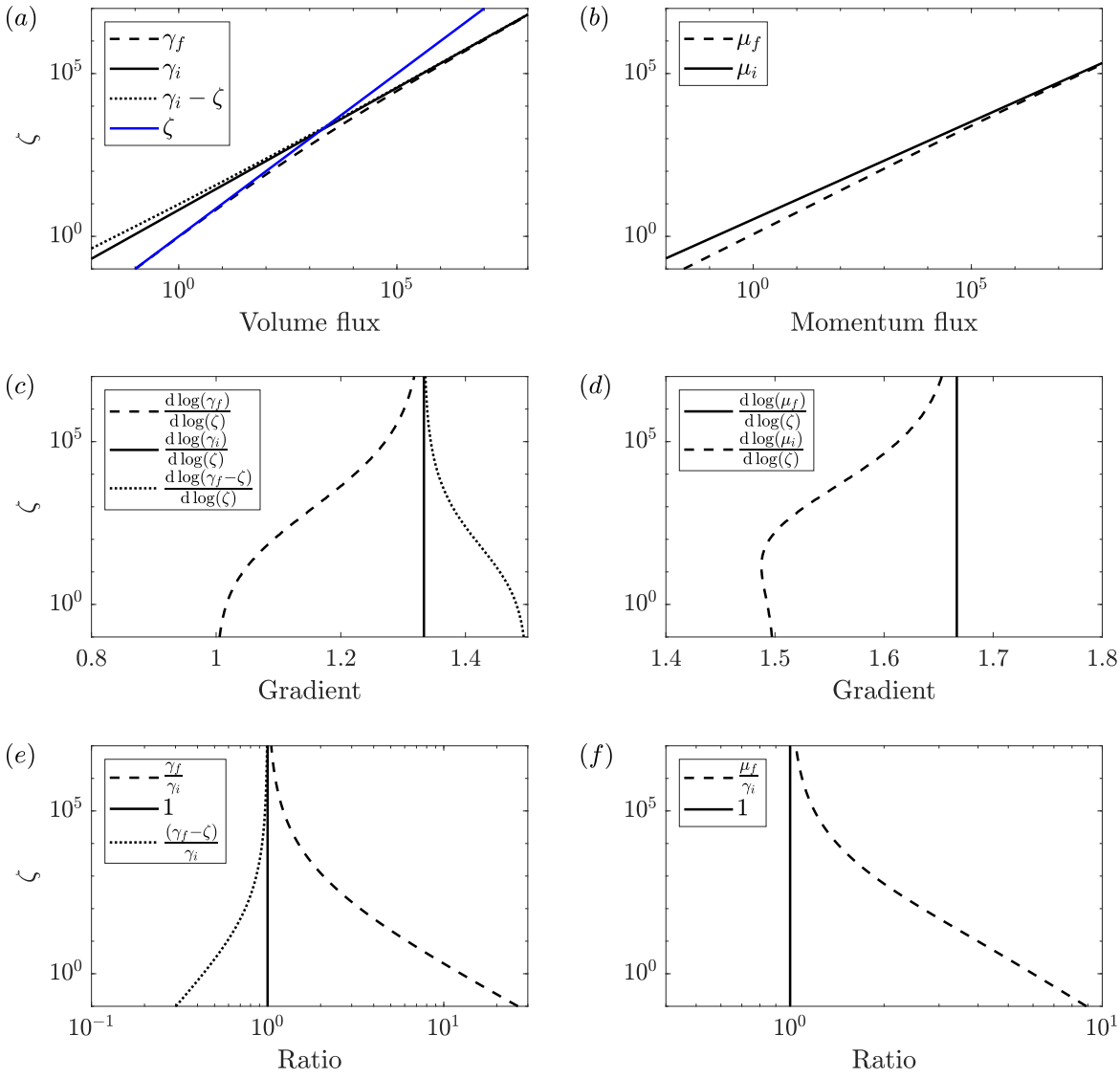

Fig. 6.1 Non-dimensional ideal (black solid) and finite flux (dashed) plume solutions of the (*a*) volume and (*b*) momentum flux. (*c, d*) Gradient of the logarithm of the solutions with respect to the logarithm of the vertical distance. Ratio of the solutions to the ideal plume solutions for the (*e*) volume and (*f*) momentum flux. The blue line in (*a*) shows the cumulative source flux in non-dimensional form and the dotted lines in (*a*), (*b*) and (*c*) show the respective properties of the cumulative source volume flux, $Q_e(z) = Q_p(z) - qz$, in non-dimensional form which may be expressed as $\gamma_f - \zeta$. An entrainment value of $\alpha = 0.068$ and a shear stress coefficient of $C = 0.15$ were used and the initial conditions are described in the text.

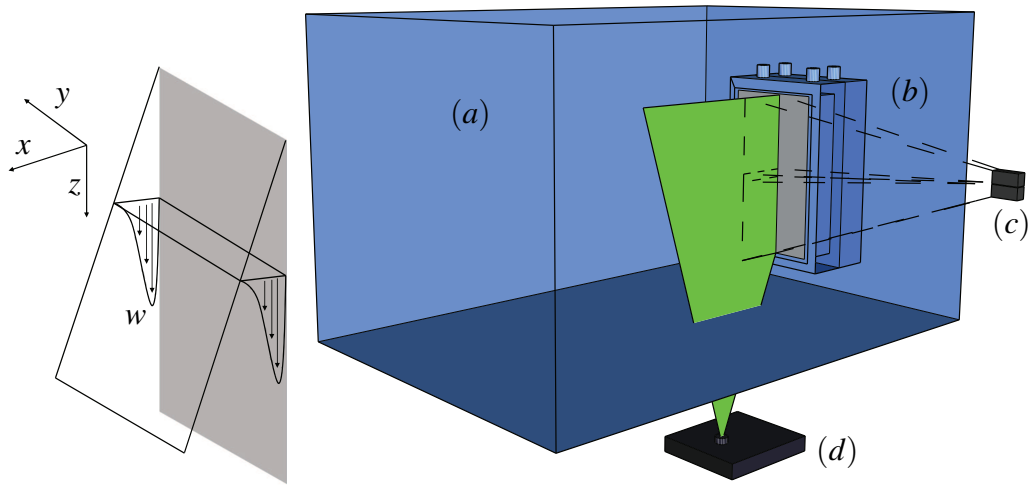

Fig. 6.2 Experimental set-up used to create and measure a vertically distributed buoyancy source. The coordinate system is shown on the left and on the right (*a*) the large reservoir, (*b*) the source chamber and porous wall structure, (*c*) the two cameras (*d*) and the laser. The camera set-up shown was used to perform PIV over the whole height of the wall. However, for the simultaneous PLIF and PIV measurements the two camera measuring-windows coincided.

approach the ideal plume solutions for increasing vertical distance. It can also be seen in figures 6.1 (*c*) and (*d*) that the gradients, with respect to vertical distance, of the finite flux plume solutions are everywhere smaller than those of the pure plume solutions. The ideal plume solution of the volume flux may be inferred more accurately from the finite flux solution, however, by considering the cumulative entrained volume flux, Q_e, which was not considered by Kaye and Cooper (2018). In non-dimensional form this may be expressed as $\gamma_f - \zeta$. This compensated volume flux is shown by the dotted curve in figures 6.1 (*a*), (*b*) and (*c*), where figure 6.1 (*c*) shows a faster convergence rate to the ideal plume solution as compared to γ_f. Given that the source volume flux does not directly contribute to the vertical momentum an equivalent correction can not be made for the momentum flux. How these results relate to our experiments is discussed in § 6.4.

6.3 Experiments and analysis

6.3.1 Experimental details

The experiments were designed to create vertically distributed buoyant plumes with a uniform buoyancy flux which could be examined by performing simultaneous measurements of the buoyancy and velocity field. The experiments were performed in a Perspex acrylic

Parameter	Definition	Exp 1	Exp 2	Exp 3	Exp 4	Exp 5	Exp 6	Exp 7	Exp 8
Wall-source volume flux	$\overline{q}\,[\times 10^{-4}\,\mathrm{m\,s^{-1}}]$	1.33	1.33	1.8	1.8	1.33	1.33	1.8	1.8
Variation in wall volume flux	$(q(H)-q(0))/\overline{q}$	0.029	0.029	0.020	0.020	0.029	0.029	0.020	0.020
Wall-source buoyancy flux	$f\,[\times 10^{-5}\,\mathrm{m^2\,s^{-3}}]$	3.7	3.7	5.0	5.0	3.7	3.7	5.0	5.0
Reynolds number	Re	-	-	-	-	659	630	668	788
Turbulent Reynolds number (z=0.37 m)	Re_λ	-	-	-	-	62	56	47	50
Kolmogorov length scale	$\eta\,[\times 10^{-4}\,\mathrm{m}]$	-	-	-	-	3.5	3.3	2.2	2.6
Batchelor length scale	$\lambda_B[\times 10^{-5}\,\mathrm{m}]$	-	-	-	-	1.6	1.5	1.0	1.2
Taylor microscale	$\lambda\,[\times 10^{-3}\,\mathrm{m}]$	-	-	-	-	5.4	4.8	3.0	3.6
PIV vector spacing	$\Delta x\,[\times 10^{-3}\,\mathrm{m}]$	1.29	1.29	1.29	1.29	0.88	0.88	0.88	0.88
PLIF pixel spacing	$\Delta x\,[\times 10^{-4}\,\mathrm{m}]$	1.08	1.08	1.08	1.08	0.74	0.74	0.74	0.74
Time separation	$\Delta t\,[\times 10^{-2}\,\mathrm{s}]$	1.0	1.0	1.0	1.0	1.0	1.0	1.0	1.0
Kolmogorov time scale	$\tau_\eta\,[\times 10^{-2}\,\mathrm{s}]$	-	-	-	-	12.3	10.7	5.0	6.9

Table 6.1 Experimental parameters and measured-length and time scales of the experiments. Since the measurements are performed over the whole height in experiments 1 - 4 the characteristic scales are not included. For experiments 5 - 8 the characteristic scales are measured at z=0.37 m, which is approximately the mid-height of the measurement window. Definitions are provided in the text.

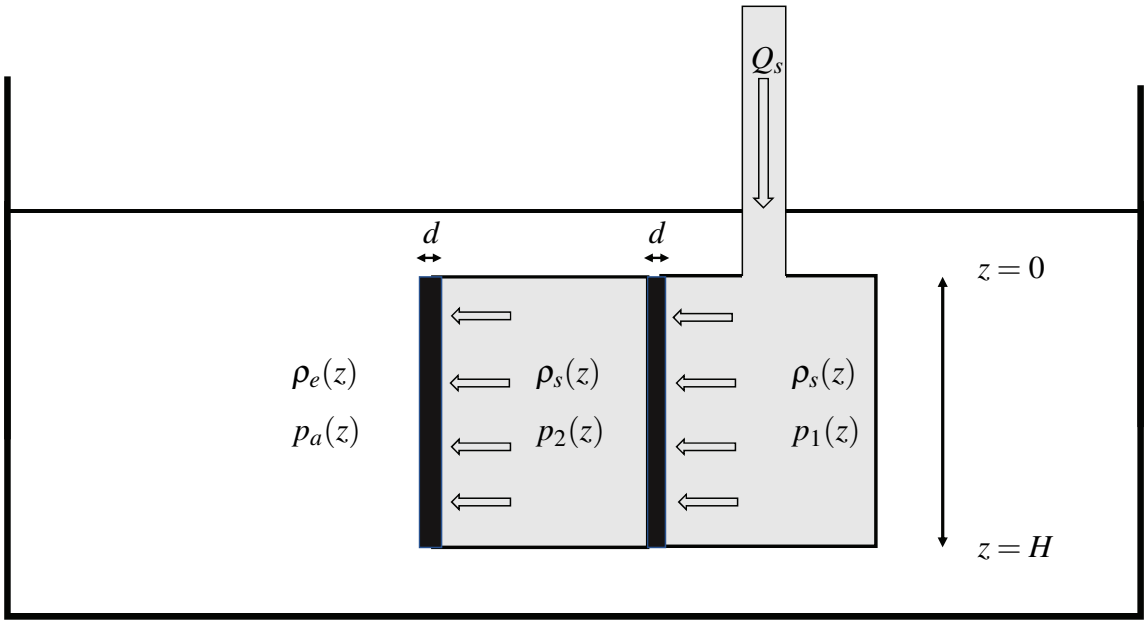

Fig. 6.3 Simplified diagram (not to scale) of the structure used to force relatively dense source fluid with a density of ρ_s through two porous plates of thickness d at a bulk flow rate per unit width of Q_s.

tank of horizontal cross-section $1.2\,\mathrm{m} \times 0.4\,\mathrm{m}$ filled with dilute saline solution of uniform density ρ_a to a depth of $0.75\,\mathrm{m}$. The buoyant wall source was created by forcing relatively dense sodium nitrate solution through two porous stainless steel plates, with a very low permeability of $P_0 = 2.20 \times 10^{-13}\,\mathrm{m}^{-2}$, of dimensions $0.48\,\mathrm{m} \times 0.23\,\mathrm{m}$ and thickness $d = 5.0\,\mathrm{mm}$, connected in series via two source chambers. The stainless steel porous plates were manufactured by SINTERTECH® and had a stainless steel alloy grade of SS 316 L. The maximum thickness of the porous plates available was $d = 5.0\,\mathrm{mm}$, so two plates were used in series to create an effective thickness of $d = 10.0\,\mathrm{mm}$, as justified below, in order to increase the uniformity of the flow. A diagram of the experimental set-up is shown in figure 6.2. In order to have a uniformly vertically distributed buoyancy source we require that the flow rate across the whole height of the porous plate is uniform. Here we consider the uniformity of the flow rate through the porous plate.

The flow through the porous plates can be characterised by Darcy's law that states that in a laminar flow, the pressure drop between the porous media is linearly proportionally to the flow rate through the porous media. The Reynolds number for the flow through the porous plates may be estimated by $Re = qd_p/\nu$, where d_p is the average pore-hole size of the plate and q is the volume flux per unit area through the plate. The pore size of the porous plate is $\sim 1.0\,\mu\mathrm{m}$ and the range of q used in the experiments are given in table 6.1. These values

suggest $Re \sim 10^{-4}$, so that Darcy's law is valid for this flow. Darcy's law may be expressed as

$$q = \frac{P_0 \Delta p}{d\eta_d}, \tag{6.32}$$

where Δp is the pressure difference either side of the porous plate and η_d is the dynamic viscosity of the source solution. A diagram of the following model is shown in figure 6.3.

The gear pump supplies fluid of density ρ_s and dynamic viscosity η_d to the first chamber which results in pressure $p_1(z)$, where

$$p_1(z) = p_1(0) + \rho_s g z, \tag{6.33}$$

and $p_1(0)$ is the pressure at the top of the chamber which is imposed via a gear pump. Similarly, the pressure in the second chamber is given by

$$p_2(z) = p_2(0) + \rho_s g z, \tag{6.34}$$

and the pressure in the ambient is given by

$$p_a(z) = p_a(0) + g \int_0^z \rho_e(z) \mathrm{d}z, \tag{6.35}$$

where we assume the ambient density $\rho_e(z)$ is height dependent for the general case of say a stratified experiment. Applying Darcy's law (6.32) to the first porous plate gives

$$q_1(z) = \frac{P_0(p_1 - p_2)}{\mathrm{d}\eta_d}, \tag{6.36}$$

where $q_1(z)$ is the volume flux per unit area through the first porous plate. Similarly, for the second porous plate

$$q_2(z) = \frac{P_0(p_2 - p_a)}{\mathrm{d}\eta_d}, \tag{6.37}$$

where $q_2(z)$ is the volume flux per unit area through the second porous plate. Assuming that $q(z) = q_1(z) = q_2(z)$ and substituting in equations (6.33) and (6.34) results in

$$q(z) = \frac{P_0}{2d\eta_d} \left(p_0 + g\rho_s z - g \int_0^z \rho_e(z) \mathrm{d}z \right), \tag{6.38}$$

where $p_0 = p_1(0) - p_a(0)$. The difference in the volume flux per unit area between the top and bottom of the porous plate, relative to the mean flow rate, is given by

$$\frac{q(H) - q(0)}{\overline{q}} = \frac{P_0 g}{2\overline{q}\mathrm{d}\eta_d}\left(\rho_s H - \int_0^H \rho_e(z)\mathrm{d}z\right). \tag{6.39}$$

where $\overline{q} = Q_s/H$. The maximum difference in flow rate may be evaluated by considering the case $\rho_e(z) = \rho_a$, i.e. where the ambient is unstratified. In practice a chosen volume flux Q_s, as opposed to a chosen pressure, is imposed through the porous plate. The maximum difference in flow rate can therefore be written in terms of the initial density difference and the mean flow rate

$$\frac{q(H) - q(0)}{\overline{q}} = \frac{P_0 g H\,(\rho_s - \rho_a)}{2\overline{q}\mathrm{d}\eta_d}. \tag{6.40}$$

These values are shown in table 6.1, which show that there is at most a 1.5% variation in the source volume flux per unit area, relative to the mean source volume flux per unit area. We therefore make the approximation that the volume flux per unit area is uniform and equal to the mean volume flux per unit area which we refer to from herein by q. Note that (6.40) shows that two porous plates, of equal thickness d, in series is equivalent to one plate with thickness $2d$.

The source fluid, at a relative buoyancy of b_s, was supplied by a gear pump which resulted in a mean buoyancy flux per unit area $f = qb_s$. Cooper and Hunt (2010) used a similar experimental set-up to study vertically distributed buoyant plumes. However, as highlighted in their study, the relatively high porosity of the wall led to a non-uniform buoyancy flux. This problem is significantly reduced in the set-up used here.

Results given in § 6.2 may be used to determine how the added mass from the wall source modify the theoretical flow from the ideal solutions of zero mass flux. From table 6.1 the non-dimensional maximum vertical distance of the experiment may be calculated to give $\zeta = 8.4 \times 10^6$ for experiments 1, 2, 5 and 6 and $\zeta = 3.1 \times 10^6$ for experiments 3, 4, 7 and 8. The results from figure 6.1 suggest that volume and momentum flux of the finite flux plume are within 10% of the ideal plume solutions for the upper half of the vertical extent of the experiment. This theory assumes that the buoyancy flux is uniform across the full height of the wall. This is true in the current experiment to within 1.5%, i.e. the variation in the buoyancy flux is equal to the variation in volume flux given that the source buoyancy was constant. However, the theory also assumes that the plume is turbulent over the whole height, which is effectively modelled by a constant entrainment coefficient. This assumption is clearly not valid in the laminar region of the plume which accounts for approximately 15% of the total height, consistent with the observation of Cooper and Hunt (2010). Further, as noted by Kaye and Cooper (2018), it is not possible to define a virtual origin elsewhere

to the physical origin. In order to identify the laminar region, determine the effect of the laminar region on the flow and in particular identify the region which follows the scalings predicted by Cooper and Hunt (2010) we first performed velocity measurements over the whole height of the porous wall. Two cameras were recorded simultaneously, one for the region $z = 0\,\mathrm{m}$ to $z = 0.24\,\mathrm{m}$ and another for the region $z = 0.24\,\mathrm{m}$ to $z = 0.48\,\mathrm{m}$.

Given the results of the velocity measurements over the total height, a further set of simultaneous velocity and buoyancy field measurements were performed within the region $z = 0.30\,\mathrm{m}$ to $z = 0.42\,\mathrm{m}$ which was sufficiently far from the source so that the plumes can be considered turbulent and self-similar. Further, the flow is shown to be consistent with both the ideal plume solutions (6.18) - (6.20) and previous experimental and numerical investigations of turbulent vertically distributed buoyancy sources, including those with zero added source mass flux.

The experimental technique and set-up used to measure and process the velocity (using PIV) and buoyancy field (using PLIF) is identical to that described in § 5.3.1, so is not repeated here. The restriction of planar measurements does not present a significant limit to our analysis in this chapter, because the focus is on the time-averaged velocity and buoyancy measurements, that are statistically independent of the span wise direction, and not instantaneous statistics based on, for example, the plume TNTI as for chapters 4 and 5. Videos were recorded and processed at a frame rate of 100 Hz. A total of eight plumes were studied, the velocity field of four plumes over the whole height of the wall and four simultaneous measurements in the self-similar region. The experimental source parameters are given in table 6.1.

6.4 Results

6.4.1 Velocity measurements over the full height

Figure 6.4 shows an instantaneous buoyancy field taken from one of the experiments. The image shows the typical width of the turbulent plume in the experiments of approximately 20 mm. In order to increase the precision of the velocity measurements it was necessary to focus on a smaller region. In order to identify the optimal region to focus on, where the plume has fully developed and may be considered pure, we first present results of the experiments examining the whole height of the vertically distributed plume.

The height at which the flow transitions to turbulence may be determined by examining the Reynolds stress. Figures 6.5 (*a*) - (*d*) show the Reynolds stress for the four experiments and figure 6.5 (*e*) shows the maximum Reynolds stress as a function of height for the region

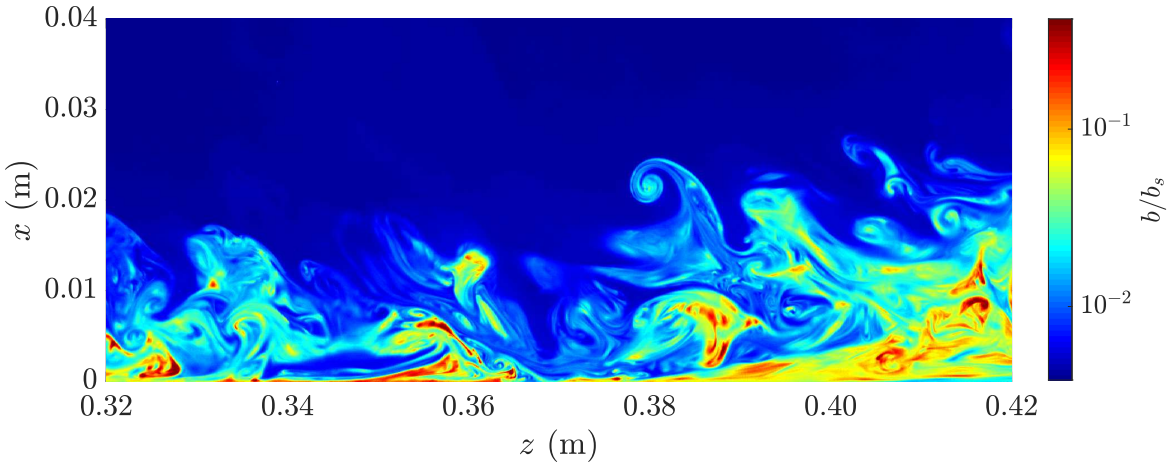

Fig. 6.4 An instantaneous buoyancy field of the turbulent plume resulting from the vertically distributed buoyancy source. The figure is rotated for clarity.

$z \leq 0.16$ m. The data suggest that the transition to turbulence occurs at approximately 0.08 m. Figure 6.6 (*a*) shows the Richardson number, defined by $Ri = fzQ_p^3/M^3$, as a function of the distance from the base of the source $z = 0$ m for the four experiments performed. The Richardson number decreases from a relatively large value and tends to a constant value of $Ri \approx 0.29$. A high Richardson number is expected in the laminar region given that the buoyancy flux is being forced through the plate at very low momentum, i.e. there will be an excess buoyancy force relative to the momentum. As the flow transitions to turbulence the Richardson number decreases. The figure suggests that the Richardson number reaches a statistically steady value at $z \approx 0.25$ m suggesting that the plume is fully developed for $z > 0.25$ m. Figure 6.6 (*b*) shows the volume flux of the four experiments. As discussed in § 6.2, the cumulative entrained flux, that is $Q_e = Q - qz$, provides are more robust analogy of the ideal plume volume flux. For this reason, we present and compare Q_e to the theoretically derived results of an ideal source. Unless otherwise stated, we refer to the volume flux as this cumulative entrained flux, however, to avoid confusion we maintain the notation Q_e. The compensated plot of the volume flux, where the volume flux is scaled on the predicted scaling of $z^{4/3}$, is shown in figure 6.6 (*c*). Figure 6.6 (*d*) shows the gradient of the logarithm of the volume flux. The average value, for a given height, across all of the experiments is shown by the black curve. The standard deviation $\sigma(z)$ across all four experiments was calculated and the height-averaged value is defined by $\overline{\sigma}$. The horizontal dashed and dot-dashed lines show the predicted scaling value of $4/3$ and $4/3 \pm \overline{\sigma}$, respectively. Higher resolution simultaneous buoyancy and velocity measurements were performed within the region for which the mean value of the data lies within the range $4/3 \pm \overline{\sigma}$. This region

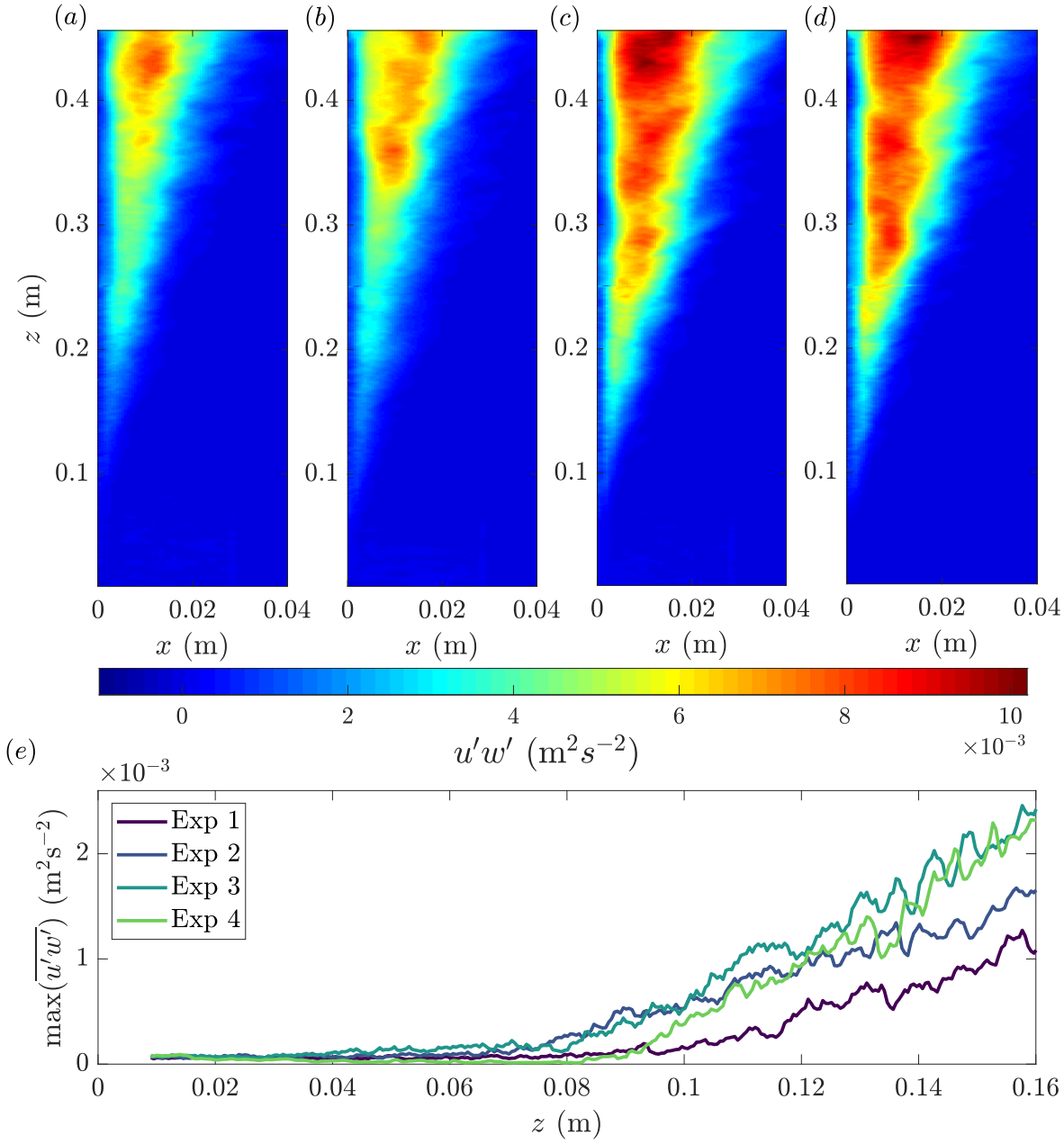

Fig. 6.5 (*a*) - (*d*) Time-averaged Reynolds stress for experiments 1 - 4, respectively and (*e*) the maximum time-averaged Reynolds stress, for a given height, highlighting the transition to turbulence in the flow. Note that in figures (*a*) - (*d*) the horizontal coordinate is scaled, relative to the vertical coordinate, in order to aid clarity.

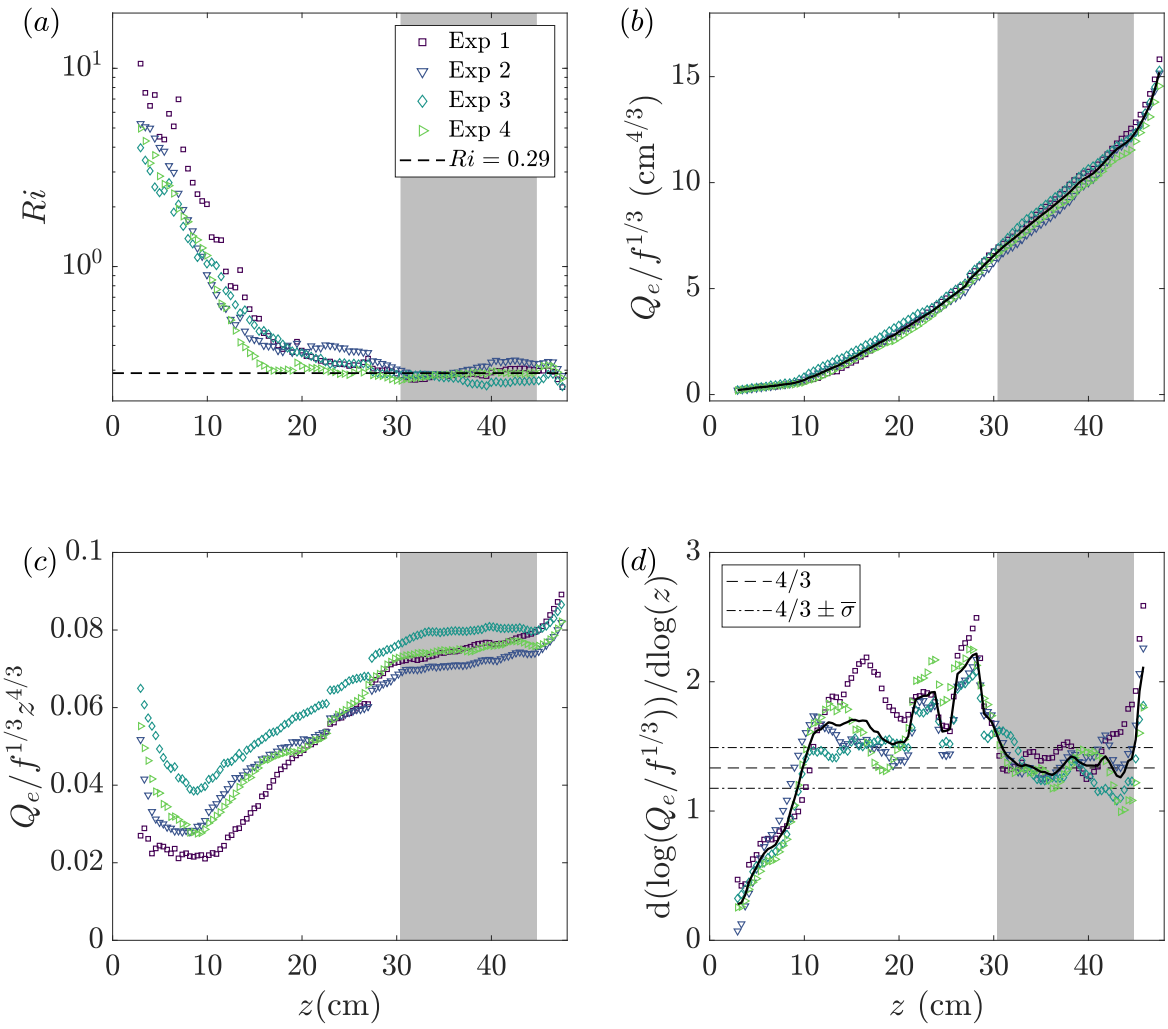

Fig. 6.6 (*a*) Richardson number, (*b*) volume flux, (*c*) compensated plot of the volume flux and (*d*) the gradient of the logarithm of the volume flux of the vertically distributed buoyant plume for experiments 1 - 4. The scaling $Q \sim z^{4/3}$, predicted by Cooper and Hunt (2010), is shown in (*c*). The grey highlighted region in all four plots indicate the region where the Richardson number has reached a statistically steady state and where the volume flux follows the predicted scaling, determined from the region where the mean gradient of the logarithm of the volume flux (black curve) is within one space-averaged standard deviation, $\overline{\sigma}$, of $\mathrm{d}\left(\log Q_e/f^{1/3}\right)/\mathrm{d}z = 4/3$, where $\sigma(z)$ is the standard deviation of all four experiments measured at a given distance. This region was identified in order to examine the plume at higher resolution with simultaneous velocity and buoyancy measurements. The average volume flux across the experiments is shown by the black curve in (*b*). The mean value of the Richardson number within this region of $Ri = 0.29$ is shown by the horizontal dashed line in (*a*).

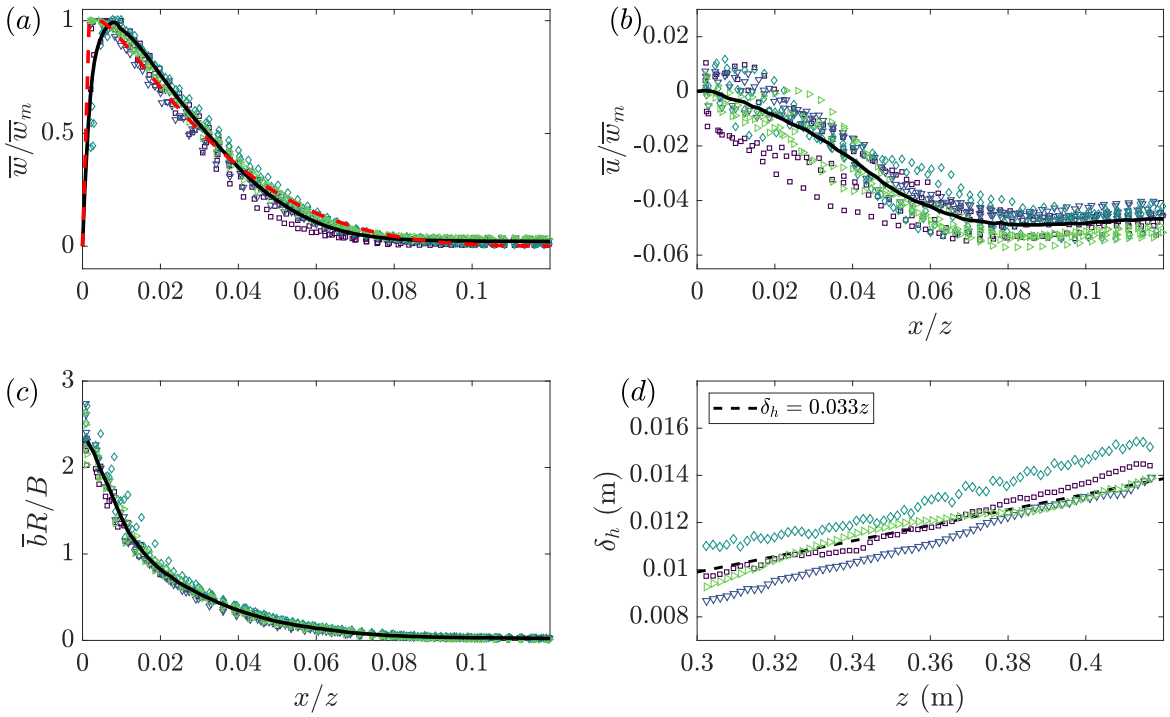

Fig. 6.7 Time-averaged scaled (a) vertical and (b) horizontal velocity and (c) buoyancy profiles of the vertically distributed turbulent plume for heights $z = 0.302$, 0.331, 0.360, 0.389 and 0.418 m from each of the four simultaneous experiments. The average values (black curve) of all of the data are shown in each case. The profile of best fit from the velocity data of Vliet and Liu (1969), which agrees well with the data of Cheesewright (1968), is shown by the dashed red curve. Vliet and Liu (1969) scaled the horizontal distance by the displacement thickness defined by $\delta_h = \int_0^\infty \overline{w}/\overline{w}_m \mathrm{d}x$. A least-squares linear fit between the displacement thickness and the vertical distance was found in (d) to rescale the data of Vliet and Liu (1969) by the vertical distance.

is highlighted in grey in all four plots. The porous wall was suspended above the base of the ambient tank. The effect of this on the flow can be see in the region $z > 0.44$ m in figure 6.6 (c), where the scaling deviates from the predicted value. We therefore choose to perform further higher resolution simultaneous velocity and buoyancy measurements within the region $0.30\,\mathrm{m} < z < 0.42\,\mathrm{m}$. The next section presents the results within this region.

6.4.2 Velocity and buoyancy measurements

In this section we present the high-resolution simultaneous velocity and buoyancy measurements of the vertically distributed source within the developed region of $0.30\,\mathrm{m} < z < 0.42\,\mathrm{m}$.

Figure 6.7 shows the scaled vertical and horizontal velocities and buoyancy profiles for heights $z = 0.302, 0.331, 0.360, 0.389$ and 0.418 m from each of the four simultaneous experiments. A good collapse of the data on to a single curve is seen in each plot. The average values of the vertical velocity and buoyancy of all the experiments are shown by the black curves and the vertical velocity data are compared to the profile of best fit to the previous data of Vliet and Liu (1969), shown by the dashed red curve. Note that Vliet and Liu (1969) non-dimensionalise the cross stream distance by the displacement thickness defined by $\delta_h = \int_0^\infty \overline{w}/\overline{w}_m \mathrm{d}x$. We have rescaled the data by identifying a linear relationship between the displacement thickness and vertical distance shown in figure 6.7 (*d*). Our vertical velocity data show good agreement with that of Vliet and Liu (1969). Note that only the function of the average temperature data is presented in Vliet and Liu (1969), therefore the corresponding buoyancy profile will vary according to the experimental parameters, so it is not compared to our buoyancy data. The time-averaged volume and momentum fluxes for each experiment are shown in figure 6.8 where the fluxes are compensated by their predicted scalings. The averages of the data across the experiments are shown by the dashed line in each case. Good agreement between the data and the predicted scalings of (6.23) - (6.25) are observed in both cases. Also shown in figure 6.8 (*c*) are the compensated buoyancy integral data. Equation (6.19) suggests that $B = c_B z^{2/3}$ for some constant prefactor c_B. Gayen et al. (2016) also observe the scalings found above for the volume and momentum fluxes, however, they identify modified scaling prefactors to those predicted by (Cooper and Hunt, 2010). Instead, they observed that $Q = c_Q f^{1/3} z^{4/3}$ and $M = c_M f^{2/3} z^{5/3}$, where $c_Q = 0.076$ and $c_M = 0.13$. Our results in figure 6.8 show reasonable agreement with Gayen et al. (2016), with $c_Q = 0.069 \pm 0.006$ and $c_M = 0.105 \pm 0.020$. In addition we find that $c_B = 0.53 \pm 0.07$.

In the region being examined, the entrainment flux $\mathrm{d}Q_e/\mathrm{d}z$ is much larger than the source volume flux q. In particular, $q/(\mathrm{d}Q_e/\mathrm{d}z) < 0.07$ for $z > 0.30$ m for all the experiments. Further, $q/(\mathrm{d}Q_e/\mathrm{d}z)$ varies by at most 10% in a given experiment, so it is not expected that the change in this ratio significantly affects the plume dynamics over the range of heights we are considering.

The mean wall drag coefficient, based on the top-hat vertical velocity, may be estimated using (6.19) and the above results to find that $C \approx 0.15$. This value is lower than the value $C \approx 0.18$ obtained by Gayen et al. (2016). However, as they note, the values are likely to differ in experiments where there is a wall source mass flux, such as Cooper and Hunt (2010) and the present experimental set-up, as compared to only buoyancy diffusing from the boundary, such as that of McConnochie and Kerr (2015) and Gayen et al. (2016). The drag coefficient is an order of magnitude greater than the wall plume drag coefficient,

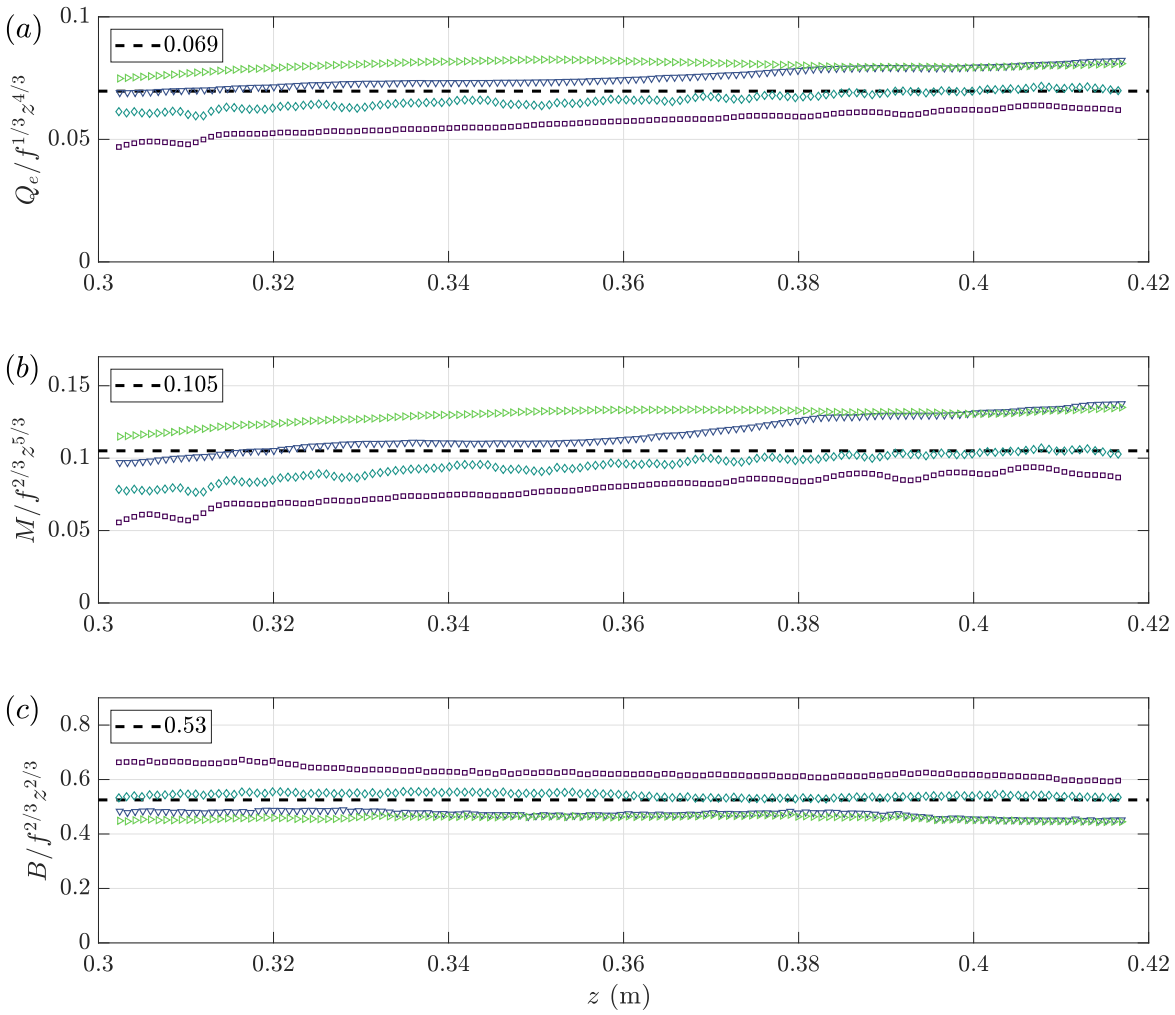

Fig. 6.8 Compensated plots of time-averaged (*a*) volume flux, (*b*) momentum flux and (*c*) buoyancy integral as functions of height. The height averaged data, and averaged across the experiments, are shown in each case by the dashed line, with the value shown in the legend.

$C \approx 0.015$, measured in § 5.5.3. An explanation for the significant difference in the drag coefficient is discussed in § 6.4.4.

The entrainment coefficient may be estimated by using the relation $3\alpha/4 = \mathrm{d}R/\mathrm{d}z$, which may be derived from the solutions (6.23) - (6.24). Using the values determined above gives

$$\alpha = \frac{4}{3}\frac{\mathrm{d}}{\mathrm{d}z}\left(\frac{Q_e^2}{M}\right) = 0.061 \pm 0.009. \tag{6.41}$$

The entrainment coefficient should, however, be thought of as the ratio of the entrainment flux to the mean velocity. In which case, the corrected volume flux (i.e. Q_e) should not be used in the calculation of the mean velocity. The entrainment coefficient may be calculated more robustly by considering

$$\frac{Q_p}{M}\frac{\mathrm{d}Q_e}{\mathrm{d}z} = \frac{Q_p}{M}\overline{u}_\infty = 0.068 \pm 0.006. \tag{6.42}$$

The data $\overline{u}_\infty$ as a function of height for each experiment are plotted in figure 6.9. As expected, the value of α calculated from (6.42) is larger than that of (6.41), however, the two values agree reasonably well. Our calculated entrainment value falls within the range of previously reported entrainment values, which are calculated using velocity measurements, of $\alpha = 0.056$ by Gayen et al. (2016), $\alpha = 0.048 \pm 0.006$ by McConnochie and Kerr (2015) and $\alpha = 0.08$ by Caudwell et al. (2016).

The ideal plume solutions (6.23) - (6.25) implicitly assume that $\theta \approx 1$, where we recall that θ is the, assumed, constant

$$\theta = \frac{FQ_p}{BM}, \tag{6.43}$$

that encapsulates the relation between the integral buoyancy B and the buoyancy flux F. Figure 6.10 shows the value of θ for the full height of the measurement window for all four experiments. An average value, across all the experiments, of $\theta = 1.19$ was found. We may therefore assume that any analysis involving the volume flux solution is not significantly affected by ignoring the θ term in (6.23), since the solution is modified by a factor of only $\theta^{1/3} = 1.06$.

6.4.3 Turbulent fluctuations

Figure 6.11 presents the normalised root mean square (rms), denoted by *rms*, velocity and buoyancy profiles, Reynolds stress and the horizontal and vertical buoyancy fluxes for heights $z = 0.302$, 0.331, 0.360, 0.389 and 0.418 m from each of the four simultaneous experiments. The black curves show the average across all experiments. The only available

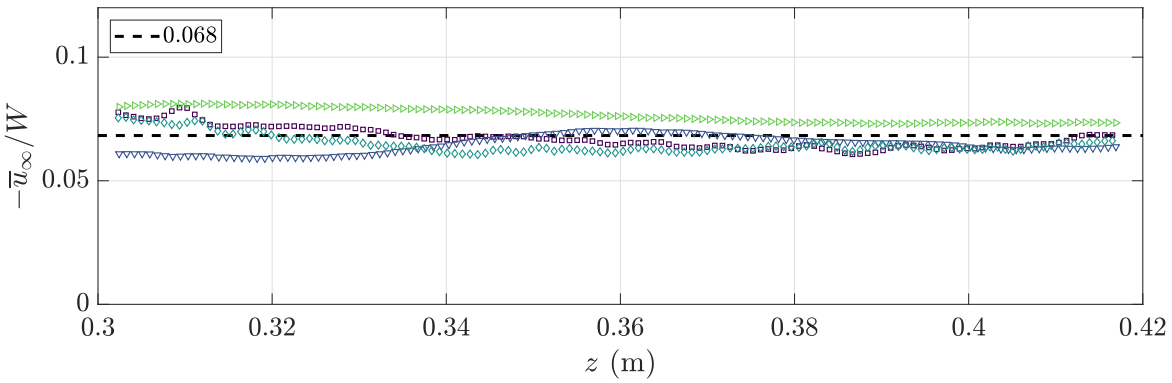

Fig. 6.9 Entrainment coefficient measured directly from the far field horizontal velocities, $\overline{u}_\infty$, and the mean top-hat velocity, W. The mean far field horizontal velocity, for a given height, was calculated by averaging, in the horizontal direction, the horizontal velocities between $x_1 = 36\,\text{mm}$ and $x_2 = 48\,\text{mm}$, so that $\overline{u}_\infty(z) = \int_{x_1}^{x_2} \overline{u}(x,z)\mathrm{d}x$.

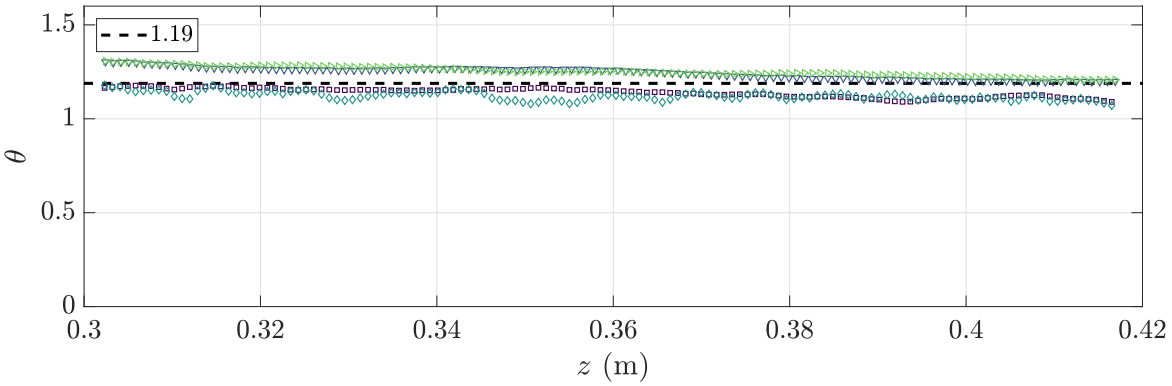

Fig. 6.10 Measurements of $\theta = FQ_p/BM$ from the four experiments. The average value across all heights and experiments is $\theta = 1.19$ shown by the dashed line.

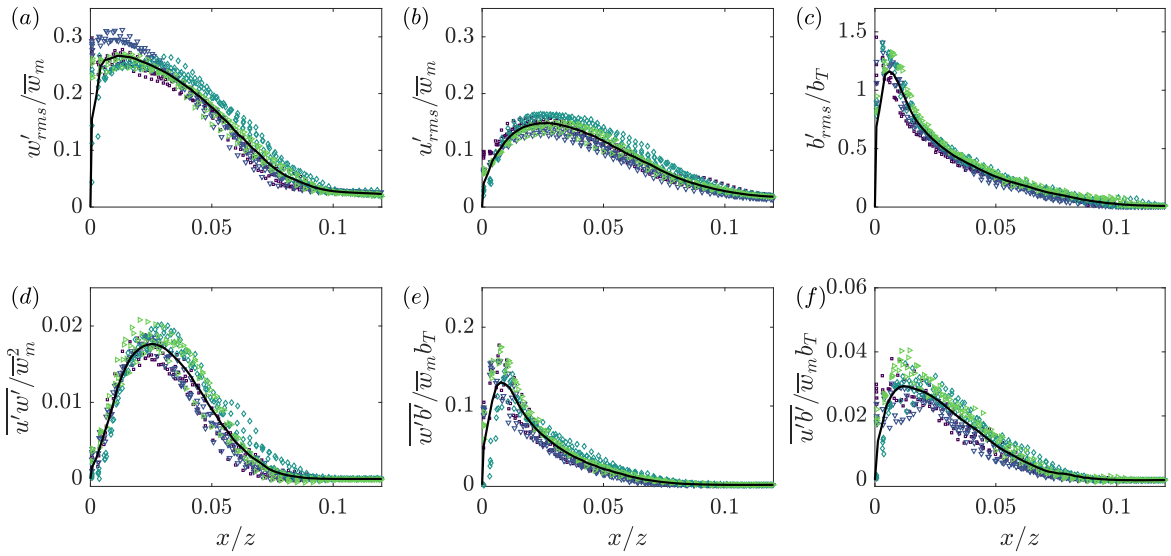

Fig. 6.11 Time-averaged scaled turbulent fluctuations of (*a*) vertical velocity, (*b*) horizontal velocity and (*c*) buoyancy, (*d*) Reynolds stress and (*e*) vertical and (*f*) horizontal turbulent buoyancy flux for heights $z = 0.302$, 0.331, 0.360, 0.389 and 0.418 m from each of the four simultaneous experiments. The black curves are the averages of the data.

data to compare to previous studies are the rms of the vertical velocities of Vliet and Liu (1969). Although their data is relatively scattered, a peak value of approximately 0.25 is observed, in good agreement with a peak value of about 0.27 observed in our measurements.

6.4.4 Comparison with wall line plume

Here we compare the vertically distributed buoyant plume to its equivalent-geometry conserved buoyancy flux counterparts, that is the free and wall (line) plume studied in § 5. As highlighted by Kaye and Cooper (2018), *'plumes generated by vertically distributed sources of buoyancy have been observed to have substantially lower entrainment coefficients than their equivalent-geometry constant buoyancy flux plumes'*. Kaye and Cooper (2018), however, primarily refer to the free plume as the equivalent-geometry plume to the vertically distributed plume and discuss reasons for the reduced entrainment between these two flows, including the shear stress and the suppression of eddy meandering. Our findings support their observation that the vertically distributed plume has a significantly lower entrainment coefficient, $\alpha = 0.068 \pm 0.006$, than the free plume, $\alpha_f = 0.135 \pm 0.010$, however, we find only a small reduction compared to the wall plume, $\alpha_w = 0.076 \pm 0.006$. The relative difference between these values is noticeably smaller than previous findings, $\alpha = \{0.014, 0.08\}$

(Bonnebaigt et al., 2018; Caudwell et al., 2016; Cooper and Hunt, 2010; Gayen et al., 2016; McConnochie and Kerr, 2015) and $\alpha_w = 0.1$ (Bonnebaigt et al., 2018), which merited such an in depth discussion by Kaye and Cooper (2018). Comparing these values suggests that the reduction in the entrainment value in the vertically distributed plume is primarily a result of the presence of the wall rather than a consequence of the vertically distributed buoyancy source. However, the slightly lower value, compared to the wall line plume, suggests that the nature of the vertically distributed buoyancy also contributes to reducing the value. A discussion about the reduction in entrainment due to the presence of the wall would for the most part follow the discussion in § 5.5, we therefore choose to only compare the vertically distributed plume and the wall line plume.

Figure 6.12 compares the velocity, buoyancy and the Reynolds stress of two flows. The wall plume data have been scaled using the source buoyancy flux, that is $F = F_0$. Further, the vertical distance includes a virtual origin correction. Figure 6.12 (*a*) shows larger peak velocities in the wall plume, for a given buoyancy flux. However, figure 6.12 (*b*) shows significantly larger peak buoyancy in the vertically distributed plume. This is opposite to the observation of larger peak velocities *and* buoyancy in the wall plume, relative to the free plume (figure 5.22), which suggested the larger velocities were a result of additional buoyancy forcing. This implies, therefore, that the buoyancy is less able to be effectively mixed in the vertically distributed plume, as the lower peak Reynolds stress values in figure (*c*) suggest, so that the constrained buoyancy leads to a peak velocity very close to the wall, as can be seen figure 6.12 (*a*), which leads to a large shear stress. A peak velocity very close to the wall has also been observed in Gayen et al. (2016) which they argue leads to large momentum drag. This is reflected in the value of the shear stress coefficient found of $C = 0.15$, equivalent to 65% of the buoyancy force which was also observed in Gayen et al. (2016), compared to $C = 0.015$ in the wall plume, which is equivalent to 15% of the buoyancy force.

6.5 Application to a confined space

6.5.1 Sealed confined space

When a vertically distributed buoyancy source is placed within a confined environment the (negatively) buoyant plume reaches the (bottom) top surface and spreads across it creating a layer of buoyant fluid and a density interface between the buoyant and ambient fluid (Baines and Turner, 1969) (see diagram in figure 6.13). This is the 'filling-box' which establishes a stable stratification in the space. As time evolves, buoyant fluid continues to accumulate

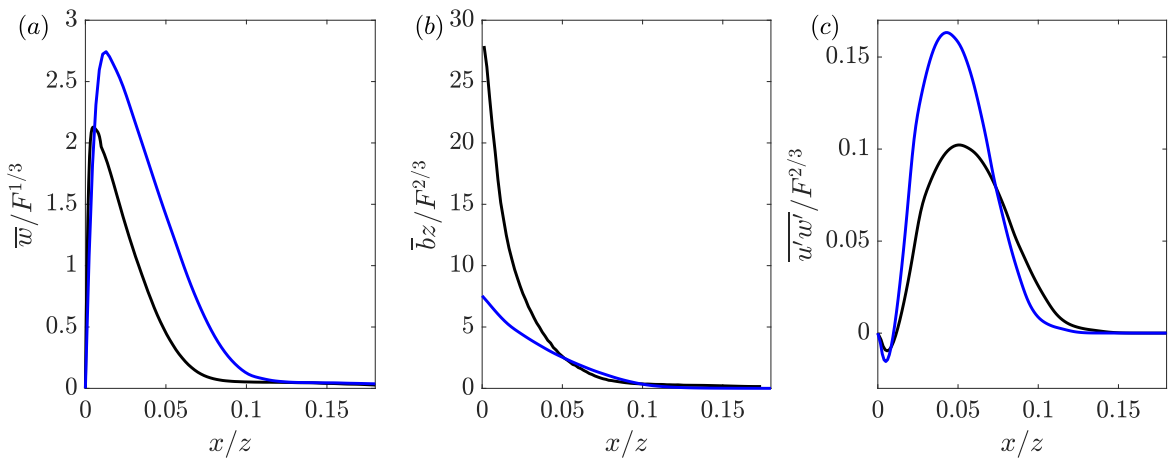

Fig. 6.12 Comparison of the average profiles of the time-averaged scaled (*a*) vertical velocity, (*b*) buoyancy and (*c*) Reynolds stress from the vertically distributed plume (black) and the wall line plume (blue) using data from § 5. In the case of the wall line plume, the vertical distance has been corrected using a virtual origin and the source buoyancy flux is used, i.e. $F = F_0$ from § 5.

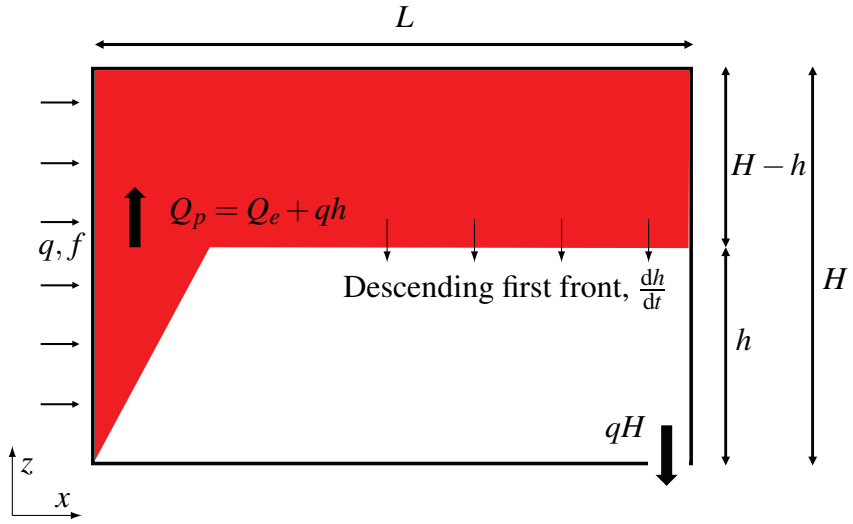

Fig. 6.13 Schematic of the sealed vertically distributed buoyant plume with a finite source volume flux, where the box is connected to the exterior environment by an open vent at the bottom of the box. The rate of descent of the first front must balance the plume volume flux entering the stratified region and the additional source volume flux within the stratified region (i.e. $\mathrm{d}h/\mathrm{d}t = -(Q_p + q(H-h))L^{-1}$) where we assume that the plume width is much smaller than L.

and the position of the density interface moves vertically downwards (upwards) at a rate determined by the volume flux of the plume at the height of the interface. We will refer to this falling interface as the first front. The position of the first front with time of a filling-box was first determined by Baines and Turner (1969) for the case of a turbulent axisymmetric plume filling a sealed box. This theory was later adapted to a vertically distributed turbulent plume filling a box by Cooper and Hunt (2010). This analysis was extended to account for the additional source volume flux, such as the current experimental method, in Kaye and Cooper (2018), where they determined the height $h(t)$ of the first front from

$$\frac{\mathrm{d}h}{\mathrm{d}t} = -\frac{1}{L}(Q_p + q(H-h)) = -\frac{1}{L}(Q_e + qH), \tag{6.44}$$

where H is the total height of the wall and L is the y-horizontal length of the box. By assuming that the volume flux follows the solution (6.23) and ignoring the source volume flux (i.e. setting $q = 0$) (6.44) may be solved to give

$$\frac{h(t)}{H} = \left(1 + \frac{1}{4}\left(\frac{4}{5}\right)^{1/3}\left(\frac{f}{1+\frac{4C}{5\alpha}}\right)^{1/3}\alpha^{-2/3}L^{-1}H^{1/3}t\right)^{-3}, \tag{6.45}$$

and the entrainment coefficient may be determined by experimentally tracking the first front $h(t)$. This method was used by Cooper and Hunt (2010) and Bonnebaigt et al. (2018) to find entrainment values of $\alpha = 0.02$ and $\alpha = 0.018$, respectively, where the shear stress was ignored, i.e. $C = 0$. Kaye and Cooper (2018) give a detailed review of these experiments and suggest reasons why this method may give significantly reduced entrainment values, including the neglect of the shear stress in the model. A further possible explanation for the lower entrainment values is that the volume flux of the plume, effectively being inferred from the rate of change of the first front, is turbulent but not fully developed at the heights being measured since, as we have seen, it takes a relatively long distance before the plume fully develops. McConnochie and Kerr (2015) also use the volume flux determined from the filling-box method, accounting for wall shear stress, in order to determine an entrainment value of $\alpha = 0.048$. This value is closer to our observed value.

Due to the accumulation of buoyant fluid within the ambient, the equations for the unstratified case, (6.18) - (6.20), are modified to include a stratified ambient environment where the buoyancy of the ambient is defined by $b_e = g(\rho_a - \rho_e)/\rho_a$, where $\rho_e = \rho_e(z,t)$ is the density of the ambient and $\rho_a = \rho_e(z,0)$ is the initial ambient density which is unstratified. The buoyancy of the plume fluid is now defined relative to the varying ambient density, $b = g(\rho_e - \rho)/\rho_a$, with the initial ambient density ρ_a as a reference density.

The plume conservation equations are modified as

$$\frac{\mathrm{d}Q_p}{\mathrm{d}z} = \alpha\frac{M}{Q_p} + q, \tag{6.46}$$

$$\frac{\mathrm{d}M}{\mathrm{d}z} = \frac{FQ_p}{\theta M} - C\left(\frac{M}{Q_p}\right)^2, \tag{6.47}$$

$$\frac{\mathrm{d}F}{\mathrm{d}z} = -Q_p\frac{\partial b_e}{\partial z} + f = -Q_pN_e^2 + f, \tag{6.48}$$

where $N_e^2 \equiv \partial b_e/\partial z$ is the buoyancy frequency of the ambient.

Further adapting the work of Baines and Turner (1969), Cooper and Hunt (2010) developed a numerical filling-box model of the evolving stratification of the ambient. The ambient stratification was assumed to develop such that the vertically distributed plume continually lays down a thin layer of fluid, of buoyancy $fH/Q_p(H)$, at the top $z = H$ of the confined box. Diffusion was ignored and it was assumed that the time scale of the plume to fill the box was much greater than the time scale of the plume to rise through the box, i.e.

$$\frac{HL}{Q_p(H)}\frac{W(H)}{H} = \frac{4L}{3\alpha H} \gg 1. \tag{6.49}$$

Consequently, the ambient buoyancy evolves according to the advection equation

$$\frac{\partial b_e}{\partial t} = \frac{Q_p}{L}\frac{\partial b_e}{\partial z}. \tag{6.50}$$

Although Cooper and Hunt (2010) observed qualitative agreement between experiments and the numerical predictions outlined above they did not find quantitative agreement. In particular, the step-change in buoyancy predicted at the first front in the numerical model was not observed in experiments. Stratification profiles of the filling-box problem have also been measured in McConnochie and Kerr (2015), Caudwell et al. (2016) and Bonnebaigt et al. (2018). Caudwell et al. (2016) also found the numerical model of Cooper and Hunt (2010) was largely unsuccessful in predicting the quantitative profiles, even if an adaptive entrainment coefficient is used in the model. Bonnebaigt et al. (2018), however, was able to effectively model the stratification by assuming a peeling model, originally developed by Hogg et al. (2017) for a filling-basin model of an inclined gravity current, where the plume velocity and buoyancy profiles are assumed to have linear, as opposed to top-hat, profiles and the plume fluid at the outer edge of the plume peels and moves to its neutral buoyancy height, without further mixing, once the first front is reached. Bonnebaigt et al. (2018) assumed an ideal source with no shear stress in their model. In what follows we describe the general peeling method used by Bonnebaigt et al. (2018), without restricting

attention to the ideal case, so that the results of a non-ideal source above may be applied. Before we describe the peeling method used by Bonnebaigt et al. (2018) it is convenient to introduce dimensionless variables where we use the non-dimensionalisation of Cooper and Hunt (2010), which were also used by Bonnebaigt et al. (2018), as

$$\left.\begin{aligned} &\xi = zH^{-1}, \quad \tau = \alpha^{2/3}H^{1/3}L^{-1}f^{1/3}t, \quad \delta_e = \alpha^{2/3}H^{1/3}f^{-2/3}b_e, \\ &\mathcal{Q} = \alpha^{-2/3}H^{-4/3}f^{-1/3}Q, \ \mathcal{M} = \alpha^{-1/3}H^{-5/3}f^{-2/3}M, \ \mathcal{F} = H^{-1}f^{-1}F. \end{aligned}\right\} \tag{6.51}$$

where Q may be Q_p or Q_e. We denote the non-dimensional height of the first front as ξ_0, so that the volume flux and mean buoyancy of the plume at the height of first front may then by given as a function of time by $\mathcal{Q}(\xi_0(\tau))$ and $\delta_0(\xi_0(\tau)) = \mathcal{F}(\xi_0(\tau))/\mathcal{Q}(\xi_0(\tau))$, respectively. According to the model of Hogg et al. (2017) and Bonnebaigt et al. (2018) the plume fluid entering the stratified region at the first front height then peels to its neutral buoyancy height without any further mixing. Therefore, a cumulative buoyancy distribution of volume flux at the first front must be incorporated into the model. The cumulative buoyancy distribution of volume flux $\mathcal{Q}_\delta(\delta^*, \xi)$ is defined, for a given height, as the volume flux of the plume with plume fluid greater than a given buoyancy δ^*. For example, Bonnebaigt et al. (2018) found that for linear plume velocity and buoyancy profiles, i.e.

$$\frac{\mathcal{W}}{\mathcal{W}_m} = \begin{cases} 1-\chi, & \chi < 1, \\ 0, & \chi > 1, \end{cases} \quad \text{and} \quad \frac{\delta}{\delta_m} = \begin{cases} 1-\chi, & \chi < 1, \\ 0, & \chi > 1, \end{cases} \tag{6.52}$$

where $\mathcal{W}$ is the non-dimensional plume velocity and $\chi = x/R$ is the non-dimensional cross-stream distance, the cumulative buoyancy distribution of volume flux at the position of the first front is given by

$$\frac{\mathcal{Q}_\delta(\delta^*, \xi_0)}{\mathcal{Q}(\xi_0)} = \begin{cases} 1 - \left(\dfrac{2\delta^*}{3\delta_0}\right)^2, & \dfrac{\delta^*}{\delta_0} < \dfrac{3}{2}, \\ 0, & \dfrac{\delta^*}{\delta_0} > \dfrac{3}{2}, \end{cases} \tag{6.53}$$

where we have used the result that $\delta_m(\xi_0) = 3\delta_0/2$ since it is useful to express $\mathcal{Q}_\delta$ in terms of the top-hat buoyancy. The height ξ^* at which the fluid of buoyancy δ^* is located is then calculated by finding the cumulative volume flux of fluid of buoyancy greater than δ^*. This may be expressed by

$$\xi^*(\delta^*, \tau) = 1 - \int_0^\tau \mathcal{Q}_\delta\left(\delta^*, \xi_0(\tau)\right) \mathrm{d}\tau. \tag{6.54}$$

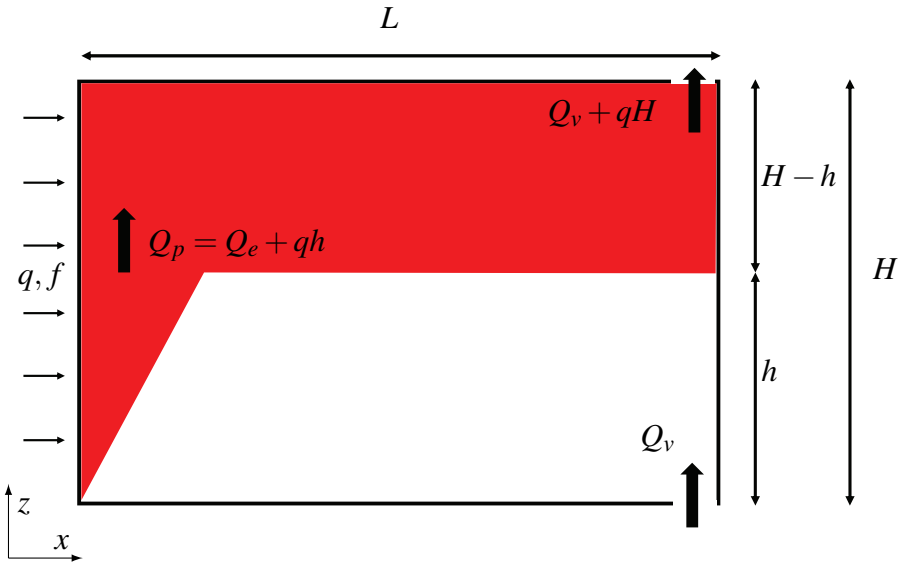

Fig. 6.14 Schematic of the mechanically vertically distributed buoyant plume with a finite source volume flux, where the box is connected to the exterior environment by an open vent at the bottom of the box and a gear pump is forcing ventilation through openings at the top.

Bonnebaigt et al. (2018) accounted for the additional source buoyancy in the stratified region by adding the source buoyancy to the buoyancy profile calculated above at each height. This additional buoyancy, $\Delta\delta(\xi,\tau)$, at each height and time may be expressed by

$$\Delta\delta(\xi,\tau) = \int_{\tau_0(\xi)}^{\tau} \mathrm{d}\tau, \tag{6.55}$$

where $\tau_0(\xi)$ is the time at which the first front reaches ξ. The final buoyancy profile is thus given by $\delta^*(\xi^*,\tau) + \Delta\delta(\xi^*,\tau)$. We compare this model with experiments in § 6.5.5.1 and suggest some adaptations to the ideal plume model considered by Bonnebaigt et al. (2018).

6.5.2 Ventilated confined flow

In this section we consider the ventilation of a system where openings are placed at the top and bottom of the box (see diagram in figure 6.14). This type of ventilation is commonly called displacement ventilation (Linden et al., 1990), whereby buoyant fluid is extracted from the top opening and fresh ambient (i.e. relatively dense) fluid is introduced from the exterior environment through the bottom opening. A stable stratification is therefore produced within the ambient. The buoyant fluid from the top opening may be extracted naturally, where the ventilation is driven only by the hydrostatic pressure difference between the box and the external environment, or by forced ventilation, commonly called mechanical

ventilation. The mechanical ventilation is forced at a flow rate of $Q_v + qH$ through the top opening which results in a ventilation flow rate of Q_v through the bottom opening. Assuming that the ventilation flow rate is smaller than the flow rate of the plume at the top of the box, the first front reaches a steady state at the height at which the ventilation flux matches the cumulative volume flux, i.e. the height h such that $Q_e(h) = Q_v$. The mechanical ventilation of a vertically distributed buoyancy plume has been examined by Cooper and Hunt (2010). Cooper and Hunt (2010) adapted the numerical scheme for the sealed box to include the ventilation flow rate of ambient fluid so that the advection equation could be written, in dimensional form, as

$$\frac{\partial b_e}{\partial t} = \frac{(Q_e - Q_v)}{L}\frac{\partial b_e}{\partial z}. \tag{6.56}$$

As for the filling-box, Cooper and Hunt (2010) found that the numerical scheme was not able to predict the quantitative transient or steady state ambient buoyancy profile.

Gladstone and Woods (2014) studied the mechanical ventilation of a vertically distributed line source. They showed that within the stratified environment in the steady state there was no net plume entrainment, due to a balance of entrainment of ambient fluid and detrainment in to the ambient. Consequently, the time-averaged volume flux of the plume was invariant with height. Gladstone and Woods (2014) suggested that in such a system the local entrainment and detrainment is controlled by the local difference in the mean plume and ambient buoyancy and, further, this local difference allows the plume to descend within the stratified environment. Given that the system is in steady state, it was suggested that this local difference of buoyancy should be independent of height. Since the buoyancy flux increases linearly with height and the volume flux remains constant within the stratified environment, the mean plume buoyancy, and therefore the ambient buoyancy, should also increase linearly with height. In particular, the gradient of the ambient buoyancy should follow the relation

$$\frac{\partial b_e}{\partial z} = \frac{f}{Q_v}, \tag{6.57}$$

since the volume flux entering the stratified region in steady state will match the ventilation flux.

In the remaining part of this chapter we present the experiments performed in order to study the filling and mechanically ventilated box of a vertically distributed buoyancy source and apply the theory of Gladstone and Woods (2014) to our results. We first describe the experimental set-up used to perform the experiments.

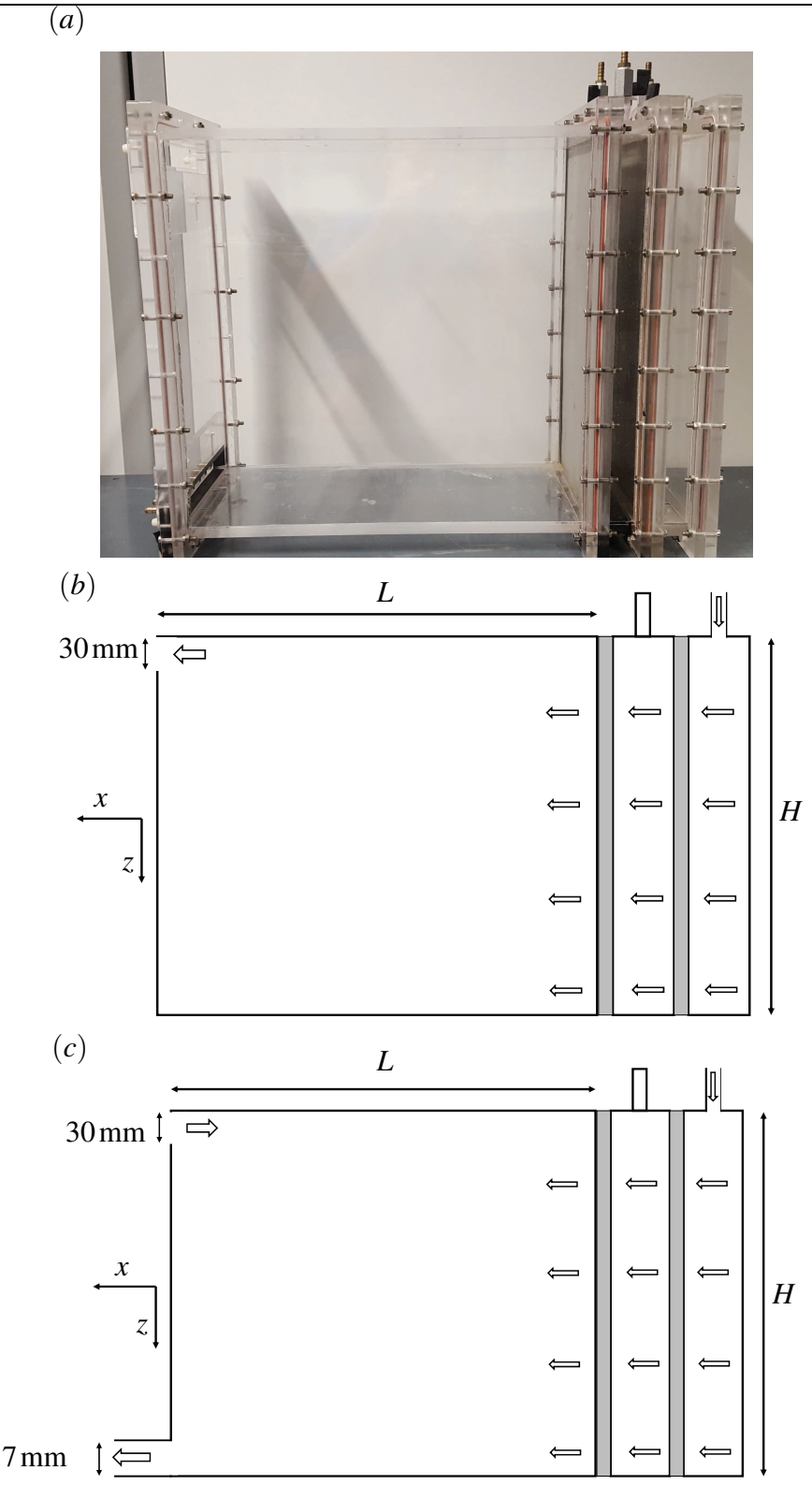

Fig. 6.15 (*a*) The experimental apparatus used to study a filling-box and a mechanically ventilated box and a diagram of the above apparatus for the (*b*) filling-box and (*c*) the mechanically ventilated box. The openings at the bottom of the tank may be open or closed using a series of valves.

6.5.3 Experimental details

In order to create a filling-box and a mechanically ventilated box of a vertically distributed buoyancy source, we enclosed the porous plate described in § 6.3.1 in a perspex box with height H and length L, $0.48\,\mathrm{m} \times 0.50\,\mathrm{m}$, and spanwise length $0.23\,\mathrm{m}$ (see figure 6.15). This was placed inside a Perspex acrylic tank of horizontal cross-section $1.20\,\mathrm{m} \times 0.40\,\mathrm{m}$ filled with dilute saline solution of uniform density ρ_a. The end wall had rectangular openings at the top of the wall which allowed an exchange flow to the exterior ambient. Seven valves were connected at the bottom of the end wall which could be closed for a filling-box experiment or connected to a pump for the mechanically ventilated experiments. In order to force a ventilation flow for the mechanically ventilated experiments a gear pump (ISMATEC BVP-Z, 1.17 mL/rev), which offered a large maximum flow rate, was used. The source flow was also pumped using a gear pump (Cole-Parmer Digital Gear Pump System, 0.91 mL/rev). Dye attenuation was used in order to measure the ambient buoyancy stratification. This method is described in detail in § 6.5.4.

The experimental parameters of the filling-box and mechanically ventilated experiments are shown in table 6.2. The ventilation flux Q_v in table 6.2 is defined as the difference in the physical flux pumped out at the base of the tank and the total source volume flux qH. The ratio of the ventilation flux to the to the maximum theoretical volume flux of the plume (i.e. at $z = H$ in an unstratified environment) is defined by $\psi = Q_v/Q_e(H)$, where $Q_e(H)$ was calculated using the ideal pure plume solution of the volume flux (6.23) with the entrainment value and shear stress coefficient determined in § 6.4.2.

6.5.4 Dye attenuation

While planar laser-induced fluorescence (PLIF) can produce high quality density measurements on a plane, the technique is limited to examining relatively short experiments, or to be more precise, experiments where a given fluid parcel with fluorescence dye tracer remains in the laser sheet for a relatively short time. This is because photobleaching of the dye is likely to occur which has a significant effect on the light emissivity of the dye (Crimaldi, 1997). Given the time scale of a typical filling-box or mechanically ventilated experiment ($\sim 10 - 60$ mins), PLIF was not a suitable technique to use in order to measure the density field. Instead we used dye attenuation.

Dye attenuation was performed by illuminating the tank from behind using a white-LED light-bank, as shown in figure 6.16, and measuring the attenuation of light, due to added tracer dye in the source solution, as it passes through a fluid. The Bouguer-Lambert-Beer law may then be used to deduce the integrated concentration of dye along the light path

Experiment	$b_s\,[\mathrm{m\,s^{-2}}]$	$f\,[\times 10^{-5}\,\mathrm{m^2\,s^{-3}}]$	$qH\,[\times 10^{-4}\,\mathrm{m^2\,s^{-1}}]$	$Q_v\,[\times 10^{-4}\,\mathrm{m^2\,s^{-1}}]$	$\psi = Q_v/Q_e(H)$
1	0.23	2.44	0.50	0	0
2	0.23	2.44	0.50	1.04	0.126
3	0.23	4.26	0.89	1.76	0.178
4	0.23	2.44	0.50	1.56	0.188
5	0.23	2.44	0.50	1.84	0.222
6	0.23	2.44	0.50	2.17	0.262
7	0.23	2.44	0.50	2.61	0.315
8	0.23	2.44	0.50	3.17	0.382
9	0.23	2.44	0.50	3.64	0.439
10	0.23	2.44	0.50	4.32	0.522
11	0.23	2.44	0.50	5.33	0.643
12	0.23	2.44	0.50	1.85	0.224

Table 6.2 Experimental parameters of the filling-box (experiment 1) and the mechanically ventilated experiments (experiment 2 - 12). The last column, $\psi = Q_v/Q_e(H)$, shows the ratio of the ventilation flow rate compared to the theoretical maximum volume flux of the plume in an unstratified environment, calculated from pure plume solutions. In experiment 12, blue dye was added to the source solution once the ambient had reached steady state in order to assess the motion of the stratified ambient.

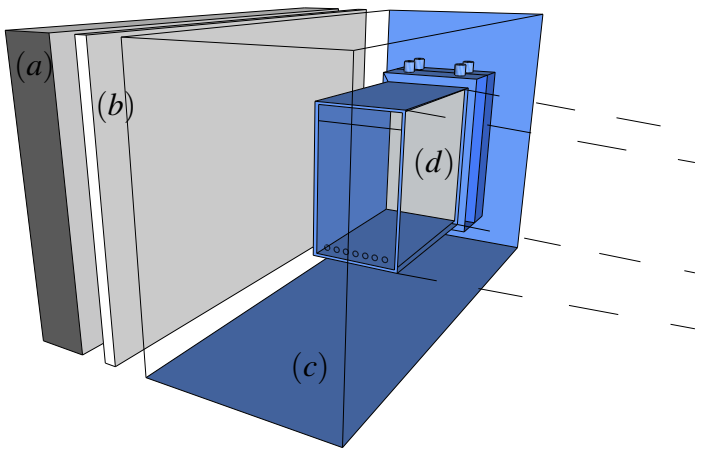

Fig. 6.16 Diagram of the experimental set-up used to perform dye attenuation of the filling-box and mechanically ventilated experiments showing the (*a*) LED light-bank, (*b*) light diffuser, (*c*) large reservoir tank and (*d*) apparatus shown in figure 6.15. The dashed lines indicate the measuring-window of the camera which is placed 10 m from the edge of the large reservoir to minimise the parallax error.

(Cenedese and Dalziel, 1998). The LED light-bank is composed of uniformly spaced LEDs with a light diffuser placed between the tank and the array of LEDs. This creates a uniform background distribution of light for the experiments. Further, the light-bank is driven by a DC power supply which eliminates the 'beating' effect observed with fluorescent lighting where the light intensity of the light-bank fluctuates, due to the power supply, at a different frequency to the camera capture frame rate. The experiments were captured using an AVT Bonito CMC-4000 4 megapixel CMOS camera with a $80-200$ mm f2.8 Nikon lens at a frame rate of 1 Hz which allowed 200 minutes of recording time. The camera intensity response is linear with a black offset of $b = 0.0029$. The resolution of the images was $0.37\,\text{mm pixel}^{-1}$.

The dye used was red food colouring "Fiesta Red" (Allura Red AC, E129). The molecular diffusivities of the dye and salt are both a few orders of magnitude lower than the kinematic viscosity of the salt solution ($\nu \sim 10^{-6}\,\text{m}^2\,\text{s}^{-1}$) so that the dye acts as an effective tracer for the salt concentration (Dalziel et al., 2008). This dye has shown to be effective in previous dye attenuation investigations (e.g. Cenedese and Dalziel (1998); Coomaraswamy and Caulfield (2011)). Coomaraswamy and Caulfield (2011) observed a dark red precipitate when the dye was added to concentrated sodium chloride solution, instead sodium carbonate solution was used to achieve a density difference. No such precipitation was observed in our experiments which may be as a result of the significantly lower concentrations of sodium chloride used in our source solutions, 3.5% Mass, as compared to Coomaraswamy and Caulfield (2011), 22% Mass (estimated using the density of the sodium carbonate source solution used). The experiments were assumed to be independent of width (i.e. the y-direction) so in order to determine the height dependent profile the light rays should follow horizontal paths. In order to minimise the parallax error, within the constraints of the equipment and the laboratory, the camera was placed 10 m from the experiment. Since the dye acts as a tracer for the sodium chloride solution, the attenuation due to the sodium chloride must also be considered. By assuming the dye concentration is approximately constant along the light path (i.e. the y direction) the dye concentration may be inferred for all points along the light path. This results in an equivalent measurement to a plane concentration field measurement. The Bouguer-Lambert-Beer law may be used to relate a reference intensity, with no dye or sodium chloride added to the relative medium, of the integrated path along y recorded by the camera, $I_0(x,z)$, to the intensity of the integrated path along y with known concentrations of dye and sodium chloride, $I(x,z,t)$, as

$$I(x,z,t) = I_0(x,z)\exp\left(-\left(\varepsilon_d c_d + \varepsilon_{sc} c_{sc}\right) L_y\right), \tag{6.58}$$

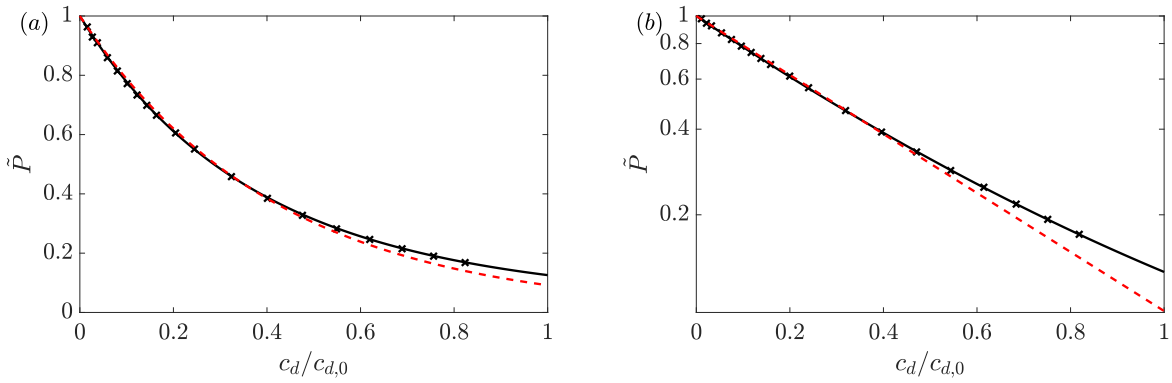

Fig. 6.17 Dye attenuation calibration curve for the food colouring dye. The space-averaged normalised pixel intensity reading against the normalised dye concentration on a (*a*) linear-linear axis and a (*b*) log-linear axis. A linear relationship may be approximately observed in (*b*), however, a best-fit quadratic curve was used to provide a more accurate relationship. The solid curves correspond to a least squares quadratic fit for $c_d/c_{d,0}$ in $\log\tilde{P}$, where $c_d/c_{d,0} = 0.487\left(\log\tilde{P}\right)^2 - 0.256\log\tilde{P}$. The red dashed curves correspond to a least squares linear fit for the data points within the region $0 < c_d/c_{d,0} < 0.5$ for $c_d/c_{d,0}$ in $\log\tilde{P}$, where $c_d/c_{d,0} = -0.239\log\tilde{P}$. All concentration measurements in the experiments were within this range.

where ε_d, ε_{sc} and c_d, c_{sc} are the extinction coefficients and concentrations of the dye and sodium chloride, respectively, and L_y is the total distance traversed by the ray of light in the relative medium. In practice, a batch solution of sodium chloride and dye is made so that the relative concentrations of sodium chloride and dye remains constant, i.e. $c_{sc}/c_d = \beta$. Equation 6.58 may therefore by rewritten in terms of β and the dye concentration,

$$I(x,z,t) = I_0(x,z)\exp\left(-\left(\varepsilon_d + \varepsilon_{sc}\beta\right)c_d L_y\right), \tag{6.59}$$

where the constant $\varepsilon_d + \varepsilon_{sc}\beta$ may be determined empirically by a calibration.

The calibration was performed by filling the tank with a uniform concentration of the batch solution and recording 200 images of the field of view. The images were then time-averaged to give an intensity reading, for each camera pixel, for a given dye concentration which is used as a proxy for both the dye and sodium chloride concentration. A space-averaged normalised pixel intensity reading $\tilde{P}$ was calculated for each concentration by the following

$$\tilde{P} = \frac{1}{A}\int_A \frac{P(x,y) - b}{P_0(x,y) - b}\mathrm{d}x\mathrm{d}z, \tag{6.60}$$

where $P_0(x,y)$ was the intensity reading with a zero dye and sodium chloride concentration, A is the area of the space-averaged region and b is the camera black offset. In performing

the calibration, it is convenient to normalise the dye concentration by the source dye concentration used in the experiments, $c_{d,0}$. The data are plotted in figure 6.17. Figure 6.17 shows an approximately linear relationship between $\log\tilde{P}$ and $c_d/c_{d,0}$. The relationship is, however, more accurately fitted by a quadratic curve. The following relationship was found to provide a least squares quadratic fit

$$\frac{c_d}{c_{d,0}} = 0.487\left(\log\tilde{P}\right)^2 - 0.256\log\tilde{P}. \tag{6.61}$$

It should be noted, however, that the maximum concentration measurements in the region of interest of the experiments (i.e. ignoring regions containing a thin layer of very dense fluid which could not be effectively pumped out by the ventilation) corresponded to a concentration of $c_d < 0.5c_{d,0}$. There is a good linear relationship between $\log\tilde{P}$ and $c_d/c_{d,0}$ for this range with a linear best-fit of

$$\frac{c_d}{c_{d,0}} = -2.39\log\tilde{P}. \tag{6.62}$$

It is not clear as to why a linear relationship is not observed for the whole range of concentrations, however, a non-linear relationship was also observed for larger concentrations in Coomaraswamy (2011) and may be a result of refractive index variations.

6.5.5 Results

For convenience, the experiments were performed using a relatively dense source solution so that the convention is vertically opposite relative to theory presented in § 6.5.1 and § 6.5.2, i.e. in the experiments the plume descends and the first front rises whereas in the theory described the plume rises and the first front descends (figures 6.15 (*b*) and (*c*)). We therefore vertically invert the presented experimental images in order to maintain an analogy between our experiments and a heated room (figures 6.13 and 6.14). Since the experiments and the full scale flows are Boussinesq the inverted problems are equivalent. Therefore, we have that $z = 0\,\mathrm{m}$ and $\xi = 0$ are at the top of the experimental tank but the bottom of the filling-box and that $z = H$ and $\xi = 1$ are at the bottom of the experimental tank but at the top of the filling-box.

6.5.5.1 Filling-box experiment

We first consider the evolution of the first front of the filling-box which has been used to determine the entrainment coefficient in previous studies. Kaye and Cooper (2018) showed that by ignoring the shear stress and source volume flux when applying the first front theory of Baines and Turner (1969), artificially low entrainment values may be calculated. We

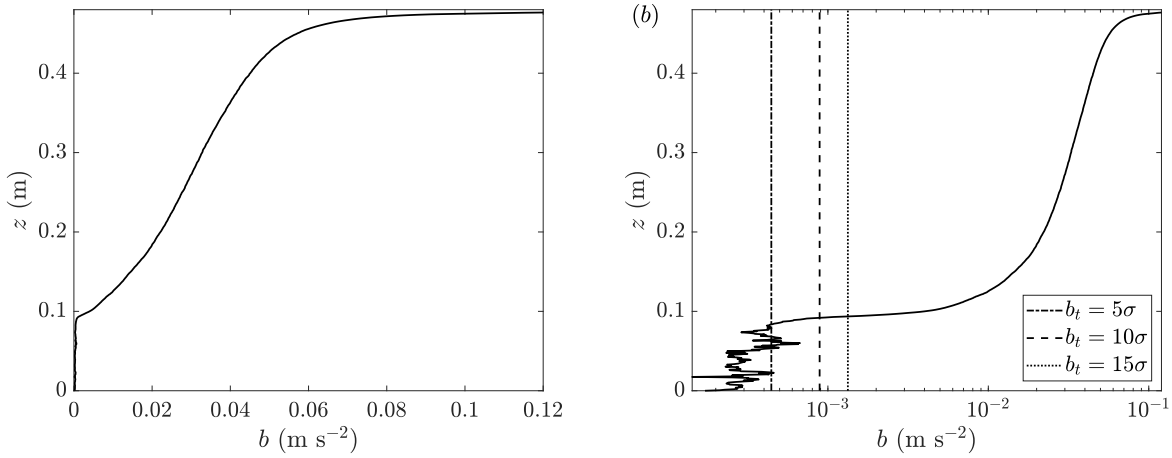

Fig. 6.18 (*a*) Ambient buoyancy profile of the filling-box experiment. (*b*) Ambient buoyancy profile of the filling-box experiment as in (*a*) with logarithmic buoyancy scale. The vertical dashed line shows the threshold $b = b_t = 10\sigma$ used to identify the first front interface, where σ is the standard deviation of the ambient buoyancy from a background image with no dye in. The other two lines show show $b = 0.5b_t$ and $b = 1.5b_t$.

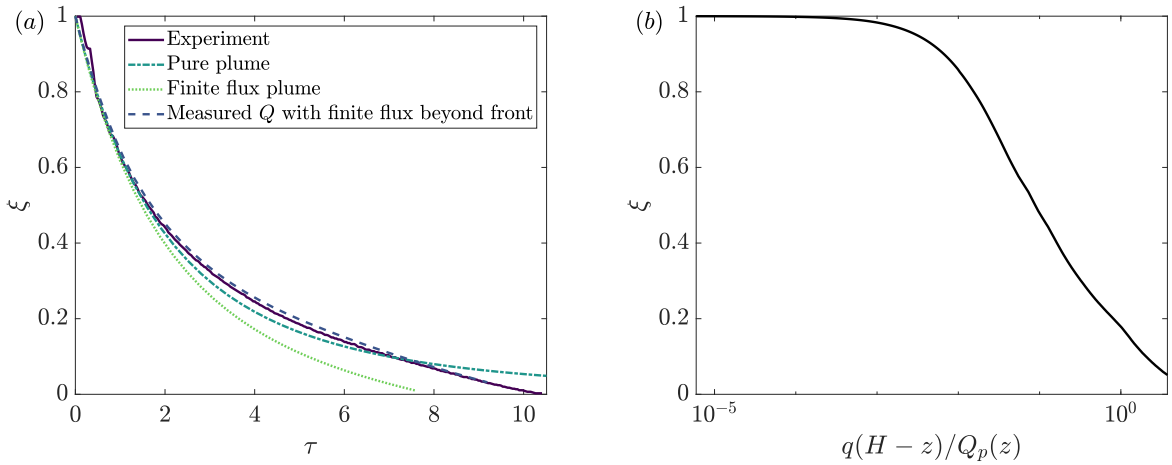

Fig. 6.19 (*a*) Comparison of the predictions of the position of the first front with experiment 1 (solid) for FFM (i) (dot-dashed) FFM (ii) (dotted) and FFM (iii) (dashed) discussed in the text. An entrainment coefficient of $\alpha = 0.068$, based on (6.42), has been used for all the plots. (*b*) Ratio of source volume flux contribution to plume volume flux contribution to the first front movement of the first front. The volume flux, $Q(z)$, used in (*b*) is from the velocity measurement over the total height of the wall from § 6.4.1.

show that it is also important to only consider the evolution of the first front in the region where the plume is fully developed.

The height of the first front for each image was calculated by first space-averaging the processed experimental images of the buoyancy field in the ambient fluid over the range $0.20\,\mathrm{m} < x < 0.45\,\mathrm{m}$ so that the plume structure was not included in the space-average. The standard deviation σ across this region was calculated for a background buoyancy field image with no dye added and a threshold of $b_t = 10\sigma$ was used for identifying the interface. A typical ambient buoyancy profile taken from the filling-box experiment is shown in figure 6.18 (*a*) and the same profile with a logarithmic scale also showing the buoyancy threshold in (*b*). The identified position of the interface was insensitive to the choice of threshold, in particular using a threshold of $b_t = 5\sigma$ and $b_t = 15\sigma$, also shown in figure 6.18 (*b*), resulted in a mean difference in the identified interface height of 1.2 and 1.3 pixels, respectively.

Figure 6.19 (*a*) shows the experimentally measured first front against non-dimensional time. Also plotted are three different first front models (FFM) used to predict the position of the first front. These were predicted by assuming:

(i) an ideal plume (with zero source flux) where the volume flux is given by (6.23) and the first front descends according to (6.45),

(ii) a finite flux plume where the numerical solution of the volume flux of (6.18) - (6.20) was used in the unstratified region and the first front descends according to (6.44) with the source flux included,

(iii) the volume flux determined in § 6.4.1 from the velocity measurements over the whole height of the wall and the first front descends according to (6.44) with the source flux included.

In FFM (ii) and (iii), equation (6.44) was integrated numerically to obtain the first front position. Kaye and Cooper (2018) also considered the evolution of the first front where the finite source volume flux is included in the conservation plume equations (6.18) - (6.20), and numerically integrated the equations to determine the plume volume flux in the unstratified region.

Both the plume volume flux entering the stratified region and the additional source volume flux within the stratified region contribute to the rate of descent of the first front. Figure 6.19 (*a*) shows that all three of the models are successful in predicting the first front position for the region $\xi > 0.6$. In particular, without accounting for the source volume flux in the stratified region, the pure plume model shows good agreement within this region. This

suggests that the contribution of the source volume flux within the stratified region is relatively small compared to the plume volume flux entering the stratified region at the height of the first front. Figure 6.19 (*b*) shows the relative contributions of the source volume flux to the plume volume flux in the rate of descent of the first front movement for a given height. The plume volume flux used in this calculation was taken from the velocity measurements over the whole height of the wall discussed in § 6.4.1. This shows that the contribution of the source volume flux to the first front movement is less than 5% that of the plume entering the stratified region for the region $\xi > 0.6$.

The inclusion of the source volume flux in the stratified region of the pure plume model (FFM (i), marked by the dotted curve) increases the rate of descent of the first front. The experimentally measured first front, however, descends at a slower rate than the pure plume model with zero source flux (FFM (ii), marked by the dashed-dotted). This can be explained using the velocity measurements over the whole height of the wall, where a laminar region was observed for $\xi < 0.15$. Beyond this, the plume was not fully developed within the region $\xi < 0.6$ so the ideal plume model did not provide an accurate prediction of the volume flux within this region.

Figure 6.19 (*a*) shows that the first front position may be successfully predicted for the entire descent by including the volume flux measurements in the first front equation and including the contribution of source volume flux in the model (FFM (iii), marked by the dashed line).

The evolution of the ambient buoyancy of experiment 1 is shown in figure 6.20. These buoyancy profiles were calculated by space-averaging the processed experimental images of the buoyancy field in the ambient fluid over the range $0.20\,\mathrm{m} < x < 0.45\,\mathrm{m}$ so that the plume structure was not included in the space-average. Figure 6.20 (*a*) shows the evolution of the ambient buoyancy with time where the position of the first front has been overlayed. Figure 6.20 (*b*) shows the buoyancy profiles for given times. The profiles are qualitatively similar to those of Caudwell et al. (2016) and Bonnebaigt et al. (2018), with a sharp tail of rapidly decreasing buoyancy from the top of the box to an approximately linear region. Cooper and Hunt (2010) did not present results of the filling-box ambient buoyancy profiles. We now consider the filling-box peeling model based on the work of Bonnebaigt et al. (2018) discussed in § 6.5.1 and compare the model to the experimental results. We consider three filling-box peeling models (FBPM). In the first model, FBPM (i), we use the ideal plume solutions (6.23) - (6.25), using the experimentally determined entrainment and shear stress coefficient. The position of the first front is then determined analytically by (6.45). In this model, as in Bonnebaigt et al. (2018), linear plume velocity and buoyancy profiles are assumed as defined in (6.52), which give a cumulative buoyancy distribution of volume flux

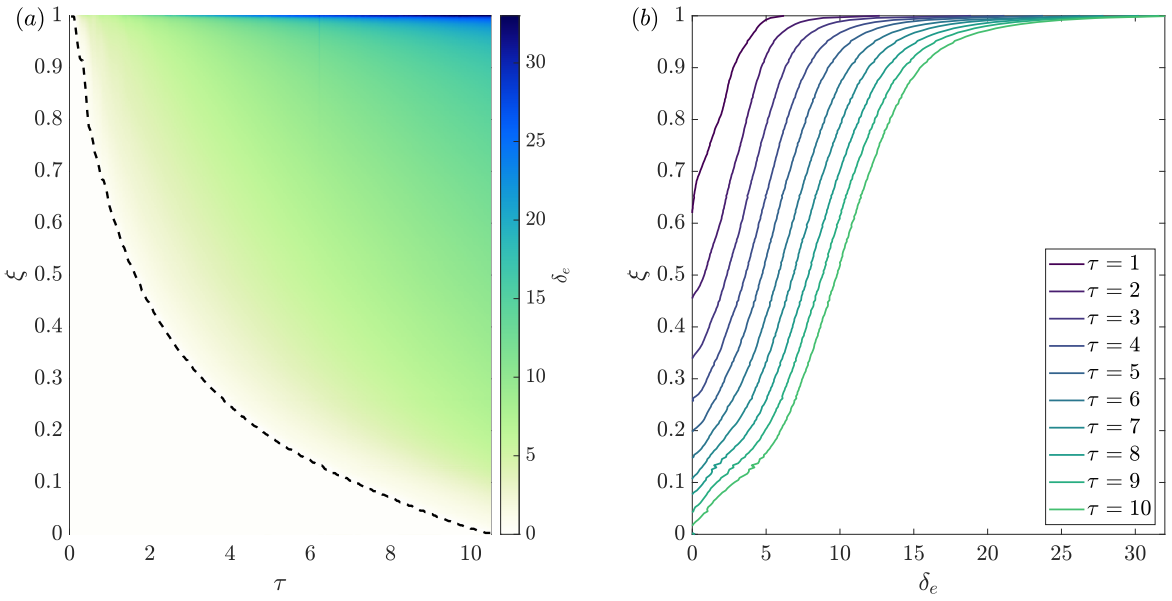

Fig. 6.20 (*a*) The evolution with time of the space-averaged ambient density field for the filling-box experiment 1 (see table 6.2) and (*b*) the space-averaged ambient density profiles for non-dimensional time $\tau = n \in \{1, ..., 10\}$. The dashed curve in (*a*) shows the position of the first front.

as defined in (6.53). This model only differs to that of Bonnebaigt et al. (2018) with the inclusion of a shear stress coefficient.

In the second model, FBPM (ii), the ideal plume solutions are again used to calculate the volume flux entering the stratified region. The difference is, however, the cumulative buoyancy distribution of volume flux imposed at the first front was experimentally determined by conditionally averaging the simultaneous velocity and buoyancy data presented in § 6.4.2. The cumulative buoyancy distribution of volume flux was calculated from the data by the following calculation

$$Q_b(b^*, z) = \frac{1}{T}\int_0^T \int_0^\infty w(x,z,t)\mathcal{H}(b(x,z,t) - b^*)\mathrm{d}x\mathrm{d}t, \tag{6.63}$$

where $\mathcal{H}$ is the Heaviside step function. The mean cumulative buoyancy distribution of volume flux is shown in figure 6.21 (black) scaled by the total volume flux and the buoyancy scaled by the top-hat buoyancy. The curve shows the average, across all heights measured, of the scaled data. Also shown in figure 6.21 are the cumulative distribution function assumed by Bonnebaigt et al. (2018) (blue) and the result of assuming a top-hat profile (dashed). The experimental data shows there is a large transport of buoyant fluid, approximately 25%, which is greater than the maximum buoyancy predicted by the model of Bon-

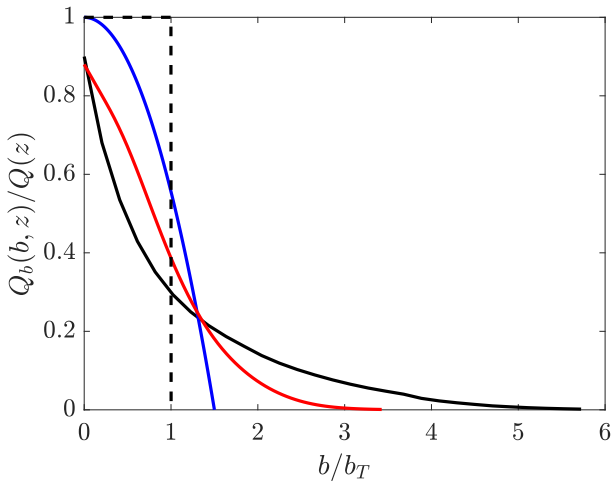

Fig. 6.21 The cumulative buoyancy distribution of volume flux of the vertically distributed plume in an unstratified environment (black) calculated using the simultaneous velocity and buoyancy data from § 6.4.2. The cumulative buoyancy distribution of volume flux used by Bonnebaigt et al. (2018) (blue) and the resulting distribution from assuming a top-hat velocity and buoyancy profile (dashed). Also shown is the cumulative buoyancy distribution of volume flux of a wall plume resulting from a horizontal line source of buoyancy adjacent to a wall (red), calculated from the data presented in § 5.5. The buoyancy has been scaled by the top-hat buoyancy, b_T.

nebaigt et al. (2018). Figure 6.21 shows that, for the experimental data, $Q_b(0,z) < Q_p(z)$. This is due to the transport of ambient fluid by the vertically distributed plume, which is equal to $Q_p(z) - Q_b(0,z)$. The good agreement between the measurements of the first front descent of the experiments and FFM (iii) based on the velocity measurements over the full height of the wall suggests that the ambient fluid that is transported into the stratification is then mixed, as opposed to detraining back in to the unstratified ambient. In order to use the experimental cumulative distribution function data in the peeling model we therefore rescale the experimental data $Q_b(b^*,z)$ by the volume flux of plume fluid $Q_b(0,z)$. The buoyancy is then rescaled in order to conserve buoyancy flux, i.e. the following relation

$$\frac{1}{b_T Q(z)} \int_0^\infty Q_b(b^*,z) \mathrm{d}b^* = 1, \tag{6.64}$$

must hold.

The third model, FBPM (iii), uses the same method as FFM (iii) discussed above in order to predict the position of the first front. The peeling procedure discussed for FBPM (ii) is then used to determine the ambient density profile.

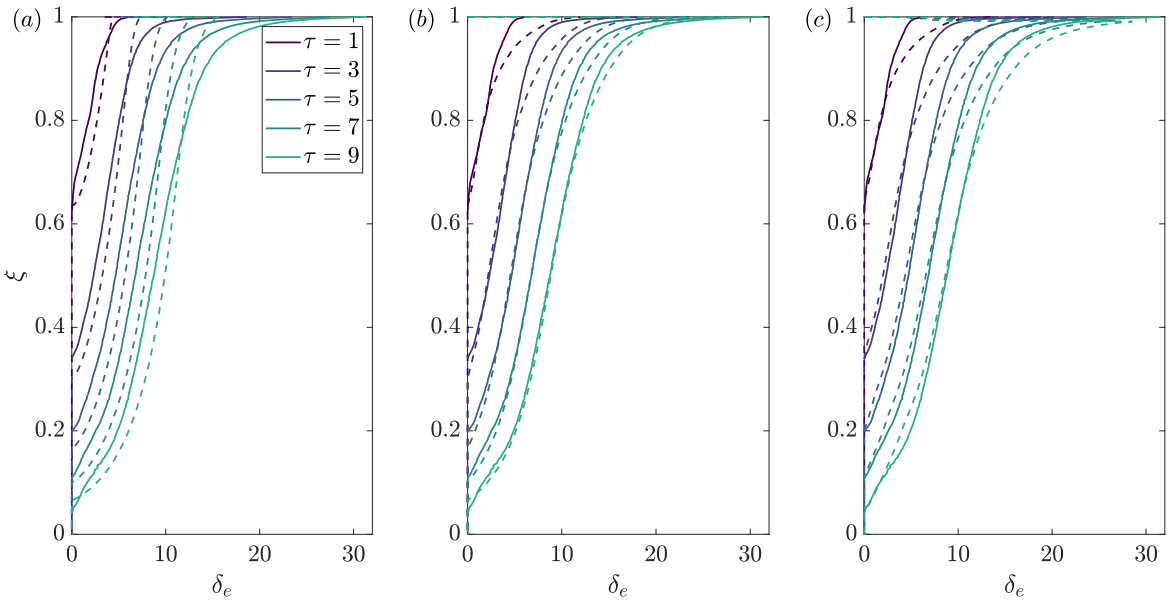

Fig. 6.22 Comparison of the filling-box peeling models (dashed curves) compared with experiment (solid curves) 1 for non-dimensional times $\tau = \{1,3,5,7,9\}$ for (a) FBPM (i) (b) FBPM (ii) and (c) FBPM (iii) discussed in the text.

Figure 6.22 shows the results of the three peeling models described compared against the experimental data. The first front position with time is identical in FBPM (i) and FBPM (ii). FBPM (ii), however, is able to predict the buoyancy gradient of the approximately linear region observed in experiments. FBPM (i) underestimates the buoyancy observed in the experiments within the region $\xi > 0.75$ and vice-versa, whereas FBPM (ii) overestimates the buoyancy observed in the region $\xi > 0.75$. This observation in FBPM (i) is most likely a consequence of the approximation of the velocity and buoyancy profiles, which may overestimate the mixing that occurs within the plume and any additional mixing as the plume enters the stratified region. The opposite problem occurs in FBPM (ii) where the cumulative buoyancy distribution of volume flux has been imposed from direct measurements and no further mixing is assumed as the plume enters the stratified region. FBPM (iii), which follows the first front position more accurately by using the method described in FFM (iii), does not show improvement over FBPM (ii).

The results above suggest that it is possible to modify the experimentally determined cumulative distribution function, which could be thought of as a mixing parameterisation of the plume entering the stratified region, so that the peeling model more accurately describes the buoyancy profiles. It is expected, however, that the cumulative buoyancy distribution is not self-similar in the developing, and especially, the laminar region of our experiment.

Figure 6.21 also shows the cumulative buoyancy distribution of volume flux of the wall plume calculated from the same data presented in § 5.5. It is clear that, relative to the top-hat buoyancy, the vertically distributed plume exhibits a greater range of buoyancy scales than the wall plume. This is due to the continued supply of buoyant fluid at the wall as well as the ongoing mixing of ambient fluid. Bonnebaigt et al. (2018) also examined the filling-box of a wall plume, where the top-hat model of Baines and Turner (1969) was shown to accurately predict the developing buoyancy stratification. It was emphasised that it is not yet clear when it is better to approximate the density distribution across the plume using a one-dimensional top-hat profile, or when it is necessary to assume a two-dimensional density and velocity profile. We see in figure 6.21 that the wall plume distribution better approximates an idealised top-hat buoyancy profile, therefore this provides some insight in to the suitability of modelling the plume profiles according to this top-hat profile.

6.5.5.2 Mechanically ventilated experiments

We first examine the steady state interface height of the mechanically ventilated experiments. Following Baines (1983) and Gladstone and Woods (2014) the height of the steady state interface, h_i or ξ_i in non-dimensional form, is measured from experiments and the interface height is predicted by assuming the ventilation flow rate matches the volume flux of the plume at the height of the interface (Baines, 1983). We, therefore, have that

$$Q_v = Q_p(h_i) - qh_i = Q_e(h_i). \tag{6.65}$$

By assuming the pure plume solution for the cumulative entrained volume flux (6.23), equation (6.65) may be used to express the interface height in terms of the ventilation flow rate as

$$\frac{h_i}{H} = \left(\frac{4Q_v}{3}\right)^{3/4} \left(\frac{4\alpha^2 f H^4}{5}\right)^{-1/4} \left(1 + \frac{4C}{5\alpha}\right)^{1/4} = \psi^{3/4}, \tag{6.66}$$

where we recall that $\psi = Q_v/Q_e(H)$. We also predict the interface by assuming the volume flux determined from the velocity measurements over the full height of the wall. The interface height is then given by $h_i = z(Q_v)$, where $z(Q_e)$ is the inverse relationship of the best fit curve of the experimental data shown in figure 6.6 (*b*). Figure 6.23 (*a*) shows a typical evolution of the ambient stratification in a mechanically ventilated experiment, as it ultimately reaches steady state. Figure 6.23 (*b*) shows the predicted interface heights for both models discussed above compared with the measured interface height from the experiments.

Figure 6.23 (*b*) shows that, while the ideal plume model (filled diamonds) is able to predict the interface height for the region $\xi > 0.55$. This is consistent with the observation

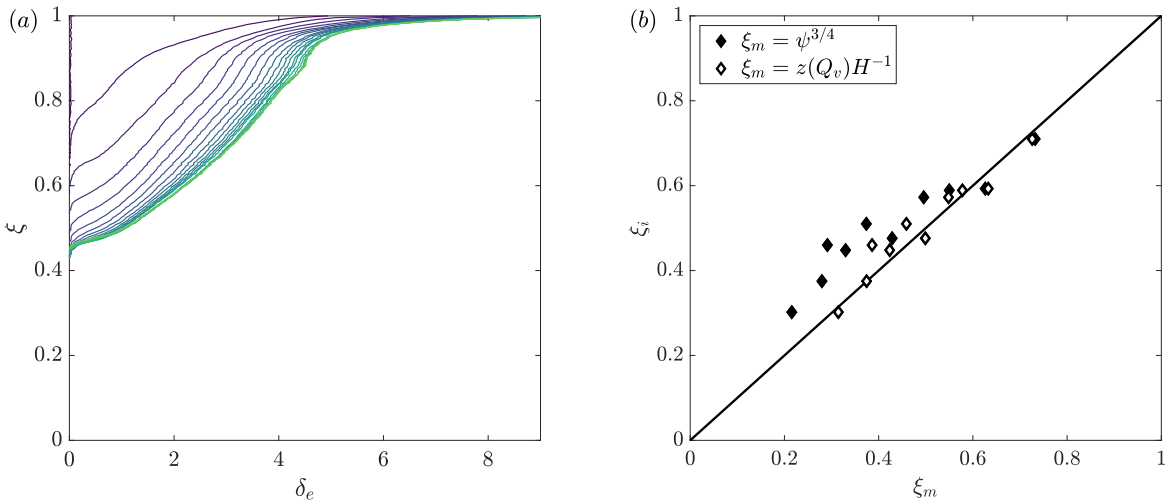

Fig. 6.23 (*a*) An example of the evolution of the ambient buoyancy profile, taken from experiment 5 (table 6.2), as it tends to a steady state. (*b*) Comparison of the predicted steady state interface heights for the two models described in the text with the measured interface height from the experiments.

that the ideal plume model FFM (i) is also able to accurately predict the first front height of the filling-box model, discussed in § 6.5.5.1, since the plume is fully developed within this region and follows the pure plume theory. The ideal plume model predictions, however, become increasingly poor as the interface height decreases, i.e. as the ventilation flow ratio ψ decreases. For this lower region the reason for the inaccuracy is the same as for the inaccuracy of the first front position for a filling-box as in § 6.5.1, so is not repeated here. The model is improved by incorporating volume flux measurements over the whole height of the wall (unfilled diamonds), in particular this model is able to the predict the interface heights of the low ventilation flow rate ratios.

Figure 6.24 shows the steady state buoyancy profiles across all the mechanically ventilated experiments. The buoyancy profiles are qualitatively similar to those observed by Cooper and Hunt (2010) and Gladstone and Woods (2014) by following an S-shaped curve, where the buoyancy rapidly increases from the interface height towards an approximately linear region. Beyond this exists a relatively well-mixed region before rapidly increasing buoyancy. The well-mixed region is a result of the gravity current formed at the base of the tank, and the rapidly increasing buoyancy may be a result of the position of the ventilation openings at the far wall, as opposed to Cooper and Hunt (2010) where the ventilation openings were along the base of the box. An interface, separating the gravity current at the base of the tank and the approximately linear ambient buoyancy, at approximately $\xi = 0.85$ can be observed in each of the experiments in figure 6.24. In order to identify the dynamics of

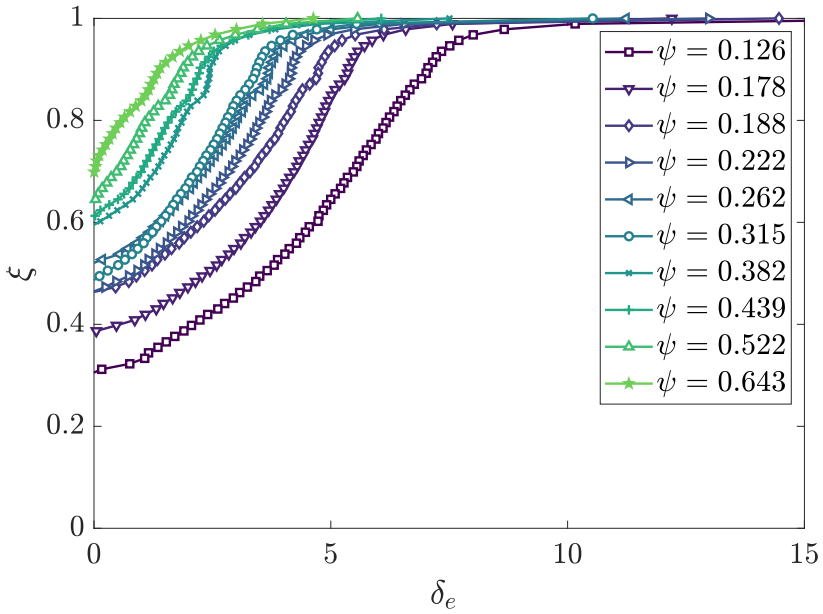

Fig. 6.24 Steady state ambient buoyancy profiles of the mechanically ventilated experiments. The data points shown are sub-sampled to aid clarity to the figure.

the ambient within the stratified region, relatively concentrated blue dye was added to the source solution in experiment 12 after steady state had been achieved. In order to perform the analysis on the data, it was convenient to study the raw experimental images. A time-average of the experiment during steady state, before any blue dye had been added, was used as a background image in order to aid clarity to the motion of the dye (figure 6.25 (*a*)). Figure 6.25 (*b*) shows an instantaneous image of the experiment 40 min after the blue dye had been added to the source. This image is corrected by element-by-element subtracting the background image in 6.25 (*a*). Since the technique was used for dye visualisation only, and not quantitative measurements, element-by-element subtraction was sufficient to highlight dyed fluid relative to the background image. The corrected image is shown in 6.25 (*c*).

For each experimental frame, after the blue dye had been added to the source, a horizontal and vertical space-average was performed in the region shown by vertical and horizontal grey bars, respectively, in figure 6.25 (*c*). The mean vertical and horizontal motion of the dye within the stratified region could then be assessed over time. Figure 6.25 (*c*) shows that there is a region within the stratified zone, approximately $x < 0.20\,\text{m}$, where the dyed source fluid has entered the ambient region. This structure developed shortly after the dye had been added, however, it remained bounded within this region and did not spread further into the ambient fluid. The region used to identify the mean vertical motion was therefore placed

outside of the structure identified from the dye. Similarly, the region used to identify the horizontal motion was placed outside the gravity current, which can be seen at the top of the figure in 6.25 (*c*). The evolution of the dye within the regions highlighted in grey in 6.25 (*c*) are shown in figure 6.26. The flushing time of the source chamber is approximately 10 min for the source flow rate used. Therefore, the source solution gradually becomes more concentrated until reaching a uniform dye concentration. The effect of this can be observed in figures 6.26 (*a*) and (*b*), where the dye concentration gradually increases. Figure 6.26 (*a*) shows the vertical motion of the dye. The dye clearly shows the vertical extent of the gravity current at the base of the tank. The maximum height of the dye remains approximately constant from 20 min, and the deviation in the maximum height is estimated to be 5 mm for the remainder of the experiment. Any vertical intrusion of the dye into the ambient is therefore estimated to occur at a speed of less than $2.5 \times 10^{-6}\,\mathrm{m\,s^{-1}}$ which corresponds to $0.02Q_v/L$.

Figure 6.26 (*a*) shows the horizontal motion of the dye. The figure suggests that there is a mixing zone in the region $x < 0.20\,\mathrm{m}$, which can also be seen in figure 6.25, since the dyed source fluid rapidly replaces any un-dyed source fluid within this zone. The (horizontal) width of this mixing zone was not uniform across the spanwise y direction. This is highlighted in the figure by the labels where separate intrusions at different y locations occurred. As the depth of intrusion A decreases, the depth of intrusion B increases, which suggests that the entrainment and detrainment balance. Similar results were observed Gladstone and Woods (2014). There is, however, a continued supply of source fluid within this region, so we hypothesize that within this region the time-average plume volume flux is given by $Q(z) = Q_v + qz$. Based on this assumption we may adapt the theory developed by Gladstone and Woods (2014) for a vertically distributed buoyant line plume to a vertically distributed buoyant wall.

As discussed in 6.5.2, Gladstone and Woods (2014) suggested that the absence of any vertical transport within the ambient implies there is a buoyancy difference Δb between the mean plume and ambient density within the stratified region which serves to maintain the vertical motion of the plume. Since the system is in steady state this buoyancy difference should remain independent of depth. The mean plume buoyancy, in dimensional form, in the unstratified region is given by

$$b_T = \frac{fz}{Q_p} = \frac{4}{3}\left(\frac{5}{4}\right)^{1/3} \alpha^{-2/3}\phi^{2/3}\left(1+\frac{4C}{5\alpha}\right)^{1/3} z^{-1/3}. \tag{6.67}$$

In the stratified region, assuming the volume flux is given by $Q_p(z) = Q_v + qz$, the mean plume buoyancy is given by

$$b_T = \frac{fz}{Q_v + qz}. \tag{6.68}$$

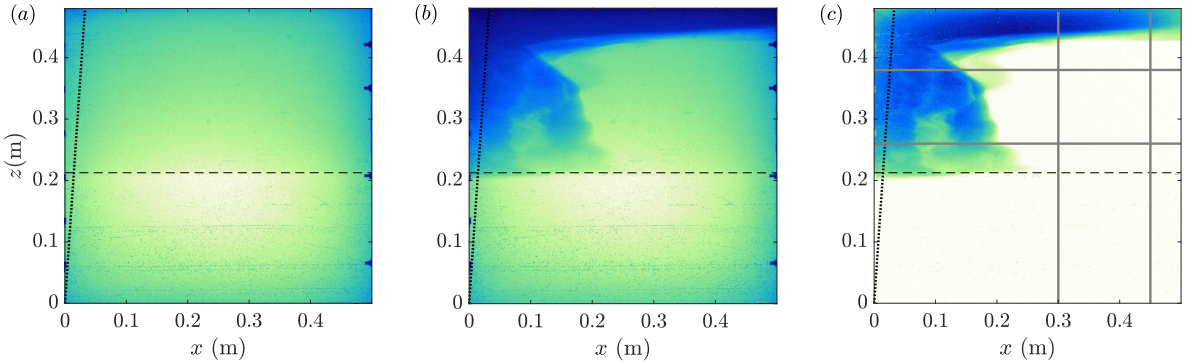

Fig. 6.25 (*a*) Time-average of the raw experimental images recorded during the steady state before the blue dye had been added to the source solution in experiment 12. (*b*) Raw experimental image of the experiment 40 min after the blue dye had been added to the source solution in experiment 12. (*c*) Corrected image where the image from (*a*) is subtracted element-by-element from (*b*). The area in between the horizontal and vertical grey lines show the regions used to vertically and horizontally average the image, for each frame, in order to identify the mean horizontal and vertical motion of the dye in to the ambient, respectively (figure 6.26). The dashed line shows the height of the steady state interface.

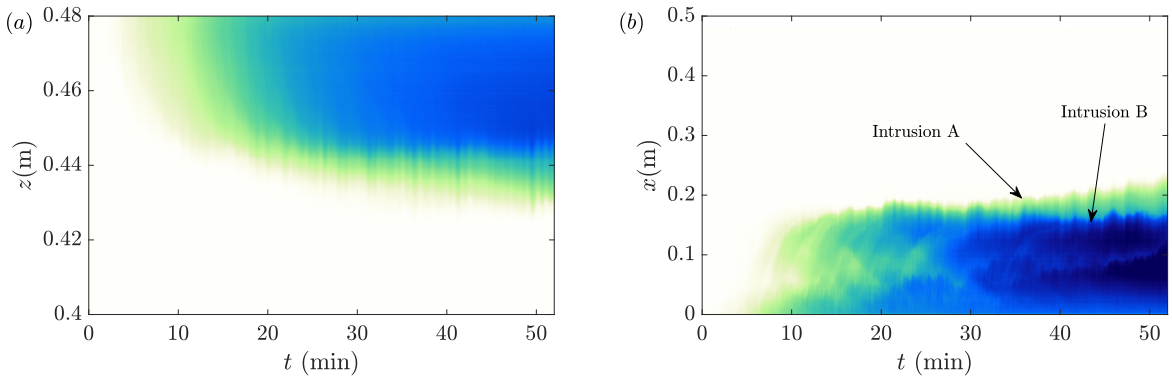

Fig. 6.26 (*a*) Horizontally and (*b*) vertically space-averaged evolution of the blue dye added to the source solution in experiment 12. The regions used to space-average are shown by the grey lines in figure 6.25 (*c*). The figures suggest that there is no net vertical motion within the stratified ambient region $0.20\,\mathrm{m} < x < 0.50\,\mathrm{m}$, $h_i < z < 0.46\,\mathrm{m}$.

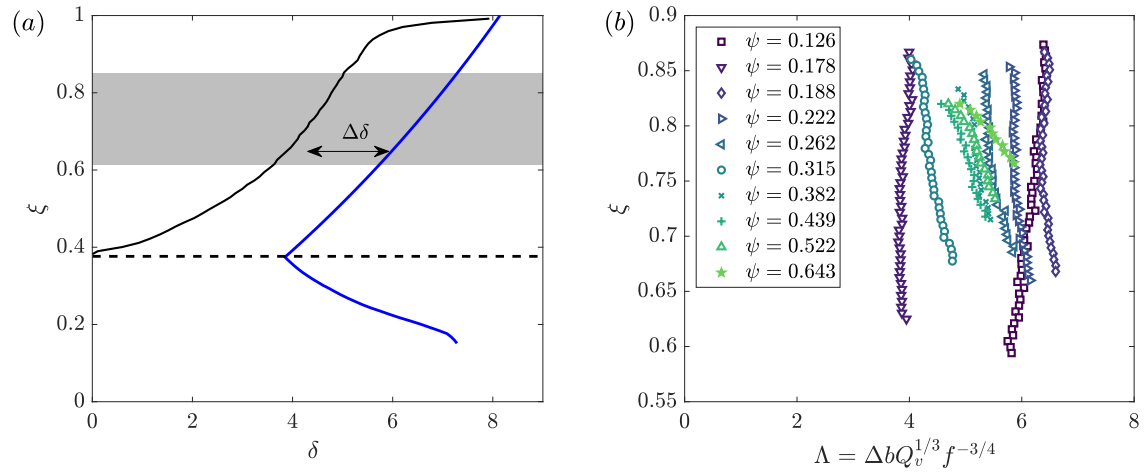

Fig. 6.27 (*a*) The steady state mechanical ventilation model (6.67) and (6.68) (blue), which has been adapted from the model of Gladstone and Woods (2014), compared to experiment 3 (black). The dashed line shows the height of the interface. The height-invariant buoyancy difference between the plume and ambient fluid, predicted by Gladstone and Woods (2014), is shown in the figure. (*b*) Normalised buoyancy difference, $\Lambda = \Delta b Q_v^{1/4} f^{-3/4}$, as a function of height within the stratified core (for example the grey region in (*b*) for experiment 3).

If the source volume flux is ignored, the linear growth rate of plume buoyancy is recovered as derived by Gladstone and Woods (2014). Figure 6.27 (*a*) shows the model prediction for experiment 3 compared against the experimental steady state buoyancy profile. Note the nonlinear profile of the model mean plume buoyancy, which qualitatively follows the ambient buoyancy. In order to test whether the plume and ambient buoyancy difference is independent of depth in the core of the stratified region the buoyancy difference was calculated as a function of height for each experiment. We define the core of the stratified region as the heights between the gravity current and half way between the gravity current and the interface, as highlighted in grey for experiment 3 in figure 6.27 (*a*). In order to identify this stratified core the heights of the inflection points of the steady state profiles were calculated, i.e. the heights ξ_0 such that $\delta_e''(\xi_0) = 0$. The gravity current was then defined as the region $\xi > \xi_0$, where ξ_0 is the second inflection point moving from $\xi = 1$ in the negative ξ direction. Figure 6.27 (*b*) shows the results, where the buoyancy difference has been normalised using $\Lambda = \Delta b Q_v^{1/4} f^{-3/4}$. Figure 6.27 (*b*) shows that the buoyancy difference remains approximately constant for experiments with $\psi < 0.4$. For experiments with $\psi >$ 0.4 there is a noticeable reduction in the buoyancy difference with increasing height. The stratified region within these experiments is relatively small, especially considering only the stratified core. It may be, therefore, that these experiments are unable to develop a balanced entrainment/detrainment region. Gladstone and Woods (2014) suggested that Λ,

or the equivalent non-dimensional constant for a vertically distributed buoyant line plume, should be a constant of order unity because the flow is turbulent so the buoyancy difference should depend only the ventilation flow rate and buoyancy flux per unit area. There is no distinguishable trend of the mean value of Λ for each experiment as a function of ψ, indeed the maximum variation between experiments occurs between experiments with $\psi = 0.126$ and $\psi = 0.178$. Based on the experiments we give a value of $\Lambda = 5.3 \pm 0.8$, which is the mean and standard deviation of the mean value from each experiment.

6.6 Conclusions

The flow resulting from a vertically distributed source of buoyancy was studied by forcing dense source solution through a porous wall. By extending the numerical model of Kaye and Cooper (2018), the plume equations were solved to account for both a finite source volume flux and shear stress coefficient. The plume equations, however, do not account for the laminar region and a virtual origin correction is not possible so in order to identify the laminar region, determine the effect of the laminar region on the flow and in particular identify the region which follows the scalings predicted by Cooper and Hunt (2010), two-dimensional plane velocity measurements normal to the wall were first performed over the whole height of the porous wall. The transition to turbulence was observed to occur at a height of approximately 0.08 m, although a pure plume state was not reached until approximately 0.25 m, where the pure plume criterion was based on a constant Richardson number.

High-resolution simultaneous two-dimensional plane velocity and buoyancy measurements normal to the wall were performed in a region found to the exhibit the scaling laws predicted by Cooper and Hunt (2010), $0.30\,\text{m} < z < 0.42\,\text{m}$. An entrainment coefficient of $\alpha = 0.068 \pm 0.006$ was found and a shear stress coefficient of $C = 0.15$. The entrainment coefficient is not significantly smaller than the entrainment coefficient found for the wall plume in § 5.5.2 of $\alpha_w = 0.076 \pm 0.006$, suggesting that the reduction in entrainment compared to free plume, $\alpha_f = 0.135 \pm 0.010$, is primarily due to the presence of the wall rather than the effect of the vertically distributed buoyancy.

By enclosing the vertically distributed buoyancy source the classical filling-box problem was investigated by using dye attenuation to measure the ambient buoyancy field. By adapting the peeling model of Bonnebaigt et al. (2018) to include direct measurements of the cumulative buoyancy distribution of volume flux, the developing buoyancy stratification was successfully predicted. The mechanically ventilated box problem was also studied. For a fixed buoyancy flux per unit area the developing buoyancy stratification, and in particular the steady state profile, was measured for varying ventilation flow rates. The theory devel-

oped by Gladstone and Woods (2014), whereby a height-invariant buoyancy difference Δb between the mean plume density and the ambient in the stratified region was suggested for a vertical line source of buoyancy, was adapted to the present configuration suggesting that the steady state ambient buoyancy is given by

$$b_e = \frac{fz}{Q_v + qz} - \Delta b, \tag{6.69}$$

within the stratified region, and the buoyancy difference can be expressed as $\Lambda = \Delta b Q_v^{1/4} f^{-3/4}$ for some non-dimensional constant Λ of order unity. Although the theory correctly predicted an invariant buoyancy difference for the lower ventilation experiments within the core of the stratified region, for the higher ventilation flow rates there was an obvious trend that $\mathrm{d}\Delta b/\mathrm{d}z < 0$. The calculated non-dimensional constant Λ was relatively scattered, even across those that followed the theory well, with a value of $\Lambda = 5.3$ with a standard deviation across the ten experiments of 0.8.

Chapter 7

Conclusions

7.1 Review of findings

7.1.1 Axisymmetric plume

In chapter 4 we investigated the turbulent entrainment process in an axisymmetric pure plume. By performing conditional statistics, based on the presence or absence of plume fluid, on the velocity field, it was found that relatively large velocities, $\sim 30\%$ of the maximum vertical velocities, exist within the ambient. Further, the vertical transport of ambient fluid is approximately 5% of the total, whereas the vertical transport of engulfed fluid is approximately 7% of the total. These results indicate that significant vertical momentum is imparted to the ambient fluid before reaching the TNTI and the ambient fluid is accelerating during the engulfment process. Further conditioning of the data by the presence or absence of large coherent structures (eddies) revealed that almost all the vertical transport of ambient fluid occurs at regions with eddies absent, i.e. at heights between eddies. This suggests that the passage of the large eddies drives the pockets of ambient fluid at heights between the eddies providing the vertical momentum necessary to be engulfed by the plume. We conclude that the engulfment of ambient fluid by large scale structures provides a significant contribution to the turbulent entrainment process in pure plumes.

7.1.2 Free and wall line plume

In chapter 5 we investigated the turbulent flow resulting from a horizontal line source of buoyancy in a free environment absent of any boundaries and a line source placed adjacent to a vertical wall. The two configurations were compared and a reduced entrainment coefficient of $\alpha_w = 0.076 \pm 0.006$ in the wall plume was found compared to the free plume of

$\alpha_f = 0.135 \pm 0.010$ consistent with previous studies (e.g. Grella and Faeth (1975); Paillat and Kaminski (2014a); Ramaprian and Chandrasekhara (1989); Sangras et al. (2000)). This corresponds to the free plume entraining 2.5 times more ambient fluid per unit height for a given buoyancy flux, suggesting that each edge of the free plume entrains ambient fluid more efficiently than the wall plume. The reduction in entrainment in the wall plume was investigated by performing an energy decomposition of the wall plume entrainment coefficient based on the decomposition performed by Paillat and Kaminski (2014a) for the free plume entrainment coefficient. The relative contributions from buoyancy, turbulent production and viscous terms to the wall plume entrainment coefficient could be isolated in this way and it was found that the reduction in the turbulent production term, $\sim 30\%$ compared to the free plume, was approximately equal in magnitude to the viscous terms. This suggests that both the momentum drag and the suppression of turbulence production, via suppression of large coherent structures and meandering, by the wall contribute to the reduced entrainment.

The meandering of the free plume was quantified where it was shown that there is a significant probability, $\sim 15\%$, of ambient fluid existing at the mean centreline of the plume that is connected to the ambient far field. This was compared to an axisymmetric plume, using the data from chapter 4, where the equivalent probability is small, $\sim 1\%$. It was hypothesized that increased meandering leads to stretching of the TNTI which was tested by first box-filtering the images with filter size Δ and measuring the time-averaged lengths of the TNTIs for both the free and wall plume. It was shown that the total length of the TNTI of the free plume is, on average, greater than that of the wall plume by a factor of atleast 2.2.

The data were presented in a plume coordinate system defined relative to the instantaneous TNTIs. It was observed that for the region $x_P/X < 0.95$ (i.e. within the plume but outside the adjustment region close to the TNTI) the buoyancy of the free plume varied by at most 9% of the mean buoyancy within that region, whereas the corresponding variation in the wall plume was 52%. This shows that the buoyancy within the free plume is more uniformly mixed than the wall plume, which results in a more top-hat vertical velocity profile in the free plume. The Reynolds stress and horizontal turbulent buoyancy flux were observed to change sign crossing the TNTI for both the free and wall plume. Although not observed in Eulerian coordinates, due to the Reynolds stress in the plume masking the ambient statistics, this is consistent with the entrainment process described by Odier et al. (2012) whereby streamwise momentum and buoyancy are transported towards the plume centreline.

Based on the definition of Craske et al. (2017) of the integral turbulent Prandtl number for an axisymmetric plume, the equivalent integral turbulent Prandtl number was defined for the free plume where an expression was derived in terms of the ratio of the width of the

buoyancy profile to the velocity profile Φ, assuming the profiles have the same shape. The expression of the integral turbulent Prandtl number was compared to the result of Craske et al. (2017) where it was found that, for a given integral turbulent Prandtl number, Φ is greater in the free plume than the axisymmetric plume, which agreed with experimental observations of the free plume compared to previous studies on axisymmetric plumes. The turbulent Prandtl number, as a function of horizontal distance, was calculated for each experiment by height-averaging the scaled data. A characteristic turbulent Prandtl number Pr_{Tc} was defined by the space average of the turbulent Prandtl number within the region where $\overline{w} > 0.01\overline{w}_m$. An average value of $Pr_{Tc} = 0.56 \pm 0.04$ was determined which showed good agreement with the integral turbulent Prandtl number $Pr_{Tm} = 0.47 \pm 0.05$ based on the experimentally determined values of Φ. The results suggest that the integral turbulent Prandtl number provides a robust characterisation of the turbulent Prandtl number within the turbulent region of the free plume.

7.1.3 Vertically distributed plume

In chapter 6 we investigated the turbulent flow resulting from a vertically distributed buoyancy source by forcing relatively dense source solution through a porous wall. Simultaneous velocity and buoyancy field measurements were performed on a vertical plane normal to the wall. An entrainment coefficient of $\alpha = 0.068 \pm 0.006$ was determined which is within the range of previously reported values of $\alpha = [0.014, 0.08]$ (Bonnebaigt et al., 2018; Caudwell et al., 2016; Cooper and Hunt, 2010; Gayen et al., 2016; McConnochie and Kerr, 2015). The entrainment coefficient is similar to that of the wall plume, $\alpha_w = 0.076 \pm 0.006$, which in turn are both significantly lower than the entrainment coefficient of the free line plume, $\alpha_f = 0.135 \pm 0.010$, suggesting that the reduced entrainment in the vertically distributed plume is a result of the processes as described in chapter 5. The shear stress coefficient of $C = 0.15$ was calculated, slightly lower than the value of $C = 0.18$ reported by Gayen et al. (2016). However, as noted by McConnochie and Kerr (2015), a reduced shear stress may be expected in experiments with a convective wall source, such as the present configuration, as compared to experiments with a mostly diffusive wall source, such as that of Gayen et al. (2016). The filling-box and emptying filling-problem was investigated by performing ambient density measurements using dye attenuation. The developing ambient buoyancy stratification of the filling-box was predicted by extending the peeling model of Bonnebaigt et al. (2018) to account for the empirically determined cumulative buoyancy distribution of volume flux. The updated model provided a more accurate prediction of the experimentally measured stratification profiles than the original model of Bonnebaigt et al. (2018). The developing ambient buoyancy, and steady state, profiles were measured for the

emptying filling-box problem for a fixed buoyancy flux per unit area and varying ventilation flow rates. By adding concentrated dye to an experiment after steady state had been established, vertical motion within the ambient fluid was observed to be negligible. The theory of Gladstone and Woods (2014), originally developed for a vertically distributed line source of buoyancy where negligible vertical motion within the steady state ambient was also observed, was adapted to the present configuration and tested against measurements. The theory correctly predicted an invariant buoyancy difference between the mean plume buoyancy and the ambient buoyancy, within the core of the stratified region, for relatively low ventilation flow rates. As the ventilation flow rate increased, however, there was a clear trend that $\mathrm{d}\Delta b/\mathrm{d}z < 0$. Further, a collapse of the scaled buoyancy difference predicted by theory of Gladstone and Woods (2014), $\Lambda = \Delta Q_v^{1/4} f^{-3/4}$, was not observed, even considering only the low ventilation flow rates, with values ranging between $\Lambda = 0.4$ and $\Lambda = 0.7$.

7.2 Further work and applications

Here we discuss possibilities for future study of the material presented in this thesis.

In deriving the free line plume conservation equation for momentum (5.16), the following assumption was made

$$\int_{-\infty}^{\infty} \overline{w'^2} + \frac{1}{\rho_a}\frac{\mathrm{d}\overline{p}}{\mathrm{d}z}\mathrm{d}x \ll \int_{-\infty}^{\infty} \overline{w^2}\mathrm{d}x, \tag{7.1}$$

which was justified from experimental measurements of a free jet (Bradbury, 1965; Miller and Comings, 1957). A useful addition to the current study would be a DNS of a free plume, similar in scope to that of Van Reeuwijk et al. (2016) for an axisymmetric plume, which would allow direct calculation of the individual terms in (7.1) to determine the validity of the approximation. The analogous approximation was also made in the wall plume, therefore a DNS study would also provide a valuable addition to the current study. For the wall plume the DNS study could also help to isolate the contribution to the reduction in entrainment from the no-slip, as opposed to the impermeability, condition of the wall by comparing a no-slip and free-slip boundary condition at the wall, as has been performed for an inclined gravity current by Holzner et al. (2016). Given the large shear stress coefficient found in the vertically distributed plume, a similar comparison between a no-slip and free slip DNS with this configuration would be particularly interesting.

The study of the vertically distributed plume concerned the flow resulting from a vertically distributed buoyant wall. As discussed in 6.1, this has application to a downdraught, a natural convective flow resulting from a relatively cold vertical surface within a build-

ing. Downdraughts, and in particular the gravity current that results from the downdraught spreading along the floor, may be undesirable in cases where the floor is occupied and velocity and relative temperatures exceed comfortable limits. In domestic buildings it is common to place a central heating radiator underneath a window to ameliorate the draught and produce a more pleasant internal environment (CIBSE, 2016). Increasingly, nondomestic buildings have tall glass façades, often located in an atrium, that produce strong undesirable downdraughts in cold weather (Heiselberg, 1994), and various measures are put in place to reduce their effect (Joe et al., 2017; Schellen et al., 2012). These include building balconies and/or providing localised heating to parts of the façade. However, it is acknowledged in the industry that these measures are largely *ad hoc* and that their effectiveness is unknown. In practice there is a lack of assessment methods to quantify the downdraught risk and its effect on occupant thermal comfort. Often expensive computational fluid dynamics studies are required to inform design and identify whether cold drafts compromise performance. Highly glazed spaces, e.g. glazed atria, entrances and courtyards, are often questioned with regard to whether they fulfil their purpose year round and provide an adequately inviting environment. A method with which practitioners can identify and estimate the draft risk would be of great value. An extension to the vertically distributed plume study performed in this thesis could therefore be made by considering passive downdraught mitigation measures adjacent to the wall. The investigation could study the effectiveness and optimisation of a varying number of barriers of varying size and location. In addition, the resulting ambient stratification could measured for the above cases.

In practice, the stratifications that develop within internal spaces are a result of numerous and varied heat sources, e.g a heated wall, multiple occupants and their computers. The next step towards having a complete model of stratification in rooms would be to combine the theories we now have for point sources, distributed horizontal sources and vertically distributed sources into one model.

7.3 Conclusions on turbulent entrainment

The objective of this thesis was to provide novel insights into the large scales processes of turbulent entrainment in buoyancy-driven flows and the mechanisms that result in a reduction of turbulent entrainment in buoyancy-driven wall-bounded flows.

The investigations of the free shear flows (i.e the axisymmetric and free line plumes) have led to novel insights on the role of large coherent structures in the turbulent entrainment process and led to reinterpretation of some previous work on turbulent entrainment. Some of the novel results concerned the effect of the turbulent plume region on the non-turbulent am-

bient region, in particular that significant velocities exist at, and continue to exist relatively far from, the plume edge in vertical regions between two large eddies. So it was reasoned that large eddies provide a mechanism to impart momentum over long ranges through pressure gradients. In addition, the use of conditional statistics based on the presence of ambient fluid showed that significant Reynolds stress magnitudes exist in the ambient when the ambient is close to the centreline of the axisymmetric plume, further demonstrating the effect of the turbulent fluid on the ambient before the fluid is entrained. Previous studies have focused on the effect of the large scale processes only through the mechanism of engulfment (Bisset et al., 2002; Westerweel et al., 2009). While we conclude that engulfment contributes significantly to turbulent entrainment, we also conclude that the effect of the large scale eddies, through the mechanism descried above, plays a dominant role in the engulfment mechanism that has previously been overlooked in the turbulent entrainment process.

A significant part of this thesis was concerned with identifying the differences in turbulent entrainment between the free and wall plume that result in a lower observed entrainment coefficient in the wall plume. The meandering of the free plume has previously been linked to an increase in turbulent production (Sangras et al., 1999, 1998; Turner, 1973). While our conclusions also support this observation we also show that the increased meandering leads to an increased surface area of the TNTI in the free plume, thus more surface for nibbling and enhanced entrainment across the TNTI. Previous studies have attributed the reduction in entrainment almost entirely due to the impermeability condition of the wall (Grella and Faeth, 1975), which results in a reduction in lateral spreading. However, we have identified, through an entrainment decomposition, that the momentum drag of the wall (i.e. the effects of the no-slip condition) plays an equally important role.

Our results for the vertically distributed wall plume show that, in contrast to previous investigations of Bonnebaigt et al. (2018) and Cooper and Hunt (2010) and conclusions from Kaye and Cooper (2018) the entrainment coefficient in the vertically distributed plume to be almost identical to the wall plume. We reasoned that similar mechanisms to the wall plume resulted in reduced entrainment, as compared to the free plume. Much previous work on vertically distributed plumes has been focused on identifying reasons for the significantly reduced entrainment, where observations showed lower values as compared to the wall plume. This study sheds a different light on the two flows suggesting that the entrainment mechanisms are essentially the same which result in very similar entrainment values.

References

Antonia, R. and Browne, L. (1987). Conventional and conditional prandtl number in a turbulent plane wake. *International journal of heat and mass transfer*, 30(10):2023–2030.

Attili, A. and Bisetti, F. (2012). Statistics and scaling of turbulence in a spatially developing mixing layer at reλ= 250. *Physics of Fluids*, 24(3):035109.

Baines, W. D. (1983). A technique for the direct measurement of volume flux of a plume. *Journal of Fluid Mechanics*, 132:247–256.

Baines, W. D. and Turner, J. S. (1969). Turbulent buoyant convection from a source in a confined region. *Journal of Fluid Mechanics*, 37:51–80.

Batchelor, G. (1954). Heat convection and buoyancy effects in fluids. *Quarterly journal of the royal meteorological society*, 80(345):339–358.

Bejan, A. and Lage, J. (1990). Prandtl number effect on the transition in natural convection along a vertical surface. *Journal of Heat Transfer*, 112(3):787–790.

Bisset, D. K., Hunt, J. C., and Rogers, M. M. (2002). The turbulent/non-turbulent interface bounding a far wake. *Journal of Fluid Mechanics*, 451:383–410.

Bonnebaigt, R., Caulfield, C. P., and Linden, P. F. (2018). Detrainment of plumes from vertically distributed sources. *Environmental Fluid Mechanics*, 18(1):3–25.

Borg, A., Bolinder, J., and Fuchs, L. (2001). Simultaneous velocity and concentration measurements in the near field of a turbulent low-pressure jet by digital particle image velocimetry–planar laser-induced fluorescence. *Experiments in fluids*, 31(2):140–152.

Bradbury, L. (1965). The structure of a self-preserving turbulent plane jet. *Journal of Fluid Mechanics*, 23(1):31–64.

Burridge, H., Partridge, J., and Linden, P. (2016). The fluxes and behaviour of plumes inferred from measurements of coherent structures within images of the bulk flow. *Atmosphere-Ocean*, 54(4):403–417.

Burridge, H. C., Parker, D. A., Kruger, E. S., Partridge, J. L., and Linden, P. F. (2017). Conditional sampling of a high Péclet number turbulent plume and the implications for entrainment. *Journal of Fluid Mechanics*, 823:26–56.

Canny, J. (1986). A computational approach to edge detection. *IEEE Transactions on Pattern Analysis and Machine Intelligence*, 646:679–698.

Carazzo, G., Kaminski, E., and Tait, S. (2006). The route to self-similarity in turbulent jets and plumes. *Journal of Fluid Mechanics*, 547:137–148.

Caudwell, T., Flór, J.-B., and Negretti, M.-E. (2016). Convection at an isothermal wall in an enclosure and establishment of stratification. *Journal of Fluid Mechanics*, 799:448–475.

Cenedese, C. and Dalziel, S. B. (1998). Concentration and depth fields determined by the light transmitted through a dyed solution. *Proceedings of the 8th International Symposium on Flow Visualization*.

Chandrasekhar, S. (1957). *An Introduction to the Study of Stellar Structure*. Dover Publications.

Chauhan, K., Philip, J., de Silva, C. M., Hutchins, N., and Marusic, I. (2014). The turbulent/non-turbulent interface and entrainment in a boundary layer. *Journal of Fluid Mechanics*, 742:119–151.

Cheesewright, R. (1968). Turbulent natural convection from a vertical plane surface. *Journal of Heat Transfer*, 90:1–6.

CIBSE (2016). *GVB1/16 CIBSE Guide B1: Heating 2016*. Chartered Institution of Building Services Engineers (CIBSE).

Coomaraswamy, I. and Caulfield, C. (2011). Time-dependent ventilation flows driven by opposing wind and buoyancy. *Journal of Fluid Mechanics*, 672:33–59.

Coomaraswamy, I. A. (2011). Natural ventilation of buildings: Time-dependent phenomena (doctoral thesis).

Cooper, P. and Hunt, G. (2010). The ventilated filling box containing a vertically distributed source of buoyancy. *Journal of Fluid Mechanics*, 646:39–58.

Corrsin, S. and Kistler, A. L. (1955). Free-stream boundaries of turbulent flows. *Tech. Rep.* National Advisory Committee for Aeronautics.

Crapper, P. F. and Linden, P. F. (1974). The structure of turbulent density interfaces. *Journal of Fluid Mechanics*, 65(1):45–63.

Craske, J., Salizzoni, P., and van Reeuwijk, M. (2017). The turbulent Prandtl number in a pure plume is 3/5. *Journal of Fluid Mechanics*, 822:774–790.

Crimaldi, J. (1997). The effect of photobleaching and velocity fluctuations on single-point LIF measurements. *Experiments in Fluids*, 23(4):325–330.

Crimaldi, J. (2008). Planar laser induced fluorescence in aqueous flows. *Experiments in fluids*, 44(6):851–863.

da Silva, C. B., Hunt, J. C., Eames, I., and Westerweel, J. (2014). Interfacial layers between regions of different turbulence intensity. *Annual review of fluid mechanics*, 46:567–590.

da Silva, C. B. and Taveira, R. R. (2010). The thickness of the turbulent/nonturbulent interface is equal to the radius of the large vorticity structures near the edge of the shear layer. *Physics of Fluids*, 22(12):121702.

Dalziel, S. B. (2017). *DigiFlow User Guide*. Dalziel Research Partners.

Dalziel, S. B., Carr, M., Sveen, J. K., and Davies, P. A. (2007). Simultaneous synthetic schlieren and piv measurements for internal solitary waves. *Measurement Science and Technology*, 18(3):533.

Dalziel, S. B., Patterson, M. D., Caulfield, C., and Coomaraswamy, I. A. (2008). Mixing efficiency in high-aspect-ratio rayleigh–taylor experiments. *Physics of Fluids*, 20(6):065106.

de Silva, C. M., Philip, J., Chauhan, K., Meneveau, C., and Marusic, I. (2013). Multiscale geometry and scaling of the turbulent-nonturbulent interface in high Reynolds number boundary layers. *Phys. Rev. Lett.*, 111:044501.

Ellison, T. H. and Turner, J. S. (1959). Turbulent entrainment in stratified flows. *Journal of Fluid Mechanics*, 6:423–448.

Ezzamel, A., Salizzoni, P., and Hunt, G. R. (2015). Dynamic variability of axisymmetric buoyant plumes. *Journal of Fluid Mechanics*, 765:576–611.

Ferrier, A. J., Funk, D. R., and Roberts, P. J. W. (1993). Application of optical techniques to the study of plumes in stratified fluids. *Dynamics of Atmospheres and Oceans*, 20(1):155 – 183. American Geophysical Union Ocean Sciences Meeting.

Fischer, H., List, J., Imberger, J., Koh, C., and Brooks, N. (1979). *Mixing in Inland and Coastal Waters*. Academic Press.

Gampert, M., Boschung, J., Hennig, F., Gauding, M., and Peters, N. (2014). The vorticity versus the scalar criterion for the detection of the turbulent/non-turbulent interface. *Journal of Fluid Mechanics*, 750:578–596.

Gayen, B., Griffiths, R. W., and Kerr, R. C. (2016). Simulation of convection at a vertical ice face dissolving into saline water. *Journal of Fluid Mechanics*, 798:284–298.

Gladstone, C. and Woods, A. W. (2014). Detrainment from a turbulent plume produced by a vertical line source of buoyancy in a confined, ventilated space. *Journal of Fluid Mechanics*, 742:35–49.

Grella, J. J. and Faeth, G. M. (1975). Measurements in a two-dimensional thermal plume along a vertical adiabatic wall. *Journal of Fluid Mechanics*, 71:701–710.

Heiselberg, P. (1994). Draught risk from cold vertical surfaces. *Building and Environment*, 29(3):297 – 301. Special Issue Papers from Indoor Air '93.

Hogg, C. A., Dalziel, S. B., Huppert, H. E., and Imberger, J. (2017). Inclined gravity currents filling basins: the impact of peeling detrainment on transport and vertical structure. *Journal of Fluid Mechanics*, 820:400–423.

Holling, M. and Herwig, H. (2005). Asymptotic analysis of the near-wall region of turbulent natural convection flows. *Journal of Fluid Mechanics*, 541:383–397.

Holzner, M., Avila, M., de Lozar, A., and Hof, B. (2011). A lagrangian approach to the interface velocity of turbulent puffs in pipe flow. In *Journal of Physics: Conference Series*, volume 318, page 052031. IOP Publishing.

Holzner, M., Lüthi, B., Tsinober, A., and Kinzelbach, W. (2009). Acceleration, pressure and related quantities in the proximity of the turbulent/non-turbulent interface. *Journal of Fluid Mechanics*, 639:153–165.

Holzner, M., van Reeuwijk, M., and Jonker, H. (2016). Turbulent entrainment in a gravity current. *Sustainable Hydraulics in the Era of Global Change: Proceedings of the 4th European Congress of the International Association of Hydroenvironment engineering and Research, IAHR 2016*, pages 1025–1031.

Hübner, J. (2004). Buoyant plumes in a turbulent environment (doctoral thesis).

Hunt, G. and Kaye, N. (2001). Virtual origin correction for lazy turbulent plumes. *Journal of Fluid Mechanics*, 435:377–396.

Joe, G., Kim, D., Park, S., Park, S., Yeo, M., and Kim, K. (2017). Downdraft assessment of glass curtain wall buildings with a radiant floor heating system. *Applied Sciences*, 7(10):1075.

Kaminski, E., Tait, S., and Carazzo, G. (2005). Turbulent entrainment in jets with arbitrary buoyancy. *Journal of Fluid Mechanics*, 526:361–376.

Kaye, N. and Linden, P. (2004). Coalescing axisymmetric turbulent plumes. *Journal of Fluid Mechanics*, 502:41–63.

Kaye, N. B. and Cooper, P. (2018). Source and boundary condition effects on unconfined and confined vertically distributed turbulent plumes. *Journal of Fluid Mechanics*, 850:1032–1065.

Kim, J. (1987). Evolution of a vortical structure associated with the bursting event in a channel flow. In *Turbulent Shear Flows 5*, pages 221–233. Springer.

Kotsovinos, N. (1975). Study of the entrainment and turbulence in a plane buoyancy jet. *California Institute of Technology , Pasadena, CA*.

Krug, D., Chung, D., Philip, J., and Marusic, I. (2017). Global and local aspects of entrainment in temporal plumes. *Journal of Fluid Mechanics*, 812:222–250.

Krug, D., Holzner, M., Lüthi, B., Wolf, M., Kinzelbach, W., and Tsinober, A. (2013). Experimental study of entrainment and interface dynamics in a gravity current. *Experiments in fluids*, 54(5):1530.

Krug, D., Holzner, M., Lüthi, B., Wolf, M., Kinzelbach, W., and Tsinober, A. (2015). The turbulent/non-turbulent interface in an inclined dense gravity current. *Journal of Fluid Mechanics*, 765:303–324.

Lai, M.-C. and Faeth, G. (1987). Turbulent structure of vertical adiabatic wall plumes. *Journal of Heat Transfer*, 109(3):663–670.

Landel, J. R., Caulfield, C., and Woods, A. W. (2012). Meandering due to large eddies and the statistically self-similar dynamics of quasi-two-dimensional jets. *Journal of Fluid Mechanics*, 692:347–368.

Lee, S. L. and Emmons, H. W. (1961). A study of natural convection above a line fire. *Journal of Fluid Mechanics*, 11:353–368.

Lemoine, F., Wolff, M., and Lebouche, M. (1996). Simultaneous concentration and velocity measurements using combined laser-induced fluorescence and laser doppler velocimetry: Application to turbulent transport. *Experiments in Fluids*, 20(5):319–327.

Linden, P. F., Dalziel, S. B., Zhou, Q., Partridge, J., Lefauve, A., and Caulfield, C. P. (2018). The structure and origin of confined Holmboe waves.

Linden, P. F., Lane-Serf, G. C., and Smeed, D. A. (1990). Emptying filling spaces: the fluid mechanics of natural ventilation. *Journal of Fluid Mechanics*, 212:300–335.

McConnochie, C. and Kerr, R. (2015). The turbulent wall plume from a vertically distributed source of buoyancy. *Journal of Fluid Mechanics*, 787:237–253.

Meneveau, C. and Sreenivasan, K. R. (1990). Interface dimension in intermittent turbulence. *Phys. Rev. A*, 41:2246–2248.

Miller, D. R. and Comings, E. W. (1957). Static pressure distribution in the free turbulent jet. *Journal of Fluid Mechanics*, 3(1):1–16.

Miroshnichenko, I. and Sheremet, M. (2018). Turbulent natural convection heat transfer in rectangular enclosures using experimental and numerical approaches: A review. *Renewable and Sustainable Energy Reviews*, 82:40 – 59.

Mistry, D., Dawson, J. R., and Kerstein, A. R. (2018). The multi-scale geometry of the near field in an axisymmetric jet. *Journal of Fluid Mechanics*, 838:501–515.

Mistry, D., Philip, J., Dawson, J. R., and Marusic, I. (2016). Entrainment at multi-scales across the turbulent/non-turbulent interface in an axisymmetric jet. *Journal of Fluid Mechanics*, 802:690–725.

Morton, B. R., Taylor, G. I., and Turner, J. S. (1956). Turbulent gravitational convection from maintained and instantaneous sources. *Proc. R. Soc. Lond.*, 234:1–24.

Odier, P., Chen, J., and Ecke, R. (2012). Understanding and modeling turbulent fluxes and entrainment in a gravity current. *Physica D: Nonlinear Phenomena*, 241(3):260–268. Special Issue on Small Scale Turbulence.

Odier, P., Chen, J., and Ecke, R. E. (2014). Entrainment and mixing in a laboratory model of oceanic overflow. *Journal of Fluid Mechanics*, 746:498–535.

Olsthoorn, J. and Dalziel, S. B. (2017). Three-dimensional visualization of the interaction of a vortex ring with a stratified interface. *Journal of Fluid Mechanics*, 820:549–579.

Ottino, J. M. J. M. (1989). *The kinematics of mixing: stretching, chaos, and transport /*. Cambridge University Press, Cambridge :.

Paillat, S. and Kaminski, E. (2014a). Entrainment in plane turbulent pure plumes. *Journal of Fluid Mechanics*, 755:R2.

Paillat, S. and Kaminski, E. (2014b). Second-order model of entrainment in planar turbulent jets at low Reynolds number. *Physics of Fluids*, 26(4):045110.

Panchapakesan, N. and Lumley, J. (1993). Turbulence measurements in axisymmetric jets of air and helium. part 1. air jet. *Journal of Fluid Mechanics*, 246:197–223.

Papanicolaou, P. N. and List, E. J. (1988). Investigations of round vertical turbulent buoyant jets. *Journal of Fluid Mechanics*, 195:341–391.

Papantoniou, D. and List, E. J. (1989). Large-scale structure in the far field of byoyant jets. *Journal of Fluid Mechanics*, 209:151–190.

Parker, D. A., Burridge, H. C., Partridge, J. L., and Linden, P. F. (2020). A comparison of entrainment in turbulent line plumes adjacent to and distant from a vertical wall. *Journal of Fluid Mechanics*, 882:A4.

Partridge, J., Lefauve, A., and Dalziel, S. B. (2019). A versatile scanning method for volumetric measurements of velocity and density fields. *Measurement Science and Technology*, 30(5):055203.

Philip, J., Meneveau, C., de Silva, C. M., and Marusic, I. (2014). Multiscale analysis of fluxes at the turbulent/non-turbulent interface in high Reynolds number boundary layers. *Physics of Fluids*, 26(1):015105.

Pirovano, A., Viannay, S., and Jannot, M. (1970). Convection naturelle en régime turbulent le long d'une plaque plane verticale. eur 4489. = natural convection in turbulent regime along a flat plate. eur 4489. *Proc. 9th Int. Heat Transfer Conf.*, 4:1–12.

Pope, S. B. (2000). *Turbulent Flows*. Cambridge University Press.

Prandtl, L. (1925). Bericht über untersuchungen zur ausgebildeten turbulenz. *ZAMM-Journal of Applied Mathematics and Mechanics/Zeitschrift für Angewandte Mathematik und Mechanik*, 5(2):136–139. (Available in English translation as NACA TM 1231, 1949.).

Prasad, A. (2000). Particle image velocimetry. *Current science*, 79:51–60.

Prasad, R. R. and Sreenivasan, K. R. (1989). Scalar interfaces in digital images of turbulent flows. *Experiments in Fluids*, 7(4):259–264.

Priestley, C. and Ball, F. (1955). Continuous convection from an isolated source of heat. *Quarterly Journal of the Royal Meteorological Society*, 81(348):144–157.

Ramaprian, B. R. and Chandrasekhara, M. S. (1989). Measurements in vertical plane turbulent plumes. *Journal of Fluids Engineering*, 111:69–77.

Robinson, S. K. (1991). Coherent motions in the turbulent boundary layer. *Annual Review of Fluid Mechanics*, 23(1):601–639.

Rouse, H., YIH, C. S., and Humphreys, H. W. (1952). Gravitational convection from a boundary source. *Tellus*, 4(3):201–210.

Rumble, J. R. (2019). *CRC Handbook of Chemistry and Physics, 100th Edition (Internet Version 2019)*. CRC Press/Taylor and Francis.

Sangras, R., Dai, Z., and Faeth, G. (1999). Mixture fraction statistics of plane self-preserving buoyant turbulent adiabatic wall plumes. *Journal of Heat Transfer*, 121(4):837–843. 10.1115/1.2826073.

Sangras, R., Dai, Z., and Faeth, G. (2000). Velocity statistics of plane self-preserving buoyant turbulent adiabatic wall plumes. *Journal of Heat Transfer*, 122(4):693–700.

Sangras, R., Dai, Z., and Faeth, G. M. (1998). Mixing structure of a plane self-preserving buoyant turbulent plumes. *Journal of Heat Transfer*, 120:1033–1041.

Scase, M., Caulfield, C., Linden, P., and Dalziel, S. (2007). Local implications for self-similar turbulent plume models. *Journal of Fluid Mechanics*, 575:257–265.

Schellen, L., Timmers, S., Loomans, M., Nelissen, E., Hensen, J., and van Marken Lichtenbelt, W. (2012). Downdraught assessment during design: Experimental and numerical evaluation of a rule of thumb. *Building and Environment*, 57:290 – 301.

Schlichting, H. and Gersten, K. (2017). *Boundary-Layer Theory*. Spinger-Verlag.

Schmidt, W. (1941). Turbulente ausbreitung eines stromes erhitzter luft. *ZAMM-Journal of Applied Mathematics and Mechanics/Zeitschrift für Angewandte Mathematik und Mechanik*, 21(5):265–278.

Shabbir, A. and George, W. K. (1994). Experiments on a round turbulent buoyant plume. *Journal of Fluid Mechanics*, 275:1–32.

Shan, J. W., Lang, D. B., and Dimotakis, P. E. (2004). Scalar concentration measurements in liquid-phase flows with pulsed lasers. *Experiments in Fluids*, 36(2):268–273.

Sreenivas, K. and Prasad, A. K. (2000). Vortex-dynamics model for entrainment in jets and plumes. *Physics of Fluids*, 12(8):2101–2107.

Taveira, R. R. and da Silva, C. B. (2013). Kinetic energy budgets near the turbulent/nonturbulent interface in jets. *Physics of Fluids*, 25(1):015114.

Taylor, G. I. (1945). *Dynamics of a Mass of Hot Gas Rising in Air*. U .S. Atomic Energy Commission MDDC 919. LADC 276 Los Alamos, NM: Los Alamos National Laboratory Research Library.

Tennekes, H., Lumley, J. L., Lumley, J., et al. (1972). *A first course in turbulence*. MIT press.

Terashima, O., Sakai, Y., Nagata, K., Ito, Y., Onishi, K., and Shouji, Y. (2016). Simultaneous measurement of velocity and pressure near the turbulent/non-turbulent interface of a planar turbulent jet. *Experimental Thermal and Fluid Science*, 75:137–146.

Townsend, A. (1948). Local isotropy in the turbulent wake of a cylinder. *Australian Journal of Chemistry*, 1(2):161–174.

Townsend, A. (1949a). The fully developed wake of a circular cylinder. *Australian Journal of Chemistry*, 2(4):451–468.

Townsend, A. (1949b). Momentum and energy diffusion in the turbulent wake of a cylinder. *Proceedings of the Royal Society of London. Series A. Mathematical and Physical Sciences*, 197(1048):124–140.

Townsend, A. (1976). *The structure of turbulent shear flow*. Cambridge university press.

Tsuji, T. and Nagano, Y. (1988). Characteristics of a turbulent natural convection boundary layer along a vertical flat plate. *International Journal of Heat and Mass Transfer*, 31:1723–1734.

Turner, J. (1986). Turbulent entrainment: the development of the entrainment assumption, and its application to geophysical flows. *Journal of Fluid Mechanics*, 173:431–471.

Turner, J. S. (1973). *Buoyancy effects in fluids*. Cambridge University Press.

van Reeuwijk, M. and Craske, J. (2015). Energy-consistent entrainment relations for jets and plumes. *Journal of Fluid Mechanics*, 782:333–355.

Van Reeuwijk, M., Salizzoni, P., Hunt, G. R., and Craske, J. (2016). Turbulent transport and entrainment in jets and plumes: A dns study. *Physical Review Fluids*, 1(7):074301.

Vanderwel, C. and Tavoularis, S. (2014). On the accuracy of PLIF measurements in slender plumes. *Experiments in fluids*, 55(8):1801.

Vliet, G. and Liu, C. (1969). An experimental study of turbulent natural convection boundary layers. *Journal of Heat Transfer*, 91(4):517–531. 10.1115/1.3580236.

Wang, H. and Law, A. W.-k. (2002). Second-order integral model for a round turbulent buoyant jet. *Journal of Fluid Mechanics*, 459:397–428.

Wells, A. J. and Worster, M. G. (2008). A geophysical-scale model of vertical natural convection boundary layers. *Journal of Fluid Mechanics*, 609:111–137.

Westerweel, J., Fukushima, C., Pedersen, J. M., and Hunt, J. C. R. (2005). Mechanics of the turbulent-nonturbulent interface of a jet. *Phys. Rev. Lett.*, 95:174501.

Westerweel, J., Fukushima, C., Pedersen, J. M., and Hunt, J. C. R. (2009). Momentum and scalar transport at the turbulent/non-turbulent interface of a jet. *Journal of Fluid Mechanics*, 631:199–230.

Willert, C. (1997). Stereoscopic digital particle image velocimetry for application in wind tunnel flows. *Measurement Science and Technology*, 8(12):1465.

Yih, C. S. (1991). *Turbulent buoyant plumes*. World Scientific.

Ying, C., Davidson, M., Wang, H., and Law, A. (2004). Radial velocities in axisymmetric jets and plumes. *Journal of Hydraulic Research*, 42(1):29–33.

Yuana, L.-M. and Cox, G. (1996). An experimental study of some line fires. *Fire Safety Journal*, 27(2):123–139.

Zeldovich, Y. B. (1937). The asymptotic laws of freely-ascending convective flows. *Zhur. Eksper. Teor. Fiz*, 7(12):1463–1465.

Appendix A

Here we assess the error associated with the PLIF density measurements in the free and wall plume in § 5 and the vertically distributed plume in § 6 due to the laser intensity fluctuations and the attenuation due to the dye and added salts and justify performing a two-point calibration.

A.1 Free and wall plume experiments

A two-point calibration relies on the assumption that the local illumination intensity between the calibration image of mixed dye $I_m(x,z)$ and the background $I_b(x,z)$ are approximately equal. Further, that the local illumination intensity between the calibration images and the experiment $I(x,z,t)$ are also approximately equal. Typically, however, the local illumination intensity in an experiment is not known since it varies spatially and temporally as a function of the absorption of the laser light that occurs along its path (e.g. Chandrasekhar (1957), page 190) or, as it is typically referred to, attenuation. The Bouguer-Lambert-Beer law may be used to relate the local illumination intensity of a reference medium $I_0(x,z)$ to the local illumination intensity $I(x,z,t)$ in an absorbing medium, where the light is assumed to travel parallel to the z direction, as

$$I(x,z,t) = I_0(x,z)\exp\left(-\int_0^z \sum_{i=1}^{N} \varepsilon_i c_i(x,z',t)\,\mathrm{d}z'\right), \tag{A.1}$$

where ε_i are the extinction coefficients of the absorbing media with concentrations c_i.

First we consider the free plume experiments. In order to describe the analysis we consider experiment 1, however, we give the analogous final results at the end of this section for all the experiments. The measurement window is 0.16 m in height and the bottom of the measurement window z_1, with $z = 0$ m at the top of the measurement window (see figure A.1), is at a distance 0.325 m from the base of the tank. The path of the light rays along

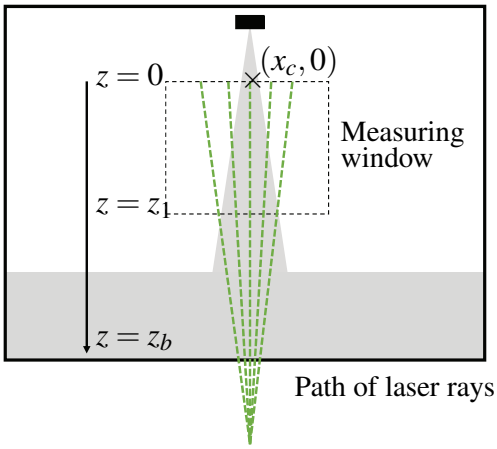

Fig. A.1 Schematic of the free plume experiment highlighting the features used in the laser beam attenuation analysis.

the mean centreline of the plume were approximately parallel to the z direction. Given that the maximum dye attenuation due to the plume is likely to occur along the mean centreline of the plume we consider the local illumination intensity at the maximum height from the base of the tank, which is at $z_b = 0.485\,\mathrm{m}$, within the measurement window at the centreline x_c of the plume, and we make the assumption that the path of the laser travels along the path $x = x_c$.

We define the local illumination intensity at the position $(x_c, 0)$ (the position of the cross in figure A.1) in the tank containing fresh water by I_0. We define the local illumination intensity in the tank containing a sodium chloride (NaCl) solution concentration c_s at the same point by I_b. These may be related to each other using (A.1) by

$$I_b = I_0 \exp(-\varepsilon_s c_s z_b), \tag{A.2}$$

where ε_s is the extinction coefficient for NaCl.

The background calibration image used in the two-point calibration contained NaCl solution at the concentration used in the ambient fluid of the experiments. The intensity I_b may therefore be considered as the background calibration image. The intensity of the mixed calibration image I_m of a known concentration c_d of Rhodamine 6G with the same NaCl solution as I_b may be related to the background image by

$$I_m = I_b \exp(-\varepsilon_d c_d z_b), \tag{A.3}$$

where ε_d is the extinction coefficient for Rhodamine 6G.

For an experiment with initial ambient NaCl concentration $c_{s,0}$ and source sodium nitrate ($NaNO_3$) and Rhodamine 6G concentration $c_{n,0}$ and $c_{d,0}$, respectively, the local illumination intensity during the experiment is given by

$$I(t) = I_0 \exp\left(-\int_0^{z_b} \gamma\varepsilon_d c_{d,0} + \gamma\varepsilon_n c_{n,0} + (1-\gamma)\varepsilon_s c_{s,0}\,\mathrm{d}z\right), \tag{A.4}$$

where ε_n is the extinction coefficient for $NaNO_3$ and $\gamma = \gamma(z,t)$ is the plume fluid concentration relative to the source solution, so that $\gamma = 0$ in the unmixed ambient fluid and $\gamma = 1$ in the unmixed source solution. The relation (A.4) can be written in terms of I_b as

$$I(t) = I_b \exp\left(-\int_0^{z_b} \gamma\varepsilon_d c_{d,0} + \gamma\varepsilon_n c_{n,0} - \gamma\varepsilon_s c_{s,0}\,\mathrm{d}z\right) \tag{A.5}$$

$$= I_b \exp\left(-(\varepsilon_d c_{d,0} + \varepsilon_n c_{n,0} - \varepsilon_s c_{s,0}) \int_0^{z_b} \gamma\,\mathrm{d}z\right) \tag{A.6}$$

$$= I_b \exp\left(-z_b(\varepsilon_d c_{d,0} + \varepsilon_n c_{n,0} - \varepsilon_s c_{s,0}) \frac{1}{z_b} \int_0^{z_b} \gamma\,\mathrm{d}z\right). \tag{A.7}$$

The value $\frac{1}{z_1}\int_0^{z_1} \gamma\,\mathrm{d}z'$ for each image may be estimated directly from the LIF measurements. The measurements from experiment 1 give a time-averaged value of

$$\frac{1}{T}\frac{1}{z_1}\int_0^T \int_0^{z_1} \gamma\,\mathrm{d}z\,\mathrm{d}t = 0.0396, \tag{A.8}$$

with a standard deviation of $\sigma = 0.0050$ and a maximum value of 0.0550. In order to provide a reasonable estimate for the worst-case attenuation for the region below the measurement window, considering the additional dilution that will result, we assume that $\gamma(z) = \overline{\gamma(z_1)} = 0.0232$ for $z > z_1$, where $\overline{\gamma}$ is the time-average of γ.

By assuming the worst-case value for the measurement window, $\gamma(z) = 0.0565$, we find that

$$\frac{1}{z_b}\int_0^{z_b} \gamma\,\mathrm{d}z = 0.0373. \tag{A.9}$$

Extinction coefficient values used in this analysis are based on a calibration performed in collaboration with Jamie Partridge (see A.3 for full details) giving values of $\varepsilon_d = 1.64 \times 10^{-2}\ \mathrm{m}^{-1}(\mu\mathrm{g/l})^{-1}$, $\varepsilon_s = 4.2 \times 10^{-3}\ \mathrm{m}^{-1}(\mathrm{g/l})^{-1}$ and $\varepsilon_n = 8.8 \times 10^{-4}\ \mathrm{m}^{-1}(\mathrm{g/l})^{-1}$. The concentrations used in the free plume experiment 1 were $c_{d,0} = 200\,\mu\mathrm{g\,l}^{-1}$, $c_{s,0} = 78\,\mathrm{g\,l}^{-1}$ and $c_{n,0} = 120\,\mathrm{g\,l}^{-1}$. Using the extinction coefficient for the Rhodamine 6G and concentration used in the mixed calibration image, $c_d = 6.7\,\mu\mathrm{g\,l}^{-1}$, gives

$$I_m = 0.949 I_b. \tag{A.10}$$

Experiment	1	2	3	4	5	6	7	8	9	10
I_m/I_b	0.949	0.947	0.947	0.952	0.952	0.957	0.957	0.957	0.954	0.954
$\min(I/I_b)$	0.948	0.945	0.955	0.948	0.945	0.947	0.944	0.946	0.947	0.952

Table A.1 Relative attenuation of the mixed calibration image to the background image, I_m/I_b, and the maximum attenuation of the experimental images relative to the background image, $\min(I/I_b)$, of the experiments.

This implies the local illumination intensity is at most 5.1% smaller in the mixed calibration than the background calibration. For the experimental images, from the relation (A.7), we find that

$$I = 0.948 I_b. \tag{A.11}$$

which shows that the local illumination intensity is at most 5.2% less in any experiment than the background calibration. Importantly, this suggests that the maximum difference between the intensity of any two of the three images is less than 5.2%. Table A.1 shows the analogous results results for all the free plume experiments showing that across all the experiments the error due to the attenuation was at most 5.5%.

Attenuation of the fluoresced dye also occurs, in particular along the path between the camera and the measurement plane. The attenuation of the fluoresced signal is known to be weaker than the incident laser light due to the change in wavelength (Lemoine et al., 1996). The maximum integrated fraction of dye concentration between the measurement plane and the camera may be estimated by

$$\int_0^{y_{1/2}} \overline{\gamma}(x = x_c, y, z = 0)\, \mathrm{d}y = 0.0045\,\mathrm{m}, \tag{A.12}$$

where $y_{1/2} = 0.075\,\mathrm{m}$ is the midway from the bounding wall to the measurement plane. This is significantly less than the estimate of the vertically integrated path within the measurement region obtained from (A.9) of $0.018\,\mathrm{m}$. This suggests that the effect of the attenuation due to the fluoresced dye along the path between the camera and the measurement plane is negligible as compared to the attenuation of the laser light within the measurement plane.

The maximum relative attenuation of the mixed calibration and experimental images may also be calculated for the wall plume where $z_1 = 0.157\,\mathrm{m}$ and $z_b = 0.352\,\mathrm{m}$. These values are given in table A.1 which shows that across all the wall plume experiments the error due to the attenuation was at most 5.6%. In addition, the effect of the attenuation of the fluoresced dye is also estimated to be negligible.

Experiment	1	2	3	4
I_m/I_b	0.983	0.983	0.979	0.979
$\min(I/I_b)$	0.985	0.982	0.980	0.979

Table A.2 Relative attenuation of the mixed calibration image to the background image, I_m/I_b, and the maximum attenuation of the experimental images relative to the background image, $\min(I/I_b)$, of the vertically distributed wall plume experiments.

A.2 Vertically distributed plume

The maximum relative attenuation of the mixed calibration and experimental images may also be calculated for the vertically distributed wall plume experiments from chapter 6 with $z_m = 0.27\,\text{m}$ and $z_1 = 0.15\,\text{m}$. These values are given in table A.2 which shows that the maximum difference between the intensity of any two of the three images used in the calibration is less than 3.1%.

A.3 Calibration of extinction coefficients [1]

A series of calibration experiments were performed to determine the extinction coefficients ε_d, ε_n and ε_s. For the Rhodamine 6G coefficient, ε_d, the laser system was positioned so that the beam passed through a 1 m long tank before reaching a Gentec-eo energy meter (model QE25LP-H-MB). To perform the calibration, first a background state E_0 was recorded with the tank filled with fresh water and then the average energy of 1000 pulses was logged on the energy meter. Subsequent recordings were made after incrementally adding Rhodamine 6G dye to the calibration tank. The decay of the energy E, due to attenuation, can be seen in figure A.2. From these data, we find that $\varepsilon_d = 1.64 \times 10^{-2}\ \text{m}^{-1}(\mu\text{g/l})^{-1}$, as shown by the dashed line in figure A.2.

The same calibration procedure was attempted for the salts, however, due to refractive index changes, the energy meter did not appear to be a robust method of capturing the attenuation. Therefore, a different calibration procedure was utilised for the salts. The same 1 m long tank was used but, instead of the laser, a DC powered LED light bank provided illumination. The light from the LED bank travelled through the length of the tank (1 m) before being recorded by a Dalsa Falcon2 4 MP CMOS camera fitted with a bandpass filter centred at the wavelength of the laser (532 nm), to ensure we are only measuring the extinction coefficient at the appropriate wavelength. Just as a dye attenuation system

[1] This section comprises analysis that was performed by Jamie Partridge contributing to the collaborative publication Parker et al. (2020).

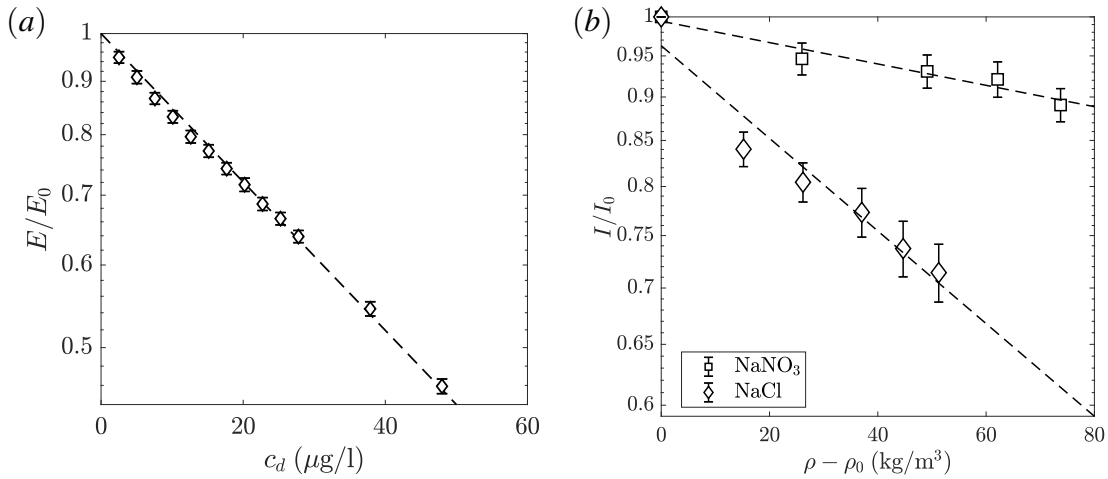

Fig. A.2 Extinction coefficient calibration experiments for (*a*) Rhodamine 6G and the (*b*) salts. The best fit lines (dashed) yield $\varepsilon_d = 1.64 \times 10^{-2}\ \mathrm{m}^{-1}(\mu\mathrm{g/l})^{-1}$, $\varepsilon_n = 1.406\ \mathrm{m}^{-1}(\Delta\rho_n)^{-1}$ and $\varepsilon_s = 6.094\ \mathrm{m}^{-1}(\Delta\rho_s)^{-1}$, where $\Delta\rho_{s/n} = \rho_{s/n} - \rho_0$ and ρ_0 is the density of fresh water.

would be calibrated, a background image was captured with fresh water I_0 and subsequent images I were captured for various salt concentrations. Figure A.2 shows the calibration results using this methodology for the salts where we find $\varepsilon_n = 1.41\ \mathrm{m}^{-1}(\Delta\rho_n)^{-1}$ and $\varepsilon_s = 6.09\ \mathrm{m}^{-1}(\Delta\rho_s)^{-1}$ as the extinction coefficients for $NaNO_3$ and NaCl, respectively. Here, $\Delta\rho_{s/n}$ signifies the change in density due to the corresponding salt, subscript s for NaCl and n for $NaNO_3$, where

$$\Delta\rho_s = 0.000685 c_s, \tag{A.13}$$

$$\Delta\rho_n = 0.000628 c_n, \tag{A.14}$$

which results in the extinction coefficients $\varepsilon_s = 4.2 \times 10^{-3}\ \mathrm{m}^{-1}(\mathrm{g/l})^{-1}$ and $\varepsilon_n = 8.8 \times 10^{-4}\ \mathrm{m}^{-1}(\mathrm{g/l})^{-1}$.